An Asymptotic Model of Electroporation-Mediated Molecular Delivery in Skeletal Muscle Tissue

by

Jonathan P. Cranford

Department of Biomedical Engineering
Duke University

Date: _____

Approved:

_____
Wanda K. Neu, Supervisor

_____
Roger C. Barr

_____
Thomas J. McIntosh

_____
Thomas P. Witelski

_____
Fan Yuan

Dissertation submitted in partial fulfillment of the requirements for the degree of
Doctor of Philosophy in the Department of Biomedical Engineering
in the Graduate School of Duke University
2014

Abstract

An Asymptotic Model of Electroporation-Mediated Molecular Delivery in Skeletal Muscle Tissue

by

Jonathan P. Cranford

Department of Biomedical Engineering
Duke University

Date: _____

Approved:

_____
Wanda K. Neu, Supervisor

_____
Roger C. Barr

_____
Thomas J. McIntosh

_____
Thomas P. Witelski

_____
Fan Yuan

An abstract of a dissertation submitted in partial fulfillment of the requirements for the degree of Doctor of Philosophy in the Department of Biomedical Engineering in the Graduate School of Duke University
2014

Abstract

Electroporation is a biological cell's natural reaction to strong electric fields, where transient pores are created in the cell membrane. While electroporation holds promise of being a safe and effective tool for enhancing molecular delivery in numerous medical applications, it remains largely confined to preclinical research and clinical trials due to an incomplete understanding of the exact mechanisms involved. Muscle fibers are an important delivery target, but traditional theoretical studies of electroporation ignore the individual fiber geometry, making it impossible to study the unique transverse and longitudinal effects from the pulse stimulus. In these long, thin muscle fibers, the total reaction of the fiber to the electric field is due to fundamentally different effects from the constituent longitudinal and transverse components of the electric field generated by the pulse stimulus. While effects from the transverse component have been studied to some degree, the effects from the longitudinal component have not been considered.

This study develops a model of electroporation and delivery of small molecules in muscle tissue that includes effects from both the transverse and longitudinal components of the electric field. First, an asymptotic model of electric potential in an individual muscle fiber is derived that separates the full 3D boundary value problem into transverse and a longitudinal problems. The transverse and longitudinal problems each have their own respective source functions: the new "transverse activating function" and the well known longitudinal activating function (AF). This separation

enhances analysis of the different effects from these two AFs and drastically reduces computational intensity. Electroporation is added to the asymptotic fiber model, and simplified two-compartment mass transport equations are derived from the full 3D conservation of mass equations to allow simulation of molecular uptake due to diffusion and the electric field. Special emphasis is placed on choosing model geometry, electrical, and pulsing parameters that are in accordance with experiments that study electroporation-mediated delivery of small molecules in the skeletal muscle of small mammals.

Simulations reveal that for fibers close to the electrodes the transverse AF dominates, but for fibers far from the electrodes the longitudinal AF enhances uptake by as much as 2000%. However, on the macroscopic tissue level, the increase in uptake from the longitudinal AF is no more than 10%, given that fibers far from the electrodes contribute so little to the total uptake in the tissue. The mechanism underlying the smaller effect from the longitudinal AF is found to be unique to the process of electroporation itself. Electroporation occurs on the short time scale of polarization via the transverse AF, drastically increases membrane conductance, and effectively precludes further creation of pores from charging of the membrane via the longitudinal AF. The exact value of enhancement in uptake from the longitudinal AF is shown to depend on pulsing, membrane, and tissue parameters. Finally, simulation results reproduce qualitative, and in some cases quantitative, behavior of uptake observed in experiments.

Overall, percent increase in total tissue uptake from the longitudinal AF is on the order of experimental variability, and this study corroborates previous theoretical models that neglect the effects from the longitudinal AF. However, previous models neglect the longitudinal AF without explanation, while the asymptotic fiber model is able to detail the mechanisms involved. Mechanisms revealed by the model offer insight into interpreting experimental results and increasing efficiency of de-

livery protocols. The model also rigorously derives a new transverse AF based on individual fiber geometry, which affects the spatial distribution of uptake in tissue differently than predicting uptake based on the magnitude of the electric field, as used in many published models. Results of this study are strictly valid for transport of small molecules through small non-growing pores. For gene therapy applications the model must be extended to transport of large DNA molecules through large pores, which may alter the importance of the longitudinal AF. In broader terms, the asymptotic model also provides a new, computationally efficient tool that may be used in studying the effect of transverse and longitudinal components of the field for other types of membrane dynamics in muscle and nerves.

To my Margot, for her patience and love through countless hours on the phone across hundreds of miles.

Contents

List of Tables

List of Figures

List of Abbreviations and Symbols

Symbols

Electrical: fiber and tissue	
$\mathbb{B}$	Potential due to Born energy barrier, used only in Appendix C
$\mathbb{B}_i, \mathbb{B}_e$	Potential due to Born energy barrier at the (i)ntracellular and (e)xtracellular interfaces, used only in Appendix C
C_m	Membrane surface capacitance
$E, \lvert E\rvert, E_t, E_l$	Electric field, magnitude, transverse component, longitudinal component
$\lvert\lvert E\rvert\rvert_\infty$	Maximum magnitude of electric field generated by electrodes throughout tissue space
$\lvert E\rvert_{th}$	Threshold field magnitude generated by electrodes, used only in the "field threshold" model (Sec. 3.3.2), not in the asymptotic model
I_m	Net total membrane current density of ions moving across membrane
$\widetilde{I_m}$	Mean-free net membrane current density of ions moving across membrane
$\overline{I_m}$	Mean net membrane current density of ions moving across membrane
P_m	Potential within membrane, used only in Appendix C
P_t	Total potential within membrane: $P_T = P_m + \mathbb{B}$, used only in Appendix C

R_m	Membrane surface resistance in absence of electropores
R_p	Membrane surface resistance due to presence of electropores
U	Nondimensional transmembrane potential
V_c	Characteristic transmembrane potential: scaling unit in Laplace's equation
V_i, V_e	Total intracellular, extracellular potential
V_{rest}	Resting transmembrane potential
μ	Ratio of extracellular to intracellular conductivities (σ_e/σ_i)
σ_i, σ_e	Intracellular, extracellular microscopic conductivity of individual fiber
$\sigma_x, \sigma_y, \sigma_z$	Transverse in x, transverse in y, and longitudinal in z macroscopic tissue conductivity
Φ_i, Φ_e, Φ_m	Total secondary intracellular, extracellular, and transmembrane potential due to microscopic presence of fibers
ϕ_i, ϕ_e, ϕ_m	Mean-free secondary intracellular, extracellular, and transmembrane potential due to microscopic presence of fibers
f_i, f_e, f_m	Mean secondary intracellular, extracellular, and transmembrane potential due to microscopic presence of fibers
τ_{ip}	Time constant of initial polarization of fiber in uniform transverse field
Ψ	Primary potential in tissue due to macroscopic presence of electrodes, neglecting microscopic presence of fibers
$\widetilde{\Psi}$	Mean-free component of Ψ: $\widetilde{\Psi} = \Psi - \overline{\Psi}$
$\overline{\Psi}$	Mean component of Ψ averaged over the fiber membrane circumference
$\langle\Psi\rangle$	Ψ averaged over intracellular transverse cross-sectional area

Pulsing Protocol and Geometry	
b	Electrode-fiber distance
d	Interelectrode distance
E_u	Uniform transverse electric field value, for uniform transverse field case only
I_s	Stimulation current, for using point electrodes only
τ_p	Pulse duration
N	Number of pulses
T_p	Period of pulse train
$\lvert V_0 \rvert$	Magnitude of voltage on needle electrodes
Electroporation	
α	Rate constant of pore creation/destruction
I_{ep}	Net membrane current density due to existence of electropores only
i_{ep}	Net membrane current through a single electropore
n	Relative entrance length of a pore
N_{ep}	Pore density in membrane
$\overline{N_{ep}}$	Circumferential average of pore density in membrane
N_0	Equilibrium pore density in membrane when $\Phi_m = 0$
q	Electroporation constant
r_m	Radius of pores
V_{ep}	Characteristic voltage of electroporation
w_o	Maximum of the nondimensional Born energy barrier within a pore
σ_p	Conductivity of aqueous solution in pores
τ_{ep}	Time scale of pore resealing

Uptake	
c_i, c_e, c_m	Intracellular, extracellular, and membrane molecular concentration
c_o	Initial extracellular concentration of molecule before pulse applied
$c_{i,ss}$	Intracellular concentration of molecule at steady state in two-compartment molecular uptake equations
D	Diffusion coefficient of molecule in intracellular and extracellular space
D_m	Diffusion coefficient of molecule in membrane pores
j_m	Molecular flux across the membrane
$\overline{j_m}$	Circumferential average of molecular flux across the membrane
$K_{i,p}, K_{e,p}$	Total number of molecules throughout tissue in intracellular, extracellular space after pores reseal, used in comparison to experiments
$K_{e,c}$	Total number of molecules throughout tissue in extracellular space before pulse is applied
L_e, L_d	Length scale due to mass transport via (e)lectric field and (d)iffusion
τ_{ss}	Time scale for steady state intracellular concentration to be reached
$\mathbf{v_i}, \mathbf{v_e}$	Intracellular, extracellular velocities due to transport via electric field
z_m	Net charge of molecule
Muscle Geometry, Coordinate System, and Time	
a	Radius of muscle fiber
h	Thickness of membrane
H	Thickness of entire muscle tissue
L_f	Length of muscle fiber

R_a, R_c	Distance from (a)node and (c)athode to a test point in tissue, for when using point electrodes only
R_b	Boundary radius of extracellular space around unit fiber in periodic structure
R_e	Radius of needle electrodes
t	Time
τ	Fast time variable in method of multiple scales
T_s	Slow time variable in method of multiple scales
x, y, z	Cartesian coordinates
γ	Ratio of extracellular to intracellular transverse cross-sectional areas of a fiber $((R_b^2 - a^2)/a^2)$
ξ	Dimension across membrane thickness, used only in Appendix C
ρ, φ, z	Cylindrical coordinates

Miscellaneous

D_u	Unitless constant in analytical solution of potential due to uniform transverse field
ϵ	Small parameter in separation of potentials: ratio of fast to slow temporal scales
T	Temperature

Abbreviations

AF	Activating function, i.e., a particular kind of source term in an equation
ALB	Artificial lipid bilayer
BC	Boundary condition
BLM	Black lipid membrane (specific type of ALB)
BVP	Boundary value problem
FDM	Finite difference method

LO	Leading order, after expansion in powers of small parameter ϵ
ODE	Ordinary differential equation
PDE	Partial differential equation
RMSE	Root mean square error
rRMSE	Relative root mean square error
SE	Smoluchowski equation, PDE for creation/evolution of electropores
UR	The molecular uptake ratio, used in comparing simulated uptake to experiments

Acknowledgements

It is often the case on long, exotic, convoluted journeys, such as graduate school, that the end product has as much to do with external interactions as it does the internal individual. In this respect, I have truly been fortunate. Many different people have provided their own brand of support over the years. I would like to explicitly give recognition and express my deep gratitude to a subset of these individuals. I also send a gentle, respectful, and very gracious nod to all of those not mentioned explicitly; we have truly done this together.

I would first like to thank my advisor, Dr. Wanda Krassowska Neu, and the entire advisory committee, for their patient support and willingness to meet with me both as a group and individually over the many years. I especially send appreciation to Dr. Neu for giving her time during long meetings, providing expert scientific advice, and for always encouraging me to dig deeper into a problem to find its truest, fundamental nature. I send many thanks to Dr. Roger C. Barr for his encouraging, sometimes humorous, and always deeply thought-provoking advice on my research, my teaching practice as his TA, and on life in general. I offer a sincere thank you to Dr. Thomas J. McIntosh, Dr. Thomas P. Witelski, and Dr. Fan Yuan for their suggestions that always helped me evaluate my research from a different perspective. I also thank Dr. John C. Neu for his help early on and encouragement near the end.

It is wonderful to have been surrounded by amazing administrative oversight, technical oversight, and community at Duke: Ned Danieley for his superhuman re-

sponse time when the computers were on the verge of a riot, even on the weekends, and Duke OIT for the clusters where my simulations found a home. I thank the DGS Dr. Adam P. Wax for his support, and Kathy Barbour, Susan Story, and the rest of the office staff for their friendly and efficient help. Also, it was a privilege to be funded by the National Science Foundation via my advisor at the beginning of my tenure at Duke. Finally, the tools and skills for balancing stress in graduate school with a sense of overall wellness offered by Student Affairs have been indispensable.

My colleagues, mentors, friends, and family have been my rock throughout the entire journey. Ann Wambaugh, Soma Kalb, and Robert Oliver welcomed me into the lab and offered their friendship. Lunches and discussions with my colleague and friend, Caroline Ring, were always welcome events. I especially send heartfelt gratitude for the mentorship received from Dr. Mazella B. Fuller. Her encouragement, uplifting spirit, wisdom, and knowledge of the process of graduate school kept me afloat when seas were very rough. Tally Balaban, Megha Bhike, Nasser Demir, James Esterline, Mary Kidd, Francesca Talenti, and Ann and John Wambaugh have given me friendship and joy away from work, and scientific knowledge to inform my work. I especially give thanks to James, for always offering his time for friendship, scientific advice, and lessons in finding the humor in life; we are the brothers we never had. I send thanks to Stan for his wisdom and cheerful presence during third shift. I am grateful for Sumi Kim, Jeremy Lipkowitz, Elizabeth Ruzzo, and Chris Tralie for their lessons in mindfulness, and for Stephen Harrod's, Daryl Lindsey's, and Little West's long-lasting friendship and faith in me. I send love to my entire family and my parents Anne and Clay Cranford: they have been there from the beginning and provide unconditional encouragement, support, and love that I can always count on. Finally, I send my love to Margot Bowen, for being with me through every single high and low during the journey, and maintaining patience, faith, equanimity, humor, trust, and love after so many years. She is my Mt. Everest of rocks.

1

Introduction

1.1 Background and Significance

As medicine evolves and becomes more focused on treating diseases at the molecular and genetic level, one of the ubiquitous challenges is efficient delivery of therapeutic drugs across the cell membrane barrier.[1,2,3] This challenge presents itself in some of medicine's potentially revolutionary techniques, including gene therapy, which holds promise for treating cancer, metabolic disorders, cardiovascular diseases, and many other of humanity's most devastating diseases.[4] To date, there have been more than 1900 gene therapy clinical trials, and Glybera® became the first approved gene therapy product in the Western world, which is a treatment for lipoprotein lipase deficiency.[5] For these gene therapy applications, an effective method of improving delivery across the membrane is to use viral vectors to efficiently transport molecules into the target cell. However, viral vectors often invade not only the targeted organ, but other organs too, and they can cause an immune response within the body.[6,7,8] An attractive alternative to viral vector delivery is electroporation-mediated delivery, which uses strong electric pulses to create transient pores in the cell membrane that

molecules may pass through, as illustrated in Fig. 1.1. This method removes the need to introduce extra biological material into the body as part of the delivery process, as it utilizes the natural response of membranes to an electric field for enhancing delivery.

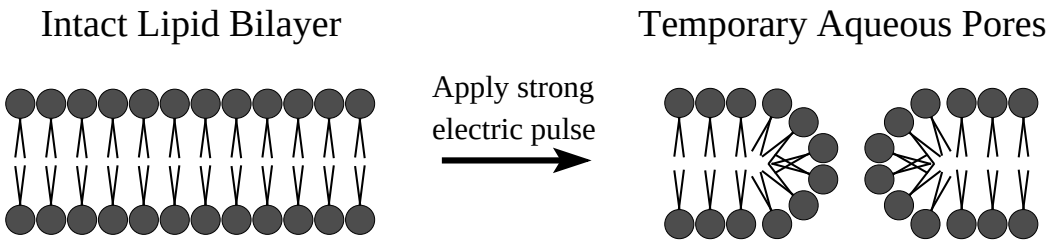

FIGURE 1.1: Illustration of electroporation in the lipid bilayer. A strong electric field causes reorganization of the lipid heads and tails to create temporary aqueous pores in the membrane.

Although electroporation holds promise for improving delivery, its results cannot always be predicted. Slightly changing the pulsing protocol results in different electroporation dynamics, which often has a dramatic effect on the uptake of molecules into the cell.[9,10,11] Moreover, the optimal pulsing protocol is a function of the type of tissue and molecule.[12,13,14,15] To advance our understanding of this technology, and enhance therapeutic applications, models are being developed to investigate the mechanism behind pore creation and delivery. Deeper understanding from these models of the physical mechanism of electroporation may lead to a better understanding of why certain pulsing protocols are better than others, providing a theoretical basis for developing improved protocols for delivery in the future.

A tissue of particular importance in drug delivery is the skeletal muscle, as it is one of the primary targets in gene therapy applications. Skeletal muscle is easily accessible, has an abundant blood vascular supply allowing efficient transport of the secreted protein (Fig. 1.2C), and can manufacture proteins for extended periods of time due to its post-mitotic nature.[1,9,16] One particular study used skeletal muscle as

a protein factory for transgenic GHRH, which promotes growth and holds promise for treating catabolic processes associated with aging and cancer.[17] Other studies focus on localized production of a desired protein in muscle, primarily dystrophin, and have shown success in increasing motor function loss from muscular dystrophy.[17] Finally, DNA vaccines are one of the most promising applications of electroporation-mediated gene therapy in muscle, and one study in phase I/II clinical trials involving prostate cancer indicated a thirty-fold increase in the antibody response that persisted for eighteen months.[17,18]

As Fig. 1.2 indicates, muscle fibers are long, thin single cells with multiple nuclei that are densely packed, except for occasional regions of larger fiber separation due to connective tissue between the fascicles, larger vessels running between fibers, etc. The research work presented here simplifies the structure of muscle by assuming the tissue is a periodic lattice of fibers with identical geometry. Furthermore, the geometry of the long, thin fibers is assumed to be exactly cylindrical. These simplifications are necessary to formulate the problem mathematically.

This chapter is divided into experimental studies and theoretical studies involving electroporation-mediated delivery to tissue, primarily skeletal muscle. Experimental studies focus on *in vivo* biological experiments using electroporation-mediated delivery of various molecules in tissue. Theoretical studies focus on computational models at the membrane level, cellular and tissue levels, as well as mass transport for simulation of movement of molecules in electroporation-mediated delivery.

1.2 Experimental Studies

There are a variety of different studies on *in vivo* electroporation-mediated delivery of molecules to muscle, yet there are commonalities in terms of equipment, animals, and pulsing parameters. The most common type of electrodes are plate electrodes applied transcutaneously and needle electrodes applied intramuscularly.[7] Transcu-

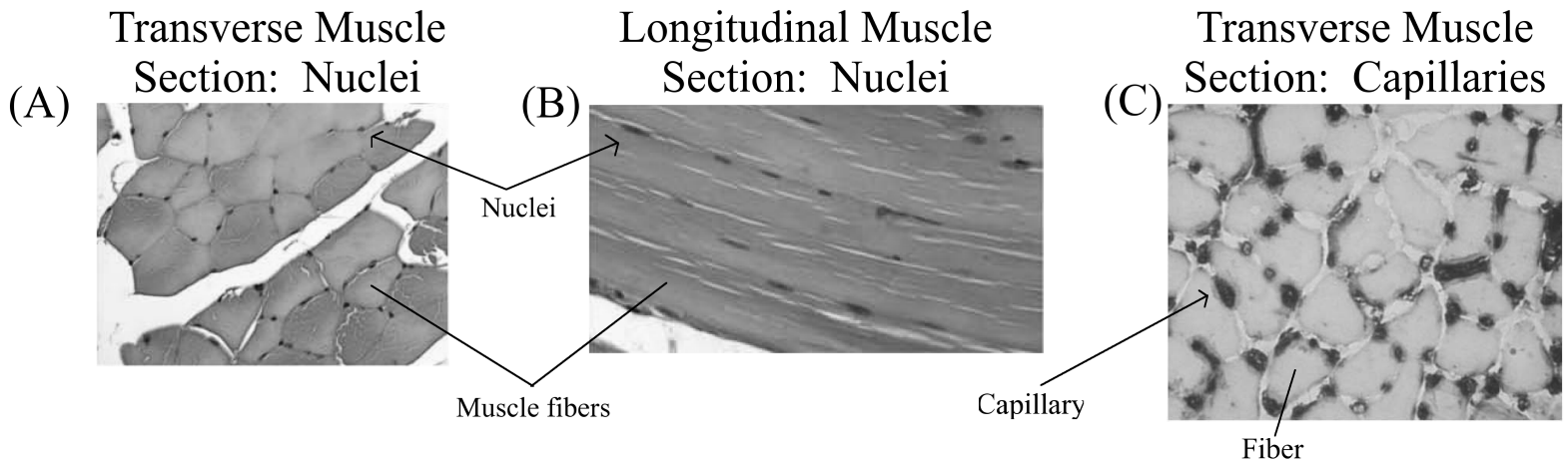

FIGURE 1.2: Structure and histology of skeletal muscle. Tissue and constituent individual muscle fibers (grey) are stained to show nuclei (small, black shapes) in transverse (A) and longitudinal sections (B). (A) There are bundles, or fascicles, of fibers that are closely packed together with very little interfiber distance. Between bundles are larger separations, due to connective tissue or larger blood vessels (white regions). (B) The long, thin fibers are single cells, but contain multiple nuclei, as shown clearly in the longitudinal section. (C) Transverse muscle section with constituent fibers (light grey) stained to show capillaries (small, black shapes), exhibiting the extensive network of vasculature in muscle. All panels show the soleus muscle of mice: panels A and B are adapted from Hsu et al.[19] with additions, while panel C is adapted from Camerino et al.[20] with additions. All figures are from publications using the Creative Commons Attribution License (http://creativecommons.org/)

taneous plate electrodes offer the advantages of being noninvasive and generally provide a more uniform field and molecular uptake in the tissue, yet high voltage needed to penetrate the skin barrier may cause burning and collateral damage to other tissues.[6] Intramuscular needle electrodes, with radii between 0.1 and 0.3 mm, offer more localized and targeted delivery, yet they are invasive and the heterogeneous field is larger near the surface and tips of the electrodes, leading to potential irreversible cell damage in these regions.[6,21,22,23] The most common animal subjects are mice and rats, where electroporation mediated uptake is often performed in the muscles of the thigh or lower leg.[24] The most important pulsing parameters are magnitude, duration, number, frequency, interelectrode distance, and orientation of the electrodes.[21,23,24] Pulse magnitude, measured as interelectrode voltage difference divided by interelectrode distance, ranges from a few hundred to a few thousand V/cm. Pulse duration ranges from a few hundred microseconds to a few hundred milliseconds, pulse number ranges from 1 to 30, and pulse frequency is approximately 1 Hz.[21,24,25] However, there are also studies that use bipolar trains of kilohertz frequency pulses with microsecond pulse duration and approximately 100 V/cm pulse magnitude.[7,23] The energy delivered to tissue is generally kept below the threshold for permanent damage to cells, resulting in large pulse magnitudes coupled with short pulse durations, and small pulse magnitudes coupled with long pulse durations. A particularly successful protocol is to use short, large magnitude pulses to electroporate the membrane, followed by long, low magnitude pulses for electrophoretic transport. This protocol is especially important when delivering large, charged molecules such as DNA.[24]

Many *in vivo* experimental studies in muscle focus on introducing genes into the intracellular space (electrotransfer), and measuring the protein product systemically or intramuscularly in the animal.[21,23,25,26] Some studies even measure the ability of electrotransfer to correct diseases, such as anemia and diabetes, showing preliminary

success.[22,27] These types of studies are particularly relevant in the field of gene therapy, as they are measuring the ability of the gene product to treat disease. In many studies, expression of gene is improved by optimizing the pulsing protocol. Optimizing pulse magnitude is usually one of the first parameters studies examine, and from these studies two thresholds have been discovered. Pulse magnitude must be greater than the first threshold to trigger permeabilization, increased magnitude results in increased expression up to a second threshold, beyond which increasing magnitude results in less expression, thought to be the result of permanent muscle damage from irreversible electroporation.[21,26,28,29] Orientation of the electrodes with respect to muscle fibers is often chosen simply based on ease of application, taking into account the type of electrodes and the location of the muscle in the animal.[21,26] However, orientation has been a topic of study for uptake of small molecules, where the electric field threshold values for electroporation are compared for longitudinal versus transverse orientation of electrodes with respect to muscle fibers.[29] However, these studies were performed with parallel plate electrodes, which does not allow study of the unique nature of the longitudinal component of fields in muscle fibers (see Sec. 1.3.2).

While experiments measuring gene products are important for optimizing electrotransfer empirically, and are directly relevant to the field of gene therapy, a closer connection to theoretical models and a mechanistic understanding of electroporation-mediated delivery is attained from studies that measure the quantity of molecule itself. Typically, radiopharmaceuticals, such as ^{99m}Tc-DTPA or ^{51}Cr-EDTA, or fluorescent molecules, such as propidium iodide (PI), are used for measurement of permeabilization and molecular uptake directly.[29,30,31,32,33] Many studies using these molecules report similar results to electrotransfer: both show a magnitude threshold for delivery and a magnitude threshold beyond which delivery success decreases. However, an important aspect of gene delivery that is not accounted for using smaller

molecules is the added effect of long pulse durations providing increased delivery success via electrophoretic transport of large, long DNA molecules. Thus, pulse protocols that use long pulse durations show a clear advantage in electrotransfer, an advantage that is not seen in delivery of small molecules.[28,34] Furthermore, negative effects of tissue damage from large pulses appear to influence the actual expression of genes more so than the molecular uptake process itself.[28] Still, measuring uptake of radiopharmaceuticals provides a quantitative value for total uptake within a given region of muscle tissue, which can be compared to the same quantity in computational models.[30,31,32] These computational models are explored in the next section.

1.3 Theoretical Studies

Models of electroporation-mediated delivery in tissue may be thought of, in broad terms, as consisting of four interconnected components: the membrane level model, the cell level model, the tissue level model, and the mass transport model. The membrane level model simulates the dynamics of electroporation in the membrane of each cell in response to a stimulus from external electrodes. The cell level model incorporates the cellular level geometry and electrical properties to simulate how the electric field (E) generated by the electrodes is distributed in the cell, and combined with the membrane model, together they describe the effect of the stimulus on electroporation in each section of the membrane. The tissue level model simulates the geometry and electrical properties of the collection of individual cells, and consequently, the distribution of the stimulus and its effects throughout the entire tissue. Finally, the mass transport model simulates the movement of molecules throughout the tissue and across the cell membrane. In general, a single study focuses on a subset of these components, while simplifying or ignoring other components. For example, published models that focus on the dynamics of electroporation in the cell membrane may only consider a small, spatially homogeneous piece of tissue, while

models that that capture whole tissue geometry may ignore the effects of individual cellular geometry.

1.3.1 The Membrane Level Model

From a broad perspective, the two different categories of cell membrane electroporation models are molecular scale models and continuum models. Molecular scale models employ molecular dynamics simulations to calculate the motion of each individual molecule in the membrane and cellular environment during electroporation.[35,36,37,38] Due to the computational intensity of molecular dynamics simulations, they are not practical for long pulse durations and tissue scale simulations in molecular uptake studies.[4,23,29,39] Continuum models are the primary practical choice for modeling electroporation-mediated uptake at the tissue scale level. Some continuum models account for electroporation by changing the conductance in localized sections of the membrane based on experiments,[40] while others use the Smoluchoswki equation (SE) to describe the mechanism of creation and evolution of the actual pores in the membrane. The SE is a partial differential equation that governs the distribution of pore density as a function of pore radii and time.[41] It has successfully been used to model electroporation in a spatially clamped, uniformly polarized membrane patch,[42,43,44] as well as to model electroporation in a single cell.[45,46,47] However, none of these studies simulate elongated fibers or more than one cell; the computational cost of simulating multiple muscle fibers for several microseconds or milliseconds makes the SE model impractical for electroporation-mediated delivery to muscle tissue.

In response to the limitations of modeling electroporation using the SE, Neu & Krassowska developed a model based on an asymptotic analysis of the SE.[48,49,50] This formulation for modeling electroporation reduces the SE to a system of simpler ordinary differential equations (ODEs), where time evolution of pore density is proportional to an exponential function of transmembrane potential (Φ_m). These

ODEs have been used to model electroporation-mediated delivery ranging from a spatially clamped, uniformly polarized membrane patch[51] to entire tissue composed of spherical cells,[52] as well as electroporation without molecular delivery ranging from a spherical cell[53,54] to liver tissue.[55] Some models simulate growing pores large enough for DNA delivery,[51,53,55] while others assume non-growing pores[54,56,57] that are too small for DNA delivery, but still large enough to admit radiopharmaceuticals and fluorescent molecules described in Sec. 1.2. Most models base electroporation parameters on experiments using artificial lipid bilayers (ALBs), except Stewart et al.,[57] which fit parameters to muscle fiber experiments. Ultimately, none of these studies using the asymptotic model of electroporation are adequate for simulating electroporation-mediated delivery in muscle tissue, given that none of these studies simulate the 3D cylindrical geometry of muscle fibers. This dissertation work builds on these previous studies by coupling the non-growing pores, ALB parameters version of the asymptotic model of electroporation to the 3D cylindrical geometry of muscle fibers.

1.3.2 The Cell Level Model

From the perspective of individual cell geometry, modeling electroporation in muscle tissue presents a particularly unique challenge compared to other types of tissue. The length of the muscle fibers ranges from two to three orders of magnitude larger than the radius of the fibers. Thus, models and simulations of muscle fibers must be simultaneously detailed and broad enough to capture the disparate spatial scales; they must account for phenomena operating on the small spatial scale of the fiber radius in transverse cross sections of the fiber, as well as phenomena operating on the long spatial scale of the fiber length. Coupling this knowledge with the fact that there are many applications for electroporation involving non-elongated cells, including electrochemotherapy and delivery in cell suspensions, it is not too surprising that

many models of electroporation are for spherical, or nearly spherical cells.[52,54,55,58] Some studies do model electroporation in spatially elongated cells, yet either assume space- and voltage-clamped conditions, enforcing spatial uniformity over the entire membrane,[57] or assume the fiber is in a transverse uniform field, enforcing uniformity along the longitudinal dimension.[59] Thus, studies modeling electroporation have been limited to spherical cells, or elongated cells where membrane dynamics depend only on the transverse component of the electric field (E_t), in the radial and angular dimensions.

However, it is well known in the stimulation modeling community that the longitudinal component of the electric field (E_l) has a significant effect on the electrical properties of elongated cells. Figure 1.3A illustrates the E_t and E_l components of the electric field. In models for stimulation, Φ_m is proportional to the derivative $-E_l$, which is called the activating function (AF).[60] In this work, the single word "AF" is synonymous to "longitudinal AF", where the word "longitudinal" is used to highlight the difference from the novel "transverse AF" that is derived. Note that the term "AF" is proper to use for both analytical and numerical derivatives of E_l,[61] and both kinds of derivatives are used in this work, although most of the work uses analytical functions. The AF is known to induce regions of reversed polarity, called virtual electrodes (VEs), at some distance away from the real electrodes (REs), as shown in Fig. 1.3B. The AF and induced VEs have been found to play a role in stimulation of elongated cells, such as nerves, muscle cells, and heart cells.[62,63,64,65,66]

Some models in the stimulation community attempt to account for the combined effects of E_t and E_l on Φ_m by adding the effects E_t to the traditional longitudinal AF, yet they operate under simplifying assumptions. Schnabel & Struijk and Yu et al. account for E_t by simply adding a term to the traditional AF.[67,68] However, the modified AF proposed by Schnabel & Struijk is valid only for fibers far from the electrodes, or when the field from the electrodes is approximately uniform and

perpendicular to the fiber.[67] Furthermore, this modified AF is independent of time. The modified AF proposed by Yu et al. is based on work done by Neu & Krassowska, who found that excitation has two stages: initial polarization and change of the physiological state.[69] However, unlike excitation, electroporation occurs on the time scale of initial polarization, but the application of their approach to electroporation is discussed in Sec. 4.1.

Another approach to combine the effects of E_t and E_l is to develop full 3D volume conductor models of electric potential in cylindrical fibers. Steady state and time dependent analytical 3D models of nerve fibers have been developed, but these studies are limited to passive fibers only.[67,70,71] Stickler et al. have numerically simulated time dependent fiber excitation in a 3D volume conductor model, yet this model does not include electroporation.[72] This dissertation work studies electroporation in a 3D volume conductor model of a skeletal muscle fiber. The full 3D BVP is reduced to transverse and and longitudinal problems, accounting for the effects of both E_t and E_l on evolution of Φ_m and electropore density in the membrane.

1.3.3 The Tissue Level Model

Many tissue level studies of electroporation in skeletal muscle neglect the cylindrical geometry of individual cells. A boundary value problem (BVP) is solved, typically by using the finite element method or the finite difference method, for the distribution of the electric field magnitude ($|E|$) throughout the muscle tissue,[29,30] although analytical solutions in two dimensions have been derived and implemented in various kinds of tissue.[73,74,75] In these tissue models, muscle is modeled as a homogenized unit of conductivity, or a conductivity tensor if anisotropy of the tissue is considered.[29,76] Some models dynamically increase the local conductivity in parts of the tissue as a function of the local $|E|$ to emulate electroporation, yet these models derive changes in conductivity empirically from experimental data.[29,76] The validity of this pro-

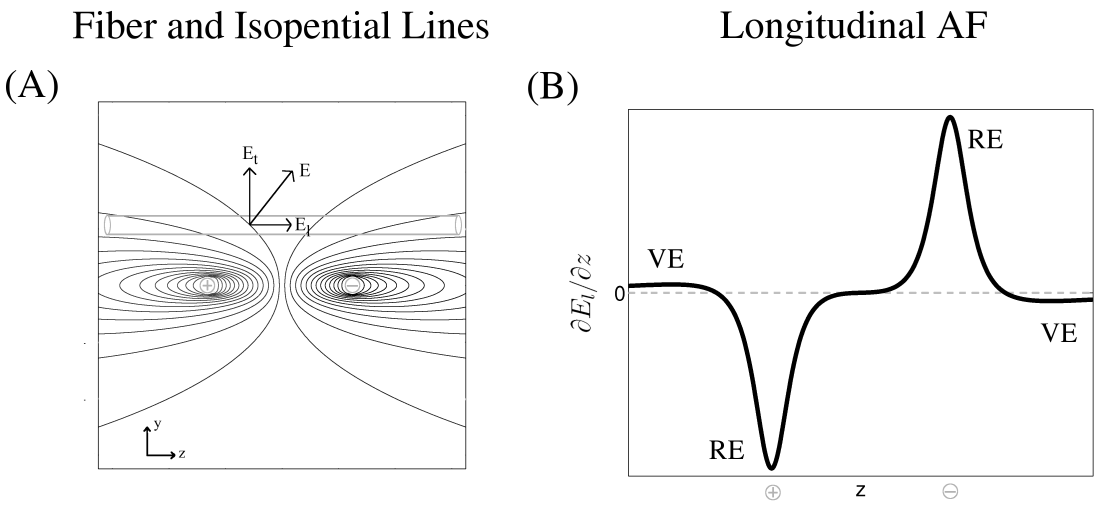

FIGURE 1.3: Muscle fiber, isopotential lines, and longitudinal AF. The anode and cathode locations are shown by a plus sign and minus sign, respectively (A) E is shown at one sample point, along with its components E_t and E_l. Fiber and needles are drawn in light grey. Isopotential lines and electrodes are to scale, but fiber radius is not drawn to scale to improve clarity; in reality the electrode radius is approximately 12 times larger than the radius of the fiber. (B) Generic form of the longitudinal AF, i.e., $-\partial E_l/\partial z$.

cedure is based on the fact that Φ_m is proportional to $|E|$ in non-electroporating spherical cells in uniform fields at steady state. However, for muscle fibers this relationship is only true in the transverse direction using E_t, and in the longitudinal direction Φ_m is proportional to derivative of E_l (the AF).[69,77,78] Without modeling individual cylindrical geometry of fibers, there is no framework to simulate the dynamic interaction of E_t and E_l, and how these interactions affect Φ_m and electroporation in a fiber.

There are only a select few studies that take into account individual cell geometry in tissue models of electroporation. Most notable are the studies by Essser et al. and Gowrishankar et al. using the transport lattice method to model liver tissue and the endothelium.[55,79,80,81] Using the transport lattice method, these studies represent intracellular, extracellular, and membrane spaces by a lattice of connected

circuit models, and these circuit models interact with the larger scale tissue model through bulk conductivities and permittivities. Not only do these studies incorporate individual cell geometry, but they also incorporate the membrane model by using the asymptotic model of electroporation, as introduced in Sec. 1.3.1. However, the transport lattice method has never been applied to fibers, and thus, has never been used to study the unique interaction of E_t and E_l in electroporation. Finally, some studies model electroporation in cardiac tissue, where the bidomain model is utilized, which simulates the entire tissue by modeling intracellular and extracellular spaces, along with membrane current, in each part of the tissue.[82,83] However, the bidomain model is only appropriate for cardiac tissue with direct electrical connection between fibers via gap junctions, and does not simulate the cylindrical geometry of individual cells. This dissertation work models whole tissue level electroporation in muscle tissue by modeling electroporation in a collection of individual cylindrical fibers, allowing the interaction of E_t and the longitudinal AF (derivative of $-E_l$) to be observed in the process of electroporation.

1.3.4 The Mass Transport Model

The transport of molecules due to diffusional and electric field forces is described by a conservation of mass equation, which is often used in studies simulating electroporation-mediated delivery in cells and tissue. Granot et al. used the diffusion equation and the asymptotic model of electroporation (Sec. 1.3.1) to simulate delivery of bleomycin in cancer tissue using needle electrodes, taking into account spherical geometry of individual cells.[52] However, they ignored transport due to electric field force, using only the diffusion equation. Zaharoff et al. exercised great care in determining an accurate permeability coefficient in their model of transport of FITC-labeled dextran molecules across the membrane through electropores, but they too simulated only the diffusion, neglecting the transport from the electric field.[84] However, transport

due to electric field force has been shown to be significant, especially for millisecond pulse durations and large molecules like DNA.[85]

One of the most advanced studies by Li and Lin incorporated transport due to both diffusional and electric field forces, and coupled transport with the asymptotic model of electroporation to simulate uptake of small molecules.[86] However, this model was only for a single cell exposed to a uniform field, and has not been applied to tissues with spatially elongated fibers. Another study by Movahed and Li adds simulation of fluid flow by using modified Navier-Stokes equations. In this study, ionic transport through electropores is simulated for a spherical cell in a uniform field, yet the dynamic creation and evolution of electropores was not considered in the model.[87] Thus, although electroporation-mediated delivery of molecules in cells and tissue have been simulated, in some cases the governing equations have been simplified, and in all cases transport was not applied to elongated fibers and muscle tissue.

Other mass transport models focus only on transport across the membrane, neglecting the shape of the cell and tissue altogether. Smith et al. incorporated both diffusional and electric field transport of DNA across the membrane, coupled with the asymptotic model of electroporation.[51] However, individual cell geometry was neglected by assuming a uniformly polarized patch of membrane, and it was assumed that extracellular concentration of DNA was constant in time. Assuming constant extracellular concentration is not suitable when modeling densely packed muscle fibers where extracellular concentrations change drastically in the small interstitial space. Furthermore, simplifying assumptions had to be made regarding modeling long molecules like DNA, specifically for the diffusion coefficient and the effect of DNA binding to the cell membrane.[88,89] To account for the unique transport behavior of long, large DNA molecules, very detailed molecular dynamics models have been used to simulate transport of DNA, siRNA, and water molecules across the

membrane through electropores, where movement of each individual molecule is accounted for.[36,90,91] However, molecular dynamics simulations are limited to a single pore or small sections of membrane due to the computational resources needed to simulate these types of models. This dissertation work begins with the conservation of mass equation, and performs an in-depth analysis to find simplified transport equations describing uptake of small molecules in skeletal muscle.

1.4 Summary of Scientific Impact

One of the most controversial assumptions in published models of electroporation-mediated delivery in muscle tissue is that the cylindrical geometry of muscle fibers is ignored, and thus, the disparate transverse and longitudinal spatial scales of individual muscle fibers are also ignored. These disparate spatial scales bring about two different effects: one from the transverse component of the electric field (E_t), and one from the derivative of longitudinal component ($-\partial E_l/\partial z$). In published models of muscle tissue it is assumed that Φ_m and electroporation depend only on the magnitude of the total field, $|E|$, while in fact this dependency is only true for E_t. In the longitudinal direction $-\partial E_l/\partial z$, or the longitudinal AF, is the mechanism that evolves Φ_m, which may effect electroporation. Studies that do simulate cylindrical geometry of individual fibers use uniform fields, which effectively removes the existence of E_l altogether, leaving membrane dynamics solely a function of E_t. Thus, while the mechanism of electroporation due to E_t has been studied, little is known about the mechanism behind electroporation when E_l is considered due to the presence of a nonuniform field. The nonuniform field generated from needle electrodes is an important example, as they are one of the major electrodes used in electroporation-mediated delivery, due to their ability to bypass the high resistance of the skin and provide more localized drug delivery in the underlying tissue.[6]

This dissertation work encompasses the derivation of a novel model of electro-

poration in skeletal muscle tissue that simulates the effects from both E_t and E_l in the individual fibers that make up the muscle tissue. Derivation is performed using generic fiber geometry and electrical properties, and thus, is also of general interest to the stimulation community for simulating the effects of E_t and E_l in nerves. The membrane level model uses the asymptotic model of electroporation with non-growing pores and parameters obtained from ALBs to enable time dependent simulations of the electroporation process. The spatiotemporal uptake of small molecules is simulated by equations derived from the conservation of mass equation that are coupled to the membrane, cell, and tissue level models. Model parameters for muscle and electrode geometry, pulsing protocol, muscle electrical properties, and molecular transport are derived from experiments that deliver small molecules across the membrane of muscle tissue in small mammals, allowing simulation results to be interpreted within the framework of experimental results. With this connection to experiments, it is possible to investigate the underlying mechanisms in electroporation-mediated delivery to skeletal muscle, providing novel insight into developing improved protocols that enhance therapeutic effect. Enhancing the therapeutic effect has potential far reaching consequences in the clinical setting, from DNA vaccines for cancer to restoring mobility to those suffering from muscular dystrophy.[17]

2

Models and Methods

2.1 Derivation and Validation of the Asymptotic Fiber Model

2.1.1 Separation of Potentials Into Mean and Mean-free components

[1]A fiber is assumed to be exactly cylindrical to allow for mathematical formulation, thus, a cylindrical fiber with radius a is placed in a homogeneous, infinite, isotropic conductive medium[2] with extracellular electrodes, as shown in Fig. 2.1. The membrane is assumed to be an infinitesimally thin boundary separating intracellular and extracellular space, given that the thickness of the membrane is four orders of magnitude smaller than the radius in a typical fiber. The intracellular potential (V_i) and extracellular potential (V_e) are split into the primary potential Ψ in the tissue established by the electrodes excluding the microscopic presence of the fiber, and the secondary potentials Φ_i and Φ_e that account for the microscopic presence of the

[1] Many of the ideas in this section are originally from our published article with Springer publishing (springerlink.com, DOI 10.1007/s11517-012-0870-3) in *Medical & Biological Engineering & Computing*: http://link.springer.com/article/10.1007%2Fs11517-012-0870-3.

[2] While a single fiber in an infinite isotropic medium is not representative of closely packed muscle fibers in muscle tissue, the analytical solutions used to validate the asymptotic fiber model (Secs. 2.1.5 and 2.1.6) are formulated assuming an infinite medium. Differences between the model described here to validate the asymptotic fiber model, and the model used to simulate electroporation-mediated molecular uptake in muscle, are highlighted in Sec. 2.2.

fiber,[67,70]

$$V_i \equiv \Psi + \Phi_i, \tag{2.1a}$$

$$V_e \equiv \Psi + \Phi_e. \tag{2.1b}$$

It is assumed that the primary potential can be computed from an analytical solution (see Secs. 2.1.6 and 2.2). The secondary potentials are governed by Laplace's equations,[67]

$$\nabla^2 \Phi_i = 0 \quad \text{in } \rho < a, \tag{2.2a}$$

$$\nabla^2 \Phi_e = 0 \quad \text{in } \rho > a, \tag{2.2b}$$

with Φ_e decaying to zero away from the fiber. Note that ρ is the radial distance from the fiber axis in cylindrical coordinates. Matching conditions on the membrane require that the current density normal to the membrane must be equal to the total membrane current per unit area,

$$\sigma_i \frac{\partial}{\partial \rho}(\Psi + \Phi_i) = \sigma_e \frac{\partial}{\partial \rho}(\Psi + \Phi_e) = -C_m \frac{\partial \Phi_m}{\partial t} - I_m \quad \text{on } \rho = a, \tag{2.3}$$

where σ_i is the intracellular conductivity, σ_e is the extracellular conductivity, C_m is the membrane surface capacitance, and I_m is the net membrane current density of ions moving across the membrane. Note that I_m may be represented by arbitrary membrane dynamics, from linear passive dynamics to nonlinear electroporation or action potential dynamics. Φ_m is the transmembrane potential, which according to Eq. 2.1 only depends on secondary potentials,

$$\Phi_m \equiv V_i - V_e = \Phi_i - \Phi_e \quad \text{on } \rho = a. \tag{2.4}$$

Solving Eqs. 2.2-2.3 involves solving a three-dimensional boundary value problem with time-dependent matching conditions on the membrane interface. Considering the ultimate goal is to simulate multiple fibers in a tissue, the problem is made

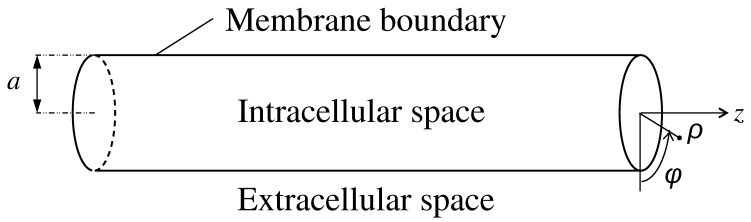

FIGURE 2.1: Illustration of a 3D muscle fiber for derivation of asymptotic fiber model. Cylindrical coordinates (ρ, φ, and z) are shown. Muscle fiber radius is a. Muscle fiber not drawn to scale to improve clarity of features: in reality fiber radius is two or three orders of magnitude smaller than fiber length.

more tractable by reducing the complexity of these governing equations. It is first recognized that there are two spatial scales: long, determined by the length constant of the fiber (millimeters), and short, determined by the fiber radius a (micrometers).[92] Next, it is recognized there are also two temporal scales: fast, determined by the time scale of polarization of the fiber by transverse currents (microseconds), and slow, determined by the time scale of fiber polarization from divergence of longitudinal currents (milliseconds).[69] Thus, it is possible to separate the fast, short-distance response from the slow, long-distance response. The method of multiple scales is used, and potentials Φ_i, Φ_e, and Φ_m are considered functions of fast time variable $\tau = t$ and slow time variable $T_s = \epsilon t$.[93] The small parameter ϵ is the ratio of the fast to the slow temporal scales,[69]

$$\epsilon = \frac{aC_m/\sigma_i}{R_m C_m} = \frac{a}{\sigma_i R_m}, \tag{2.5}$$

where R_m is the membrane surface resistance. For typical muscle fiber parameters ϵ is on the order of 10^{-5}. As real time variable t changes, the fast time variable τ changes at the same rate, while the slow time variable T_s changes more slowly,

$$\frac{\partial}{\partial t} = \frac{\partial}{\partial \tau} + \epsilon \frac{\partial}{\partial T_s}. \tag{2.6}$$

The governing equations (Eqs. 2.2-2.3) are written in cylindrical coordinates, converted to dimensionless form using the scaling units in Table 2.1, and Eq. 2.6 is

Table 2.1: Scaling units in asymptotic fiber model

Variable[a]	**Scaling Unit**[b]	**Scaling Unit Definition**
ρ	a	Short spatial scale (fiber radius)
z	$\sqrt{a\sigma_i R_m}$	Long spatial scale (longitudinal direction)
t	aC_m/σ_i	Fast time scale of transverse polarization
Ψ,Φ_i,Φ_e,Φ_m	V_c	Characteristic transmembrane potential
I_m	$\sigma_i V_c/a$	Characteristic membrane current density

[a]Scaling units are shown only for variables in the original BVP (Eqs. 2.2-2.3). The same units are used for the mean and mean-free components of potentials; the mean membrane current $\overline{I_m}$ is measured in V_c/R_m (see Appendix A) and the slow time scale $R_m C_m$ is used to convert slow time variable T_s to dimensional form in Appendix B

[b]Typical order of magnitude of units is given in text

substituted for the time derivative,[69,92]

$$\frac{1}{\rho}\frac{\partial}{\partial\rho}\left(\rho\frac{\partial\Phi_i}{\partial\rho}\right)+\frac{1}{\rho^2}\frac{\partial^2\Phi_i}{\partial\varphi^2}+\epsilon\frac{\partial^2\Phi_i}{\partial z^2}=0 \qquad \text{in } \rho<a, \tag{2.7a}$$

$$\frac{1}{\rho}\frac{\partial}{\partial\rho}\left(\rho\frac{\partial\Phi_e}{\partial\rho}\right)+\frac{1}{\rho^2}\frac{\partial^2\Phi_e}{\partial\varphi^2}+\epsilon\frac{\partial^2\Phi_e}{\partial z^2}=0 \qquad \text{in } \rho>a, \tag{2.7b}$$

$$\frac{\partial\Phi_i}{\partial\rho}=-\frac{\partial\Phi_m}{\partial\tau}-\epsilon\frac{\partial\Phi_m}{\partial T_s}-I_m-\frac{\partial\Psi}{\partial\rho} \qquad \text{on } \rho=a, \tag{2.7c}$$

$$\frac{\partial\Phi_e}{\partial\rho}=-\frac{\sigma_i}{\sigma_e}\left\{\frac{\partial\Phi_m}{\partial\tau}+\epsilon\frac{\partial\Phi_m}{\partial T_s}+I_m\right\}-\frac{\partial\Psi}{\partial\rho} \qquad \text{on } \rho=a. \tag{2.7d}$$

The potentials Φ_i, Φ_e, and Φ_m are expanded in powers of the small parameter ϵ,[93]

$$\Phi_i \sim \Phi_i^0+\epsilon\Phi_i^1+..., \tag{2.8a}$$

$$\Phi_e \sim \Phi_e^0+\epsilon\Phi_e^1+..., \tag{2.8b}$$

$$\Phi_m \sim \Phi_m^0+\epsilon\Phi_m^1+..., \tag{2.8c}$$

and they are introduced into Eq. 2.7.

In the limit $\epsilon \to 0$, the leading order (LO) problem contains spatial derivatives in ρ and φ that vary only in the transverse direction, and temporal derivatives only

with respect to fast time variable τ,

$$\frac{1}{\rho}\frac{\partial}{\partial\rho}\left(\rho\frac{\partial\Phi_i^0}{\partial\rho}\right)+\frac{1}{\rho^2}\frac{\partial^2\Phi_i^0}{\partial\varphi^2}=0 \qquad \text{in } \rho<a, \tag{2.9a}$$

$$\frac{1}{\rho}\frac{\partial}{\partial\rho}\left(\rho\frac{\partial\Phi_e^0}{\partial\rho}\right)+\frac{1}{\rho^2}\frac{\partial^2\Phi_e^0}{\partial\varphi^2}=0 \qquad \text{in } \rho>a, \tag{2.9b}$$

$$\frac{\partial\Phi_i^0}{\partial\rho}=-\frac{\partial\Phi_m^0}{\partial\tau}-I_m-\frac{\partial\Psi}{\partial\rho} \qquad \text{on } \rho=a, \tag{2.9c}$$

$$\frac{\partial\Phi_e^0}{\partial\rho}=-\frac{\sigma_i}{\sigma_e}\left\{\frac{\partial\Phi_m^0}{\partial\tau}+I_m\right\}-\frac{\partial\Psi}{\partial\rho} \qquad \text{on } \rho=a. \tag{2.9d}$$

Therefore, it is assumed that the LO potentials can be separated into fast-changing mean-free components that vary in the transverse direction (ρ, φ), and slow-changing mean components that vary only in the longitudinal direction (z),

$$\Phi_i^0=\phi_i^0(\rho,\varphi,\tau)+f_i^0(z,T_s), \tag{2.10a}$$

$$\Phi_e^0=\phi_e^0(\rho,\varphi,\tau)+f_e^0(z,T_s), \tag{2.10b}$$

$$\Phi_m^0=\underbrace{\phi_m^0(\varphi,\tau)}_{mean-free}+\underbrace{f_m^0(z,T_s)}_{mean}. \tag{2.10c}$$

The mean intracellular and extracellular potentials, f_i^0 and f_e^0, are averages over their respective cross-sectional areas, while mean transmembrane potential f_m^0 is an average over the fiber circumference.

In Eqs. 2.9c and 2.9d, there is the membrane current term, I_m, and the ρ-derivative of the primary potential, $\partial\Psi/\partial\rho$ that still have not been separated into their constituent mean and mean-free components. The goal is to formulate separate equations for transverse and longitudinal behavior of the system, which necessitates analyzing these two terms more closely. Appendix A shows that these two terms can be expressed as follows:

$$I_m=\widetilde{I_m}+\epsilon\overline{I_m}, \tag{2.11}$$

$$\frac{\partial \Psi}{\partial \rho} = \frac{\partial \widetilde{\Psi}}{\partial \rho} - \frac{\epsilon}{2}\frac{\partial^2 \langle \Psi \rangle}{\partial z^2}, \tag{2.12}$$

where the tilde over a symbol denotes the mean-free component, the bar denotes an average over the fiber circumference at a given location in z, and the brackets $<>$ denote an average over the fiber cross-sectional area at that location. Eqs. 2.11 and 2.12 indicate that the mean components of I_m and $\partial\Psi/\partial\rho$ are $O(\epsilon)$, and thus drop out of the LO problem. This finding is used in the next section in defining the equations of the transverse problem.

2.1.2 Equations of the Transverse Problem

Separated potentials (Eq. 2.10), along with I_m (Eq. 2.11) and $\partial\Psi/\partial\rho$ (Eq. 2.12) in the limit $\epsilon \to 0$, are introduced into the LO BVP (Eq. 2.9). The resulting equations describe the time evolution of the LO mean-free potentials ϕ_i^0, ϕ_e^0, and ϕ_m^0 that are spatially dependent on ρ and φ. Therefore, the following equations defining the transverse problem are solved at each longitudinal position in z and at each long-time instant T_s for the LO mean-free potentials,

$$\frac{1}{\rho}\frac{\partial}{\partial \rho}\left(\rho \frac{\partial \phi_i^0}{\partial \rho}\right) + \frac{1}{\rho^2}\frac{\partial^2 \phi_i^0}{\partial \varphi^2} = 0 \qquad \text{in } \rho < a, \tag{2.13a}$$

$$\frac{1}{\rho}\frac{\partial}{\partial \rho}\left(\rho \frac{\partial \phi_e^0}{\partial \rho}\right) + \frac{1}{\rho^2}\frac{\partial^2 \phi_e^0}{\partial \varphi^2} = 0 \qquad \text{in } \rho > a, \tag{2.13b}$$

$$\sigma_i \frac{\partial \phi_i^0}{\partial \rho} = -C_m \frac{\partial \phi_m^0}{\partial t} - \widetilde{I_m} - \sigma_i \frac{\partial \widetilde{\Psi}}{\partial \rho} \qquad \text{on } \rho = a, \tag{2.13c}$$

$$\sigma_e \frac{\partial \phi_e^0}{\partial \rho} = -C_m \frac{\partial \phi_m^0}{\partial t} - \widetilde{I_m} - \sigma_e \frac{\partial \widetilde{\Psi}}{\partial \rho} \qquad \text{on } \rho = a. \tag{2.13d}$$

Note that Eq. 2.13 has been converted back to the original dimensional variables, and as in the original BVP (Eqs. 2.2 and 2.3), the time dependence arises from matching conditions on the membrane (Eqs. 2.13c and 2.13d). Eqs. 2.13c and 2.13d

have a forcing function derived from the primary potential: $\partial\widetilde{\Psi}/\partial\rho$. This forcing function is termed the "transverse AF". It is a novel component of the asymptotic fiber model, and plays a key role in the results in Chapter 3, especially Sec. 3.2.3, and is discussed in Chapter 4, especially Secs. 4.1, 4.2, and 4.3.2.

2.1.3 Equations of the Longitudinal Problem

To derive an equation that describes the mean component of potentials, the method of homogenization is used.[92] The process is described in detail in Appendix B, but is summarized briefly here. A small length of the fiber and surrounding medium Δz long is considered, as shown in Fig. 2.2. The length of the fiber has volume v_i and is bounded by membrane (M), end cap at location z ($E_{i,1}$), and end cap at location $z + \Delta z$ ($E_{i,2}$). The length of the extracellular space has volume v_e and is bounded by membrane (M), extracellular boundary B, end cap at location z ($E_{e,1}$), and end cap at location $z + \Delta z$ ($E_{e,2}$). The scaled intracellular and extracellular Laplace equations (Eqs. 2.7a and 2.7b) are integrated over volumes v_i and v_e respectively. The divergence theorem is applied to the intracellular volume integral to relate it to the surface integrals of components of the potential gradient normal to the boundaries M, $E_{i,1}$, and $E_{i,2}$. Likewise, extracellular volume integral is related to surface integrals of the components of potential gradient normal to the boundaries M, B, $E_{e,1}$, and $E_{e,2}$. Given that Laplace's equation in intracellular and extracellular space is equal to zero for secondary potentials, the sum of the surface integrals equal zero,

$$\int_M \frac{\partial\Phi_i}{\partial\rho}ds + \epsilon\left(\int_{E_{i,2}} \frac{\partial\Phi_i}{\partial z}ds - \int_{E_{i,1}} \frac{\partial\Phi_i}{\partial z}ds\right) = 0, \tag{2.14a}$$

$$-\int_M \frac{\partial\Phi_e}{\partial\rho}ds + \epsilon\left(\int_{E_{e,2}} \frac{\partial\Phi_e}{\partial z}ds - \int_{E_{e,1}} \frac{\partial\Phi_e}{\partial z}ds\right) + \int_B \frac{\partial\Phi_e}{\partial\rho}ds = 0. \tag{2.14b}$$

Now it is important to remember nature of the medium around the fiber. The fiber is an infinite extracellular medium because the analytical solutions that are used to

validate the asymptotic fiber model in Secs. 2.1.5 and 2.1.6 are found for a fiber in an infinite medium. Therefore, the extra term in Eq. 2.14b due to the extracellular boundary B drops out because $\Phi_e \to 0$ as $\rho \to \infty$. Appendix B shows that this term also drops out for the case of closely packed fibers, as introduced in Sec. 2.2. Eqs. 2.7c and 2.7d are substituted for $\partial\Phi_i/\partial\rho$ and $\partial\Phi_e/\partial\rho$ in the surface integral over the membrane in Eq. 2.14, and taking the limit as $\Delta z \to 0$ yields the 1D equation for LO mean transmembrane potential f_m^0 (in dimensional variables),

$$\frac{\sigma_i a}{2}\frac{\partial^2 f_m^0}{\partial z^2} = \left(1+\frac{1}{\gamma\mu}\right)\left\{C_m\frac{\partial f_m^0}{\partial t} + \overline{I_m}\right\} - \left(1+\frac{1}{\gamma}\right)\frac{\sigma_i a}{2}\frac{\partial^2 \langle\Psi\rangle}{\partial z^2}, \tag{2.15}$$

where γ is the ratio of extracellular to intracellular cross-sectional areas and $\mu = \sigma_e/\sigma_i$. Again, because the fiber is placed in an infinite extracellular medium, $1/\gamma \to 0$, and Eq. 2.15 is reduced:

$$\frac{\sigma_i a}{2}\frac{\partial^2 f_m^0}{\partial z^2} = C_m\frac{\partial f_m^0}{\partial t} + \overline{I_m} - \frac{\sigma_i a}{2}\frac{\partial^2 \langle\Psi\rangle}{\partial z^2}. \tag{2.16}$$

Eq. 2.16 has the form of the cable equation with the longitudinal activating function (AF): $\partial^2\langle\Psi\rangle/\partial z^2$.[60] Primay potential Ψ has an analytical solution and thus remains true to the original definition of the AF proposed by Rattay,[60] except for Secs. 2.4, 3.3.4, 4.3.4, and 4.4.7 where primary potential is solved for numerically due to complex distribution of macroscopic tissue conductivities. However, as Rattay indicates, the AF is also a proper term when numerical solutions are used.[61] Further discussion of the relationship between the area-averaged longitudinal AF derived here ($\partial^2\langle\Psi\rangle/\partial z^2$) and the traditional AF on the fiber' axis ($\partial^2\Psi/\partial z^2$) is given in Sec. 4.1.

2.1.4 Numerical Implementation of Asymptotic Fiber Model

An algorithm for numerical solution of the transverse and longitudinal problem (Eqs. 2.13 and 2.16) on a computer is outlined below in list format. Details regarding the

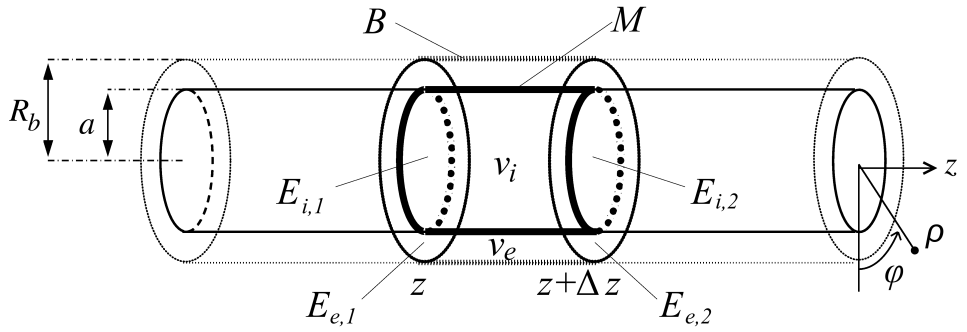

FIGURE 2.2: Short length of fiber used to derive 1D equation for mean component of transmembrane potential in the longitudinal problem (Eq. 2.16). Short length of fiber is Δz long, that has intracellular and extracellular volumes v_i and v_e. The boundaries of the short length of fiber are membrane M, end caps $E_{i,1}$ to $E_{e,2}$, and extracellular boundary B. Boundary B is drawn with arbitrary radius R_b to allow for formulation of a general equation first, and then subsequently assuming the fiber is in an infinite extracellular medium to produce the specific equation used in this section.

discretization of these equations to solve them numerically are given below the algorithm. The algorithm is divided into steps performed outside the time loop and those performed within the time loop.

Outside time loop:

1. Compute time-independent activation functions from primary potentials set up by electrodes, using analytical solution of primary potential Ψ:

   (a) At each position z along fiber, compute $\partial^2 \langle \Psi \rangle / \partial z^2$ for use in longitudinal problem

   (b) At each positions in z and φ, compute $\partial \widetilde{\Psi} / \partial \rho$ for use in transverse problem

2. Set initial conditions at t=0:

   (a) At each position in z, set mean component $f_m^0 = V_{rest}$, where V_{rest} is the resting transmembrane potential

(b) At each position in z, φ, ρ, set all mean-free components (ϕ_i, ϕ_e, ϕ_m) to zero

At each time step within time loop:

1. At each position in z along fiber:

   (a) Compute $I_m(\phi_m^0 + f_m^0)$ at each angle φ on the membrane

   (b) Compute $\overline{I_m}$ by averaging I_m over the fiber circumference, for use in the longitudinal problem

   (c) Compute $\widetilde{I_m} \equiv I_m - \overline{I_m}$ at each angle φ on the membrane, for use in the transverse problem

   (d) Use $\widetilde{I_m}$ and $\partial\widetilde{\Psi}/\partial\rho$ to solve transverse problem (Eq. 2.13) for ϕ_i^0 and ϕ_e^0 at $t + \Delta t$; for each angle φ on the membrane compute ϕ_m^0 at $t + \Delta t$ using $\phi_m^0 \equiv \phi_i^0 - \phi_e^0$ on $\rho = a$

2. Use $\overline{I_m}$ and $\partial^2 \langle\Psi\rangle / \partial z^2$ to solve longitudinal problem (Eq. 2.16) for f_m^0 at $t+\Delta t$

Step 1d within the time loop numerically solves the 2D transverse problem by transforming the system of equations using the finite difference method (FDM). In order to implement the FDM, each 2D cross-section of the fiber cylinder must be immersed in cylindrical extracellular space with radius R_b (see Fig. 2.2) large enough to assume Dirichlet boundary condition $\phi_e^0 = 0$ on $\rho = R_b$. The LO Laplace equations of the transverse problem (Eqs. 2.13a and 2.13b) are discretized using the finite difference method, and matching conditions (Eqs. 2.13c and 2.13d) are used to discretize Laplace's equation at the membrane boundary. The time derivative in the matching conditions is approximated using the backward difference.[94] Step 2 within the time loop solves Eq. 2.16 by discretizing the 1D, time-dependent problem using the Crank-Nicolson method.[95] The no-flux boundary condition in longitudinal

direction is applied on f_m^0 at the ends of the fiber, and a sufficient length of fiber is simulated so that the solution does not change with additional fiber length. The asymptotic fiber model is implemented in MATLAB, and a 30 ms simulation requires 28.7 minutes of CPU time on an x86-64 machine running Linux with a 3 GHz processor and 4 GB of memory. Values of all parameters used to simulate the asymptotic fiber model are given in Table 2.2. Two different electrode setups are used to validate the asymptotic fiber model by comparing simulation results to analytical solutions, as detailed in Secs. 2.1.5 and 2.1.6. For both validations, a passive membrane with linear dynamics is used, which defines membrane current I_m,

$$I_m(\phi_m^0 + f_m^0) = \frac{(\phi_m^0 + f_m^0) - V_{rest}}{R_m} \tag{2.17}$$

where V_{rest} is the resting transmembrane potential, and R_m is the membrane surface resistance, which is a constant value for a passive fiber.

2.1.5 Validation of Temporal Scales Separation

This first validation tests the temporal separation of short and long time scales by imposing a uniform electric field in the transverse direction to the fiber, yielding a problem that is independent of longitudinal position z. In this case, the LO potentials represent the solutions to the full BVP in Eqs. 2.2 and 2.3, and the leading order ^{0} superscripts are dropped. For a uniform field E_u the primary potential $\Psi = -E_u \rho cos(\varphi)$, and the mean-free transverse source function and membrane current are $\partial\widetilde{\Psi}/\partial\rho = -E_u cos(\varphi)$ and $\widetilde{I_m} = \phi_m/R_m$. Substituting these equations into the transverse problem (Eq. 2.13) yields a 2D BVP dependent on ρ and φ, and can be solved using separation of variables.[97] Setting initial conditions $\phi_i = \phi_e = 0$ and applying a step pulse $E_u(t) = E_u u(t)$ yields formulas for the mean-free potential in

Table 2.2: Parameters for validation of asymptotic fiber model

Symbol	Value	Definition
Fiber and medium geometry and electrical properties[96]		
a	37.5 μm	fiber radius
R_b	$3.8a = 142.5$ μm	extracellular boundary radius[a]
L_f	48 mm	length of fiber[b]
σ_i	16.7 mS/cm	intracellular conductivity
σ_e	50.0 mS/cm	extracellular conductivity
R_m	2.29 kΩcm^2	membrane surface resistance
C_m	1.3 μF/cm^2	membrane surface capacitance
Numerical implementation		
$\Delta\rho$	$a/10 = 3.75$ μm	discretization in ρ
$\Delta\varphi$	$\pi/16$ rad	discretization in φ
Δz	$L_f/1536 = 31.25$ μm	discretization in z
Δt	1 ns to 0.1 ms	discretization in t[c]
Temporal aspects of pulsing protocol		
τ_p	30 ms	pulse duration[d]
N	1	number of pulses
Specific to validation of temporal scale separation[e]		
E_u	1.48 V/cm	uniform transverse electric field
V_{rest}	-40.1 mV	resting transmembrane potential
Specific to validation of spatial scale separation		
I_s	1.32 mA	stimulation current
d	1 cm	interelectrode distance
b	$10a = 375$ μm	electrode-fiber distance
V_{rest}	0 mV	resting transmembrane potential

[a] Dirichlet BC on secondary potential, $\phi_e^0 = 0$, is applied on $\rho = R_b$, to approximate condition $\phi_e^0 \to 0$ as $\rho \to \infty$ in infinite medium

[b] Fiber is long enough so that no-flux BC on f_m^0 at ends of fiber does not effect solution

[c] Δt is adaptive based on how fast state variables change

[d] Pulse duration long enough to reach steady state

[e] E_u and V_{rest} are chosen so that maximum magnitudes of mean-free and mean potentials are the same as for validation using point electrodes, which enables the error analysis in Sec. 2.1.7

a 2D transverse cross section,[98]

$$\phi_i = -E_u \rho \cos\varphi \left\{ -1 + \frac{2\sigma_e}{\sigma_i + \sigma_e} e^{-t/\tau_{ip}} + \frac{2a}{R_m \sigma_i D_u} \left(1 - e^{-t/\tau_{ip}}\right) \right\}, \tag{2.18a}$$

$$\phi_e = -E_u \rho \cos\varphi \frac{a^2}{r^2} \left\{ 1 - \frac{2\sigma_i}{\sigma_i + \sigma_e} e^{-t/\tau_{ip}} - \frac{2a}{R_m \sigma_e D_u} \left(1 - e^{-t/\tau_{ip}}\right) \right\}, \tag{2.18b}$$

$$\phi_m = 2E_u a \cos\varphi \left(1 - \frac{a}{R_m D_u} \frac{\sigma_i + \sigma_e}{\sigma_i \sigma_e} \right) \left(1 - e^{-t/\tau_{ip}}\right), \tag{2.18c}$$

where D_u is a unitless constant,

$$D_u = 1 + \frac{a}{R_m} \frac{\sigma_i + \sigma_e}{\sigma_i \sigma_e}, \tag{2.19}$$

and τ_{ip} is the time constant governing the fast initial polarization of the fiber by the transverse field,

$$\tau_{ip} = \frac{aC_m}{D_u} \frac{\sigma_i + \sigma_e}{\sigma_i \sigma_e}. \tag{2.20}$$

Substituting $\overline{I_m} = (f_m - V_{rest})/R_m$ into the longitudinal problem (Eq. 2.16), and recognizing all derivatives with respect to z are zero, yields an equation for the evolution of the mean transmembrane potential f_m,

$$C_m \frac{df_m}{dt} = -\frac{f_m - V_{rest}}{R_m}, \tag{2.21}$$

with analytical solution $f_m(t) = V_{rest} \{1 - \exp(-t/(R_m C_m))\}$ for $f_m(0) = 0$. Setting the initial condition $f_m = 0$ instead of the physiological $f_m = V_{rest}$ allows simulation of the fast transverse polarization as well as the slow charging of the membrane to its resting state $f_m = V_{rest}$. Parameters specific to the uniform field validation are given in Table 2.2.

Results of simulating total transmembrane potential Φ_m and mean transmembrane potential f_m, computed from Eqs. 2.18 and 2.21 are shown in Fig. 2.3. There

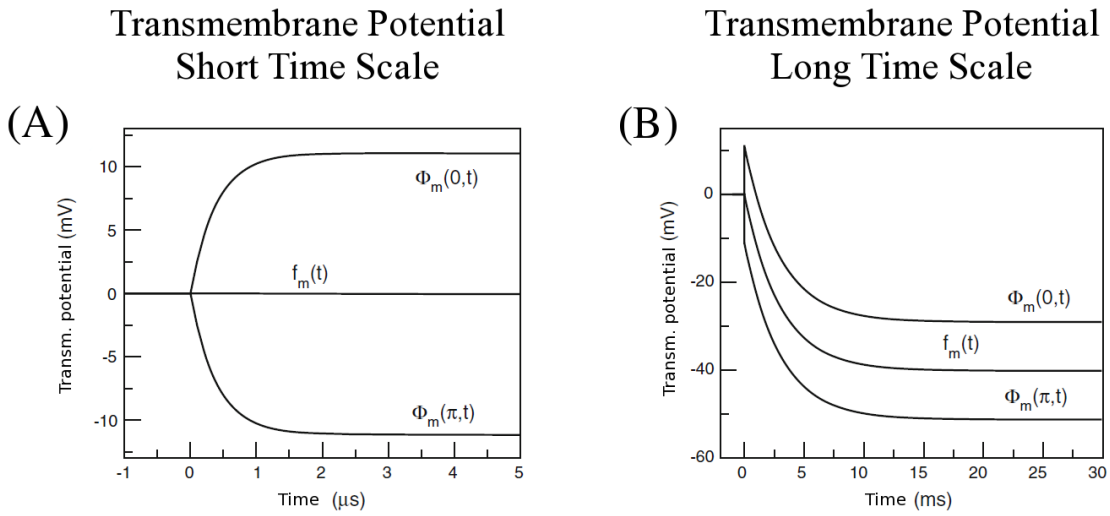

FIGURE 2.3: Validation of temporal scales separation in asymptotic fiber model. Temporal evolution of total transmembrane potential Φ_m at $\varphi = 0$ and $\varphi = \pi$ and mean component f_m are shown for a fiber in a uniform transverse field. The short time scale of transverse polarization is shown during the first 5 μs in (A), and the long time scale of evolution of mean component is shown over the entire simulation in (B).

are two temporal scales observed in the figure. First, the fast evolution of the mean-free potential ϕ_m with time constant $\tau_{ip} = 0.39$ μs in Fig. 2.3A. Second, the slow evolution of mean potential f_m with time constant $R_m C_m = 2.98$ ms in Fig. 2.3B. These disparate scales provide validation for separation of the temporal scales in the asymptotic fiber model.

2.1.6 Validation of Spatial Scales Separation

The second validation of the asymptotic fiber model compares steady state results to the analytical solution of a fiber with stimulus provided by point electrodes,[67] as illustrated in Fig. 2.4. This validation tests the separation of short and long spatial scales. Here, the primary potential has a well-known analytical solution:

$$\Psi = \frac{I_s}{4\pi\sigma_e}\left(\frac{1}{R_a} - \frac{1}{R_c}\right), \tag{2.22}$$

where I_s is the stimulus current, and R_a and R_c are distances from the anode and cathode to a point in 3D space, respectively,

$$R_a = \sqrt{\{(\rho\cos(\pi-\varphi)+b\}^2 + \{\rho\sin(\pi-\varphi)\}^2 + \left\{z+\frac{d}{2}\right\}^2}, \tag{2.23a}$$

$$R_c = \sqrt{\{(\rho\cos(\pi-\varphi)+b\}^2 + \{\rho\sin(\pi-\varphi)\}^2 + \left\{z-\frac{d}{2}\right\}^2}. \tag{2.23b}$$

For the AFs in the asymptotic fiber model, the mean-free transverse AF ($\partial\widetilde{\Psi}/\partial\rho$) is defined along the membrane circumference and mean longitudinal AF ($\partial^2\langle\Psi\rangle/\partial z^2$) is found from an average over the fiber cross-sectional area,

$$\frac{\partial\widetilde{\Psi}}{\partial\rho} \equiv \frac{\partial\Psi}{\partial\rho} - \frac{1}{2\pi a}\int_0^{2\pi a}\frac{\partial\Psi}{\partial\rho}\,ad\varphi, \tag{2.24a}$$

$$\frac{\partial^2\langle\Psi\rangle}{\partial z^2} \equiv \frac{1}{\pi a^2}\int_0^{2\pi}\int_0^{a}\frac{\partial^2\Psi}{\partial z^2}\,\rho d\rho d\varphi. \tag{2.24b}$$

The integral in Eq. 2.24a is approximated using the Riemann sum, whereas the integrals in Eq. 2.24b are approximated using the trapezoidal rule. The functions

$\partial\Psi/\partial\rho$ and $\partial^2\Psi/\partial z^2$ are derived analytically from Eq. 2.22,

$$\frac{\partial\Psi}{\partial\rho} = -\frac{I_s}{4\pi\sigma_e}\left[a + b\cos(\pi-\varphi)\right]\left\{\left[\left(z+\frac{d}{2}\right)^2 + a^2 + 2ab\cos(\pi-\varphi) + b^2\right]^{-3/2}\right. \tag{2.25a}$$

$$\left. - \left[\left(z-\frac{d}{2}\right)^2 + a^2 + 2ab\cos(\pi-\varphi) + b^2\right]^{-3/2}\right\},$$

$$\frac{\partial^2\Psi}{\partial z^2} = \frac{I_s}{4\pi\sigma_e}\left\{\right. \tag{2.25b}$$

$$\left[\left(z+\frac{d}{2}\right)^2 + \rho^2 + 2\rho b\cos(\pi-\varphi) + b^2\right]^{-5/2}\left[2\left(z+\frac{d}{2}\right)^2 - \rho^2\right.$$

$$\left. - 2\rho b\cos(\pi-\varphi) - b^2\right] - \left[\left(z-\frac{d}{2}\right)^2\right.$$

$$\left. + \rho^2 + 2\rho b\cos(\pi-\varphi) + b^2\right]^{-5/2}\left[2\left(z-\frac{d}{2}\right)^2 - \rho^2 - 2\rho b\cos(\pi-\varphi) - b^2\right]\Bigg\},$$

where it is assumed that the electrodes are directly under the fiber in the x-dimension at $x = 0$.

Initial conditions on all potentials, as well as V_{rest}, are set to zero in accordance with the analytical solution. The asymptotic fiber is simulated until 30 ms with the pulse on the entire time, approximately ten-fold longer than the slow time scale $R_m C_m = 2.98$ ms in Eq. 2.5, to ensure steady state is achieved. Parameters specific to point electrode validation are given in Table 2.2. The fibers are considered infinitely long, and thus, fiber length L_f in Table 2.2 is chosen long enough that the solution is not affected by longitudinal no-flux boundary condition applied on f_m^0 at the ends of the fiber.

The analytical steady state solution for potentials is given in a study by Schanbel

and Struijk,[67]

$$V_j = \Psi_j + \sum_{n=0}^{\infty} \int_0^{\infty} \left\{ A_n^j(k) I_n(k\rho) + B_n^j(k) K_n(k\rho) \right\} \cos(n\varphi) \cos(kz)\, dk, \qquad (2.26)$$

where $j = i$ (intracellular), e (extracellular), or m (membrane), I_n and K_n are modified Bessel functions, and A_n^j and B_n^j are constants. In this formulation, the constants A_n^j and B_n^j are determined from continuity of current and potential at the intracellular/membrane and the extracellular/membrane interfaces, with the restriction that A_n^e and B_n^i are zero to maintain boundedness of potential. Primary potential Ψ_j in Eq. 2.26 is set to zero everywhere except in the extracellular space, where Ψ_e is solved from Eq. 2.22. Although the analytical solution assumes finite membrane thickness and the asymptotic fiber model assumes infinitesimally thin membrane, the membrane is only 5 nm thick while the fiber radius is 37.5 μm, so this discrepancy is not likely to contribute to error in the asymptotic fiber model. Computer implementation of Eq. 2.26 was coded originally coded by Brian J. Kim and Wanda Krassowska Neu,[98] and follows guidelines set forth in,[67] where the integral in k is evaluated using the trapezoidal rule with decreasing Δk as $k \to 0$ to avoid infinite value of K_n at $k = 0$.

Validation in a transverse profile directly under the cathode, where error in asymptotic fiber mode is greatest, is shown in Fig. 2.5. Potential is shown in the range where $\rho < 3.8a$, where $\rho = 3.8a$ is where the Dirichlet condition on secondary potential $\phi_e^0 = 0$ is applied. Intracellular and extracellular potentials V_i and V_e computed from analytical equation (Eq. 2.26) are compared to asymptotic fiber model potentials V_i^0 and V_e^0. Potential from asymptotic fiber model and analytical solution are very close. Larger differences are found in the extracellular space: 0.456 (relative error of 0.68%) and 0.433 mV (relative error of 0.96%) on the proximal and distal sides of the fiber, respectively. These differences arise from the Dirichlet boundary

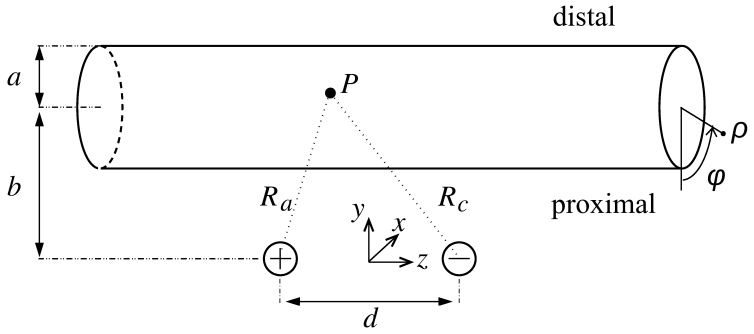

FIGURE 2.4: Illustration of a 3D muscle fiber with point electrodes. Cylindrical coordinates (ρ, φ, and z) and Cartesian coordinates (x, y, and z) are shown. Proximal side of fiber closest to electrodes is at $\varphi = 0$, and distal side of the fiber furthest from electrodes is at $\varphi = \pi$. Electric pulse is provided by two point source electrodes; symbols $\oplus$ and $\ominus$ mark positions of the point anode and point cathode, respectively. Parameters marked on illustration are fiber radius a, interelectrode distance d, and electrode-fiber distance b. A sample point in space, P, is provided to define the distance from anode R_a and distance from cathode R_c. Muscle fiber not drawn to scale to improve clarity of features: in reality fiber radius is two or three orders of magnitude smaller than fiber length.

condition on secondary potential $\phi_e^0 = 0$ at $\rho = 3.8a$, which is clearly not the case given that V_e is still 1.43 mV below primary potential on proximal side and 1.0 mV above primary potential on the distal side, meaning that secondary potential is not quite equal to zero.

Validation in the longitudinal direction is shown in Fig. 2.6. Transmembrane potential on the most distal and proximal sides of the fiber (see Fig. 2.4) from asymptotic model (Φ_m^0) and analytical solution (Φ_m) are shown to be very close. Fig. 2.6A reveals the largest magnitude of transmembrane potential occurs over the anode and cathode at ± 5 mm, and there are longitudinally adjacent regions of reversed polarity with smaller maximum magnitude. These regions of reversed polarity are called "virtual electrodes" (VEs), and are a well-known phenomenon in electrical behavior of fibers (see Fig. 1.3).[99] Profiles zoomed in around the cathode indicate that error is greatest over the cathode at $z = 5$ mm, with error reversing sign adjacent to the position of the cathode and reaching 0.226 mV (relative error of

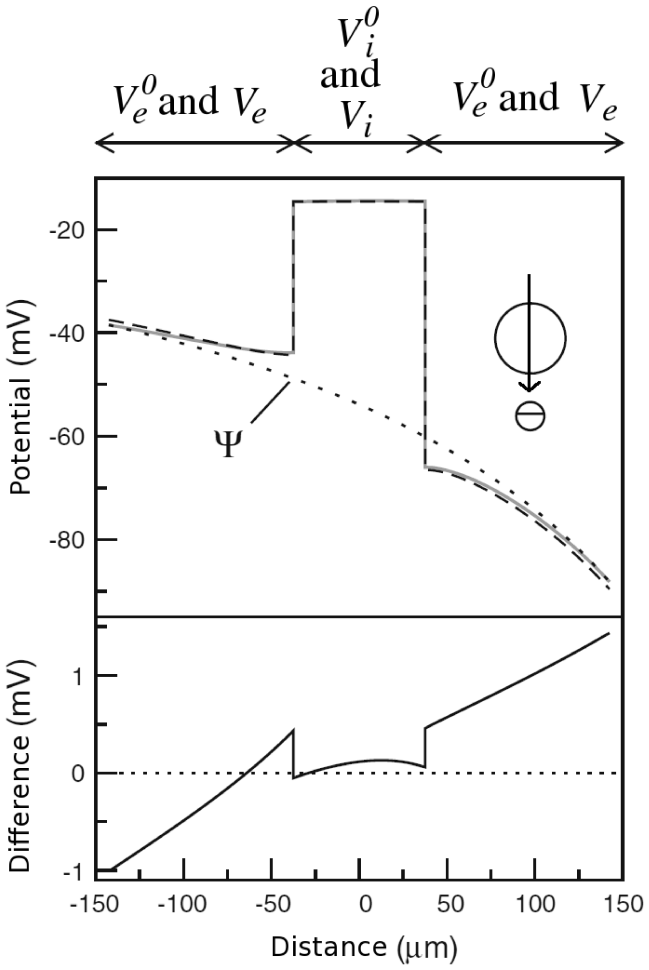

FIGURE 2.5: Transverse profile of steady state potentials for validation of spatial scales separation in asymptotic fiber model. Potentials are shown at steady state along a line bisecting fiber and extracellular space directly under the cathode ($z = 0.5$ cm) that extends out to $\rho = 3.8a = 142.5$ μm, where the Dirichlet boundary condition $\phi_e^0 = 0$ is imposed on secondary potential. Line path and cathode are marked in inset. Potentials V_i^0 and V_e^0 from asymptotic fiber model are shown in solid grey, V_i and V_e from the analytical solution in dashed black, and primary potential Ψ in dotted black. Difference between asymptotic and analytical solutions is shown at the bottom.

1.3%) at $z = 4.56$ and $z = 5.44$ mm on the distal side of the fiber.

Contour plot of the difference in transmembrane potential between asymptotic model and analytical solution over a section of membrane longitudinally centered over the cathode is shown in Fig. 2.7. Largest error occurs over the site of the cathode, and over the cathode the largest error occurs between $\varphi = 0.. \pm \pi$, rather than at the most proximal or distal angles of $\varphi = 0$ and $\varphi = \pi$. RMSE over the entire region shown in Fig. 2.7 is 0.153 mV, which is 0.295% of the maximum magnitude of Φ_m, and the correlation coefficient is 0.9999, demonstrating that the asymptotic fiber model faithfully reproduces quantitative and qualitative features of the analytical solution.

2.1.7 Sources of Error in Validations of the Asymptotic Fiber Model

Sources of error are now considered for the validations of the asymptotic fiber model presented in Secs. 2.1.5 and 2.1.6, with the goal of estimating error due to asymptotic separation alone. Five sources contribute to total error: truncation error of the analytical solution, errors from solving longitudinal and transverse problems numerically, error from using finite extracellular space when solving the transverse problem, and asymptotic separation of the 3D BVP into transverse and longitudinal problems. Truncation error of the analytical solution is below 6 nV and can be ignored.

Next, the errors introduced by the numerical solution of the transverse problem and the finite extracellular space are explored. As noted in Sec. 2.1.5, in the special case of a uniform transverse field the asymptotic model introduces no approximations and the solutions represent exact potentials. Thus, the difference between the mean-free transmembrane potentials computed numerically and from the analytical equation (Eq. 2.18c) reflects only two errors: solving the transverse problem numerically and error from using finite extracellular space. The maximum RMSE in transmembrane potential around the fiber circumference when a uniform field is

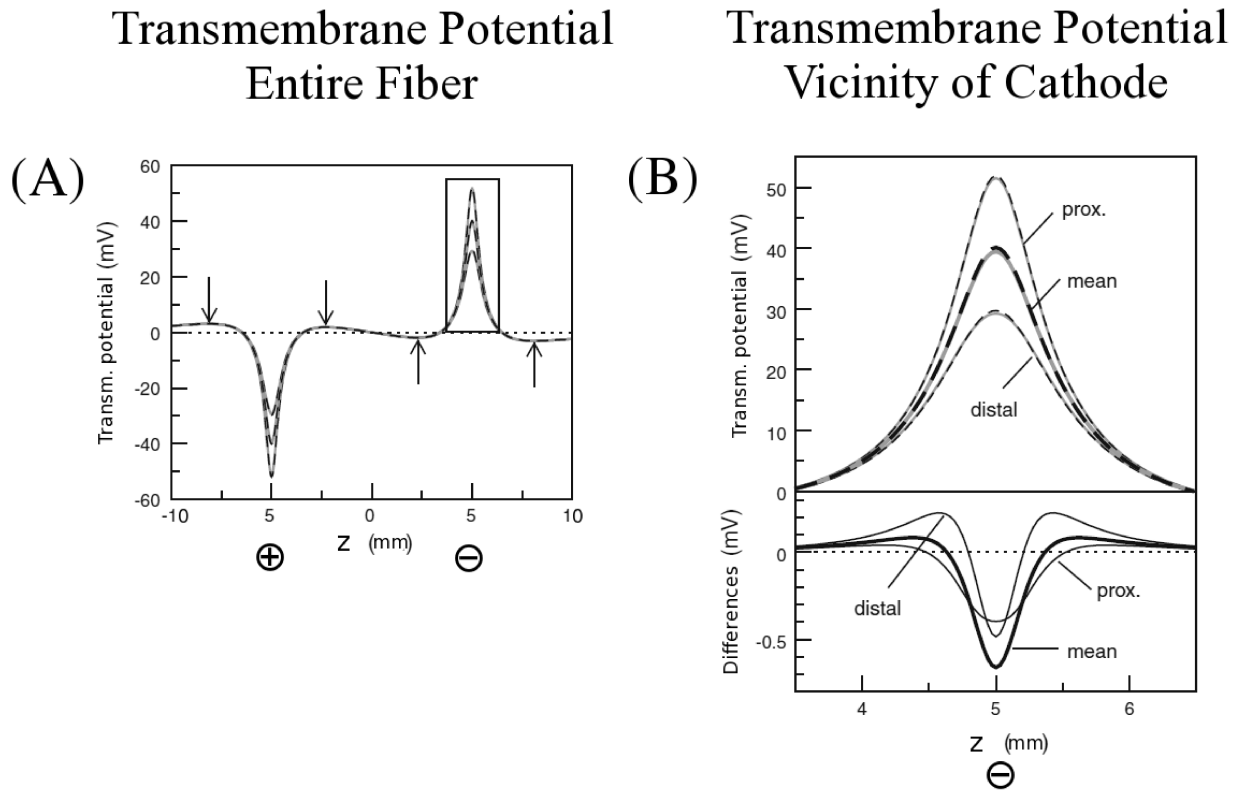

FIGURE 2.6: (A) Longitudinal profile of steady state transmembrane potential for validation of spatial scales separation in asymptotic fiber model. Transmembrane potential from asymptotic model Φ_m^0 (solid grey) and analytical solution Φ_m (dashed black) are shown at steady state in the range $-10 < z < 10$ mm, for both the proximal $\varphi = 0$ and distal $\varphi = \pi$ side of the fiber (Fig. 2.4). Circumferential mean components from asymptotic model f_m^0 (solid grey) and analytical solution $\overline{\Phi_m}$ (dashed black) are also shown. Arrows indicate maximum magnitudes of the virtual electrodes, which are areas of reversed polarity longitudinally adjacent to real electrodes. Positions of anode and cathode are marked with $\oplus$ and $\ominus$, respectively. (B) Zoomed in version of potentials in panel A, with mean transmembrane potentials now shown with thick curves. Difference between asymptotic and analytical solutions is shown at the bottom.

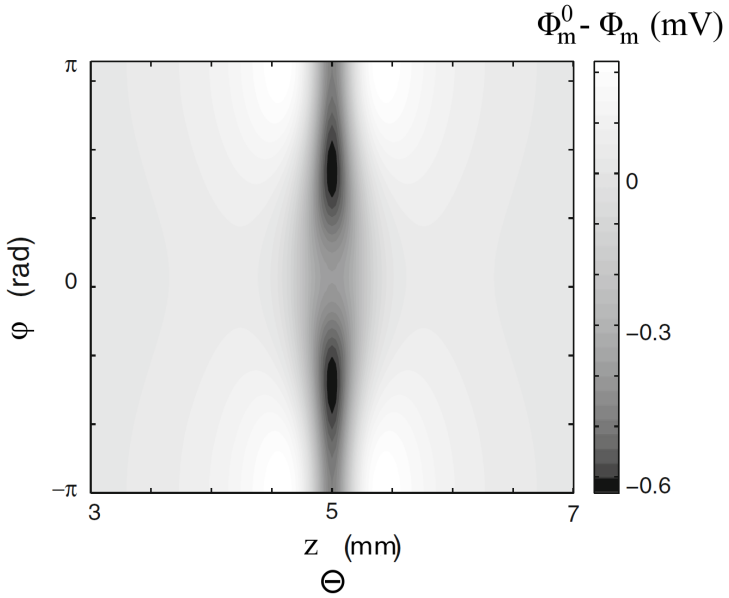

FIGURE 2.7: Contour plot of difference (in mV) in steady state transmembrane potential between asymptotic fiber model and analytical solution ($\Phi_m^0 - \Phi_m$). Difference is shown in the range $3 < z < 7$ mm and around the circumference of the fiber $\varphi = -\pi..\pi$, where $\varphi = 0$ corresponds to the proximal side of the fiber relative to electrodes, and $\varphi = \pm\pi$ corresponds to the distal side of the fiber relative to the electrodes. Position of cathode is marked with $\ominus$.

applied is 0.175 mV. For the case of point electrodes, the largest differences between asymptotic model steady state transmembrane potential Φ_m^0 and analytical solution Φ_m occur directly over the electrodes, thus, error at this longitudinal position is compared to the uniform field case. The RMSE computed around the membrane circumference under the cathode is 0.539 mV (1.04% of the maximum Φ_m), which is approximately three-fold larger than 0.175 mV error due to numerical solution of transverse problem and finite extracellular space.

Thus, combined errors of asymptotic separation and numerically solving the longitudinal problem would appear to contribute more to total error than errors from numerical solution of transverse problem and finite extracellular space. An estimated upper bound on error from numerically solving the longitudinal problem is 0.097 mV for $\Delta z = 31.25$ μm used in validation simulations. Thus, while it is unknown ex-

actly how various errors combine to produce total error, it does appear that error of asymptotic separation is slightly larger, but on the same order of magnitude as other errors present in the solution, and below 1% of the maximum transmembrane potential.

2.2 Model Alterations for Simulation of Electroporation-Mediated Uptake

The primary objective is to simulate electroporation-mediated uptake of small molecules in muscle tissue composed of individual cylindrical fibers. Emphasis is placed on bringing the model as close as possible to actual experiments performed in muscle tissue of small mammals. Therefore, several additions and modifications must be made to the model and parameters in Sec. 2.1. First, electrical current from formation of electropores in the membrane, I_{ep}, must be added to the membrane current I_m. Second, model parameters that are representative of electroporation-mediated delivery in small mammals must be defined. These parameters include tissue geometry, tissue electrical properties, experimental setup, and pulsing protocol. Note that the fiber is no longer in an infinite medium, but is now surrounded by many muscle fibers in the tissue. Finally, additional equations must be derived for mass transport of small molecules in the tissue and across the membrane so that uptake of molecules can be simulated. Addition of electroporation current density I_{ep} and model parameters are addressed in this section. Derivation of mass transport equations for the small molecule is derived in the next section (Sec. 2.3).

First, addition of electroporation current density I_{ep} to the membrane current density I_m is addressed. I_m appears as $\widetilde{I_m}$ in the matching conditions of transverse problem in Sec. 2.1 (Eqs. 2.13c and 2.13d), and as $\overline{I_m}$ in the longitudinal problem (Eq. 2.15). Later in Sec. 2.1, the membrane current was defined for a passive membrane (Eq. 2.17) as a function of LO total transmembrane potential ($\Phi_m = \phi_m + f_m$). Note that the LO superscript ^{0} has been dropped for convenience, and it is the convention in the rest of the dissertation that the LO superscripts are implied even if not explicitly shown. However, it is important to remember that all results are based on a leading order equations. In this case, I_m represents the linear leakage

current density due to non-specific ionic flow through the membrane,

$$I_m(\Phi_m) = \frac{\Phi_m - V_{rest}}{R_m}, \tag{2.27}$$

where the surface resistance R_m is constant, as shown in Fig. 2.8A. Electroporation creates a parallel pathway with variable, nonlinear conductance, as shown in Fig. 2.8B. Therefore, electroporation current is accounted for by simply adding it to Eq. 2.27,

$$I_m(\Phi_m) = \frac{\Phi_m - V_{rest}}{R_m} + I_{ep}. \tag{2.28}$$

I_{ep} is defined in terms of pore density N_{ep} and current through a single pore i_{ep},

$$I_{ep} = N_{ep} i_{ep}. \tag{2.29}$$

The pore density is governed by a first order differential equation with nonlinear dependence on Φ_m, as derived by Neu and Krassowska,[48]

$$\frac{dN_{ep}}{dt} = \alpha e^{(\Phi_m/V_{ep})^2} \left(1 - \frac{N_{ep}}{N_0 e^{q(\Phi_m/V_{ep})^2}}\right), \tag{2.30}$$

where α is the rate constant of pore creation/destruction, V_{ep} is the characteristic voltage of electroporation, q is a dimensionless electroporation constant, and N_0 is the equilibrium pore density when $\Phi_m = 0$. The current through a single pore in Eq. 2.29 has been derived from the Nernst-Planck equation by previous researchers.[54,100,101] The result is an expression for i_{ep} that is an instantaneous function of transmembrane potential, and takes into account Born energy barrier arising from charged molecules traveling through electropores surrounded by the low permittivity space of the membrane,[100,101,102]

$$i_{ep} = \frac{\pi r_m^2 \sigma_p k_B T U}{he} \frac{e^U - 1}{\frac{w_o e^{w_o - Un} - Un}{U(w_o - Un)} e^U - \frac{w_o e^{w_o + Un} + Un}{U(w_o + Un)}}, \tag{2.31}$$

where σ_p is the conductivity of aqueous solution in pores, r_m is the radius of the pore, h is the membrane thickness, w_o is maximum of the nondimensional energy barrier within a pore and n is the relative entrance length of a pore (as defined and illustrated in Appendix C, Fig. C.2).[54,100] Nondimensional transmembrane potential is defined, assuming only monovalent ions exist $|z_m| = 1$,

$$U = \frac{z_m e}{k_B T} \Phi_m, \tag{2.32}$$

where e is elementary charge, k_B is the Boltzmann constant, and T is temperature. Note that for $U = 0$ Eq. 2.31 is not defined, but using L'Hopital's rule (or rederiving assuming $\Phi_m = 0$), reveals that $i_{ep} = 0$ for $U = 0$. The only changes to the implementation algorithm in Sec. 2.1.4 is that in step 1a the membrane current I_m is computed using Eq. 2.28 with I_{ep} at the current time step, and between steps 1c and 1d, Eq. 2.30 is approximated using the forward difference to find pore density at $t + \Delta t$ for all positions on membrane. Furthermore, the pore density in the membrane is initially set to zero. Finally, electroporation parameters are based on experimental results using a uranyl modified black lipid membrane (BLM),[54,100] with the exception that V_{ep} is based on experiments using unfertilized sea urchin eggs.[54] Given that these parameters are not from muscle experiments, they create a discrepancy that is discussed in Sec. 4.4.1.

The second alteration to the asymptotic fiber model is that parameters are updated to be representative of electroporation-mediated delivery of small molecules in the soleus, gastrocnemius, and tibialis cranialis muscles of rats and mice.[29,31,32] The electric pulse is now delivered by finite-radius needle electrodes instead of point electrodes, as shown in Fig. 2.10 (figure discussed in more detail in next paragraph). Table 2.3 lists appropriate range of voltage magnitude ($|V_0|$) for interelectrode distance d so that the quantity $2V_0/d$ = 400-1000 V/cm is representative of the range used in the literature.[21,31,32,103] In accordance with the electrical properties of mus-

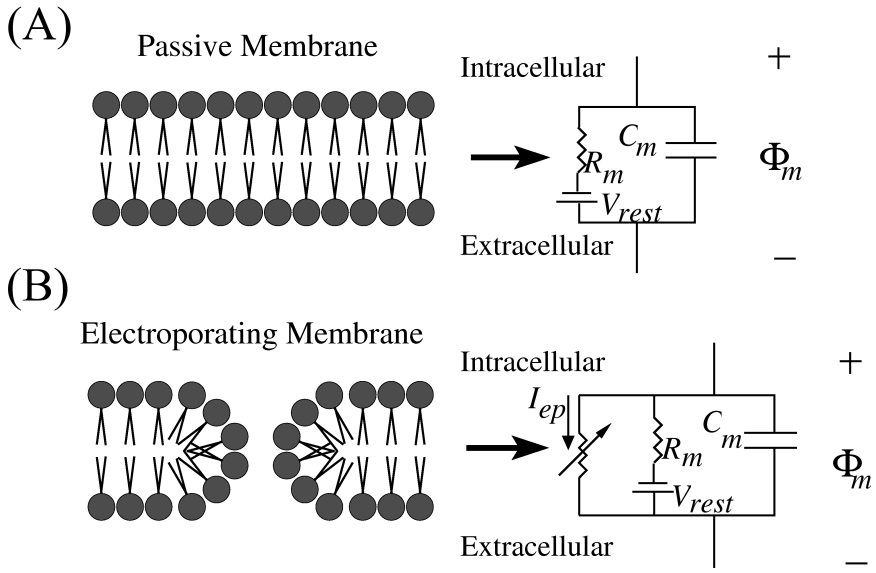

FIGURE 2.8: Electrical circuit representation of the phospholipid bilayer membrane of a muscle fiber. The circuit diagram is used to display the electrical difference between the membrane of a (A) passive and (B) electroporating fiber.

cle tissue, these needles are surrounded by an anisotropic homogeneous medium with tissue transverse conductivity σ_y and longitudinal conductivity σ_z. To compute the primary potential Ψ at the tissue level of the model, an analytical solution derived by Liheng Guo and John and Wanda Krassowska Neu is used.[75] The analytical solution is derived from solving the elliptic equation throughout the tissue,

$$\sigma_y \frac{\partial^2 \Psi}{\partial y^2} + \sigma_z \frac{\partial^2 \Psi}{\partial z^2} = 0, \tag{2.33}$$

where the Dirichlet BC is applied on the needle surfaces and current density vanishes at infinity (infinite medium), which results in

$$\Psi = -\frac{|V_0|}{\ln(2\beta)} \ln \left| \frac{\mathbb{W}_2}{\mathbb{W}_1} \right|, \tag{2.34}$$

where β is a nondimensional parameter

$$\beta = \frac{\mathbb{E}}{(\mathbb{C} + \mathbb{D})} \left(1 + \sqrt{1 - \frac{(\mathbb{C}^2 - \mathbb{D}^2)}{4\mathbb{E}^2}} \right), \tag{2.35}$$

and $\mathbb{C}$, $\mathbb{D}$, and $\mathbb{E}$ are parameters

$$\mathbb{C} = \frac{R_e}{\sqrt{\sigma_z}}, \tag{2.36a}$$

$$\mathbb{D} = \frac{R_e}{\sqrt{\sigma_y}}, \tag{2.36b}$$

$$\mathbb{E} = \frac{d/2}{\sqrt{\sigma_z}}. \tag{2.36c}$$

Parameters $\mathbb{W}_1$ and $\mathbb{W}_2$ are dimensionless

$$\mathbb{W}_1 = \frac{\mathbb{G} - \mathbb{E}}{\mathbb{C} + \mathbb{D}} \left(1 + \sqrt{1 - \frac{\mathbb{C}^2 - \mathbb{D}^2}{(\mathbb{G} - \mathbb{E})^2}} \right), \tag{2.37a}$$

$$\mathbb{W}_2 = \frac{\mathbb{G} + \mathbb{E}}{\mathbb{C} + \mathbb{D}} \left(1 + \sqrt{1 - \frac{\mathbb{C}^2 - \mathbb{D}^2}{(\mathbb{G} + \mathbb{E})^2}} \right), \tag{2.37b}$$

and

$$\mathbb{G} = \mathbb{Z} + i\mathbb{Y}, \tag{2.38a}$$

$$\mathbb{Z} = \frac{z}{\sqrt{\sigma_z}}, \tag{2.38b}$$

$$\mathbb{Y} = \frac{y}{\sqrt{\sigma_y}}. \tag{2.38c}$$

Note that Cartesian coordinate z is unchanged when expressed in cylindrical coordinates of the individual fiber, while Cartesian coordinate y becomes $\rho\cos(\pi - \varphi) + b$ when expressed in cylindrical coordinates of the individual fiber. It is assumed that tissue conductivities do not change in response to electroporation, which is addressed in Secs. 2.4 and 3.3.4. Permittivity of tissue is neglected, given that only low frequency pulses at 1 Hz are considered (Table 2.3).[104] From the analytical solution of Ψ, derivative analytical solutions are used to compute activating functions $\partial\widetilde{\Psi}/\partial\rho$ in the transverse problem and $\partial^2 \langle\Psi\rangle / \partial z^2$ in the longitudinal problem. The AFs are defined in Eq. 2.24, and the functions $\partial\Psi/\partial\rho$ and $\partial^2\Psi/\partial z^2$ are derived analytically

from Eq. 2.34,

$$\frac{\partial \Psi}{\partial \rho} = -\cos(\pi-\varphi)\frac{|V_0|}{\sqrt{\sigma_y}\ln(2\beta)} Re\left\{ \frac{i\mathbb{W}_2}{\frac{\mathbb{C}+\mathbb{D}}{2}\mathbb{W}_2^2 - \frac{\mathbb{C}-\mathbb{D}}{2}} - \frac{i\mathbb{W}_1}{\frac{\mathbb{C}+\mathbb{D}}{2}\mathbb{W}_1^2 - \frac{\mathbb{C}-\mathbb{D}}{2}} \right\}, \tag{2.39a}$$

$$\frac{\partial^2 \Psi}{\partial z^2} = -\frac{|V_0|}{\sigma_z \ln(2\beta)} Re\left\{ \frac{2\mathbb{W}_1^2(\mathbb{W}_1^2\mathbb{C} + \mathbb{W}_1^2\mathbb{D} + \mathbb{C} - \mathbb{D})}{(\mathbb{W}_1^2\mathbb{C} + \mathbb{W}_1^2\mathbb{D} - \mathbb{C} + \mathbb{D})^2 \left(\frac{\mathbb{C}+\mathbb{D}}{2}\mathbb{W}_1^2 - \frac{\mathbb{C}-\mathbb{D}}{2}\right)} \right. \tag{2.39b}$$

$$\left. - \frac{2\mathbb{W}_2^2(\mathbb{W}_2^2\mathbb{C} + \mathbb{W}_2^2\mathbb{D} + \mathbb{C} - \mathbb{D})}{(\mathbb{W}_2^2\mathbb{C} + \mathbb{W}_2^2\mathbb{D} - \mathbb{C} + \mathbb{D})^2 \left(\frac{\mathbb{C}+\mathbb{D}}{2}\mathbb{W}_2^2 - \frac{\mathbb{C}-\mathbb{D}}{2}\right)} \right\},$$

where Re indicates taking the real part of the argument. For needles oriented in the direction transverse to the direction of fibers, needed to produce the results in Sec. 3.3.1, the tissue space in Fig. 2.10 is rotated 90° and new coordinates are assigned, as shown in Fig. 2.9. Cartesian coordinate z_t is oriented along the length of the fibers, and Cartesian coordinate y_t is oriented between the electrodes and across the fibers, and can be expressed in individual fiber cylindrical coordinates as $\rho\cos(\pi-\varphi) + b_t$. Note that b_t is not the electrode-fiber distance, but rather, is simply the value in the y_p dimension that the fiber axis is at. In the transverse geometry in Fig. 2.9B, the function $\partial\Psi/\partial\rho$ can be found from $\partial\Psi/\partial z$ in the original longitudinal geometry in Fig. 2.9A,

$$\frac{\partial \Psi}{\partial \rho} = -\cos(\pi-\varphi)\frac{|V_0|}{\sqrt{\sigma_y}\ln(2\beta)} Re\left\{ \frac{\mathbb{W}_{t,2}}{\frac{\mathbb{C}_t+\mathbb{D}_t}{2}\mathbb{W}_{t,2}^2 - \frac{\mathbb{C}_t-\mathbb{D}_t}{2}} - \frac{\mathbb{W}_{t,1}}{\frac{\mathbb{C}_t+\mathbb{D}_t}{2}\mathbb{W}_{t,1}^2 - \frac{\mathbb{C}_t-\mathbb{D}_t}{2}} \right\}, \tag{2.40}$$

where now the transverse and longitudinal conductivities are switched for all param-

eters,

$$\mathbb{C}_t = \frac{R_e}{\sqrt{\sigma_y}}, \tag{2.41a}$$

$$\mathbb{D}_t = \frac{R_e}{\sqrt{\sigma_z}}, \tag{2.41b}$$

$$\mathbb{E}_t = \frac{d/2}{\sqrt{\sigma_y}}, \tag{2.41c}$$

$$\mathbb{W}_{t,1} = \frac{\mathbb{G}_t - \mathbb{E}_t}{\mathbb{C}_t + \mathbb{D}_t}\left(1 + \sqrt{1 - \frac{\mathbb{C}_t^2 - \mathbb{D}_t^2}{(\mathbb{G}_t - \mathbb{E}_t)^2}}\right), \tag{2.41d}$$

$$\mathbb{W}_{t,2} = \frac{\mathbb{G}_t + \mathbb{E}_t}{\mathbb{C}_t + \mathbb{D}_t}\left(1 + \sqrt{1 - \frac{\mathbb{C}_t^2 - \mathbb{D}_t^2}{(\mathbb{G}_t + \mathbb{E}_t)^2}}\right), \tag{2.41e}$$

$$\mathbb{G}_t = \mathbb{Z}_t + i\mathbb{Y}_t, \tag{2.41f}$$

$$\mathbb{Z}_t = \frac{y_t}{\sqrt{\sigma_y}}, \tag{2.41g}$$

$$\mathbb{Y}_t = \frac{z_t}{\sqrt{\sigma_z}}. \tag{2.41h}$$

Similarly, the function $\partial^2\Psi/\partial z_t^2$ for transverse geometry can be found from $\partial^2\Psi/\partial y^2$ in the original longitudinal geometry, with transverse and longitudinal tissue conductivities switched,

$$\begin{aligned}\frac{\partial^2\Psi}{\partial z_t^2} = -\frac{|V_0|}{\sigma_z \ln(2\beta)} Re \Bigg\{ &\frac{2\mathbb{W}_{t,2}^2(\mathbb{W}_{t,2}^2\mathbb{C}_t + \mathbb{W}_{t,2}^2\mathbb{D}_t + \mathbb{C}_t - \mathbb{D}_t)}{(\mathbb{W}_{t,2}^2\mathbb{C}_t + \mathbb{W}_{t,2}^2\mathbb{D}_t - \mathbb{C}_t + \mathbb{D}_t)^2\left(\frac{\mathbb{C}_t+\mathbb{D}_t}{2}\mathbb{W}_{t,2}^2 - \frac{\mathbb{C}_t-\mathbb{D}_t}{2}\right)} \\ &- \frac{2\mathbb{W}_{t,1}^2(\mathbb{W}_{t,1}^2\mathbb{C}_t + \mathbb{W}_{t,1}^2\mathbb{D}_t + \mathbb{C}_t - \mathbb{D}_t)}{(\mathbb{W}_{t,1}^2\mathbb{C}_t + \mathbb{W}_{t,1}^2\mathbb{D}_t - \mathbb{C}_t + \mathbb{D}_t)^2\left(\frac{\mathbb{C}_t+\mathbb{D}_t}{2}\mathbb{W}_{t,1}^2 - \frac{\mathbb{C}_t-\mathbb{D}_t}{2}\right)} \Bigg\}.\end{aligned} \tag{2.42}$$

Another alteration for simulation of electroporation-mediated uptake in muscle tissue is that each fiber is no longer surrounded by an infinite medium, rather, it is surrounded by neighboring fibers in the tissue. Despite the variation in fiber

(A)

Longitudinal Needle Orientation

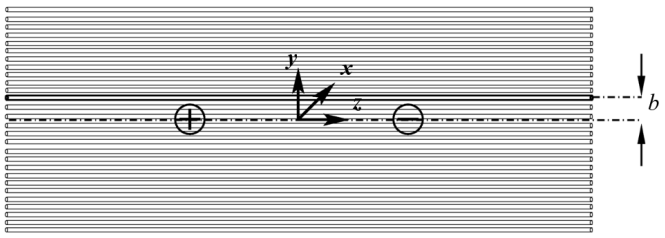

(B)

Transverse Needle Orientation

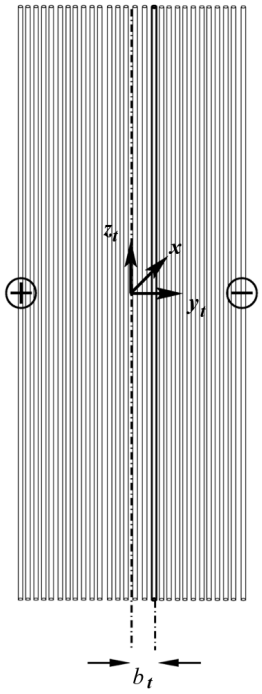

FIGURE 2.9: Longitudinal and transverse orientation of electrodes. All geometry is to scale, except for the radius of the individual fibers, which is enlarged for clarity. Tissue damage due to needles is ignored. Only one layer of fibers in the x-dimension is shown, due to uniform voltage on the needles in the x-dimension. (A) Longitudinal needle orientation, with entire tissue shown, and a bold fiber to illustrate electrode-fiber distance b. (B) Transverse needle orientation, with entire tissue shown, and new coordinates y_t and z_t are shown, with a bold fiber to illustrate an arbitrary fiber at $y_t = b_t$. See Fig. 2.10 for more details on the tissue and electrode geometry.

diameter and curvature of the fibers found in histological sections of tissue (Fig. 1.2), fibers in tissue are assumed to be structurally identical straight cylinders. These simplifications are necessary for mathematical formulation. Thus, the structure of the muscle tissue is assumed to be composed of individual fibers in a periodic lattice (Fig. 2.10), and indeed, to produce tissue scale results in Secs. 3.2.3 and 3.3 fibers are simply simulated at different distances from the electrodes. Consequently, the extracellular boundary radius R_b (Fig. 2.10B) of a period fiber in the tissue lattice is now set by the distance between fibers in the tissue. The fibers in the tissue are considered a collection of independent fibers, thus, the Dirichlet boundary condition on secondary potential $\phi_e = 0$ is applied on the boundary of each fiber at $\rho = R_b$. (Fig. 2.10B). This assumption is based on periodicity and symmetry arguments, and that the electric field generated by electrodes is approximately uniform on the transverse space scale of thin fibers separated by very small distances (Table 2.3). This assumption is less accurate for fibers that are very close to the electrodes, where the field may change significantly even for a small change in distance from electrodes, which is a weakness of the current version of the model.

Given that extracellular medium around each individual fiber is no longer infinite, the longitudinal problem equation that includes the ratio of extracellular to intracellular cross-sectional areas (γ) and ratio of extracellular to intracellular conductivities (μ) must be used (Eq. 2.15 instead of Eq. 2.16). The no-flux boundary condition in longitudinal direction on f_m is still enforced on the ends of the fiber, given that the length constant $(\gamma\mu)/(\gamma\mu+1)\sqrt{a\sigma_i R_m/2} = 1$ mm, and the length from electrode at $z = \pm 2.5$ mm to end of fiber at $z = \pm 6.5$ mm (13 mm fiber length for rat soleus muscle) is 4 mm. This equation for length constant can be found from substituting passive membrane dynamics for mean membrane current $\overline{I_m} = (f_m - V_{rest})/R_m$ into Eq. 2.15. The geometry of the model is shown in Fig. 2.10. Table 2.3 lists all parameters used in simulations of the electroporating fiber model. Note the interelectrode

distance is the distance measured from membrane to membrane of adjacent fibers, where a single fiber is assumed to have four neighbors. The equations and parameters presented in this section, along with the transverse and longitudinal problems in the asymptotic fiber model (Secs. 2.1.2 and 2.1.3), are used in derivation of the molecular uptake model (Sec. 2.3) and in the results (Chapter 3).

Table 2.3: Parameters for simulating an electroporating fiber

Symbol	Value	Definition	Source
	Fiber, tissue, and electrode geometry and electrical properties		
a	25.0 μm	radius of fiber	[105]
h	5 nm	thickness of membrane	[57]
R_b	25.5 μm	extracellular boundary radius (interfiber distance of 1 μm)	[106]
L_f	13 mm	length of fiber	[107]
σ_i	5.5 mS/cm	intracellular conductivity (cell level)[a]	[78]
σ_e	24 mS/cm	extracellular conductivity (cell level)[a]	[78]
σ_z	6.7 mS/cm	longitudinal conductivity (tissue level)[a]	[78]
σ_y	0.40 mS/cm	transverse conductivity (tissue level)[a]	[78]
R_m	10 kΩ cm^2	membrane surface resistance	[78]
C_m	1 μF/cm^2	membrane surface capacitance	[78]
V_{rest}	-89.1 mV	resting transmembrane potential	[78]
H	0.5 cm	thickness of muscle tissue	[29,108,109]
d	0.5 cm	interelectrode distance	[21,31]
b	0.48 to 2.15 mm	electrode-fiber distance	N/A
R_e	.030 cm	radius of needle electrodes	[31,32,103]
	Numerical implementation		
$\Delta\rho$	$a/20 = 1.25$ μm	discretization in ρ	N/A
$\Delta\varphi$	$\pi/32$ rad	discretization in φ	N/A
Δz	$L_f/416 = 31.25$ μm	discretization in z	N/A
Δt	1 ns to 0.1 ms	discretization in t	N/A
	Pulsing Protocol		
$\lvert V_0\rvert$	100-250 V[c]	magnitude of voltage on electrodes	[31,32,103]
τ_p	100 μs	pulse duration	[31,32]
N	8	number of pulses	[29,31,32]
T_p	1 s	period of pulse train	[29,31,32]
	Electroporation: pore creation and current[b]		
α	100 cm^{-2}ms^{-1}	rate constant	[54]
V_{ep}	258 mV	characteristic voltage of electroporation	[54]
N_0	1.5x10^5 cm^{-2}	equilibrium pore density when $\Phi_m = 0$	[54]
q	2.46	electroporation constant	[54]
r_m	0.8 nm	pore radius	[54]
σ_p	20 mS/cm	conductivity of aqueous solution in pore	[51]
w_o	2.65	dimensionless energy barrier in pore	[54]
n	0.15	relative entrance length of pore	[54]
T	310 K	body temperature of small mammals	[110]

[a] σ_z and σ_y used to compute tissue macroscopic primary potential, σ_i and σ_e used at microscopic fiber level

[b] Electroporation parameters validated with experiments on unfertilized sea urchin eggs[54]

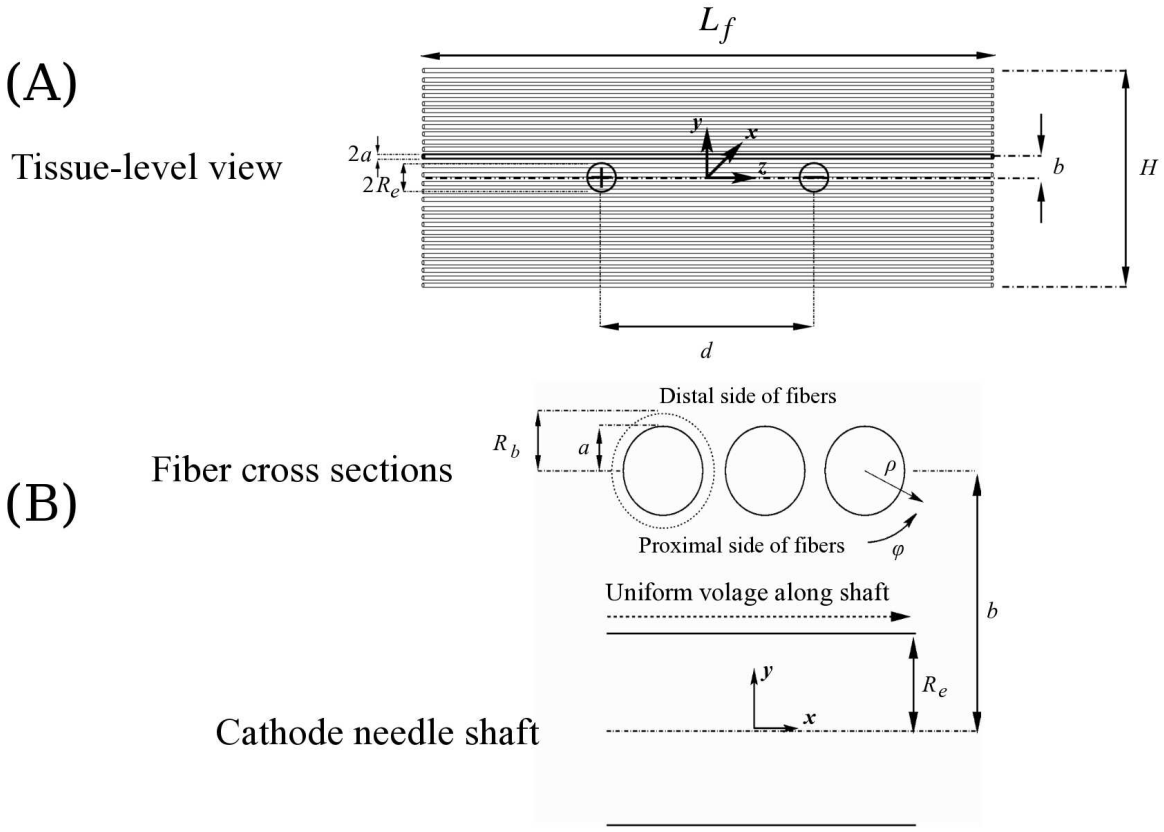

FIGURE 2.10: Geometry of muscle tissue and electrodes. All geometry is to scale, except for the radius of the individual fibers, which is enlarged for clarity. (A) Entire tissue is shown, with a bold fiber to illustrate electrode-fiber distance b. Only one layer of fibers in the x-dimension is shown, due to uniform voltage on the needles in the x-dimension. Tissue damage due to needles is ignored. (B) A zoomed in view of panel A directly over the cathode, where now the z-dimension is pointing into the page, and the fibers are viewed in cross sections taken at $z = +\frac{d}{2}$. This panel highlights the relationship between cylindrical coordinates at the single-fiber level and the Cartesian coordinates at the tissue level, and shows the geometry of fibers along the shaft of the cathode in the x-dimension, where all results are uniform from fiber to fiber.

2.3 Derivation of Molecular Uptake Model

2.3.1 The Boundary Value Problem

The 3D spatiotemporal transport of small molecules in the intracellular and extracellular regions for a muscle fiber (Fig. 2.11) is modeled using a conservation of mass equation, which takes into account transport of the molecules due to diffusional and electric field forces. In the conservation of mass equation it is assumed molecules are not metabolized and the chemical reaction term is negligible,

$$\frac{\partial c_i}{\partial t} = \nabla \cdot \{D\nabla c_i - \mathbf{v_i} c_i\} \quad \text{in } \rho < a, \tag{2.43a}$$

$$\frac{\partial c_e}{\partial t} = \nabla \cdot \{D\nabla c_e - \mathbf{v_e} c_e\} \quad \text{in } a < \rho < R_b, \tag{2.43b}$$

where c_i and c_e are the respective intracellular and extracellular concentrations, D is the diffusion coefficient in intracellular and extracellular regions, and $\mathbf{v_i}$ and $\mathbf{v_e}$ are the velocities due to the field from electrodes in the intracellular and extracellular regions. For molecules with molecular weight less than 1000 Da, the diffusion coefficient D does not vary between the intracellular and extracellular regions, so long as only the extracellular space immediately adjacent to the membrane is considered (removing macroscale tissue tortuosity effects).[111,112,113] Velocities due to electric field in Eqs. 2.43a and 2.43b are defined according to a modified version of the Einstein equation,[114]

$$\mathbf{v_i} = -D\frac{z_m e}{k_B T}\nabla V_i \quad \text{in } \rho < a, \tag{2.44a}$$

$$\mathbf{v_e} = -D\frac{z_m e}{k_B T}\nabla V_e \quad \text{in } a < \rho < R_b, \tag{2.44b}$$

where z_m is the net charge of the molecule, e is the elementary charge, k_B is the Boltzmann constant, T is the temperature, and V_i and V_e are the respective intracellular and extracellular electric potentials. It is assumed that flux across the membrane is only significant in the transverse direction, given that the total surface

area of the end caps of the fiber is three orders of magnitudes smaller than the rest of the membrane. Therefore, continuity of flux across the membrane boundary is expressed in the form of Nernst-Planck equations,

$$D\left\{\frac{\partial c_i}{\partial \rho}+\frac{c_i z_m e}{k_B T}\frac{\partial V_i}{\partial \rho}\right\}=D\left\{\frac{\partial c_e}{\partial \rho}+\frac{c_e z_m e}{k_B T}\frac{\partial V_e}{\partial \rho}\right\}=-j_m \quad \text{on } \rho=a, \tag{2.45}$$

where j_m is the molecular flux across the membrane.

Congruent with the derivation of the asymptotic fiber model in Sec. 2.1, the membrane is assumed to be an infinitesimally thin boundary separating intracellular and extracellular space. This assumption has merit given that the thickness of the membrane is four orders of magnitude smaller than the radius in a typical muscle fiber. The practical result is that the flux of molecules across the membrane, j_m, reacts instantaneously to temporal changes in c_i, c_e, and transmembrane potential Φ_m (quasi-steady flow).[101,114] It is assumed there exists a Born energy barrier arising from charged molecules traveling through electropores across the low permittivity membrane.[100,101,102] Under these assumptions, the flux across the membrane j_m can be expressed,

$$j_m=\frac{D_m}{h}\frac{c_i e^U-c_e}{\dfrac{w_o e^{w_o-Un}-Un}{U(w_o-Un)}e^U-\dfrac{w_o e^{w_o+Un}+Un}{U(w_o+Un)}}, \tag{2.46}$$

where D_m is the diffusion coefficient of the molecules in the aqueous electropores, D_0, multiplied by the porosity of the membrane,[115]

$$D_m=D_0\left(\pi r_m^2 N_{ep}\right), \tag{2.47}$$

where r_m is the radius of a pore and N_{ep} is the density of pores in the membrane (Sec. 2.2). U is the nondimensional transmembrane potential,

$$U=\frac{z_m e}{k_B T}\Phi_m. \tag{2.48}$$

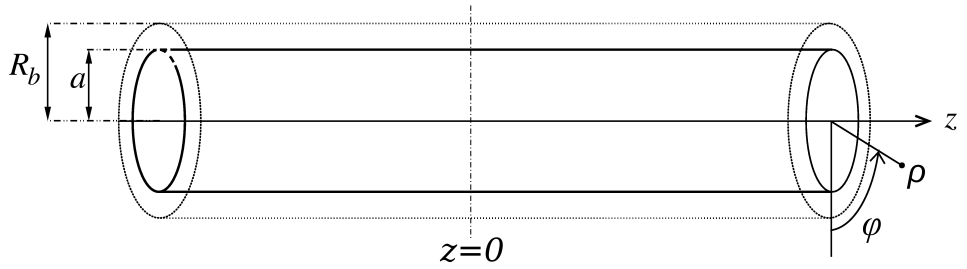

FIGURE 2.11: Single fiber geometry reference for derivation of uptake model. Extracellular boundary R_b is determined by the the interfiber distance, assuming periodicity in the tissue structure. Muscle fiber not drawn to scale to improve clarity of features: in reality fiber radius is two or three orders of magnitude smaller than fiber length.

Concentrations c_i and c_e in Eq. 2.46 are the intracellular and extracellular concentrations taken on the membrane boundary, constant w_o is maximum nondimensional Born energy barrier, and constant n is the relative entrance length of a pore.[54,100] Note that for $U = 0$ Eq. 2.46 is not defined, and an alternate equation must be used,

$$j_m = \frac{D_m}{h} \frac{c_i - c_e}{\frac{2n}{w_o} e^{w_o} - \frac{2n}{w_o} + e^{w_o} - 2ne^{w_o}}. \tag{2.49}$$

Eqs. 2.46 and 2.49 are derived in Appendix C.

2.3.2 Reduction to Two-Compartment, 1D Longitudinal Diffusion Equations

The remainder of the derivation is performed assuming the use of a typical pulsing protocol for delivery of small molecules in muscle tissue, as defined in Table 2.4. It is assumed the molecule is monovalent, $|z_m| = 1$, and $T = 310$ K is a typical body temperature in mammals. The diffusion coefficient $D = 2.01$ x 10^{-10} m^2/s is for a small molecule with molecular weight 400 Da. The diffusion coefficient is estimated using the Stokes-Einstein equation assuming the molecule is spherical, and that diffusion in the intracellular and extracellular space is three times smaller than

in water alone.[111,112,113,115] The number of pulses N is 8, and one pulse is applied every one second, thus, period of pulses $T_p = 1$ s. Finally, pulse duration τ_p is 100 μs, and the maximum magnitude throughout entire tissue of the electric field generated by electrodes $||E||_\infty = 10$ kV/cm. For a typical needle electrode geometry and pulse strength (interelectrode voltage divided by interelectrode distance) of 1 kV/cm (Fig. 2.12A), this upper bound $||E||_\infty = 10$ kV/cm is reasonable, as shown for the distribution of $|E|$ in Fig. 2.12B. These pulsing parameters are sufficient to simulate actual electroporation experiments for delivery of small molecules.[31,32,116,117,118]

Table 2.4: Molecule and pulsing parameters in molecular uptake model[a]

Parameter	**Units**	**Value**
$\|z_m\|$	Unitless	1
D	m^2 s^{-1}	2.01 x 10^{-10}
T	K	310
τ_p	μs	100
$\|\|E\|\|_\infty$	kV cm^{-1}	10
N	Unitless	8
T_p	s	1

[a] Pulsing parameters match those in Table 2.3

It is recognized that there are two time scales for uptake: one over which transport via electric field occurs, and one over which diffusion occurs. The electric field transport is considered first. For a pulsing protocol using N pulses of duration τ_p, the time scale which E generated by the electrodes is nonzero is the product $N\tau_p$. The time scale for diffusion is a little more complex. Uptake via diffusion only occurs on the time scale that pores exist in the membrane, determined from time scale of pore resealing τ_{ep}. For a single pulse, τ_{ep} is found from the pore creation and resealing equation, repeated here from Sec. 2.2 for convenience,

$$\frac{dN_{ep}}{dt} = \alpha e^{(\Phi_m/V_{ep})^2}\left(1 - \frac{N}{N_0 e^{q(\Phi_m/V_{ep})^2}}\right). \tag{2.50}$$

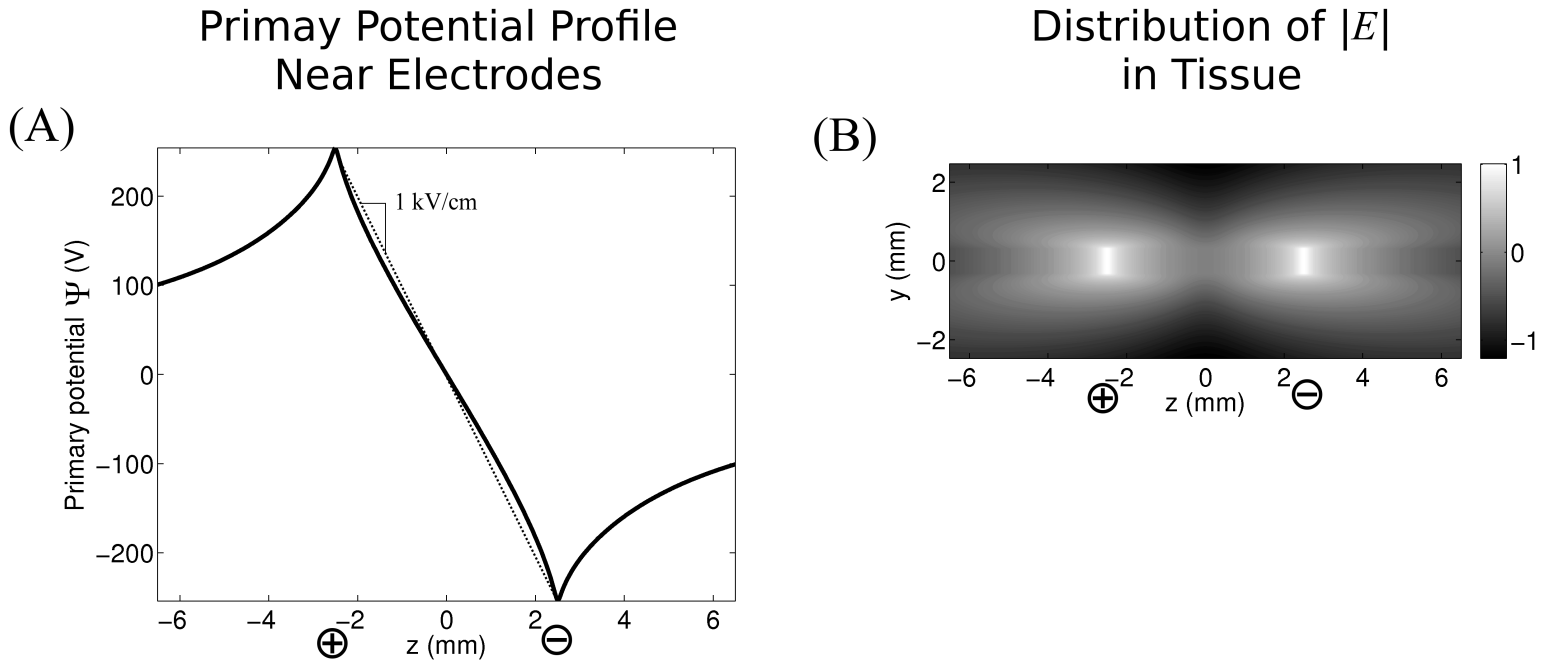

FIGURE 2.12: Primary potential (Ψ) profile and distribution of $|E|$ generated by needle electrodes throughout muscle tissue. Positions of anode and cathode are marked with $\oplus$ and $\ominus$, respectively. Parameters used to make the figures are given in Tables 2.3 and 2.4. (A) Profile of primary potential Ψ at $y = 0.3$ mm, right next to the electrodes. Pulse strength defined as the slope of line connecting potential at cathode to potential at anode. (B) Distribution of $\log_{10}(|E|)$ throughout muscle tissue, where $|E|$ is in kV/cm, calculated only for fibers outside the radius of the needle electrodes. The rectangular shapes at the electrode locations are superficial artifacts from the combination of discretization and the contour plot algorithm in MATLAB®: electrodes are indeed circular.

The time scale of Eq. 2.50 is τ_{ep},

$$\tau_{ep} = \left. \frac{N_0}{\alpha} e^{(q-1)(\Phi_m/V_{ep})^2} \right|_{\Phi_m=0} = 1.5 \text{ s.} \tag{2.51}$$

Eq. 2.51 is evaluated using parameters in Table 2.3 and assuming $\Phi_m = 0$ is a constant, given that Φ_m discharges with maximum time scale $R_m C_m = 10$ ms, two orders of magnitude smaller than the minimum value for τ_{ep} (1.5 s). Given $\tau_{ep} = 1.5$ s is four orders of magnitude larger than pulse duration τ_p, the time scale pores exist in the membrane during a single pulse is approximated as 1.5 s. The accuracy of $\tau_{ep} = 1.5$ s time scale of pore existence is confirmed for a single pulse in Fig. 2.13A. Sec. 4.4.1 compares the 1.5 s time scale of pore resealing found here to experimental results. For pulse trains, this time scale of 1.5 s only applies to the final pulse in the train. For the pulses in between, for period $T_p = 1$ s, the time scale pores are open is effectively $\tau_{ep} = T_p = 1$ s. In other words, multiple pulses effectively increase the time scale pores are open from $\tau_{ep} = 1.5$ s to $\{(N-1)T_p + \tau_{ep}\} = 8.5$ s, as illustrated for pore density taken at a single position on the membrane in Fig. 2.13. This behavior over multiple pulses has also been observed in other studies.[55] In Fig. 2.13B, at 8.5 s, pore density $N_{ep} = 2.83\text{x}10^{13}$ m^{-2} is within 4% of the expected value from exponential decay, $2.94\text{x}10^{13}$ m^{-2}, indicating 8.5 s is a good estimate of the time scale pores are open.

Thus, there are two time scales: $N\tau_p = 800$ μs for transport via electric field and $\{(N-1)T_p + \tau_{ep}\} = 8.5$ s for transport via diffusion. From these two time scales, two length scales are defined: the length scale due to mass transport via electric field (L_e), and the length scale due to mass transport via diffusion (L_d),[56,119]

$$L_e = \left(\frac{D|z_m|e}{k_B T} ||E||_\infty \right) N\tau_p, \tag{2.52a}$$

$$L_d = \sqrt{6D\left\{(N-1)T_p + \tau_{ep}\right\}}. \tag{2.52b}$$

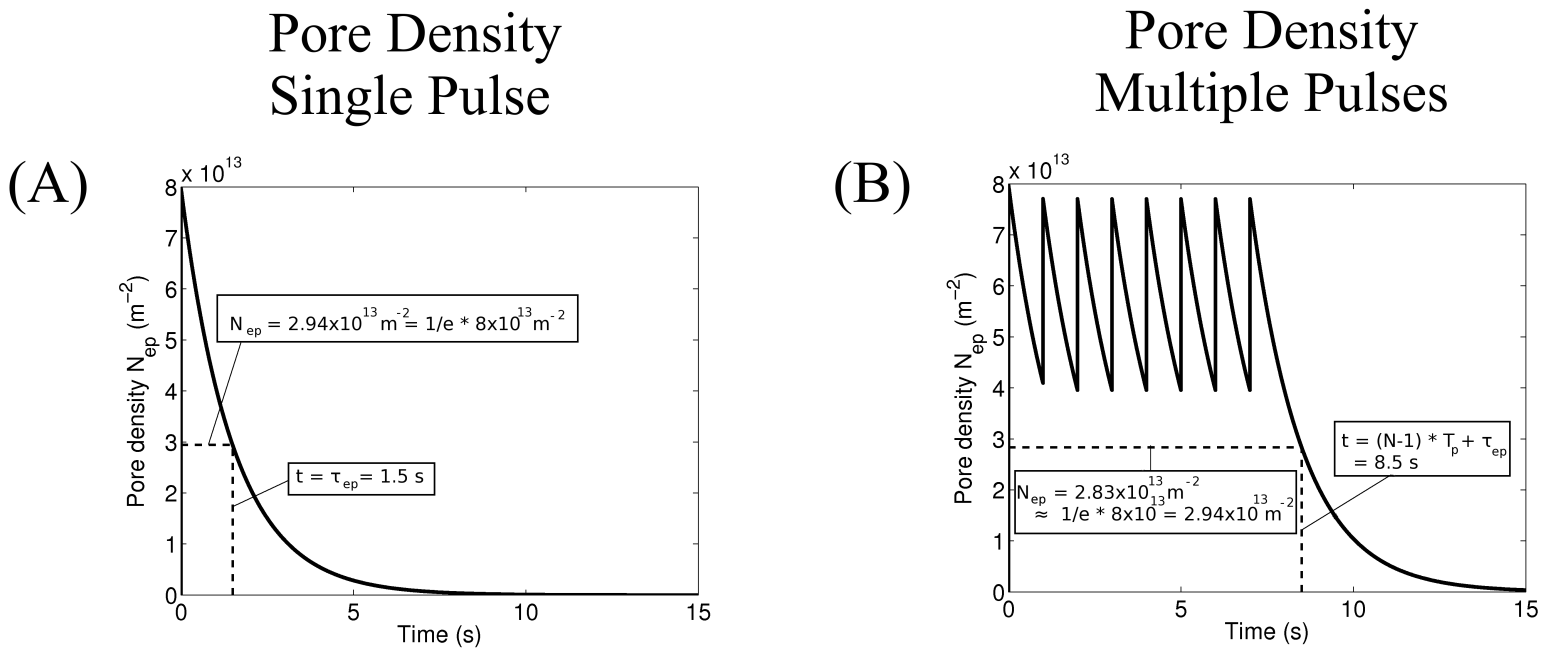

FIGURE 2.13: Pore density versus time for a single location on the membrane. (A) Single pulse ($N = 1$) is used. Value of N_{ep} at 1.5 s is indicated, and is the exact value of N_{ep} expected after one time constant decay, i.e., $(1/e)N_{ep}|_{t=100\mu s}$. (B) Eight pulses ($N = 8$) are used with a period $T_p = 1$ s. Value of N_{ep} at 8.5 s is indicated, and compared to the value of N_{ep} expected after one time constant decay, i.e., $(1/e)N_{ep}|_{t=100\mu s}$.

Using Eqs. 2.51 and 2.52, as well as parameters in Table 2.4, $L_e = 6.01$ μm and $L_d = 101$ μm. Two assumptions are made from analyzing these length scales. First, the fiber radius and thickness of the extracellular space are only 25 μm and 0.5 μm, respectively, compared to $L_d = 101$ μm. Therefore, it is assumed that transverse molecular concentration in the intracellular and extracellular spaces may be approximated reasonably well by the "well-mixed" condition. Under this assumption, intracellular and extracellular molecular concentrations $c_i(\rho, \varphi, z)$ and $c_e(\rho, \varphi, z)$ are considered functions of z only, $c_i(z)$ and $c_e(z)$, given transport has had time to spread out the concentration uniformly in the transverse direction. Second, length scale of transport via electric field is 6% of the length scale of diffusion, where this percentage is even smaller for measuring transport on the entire tissue level, given that the maximum value of $|E|$ was used in calculating L_e. Thus, transport via electric field is assumed to have negligible impact on molecular concentration. Note that effect of electric field is still allowed to remain in the membrane flux equation (Eq. 2.46) via the scaled transmembrane potential U.

Two-compartment, 1D longitudinal diffusion equations are now derived by considering a short length of fiber shown in Fig. 2.14. The two assumptions above are introduced into the derivation at the appropriate steps. First, the divergence theorem is applied to the conservation of mass equations (Eqs. 2.43a and 2.43b) for the short length of fiber that is Δz long with intracellular volume v_i and extracellular volume v_e. Using the divergence theorem, the temporal change in intracellular molecules is related to the flow of molecules across boundaries M, $E_{i,1}$, and $E_{i,2}$. Likewise, the temporal change in extracellular molecules is related to flow of molecules across the boundaries M, B, $E_{e,1}$, and $E_{e,2}$. Neglecting transport via electric field, the resulting

equations are found,

$$\int_{v_i} \frac{\partial c_i}{\partial t} dv = -\int_M j_m ds + D\left(\int_{E_{i,2}} \frac{\partial c_i}{\partial z} ds - \int_{E_{i,1}} \frac{\partial c_i}{\partial z} ds\right), \tag{2.53a}$$

$$\int_{v_e} \frac{\partial c_e}{\partial t} dv = \int_M j_m ds + D\left(\int_{E_{e,2}} \frac{\partial c_e}{\partial z} ds - \int_{E_{e,1}} \frac{\partial c_e}{\partial z} ds + \int_B \frac{\partial c_e}{\partial \rho} ds\right). \tag{2.53b}$$

An additional assumption is added that in the extracellular region the flux normal to the extracellular boundary B in Fig. 2.14 is zero, i.e., the last term on the right side of Eq. 2.53b is zero. This assumption is made based on the model of muscle fibers being packed tightly in a periodic structure (Sec. 2.2), so that the dynamics of electroporation and the resulting uptake of molecules are very similar from one fiber to its adjacent neighbors in the tissue. If each fiber behaves similarly to its neighbors, then the no-flux boundary condition on boundary B is valid. Assuming that concentration is uniform in the transverse direction in intracellular and extracellular spaces ("well-mixed" condition), and taking the limit as Δz approaches zero, Eq. 2.53 is simplified,

$$\frac{\partial c_i}{\partial t} = D\frac{\partial^2 c_i}{\partial z^2} - \frac{2}{a}\overline{j_m}, \tag{2.54a}$$

$$\frac{\partial c_e}{\partial t} = D\frac{\partial^2 c_e}{\partial z^2} + \frac{2a}{R_b^2 - a^2}\overline{j_m}. \tag{2.54b}$$

Eq. 2.54 is the two-compartment, 1D longitudinal diffusion problem with flux on the membrane $\overline{j_m}$ connecting the intracellular and extracellular compartments, where $\overline{j_m}$ is the circumferential average of membrane flux,

$$\overline{j_m} = \frac{1}{2\pi}\int_0^{2\pi} j_m \, d\varphi. \tag{2.55}$$

A detailed derivation of 2.54 is supplied in Appendix D.

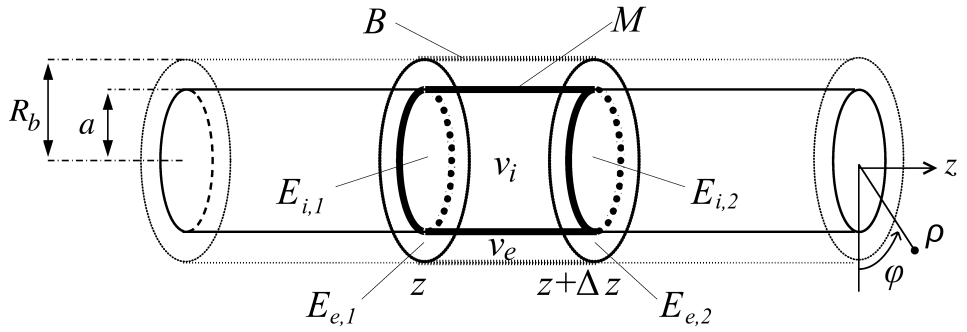

FIGURE 2.14: Short length of fiber used to derive 1D molecular uptake equation (Eq. 2.54). Short length of fiber is Δz, that has intracellular and extracellular volumes v_i and v_e. The boundaries of the short length of fiber are membrane M, end caps $E_{i,1}$ to $E_{e,2}$, and extracellular boundary B. The quantity $R_b - a$ is one-half the distance between muscle fibers. No-flux boundary condition is applied on boundary B, and membrane flux j_m is applied on boundary M.

2.3.3 Reduction to a Series of Longitudinally Independent, Two-Compartment Equations

In this section, two simplifications are made to Eq. 2.54, and both are justified by simulations. The first simplification is removal of longitudinal diffusion, i.e., the first terms on right side of Eqs. 2.54a and 2.54b. To justify removing longitudinal diffusion, the equations are simulated using student version of software package FlexPDE, version 5.1.0s, freely available from PDE Solutions Inc. (http://www.pdesolutions.com/). Concentrations are reported relative to initial extracellular concentration c_0, so choice of c_0 is arbitrary. The values of U and D_m in the membrane flux equations (Eqs. 2.46 and 2.49) are calculated by importing time-dependent longitudinal profiles of Φ_m and N_{ep} from simulations of the asymptotic fiber model. Parameters used in FlexPDE and asymptotic fiber model simulations are given in Tables 2.3 and 2.4. Φ_m and N_{ep} are produced using several different electrode-fiber distances to show the effects of longitudinal diffusion for different fibers in the muscle tissue. Uptake results are reported in Fig. 2.15. Effects from neglecting longitudinal diffusion appear very small in the uptake profile shown in panel

A, where the primary differences occur where the magnitude of $\partial c_i/\partial z$ is large. The model including longitudinal diffusion shows smoother uptake profile, but the model without longitudinal diffusion exhibits a more "jagged" profile. Note that maximum uptake in the fiber at $b = 0.48$ mm is spread over a more narrow region than the fiber at $b = 0.72$ mm, which is initially contradictory given the fiber at $b = 0.48$ mm is closer to the electrodes. However, electrode-fiber distance is not the only consideration, and the geometry must also be considered. The electric field produced by the electrodes is mostly in the transverse direction over a larger length of fiber that is far from the electrodes, relative to a fiber close to the electrodes. Thus, while the fiber at $b = 0.72$ mm is further from electrodes, the transverse component of the electric field does not decay as much in the longitudinal direction, and is able to charge and electroporate the membrane over a larger length of fiber.

In Fig. 2.15B, the relative root-mean-square error is reported, calculated from the node-by-node error in predicting intracellular concentration. The error from neglecting longitudinal diffusion is largest for the fiber closest to the electrodes, and decreases as electrode-fiber distance increases. Node-by-node error remains below 3% (Panel B), although it continues to increase beyond 20 s because diffusion in z continues to occur even after pores reseal and no further uptake occurs. However, for the purposes of molecules being transported to the nuclei of muscle fibers, crossing the membrane barrier is the critical step. It is assumed that once the molecules are in the fiber, given long enough time, they will diffuse to a nucleus, given the high density of 35 to 77 nuclei/mm along the length of the fiber.[120] Therefore, the most important metric of neglecting longitudinal diffusion is error in total uptake within the entire intracellular space, which is always below 0.12% (Panel C). Therefore, longitudinal diffusion is assumed negligible for modeling molecular uptake for pulsing protocol in Table 2.4, and Eq. 2.54 is reduced to a series of longitudinally independent,

two-compartment equations solved independently for each position in z,

$$\frac{\partial c_i}{\partial t} = -\frac{2}{a}\overline{j_m}, \tag{2.56a}$$

$$\frac{\partial c_e}{\partial t} = \frac{2a}{R_b^2 - a^2}\overline{j_m}. \tag{2.56b}$$

In the simulations presented in Fig. 2.15, and for simulations of uptake in the dissertation as a whole, it is assumed that initially the extracellular concentration c_e is uniform with value equal to c_0, and intracellular concentration c_i is uniformly zero. Assuming initial intracellular concentration implies that the molecule does not cross the membrane at rest, which is almost always the case for electroporation-mediated delivery. Assuming initial uniform extracellular concentration of molecule is more disputable. This simplification is justified in Appendix E. Briefly, the length scale of diffusion in the interstitial space associated with the time before the pulse is turned on is 155 μm, as shown in Appendix E. It is assumed each fiber has at least one capillary running parallel to it, which is justified by the significant vascularization shown in Fig. 1.2C and in the literature.[20,121] Assuming at least one capillary running parallel to each fiber, the transport in the interstitial space is in the transverse direction only. The maximum length scale in the transverse direction with interfiber distance of 1 μm is the circumference of the extracellular boundary around each fiber: 160 μm. With a diffusion distance of 155 μm, and maximal interstitial length scale of 160 μm, assuming uniform interstitial concentration immediately before the pulse is turned on is expected to be fairly accurate. However, a global pharmacokinetic analysis of the molecule's transport in the entire body, as well as microscale models of mass transport across all blood vessels and within the interstitial space would need to be developed in order to fully justify this assumption.

The second simplification to Eq. 2.54 is removal of transport via electric field in the membrane flux j_m (Eq. 2.46). Equation 2.56 is used to simulate uptake

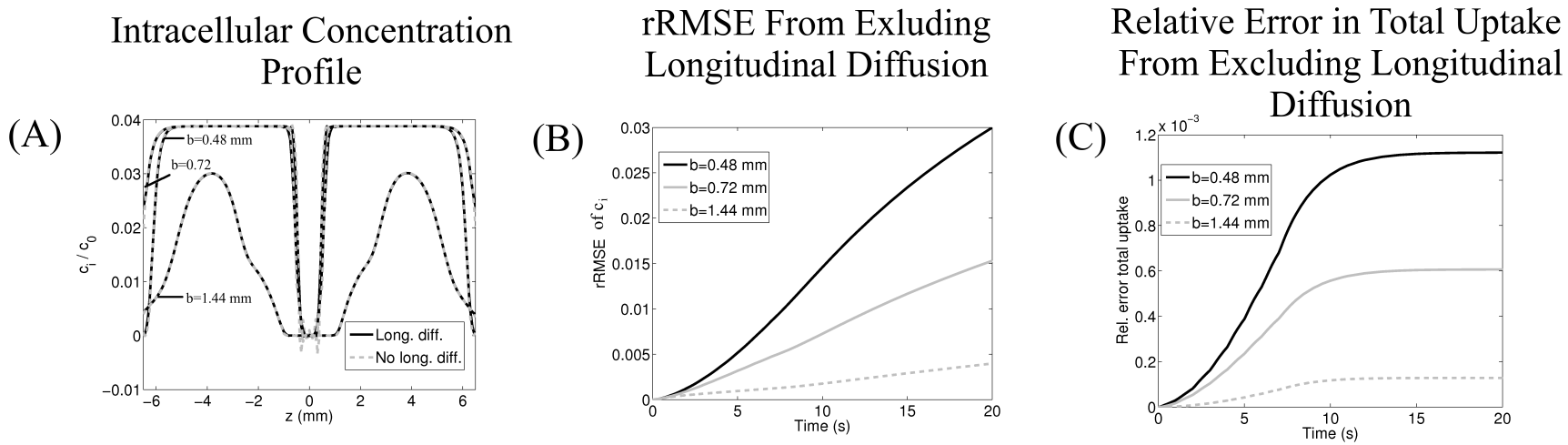

FIGURE 2.15: Effect of longitudinal diffusion on molecular uptake. Here, pulse strength, $2|V_0|/d$, is 1000 V/cm, which is the largest pulse considered for electroporation-mediated uptake in this study. (A) Longitudinal profile of intracellular molecular concentration relative to initial extracellular concentration c_i/c_0 reported at 20 s, after all pores have resealed and molecules are no longer crossing the membrane. Three different electrode fiber distances (b) are shown. (B) Relative root-mean-square error from neglecting longitudinal diffusion, calculated from by taking the root-mean-square of the node-by-node difference in c_i between the two models. (C) Relative error in total number of molecules in entire fiber from neglecting longitudinal diffusion, calculated by integrating c_i along z-dimension for each model, then calculating relative error.

in conjunction with the asymptotic fiber model for two values of pulse strength, $2|V_0|/d = 400, 1000$ V/cm, and several different electrode-fiber distances in the range $b = 0.48..2.5$ mm. Two different versions of the model are run: one including transport via electric field in j_m, and one excluding it. The profiles of intracellular concentration in panels (A) and (B) of Fig. 2.16 indicate that electric field transport is generally not the dominant force in molecular uptake, but, electric field transport does play a larger role for larger electrode-fiber distances. This trend is also found in total uptake in the entire fiber, where error between the two models increases with increasing electrode-fiber distance, until there is zero total uptake in the fiber (panel C). Transport via the electric field is more important for pulse strength of 400 V/cm compared to 1000 V/cm, given that smaller pulse strengths produce fewer pores, and the electric field driving molecules through each pore becomes more important. Although relative error from neglecting the electric field reaches just over 50% for fibers far from the electrodes, panels A and B reveal much lower total uptake for these distant fibers. Therefore, on a total tissue level, the effect of neglecting the electric field is at most 2.5% (panel D). The transport via the electric field is removed from the membrane flux j_m, and the final two-compartment uptake equations, with Eq. 2.49 substituted for j_m in Eq. 2.56, and Eq. 2.47 substituted for D_m in Eq. 2.49 are found,

$$\frac{\partial c_i}{\partial t} = \frac{2}{a}\left\{\frac{D_0\pi r_m^2/h}{\frac{2n}{w_o}e^{w_o} - \frac{2n}{w_o} + e^{w_o} - 2ne^{w_o}}\right\}(c_e - c_i)\overline{N_{ep}}, \tag{2.57a}$$

$$\frac{\partial c_e}{\partial t} = \frac{2a}{R_b^2 - a^2}\left\{\frac{D_0\pi r_m^2/h}{\frac{2n}{w_o}e^{w_o} - \frac{2n}{w_o} + e^{w_o} - 2ne^{w_o}}\right\}(c_i - c_e)\overline{N_{ep}}. \tag{2.57b}$$

Eq. 2.57 is solved independently for every position in z along the length of the fiber.

For every position in z along the fiber, the steady state value of intracellular

concentration is $c_{i,ss}$,

$$c_{i,ss} = c_o \frac{\gamma}{\gamma + 1}, \tag{2.58}$$

where c_o is the initial concentration of molecules in extracellular space and γ is the ratio of extracellular to intracellular cross-sectional areas (as in Sec. 2.1.3). At the steady state value $c_{i,ss}$, there is no further uptake of molecule in time. Uptake results in Chapter 3 normalize concentration to $c_{i,ss}$. In general, choice of initial extracellular concentration c_o is arbitrary, given that the time scale of uptake is not dependent on c_o, and that c_i and c_e can be reported relative to c_o or $c_{i,ss}$. This generalization can be seen by expressing Eq. 2.57a in terms of only c_i, which can be done by expressing c_e in terms of c_i through conservation of molecules between the intracellular and extracellular compartments. However, in Sec. 3.3.2 the uptake ratio requires a specific choice of c_o because results are compared to experiments. In these experiments, a radiolabelled molecule is injected into the blood stream of a rat. In this case, c_o is estimated as an upper bound: the initial concentration injected into the blood stream ($2.08\text{x}10^9$ molecules/mm^3)[31] scaled by the ratio of volume of solution injected (300 mm^3) to estimated blood volume of the rat (13986 mm^3). Thus, the upper bound on concentration c_o in the extracellular space of muscle is the concentration in the bloodstream alone (concentration if all molecules stay within bloodstream): $4.46\text{x}10^7$ molecules/mm^3. The aforementioned estimated blood volume of the rat is determined from an empirical formula based on body weight,[122] where body weight is 220 g, well within the range of body weights for rats used in uptake of small molecules in Grafstrom et al.[31]

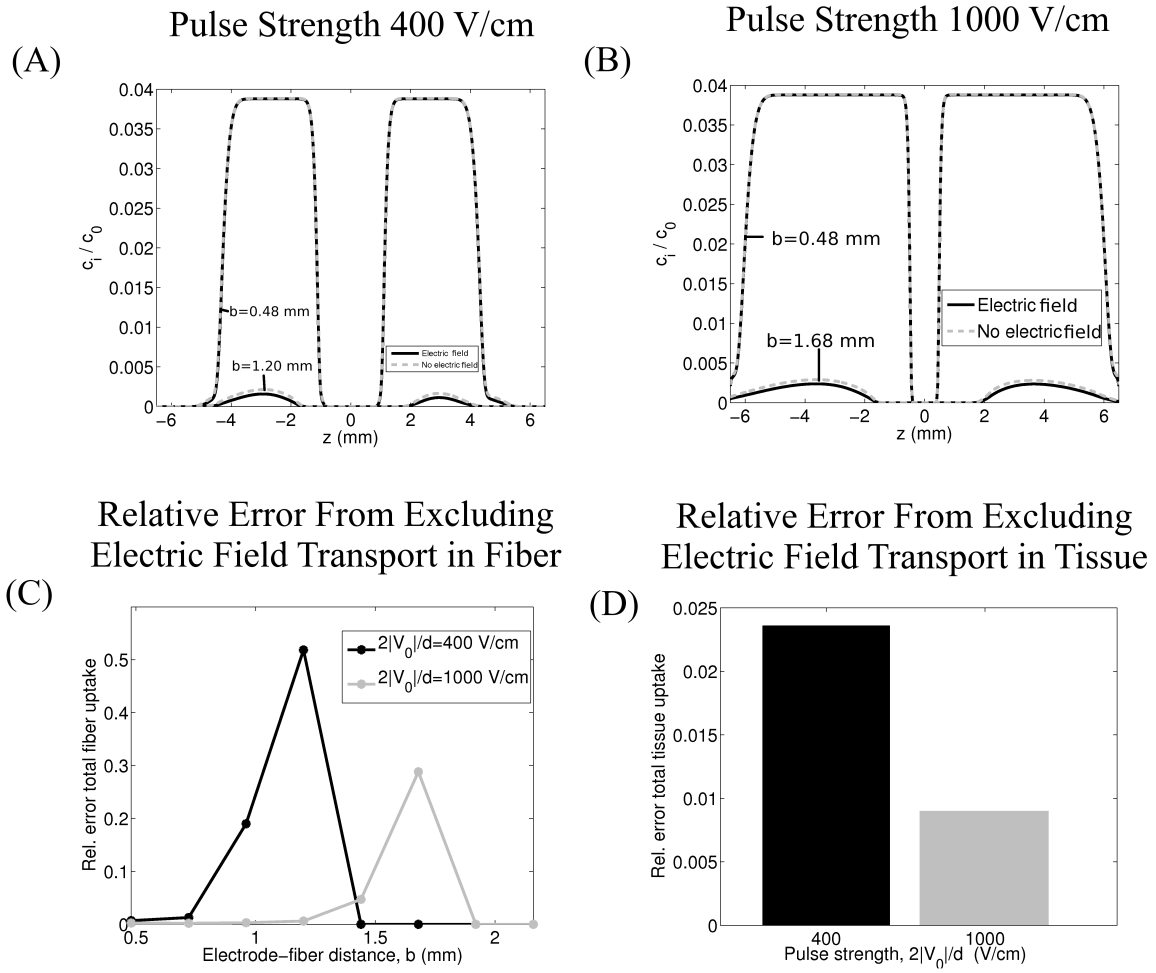

FIGURE 2.16: Effect of electric field in membrane flux on molecular uptake. (A) Longitudinal profile of intracellular molecular concentration relative to initial extracellular concentration, c_i/c_0, for pulse strength $2|V_0|/d = 400$ V/cm, which is the smallest pulse considered in this study. Profiles are shown for both model including electric field in membrane flux and model excluding it, and all profiles are taken after pores have resealed and molecules are no longer crossing the membrane. Two different electrode-fiber distances (b values) are shown. (B) Longitudinal profile of intracellular concentration for modeling including and excluding electric field transport, similar to panel A except pulse strength is the largest considered in this study, $2|V_0|/d = 1000$ V/cm. Note that also a different value of b is used for the fiber further from electrodes. (C) Relative error from neglecting electric field transport in total number of molecules in entire fiber, calculated by integrating c_i along z-dimension for each model, then calculating relative error. (D) Relative error from neglecting electric field transport in total number of intracellular molecules in entire tissue, calculated by integrating c_i over z (along length of fiber) and y (for different electrode-fiber distances) dimensions for each model, then calculating relative error. Values for y (the electrode-fiber distances) that were used are indicated by the b-values of the data point circles in panel C.

2.4 Effect of Electroporation on Tissue Conductivities

A major assumption used in computing primary potential Ψ, and the activating functions used in the longitudinal and transverse problems (Secs. 2.1.2 and 2.1.3), is that the tissue conductivities do not change in response to electroporation. However, there are numerous computational and experimental studies that report both longitudinal and transverse conductivities increase by a factor between two and four in electroporating regions of muscle tissue.[76,103,123,124] Accounting for changing tissue conductivities dynamically as the electroporation process occurs is outside the scope of the current study, and is discussed as a future direction in Sec. 4.4.7. Nevertheless, given that electroporation has been shown to change tissue level conductivities, an estimate of the error from assuming spatially and temporally uniform conductivities in the asymptotic electroporating fiber model is considered in this body of research.

To estimate error, two criteria are defined. First, the region of tissue that experiences a change in conductivities is defined. The region of elevated conductivities is shown in Fig. 2.17, and is defined as an ellipse centered midway between anode and cathode, with minor radius five-fold larger than needle radius ($5R_e$, see Table 2.3), and major radius the sum of half the interelectrode distance and $5R_e$ ($d/2 + 5R_e$). Compared to a previous study by Sel et al. using similar pulsing protocol in liver tissue, the elliptic region of elevated conductivities approximates the region of tissue that achieves threshold value of electric field magnitude $|E|$ for reversible electroporation.[125] In Sel et al., the region that achieves threshold value of $|E|$ is validated in experiments by observing the region of tissue with altered nuclei from uptake of bleomycin. For slightly different electrode setup using six needle electrodes in muscle tissue, a similar size of tissue region is observed that obtains threshold $|E|$ for electropermeabilization.[30] In approximating the region of electropermeabilization reported in literature, it is chosen to err on the side of making the region too

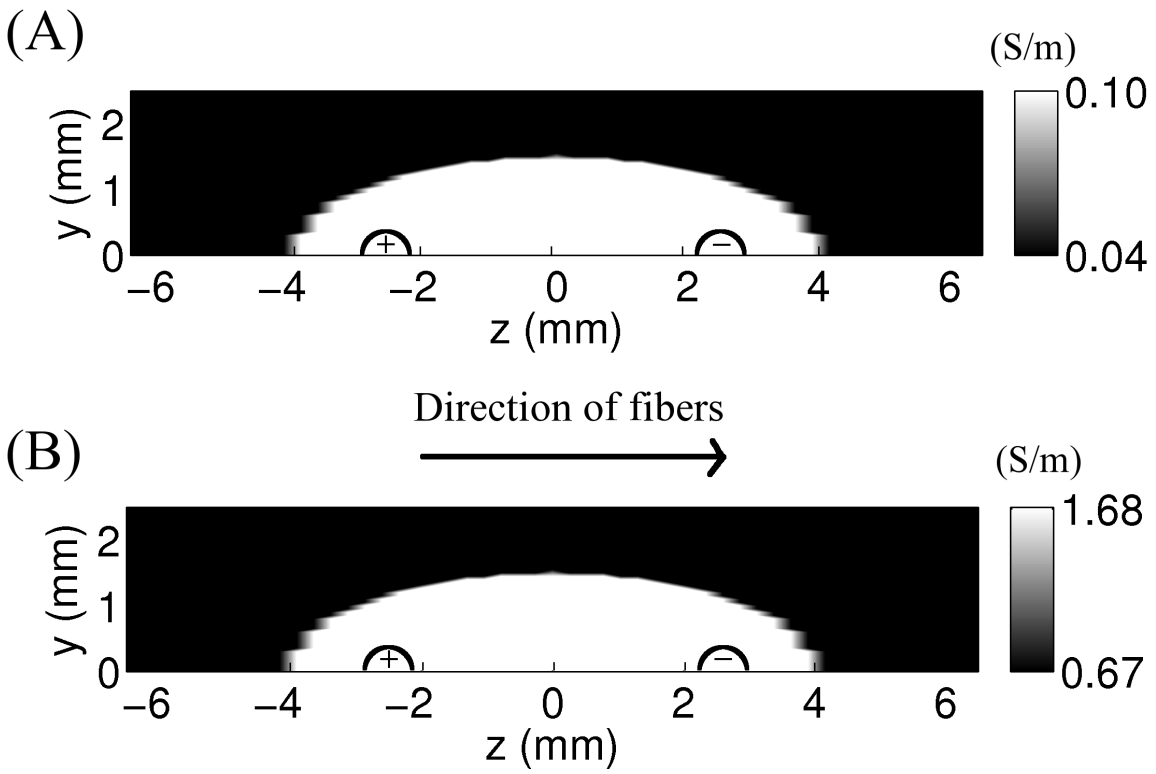

FIGURE 2.17: Contour plot of nonuniform tissue conductivities in electroporating tissue. Only the top half of the tissue is shown, given symmetry about $y = 0$. Positions of anode and cathode are marked in the tissue space by plus and minus symbols enclosed by semicircles, respectively. Contour plots are shown for the transverse (A) and longitudinal (B) conductivities.

large rather than to small, with the intent of finding an upper bound on the error introduced from assuming spatially uniform conductivities. Furthermore, temporal evolution of this region of elevated conductivities is ignored for simplicity. Note that this analysis assumes a 2D model, where variations in tissue conductivity in the x-dimension are ignored, which is an assumption that is discussed in Sec. 4.4.7.

The second criterion defined is the change in tissue conductivity in the region of tissue where electroporation is occurring. Again, a simplified rule is chosen here. It is assumed that inside the region of elevated conductivity, both transverse and longitudinal conductivities increase to maximum possible values, and outside the regions

conductivities remain at rest values, as shown in Fig. 2.17. The maximum values are based on the work of Corovic et al.[126] in skeletal muscle of small mammals. Briefly, the method they used was to first define a functional form for tissue conductivity versus electric field. In this case, a sigmoidal function is used,

$$\sigma(E) = \frac{\sigma_1 - \sigma_0}{1 + D_s \exp(-(|E| - A)/B)} + \sigma_0, \tag{2.59}$$

where σ_1 is the maximal conductivity, σ_0 is conductivity of nonpermeabilized tissue, D_s is a sigmoid function parameter, $|E|$ is the magnitude of the electric field, and parameters A and B depend on the reversible and irreversible electroporation field strengths.[29,125] Next, a sequential model consisting of a series of static finite element models of the tissue with electrodes in it is built, and the 3D version of the elliptic equation (Eq. 2.33) is solved in the volume space. In each step of the model, the the local conductivity changes in response to the local electric field according to Eq. 2.59. The sequential finite element model is simulated until the solution stabilizes. Parameters in Eq. 2.59 are chosen by matching current measured in the model to current measured in experiments in tissue of small mammals. Corovic et al. found that maximal values of both transverse and longitudinal conductivities are a factor of 2.5 larger than resting values,[126] which is the criterion used in this study.

Having defined the criteria for the region of tissue that experiences an increase in conductivities and the rule that governs how they increase, a finite element model is developed using FlexPDE Student Version 5.1.0s. The elliptic equation is solved for primary potential Ψ (Eq. 2.33), using the Dirichlet boundary condition on the needle electrode surfaces, and the no-flux boundary condition on the edge of the tissue space. One version of the program is simulated assuming uniform conductivities and the other version assigns 2.5 times larger conductivities in the defined electroporating regions. The transverse and longitudinal activating functions $\partial\widetilde{\Psi}/\partial\rho$ and $\partial^2 \langle\Psi\rangle /\partial z^2$ (Secs. 2.1.2 and 2.1.3) are then found from the numerical solution of Ψ using both

versions of the model. The AFs from both versions of the model are then used in simulations of the asymptotic electroporating fiber model to compare molecular uptake between the two versions. Results of this analysis are given in Sec. 3.3.4. Note that the original definition of the AF by Rattay is broad enough to include numerical solutions in addition to traditional analytical solutions.[61]

3

Results

3.1 Passive Versus Electroporating Fiber Close to the Electrodes

The dynamic interaction between transverse and longitudinal currents in a single, cylindrical fiber, and their role in membrane charging, electroporation, and molecular uptake, is examined. Results from passive fiber simulations are used as a framework to understand the more complex electroporating fiber, given the behavior of the passive fiber is well documented.[67,71,127,128] Finally, the effect of excluding the longitudinal component is examined, given this component has traditionally been excluded from models of electroporation in muscle tissue.[29,57,59,103]

Simulation results are shown for a fiber 0.48 mm from the center of the needle electrodes ($b = 0.48$ mm in Fig. 2.10), with $|V_0| = 200$ V ($2|V_0|/d = 800$ V/cm). See Table 2.3 for remaining simulation parameters. Results are shown only for the first pulse in the eight-pulse train, and are qualitatively representative of all the following pulses in the eight-pulse train, which has also been observed in other studies.[55] This similarity between pulses occurs because the period of the pulse is ($T_p = 1s$) and the longest time scale for membrane charging in the asymptotic model is $R_m C_m = 10$

ms, so there is ample time for potential distribution and transmembrane potentials to return to very near resting state between pulses. Thus, charging of the membrane via transverse and longitudinal currents repeats from pulse to pulse. However, the time scale of pore creation/resealing ($\tau_{ep} = 1.5$ s, Sec. 2.3.2) is on the order of the 1 s period of the pulse, which means pore density distribution at the start of the pulse may vary between the pulses, as shown for two locations on the fiber in Fig. 3.1. Larger initial membrane conductivity for subsequent pulses means that charging and further electroporation of the membrane in subsequent pulses is less extensive, and these subsequent pore density "spikes" are smaller versions of the first pulse. Yet, the key point is that the ratio of pore density between different locations on the fiber remains constant in time. For the first pulse, the ratio of maximum magnitudes is 2.2, for the second to eighth pulse, the ratio is 1.8. Thus, the uniform time constant for pore resealing, $\tau_{ep} = 1.5$ s, ensures that the relative contribution of pores between different locations on the membrane remains within approximately 8% of the first pulse.

Figure 3.2A - 3.2C shows transverse behavior of potential distribution and transmembrane potential distribution for both a passive and electroporating fiber, at the position of the cathode, $z = +d/2 = 2.5$ mm (Fig. 2.10A). In addition, pore density distribution is shown for the electroporating fiber in panel D. Time instants are chosen based on the temporal separation of the BVP (Sec. 2.1.1), where $t = 10aC_m/\sigma_i = 4.5$ μs is ten-fold larger than the time scale of the transverse problem. Time instant $t = 100$ μs is the typical pulse duration used for delivery of small molecules (Table 2.4), and is two orders of magnitude smaller than the time scale of the longitudinal problem $R_mC_m = 10$ ms.

At $t = 0^+$, the instant the electrodes acquire the command voltage, potential distribution for both passive and electroporating fibers are identical. Figure 3.2A reveals there is very little jump in potential across the membrane boundary. The

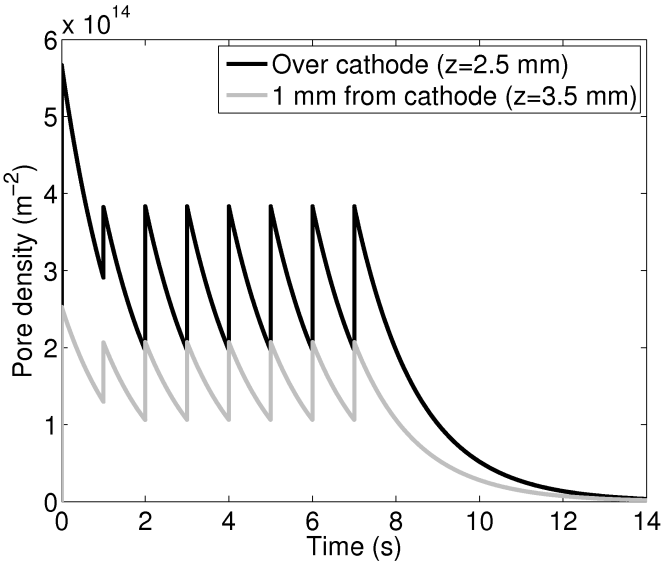

FIGURE 3.1: Pore density versus time at different locations on membrane, using 8 pulses with period 1 s. Pore density is shown at the longitudinal position directly over the cathode ($z = 2.5$ mm) and at 1 mm away from cathode ($z = 3.5$ mm). Both curves are shown at the most proximal side of the fiber, i.e., $\varphi = 0$.

intracellular and extracellular spaces are slightly distinguishable due to the relatively small resting potential $V_{rest} = -89.1$ mV, and the difference between intracellular and extracellular conductivities. The sign of potential is negative everywhere given that the cross section is taken over the cathode, but potential is more negative on the proximal side of the fiber near the cathode, and is less negative on the distal side opposite the cathode. Fig. 3.2B and 3.2C confirms that transmembrane potential is negligible at $t = 0^+$, with only a small negative value due to the negative resting potential of muscle fibers. This behavior at $t = 0^+$ is understood physically to be a consequence of the high frequency harmonics involved in the instantaneous rise time of a square pulse, bringing the effective impedance of the membrane close to zero. Thus, the medium is immediately biased by the external field.

As time progresses, the passive and electroporating fiber begin to look different. In the passive fiber, transverse currents charge the membrane after the the high fre-

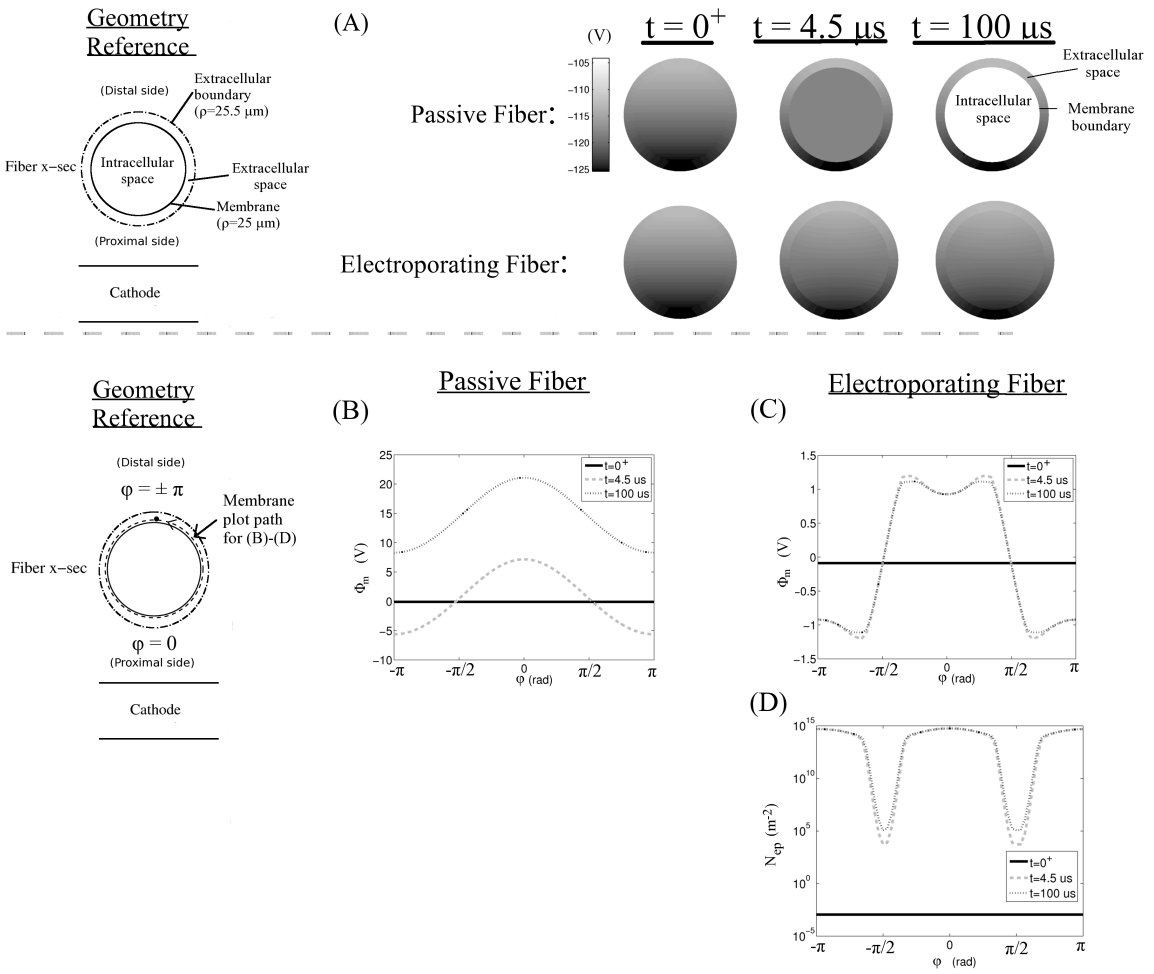

FIGURE 3.2: Distribution of potential (V_i and V_e), transmembrane potential (Φ_m), and pore density (N_{ep}) in transverse cross section of fiber directly over cathode ($z = +2.5$ mm) at three time instants. $t = 0^+$ is instant the pulse is turned on, $t = 4.5$ μs is ten-fold larger than time scale of the transverse problem, and $t = 100$ μs is the pulse duration. (A) Potential distribution for passive and electroporating fiber over entire fiber and extracellular space cross section, with geometry shown on the left. (B) Transmembrane potential distribution for passive fiber as function of angle around fiber, as shown on left. (C)-(D) Transmembrane potential and pore density distribution for electroporating fiber as function of angle around fiber.

quency harmonics introduced by turning on the pulse have faded, and the membrane impedance equals the large membrane surface resistance R_m. In Fig. 3.2A at 4.5 μs, ten-fold larger than the time scale of the transverse problem, the intracellular currents in the transverse direction have finished charging the membrane, and the intracellular distribution of potential is uniform. Thus, the intracellular space is no longer subject to the transverse component of the field set up by the electrodes. As a consequence of membrane charging, transmembrane potential has developed, as shown in Fig. 3.2B. The proximal side of the fiber has positive transmembrane potential, while the distal side is negative. Transmembrane potential is symmetric about $\varphi = 0$, due to the geometry and uniform voltage along the shaft of the needle, as shown in Fig. 2.10B. However, magnitude is slightly greater on the proximal side of the fiber than the distal side, due to the higher density of transverse current from electrodes on the proximal side. The currents charging the membrane are illustrated in Fig. 3.3A, which shows the isopotential lines and current density in the intracellular space directly over the cathode. At $t = 0^+$, these currents set up by the electrodes are illustrated, and they charge the membrane on the time scale of 0.45 μs. Fig. 3.3A reveals that the flow of positive charge is pointing down towards the negative cathode, and that current density is nearly uniform because the radius of the fiber is very small. Fig. 3.3B illustrates that the major component of the current is in the transverse direction at $t = 0^+$, with only a small component in the longitudinal direction. Due to charging from these primarily transverse currents, the membrane dielectric becomes polarized, and transmembrane potential develops. At $t = 4.5$ μs, for the passive fiber, the membrane is fully charged by these transverse currents, and distribution of potential in the intracellular space is nearly uniform (Fig. 3.3A). However, this panel also reveals there is current flow out of the intracellular space from the fiber axis radially outward to all positions on membrane, which is from the divergence of the longitudinal current flowing into, and out of, each transverse

slice (Fig. 3.3B). This outward current has no mean-free component (entirely mean current) when averaged over the intracellular cross sectional area.

On the other hand, at the same time instant $t = 4.5$ μs, the electroporating fiber has drastically increased membrane conductance due to pore creation, and therefore is not isolated from the external field like the passive fiber is, as shown in Fig. 3.2A at $t = 4.5$ μs. Comparing potential distribution at $t = 0^+$ and $t = 4.5$ μs in Fig. 3.2A, the field in the intracellular space is relatively close to the field set up by the electrodes. Figure 3.2C reveals that maximum magnitude of transmembrane potential is approximately 1 V, whereas the passive fiber is five-fold higher. The regions of suppressed transmembrane potential near $\varphi = 0$ and $\varphi = \pm\pi$ not seen in the passive fiber are a consequence of a significant increase in pore density in these regions (panel D), where electropores shunts extracellular current across the membrane, discharging the membrane. The relatively large current density in the electroporating fiber is evidenced by comparing the average current density to the passive fiber in Fig. 3.3A. Fig. 3.3A also illustrates this mechanism, which shows current flowing across the fiber from distal to proximal sides of the membrane, due to large increase in membrane conductance from the high density of pores at $\varphi = 0$ and $\varphi = \pm\pi$ in Fig. 3.2D. This increase in conductance shunts transverse current in Fig. 3.3A across the membrane rather than charging it, as evidenced by the small magnitude of transmembrane potential, relative to the passive fiber. Fig. 3.3B at 4.5 μs reveals there is still a small longitudinal component to the current that also existed at $t = 0^+$, yet any difference between current entering and exiting a transverse section of fiber simply flows through the pores across the membrane. As a result, the potential and current density distribution in Figs. 3.3A and 3.3B at $t = 4.5$ μs look very similar to $t = 0^+$.

At $t = 100$ μs, which is the duration of the pulse, the passive fiber membrane impedance is still large due to large R_m, and the intracellular space is still electri-

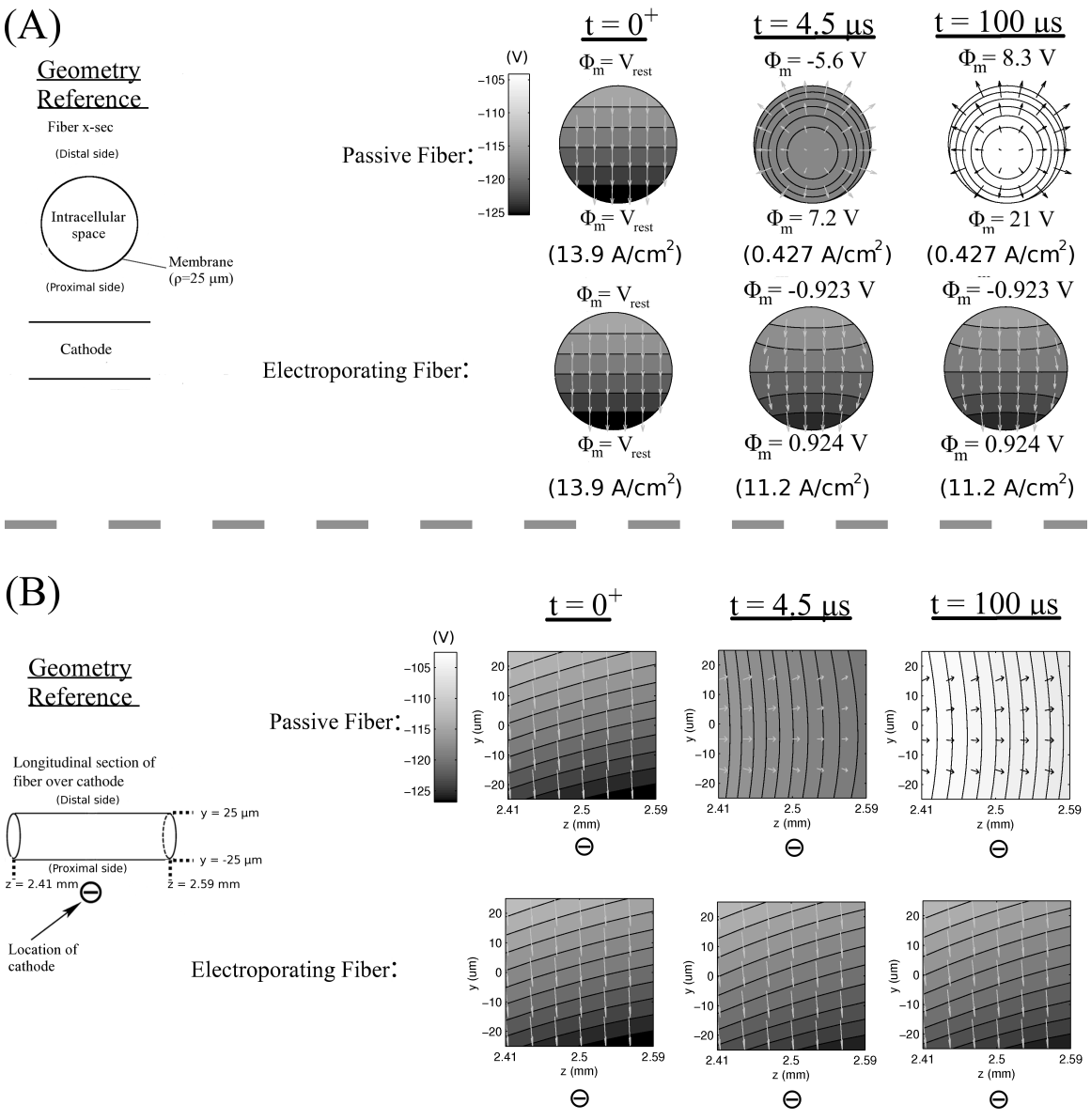

FIGURE 3.3: Current density and potential distribution in intracellular space over the cathode. Magnitude and direction of current density arrows is to scale within a single cross section, but is not comparable between different cross-sections. (A) Current density directly over the cathode in transverse cross section for passive and electroporating fiber at three time instants. Numerical value of the transmembrane potential (from Fig. 3.2) is given at the most proximal and distal locations on the membrane. Average current density is shown below each plot in parentheses. (B) Current density in the vicinity of the cathode in longitudinal cross section for passive and electroporating fiber at three time instants.

cally isolated. However, now it is the longitudinal currents that control membrane polarization. As shown in Fig. 3.2A, there is a significant increase in the mean intracellular potential, which is due to the divergence in longitudinal currents charging the membrane over the position of the cathode. This increase in intracellular potential causes a drastic increase in mean transmembrane potential: nearly three-fold larger than maximum amplitude at 4.5 μs (panel B). The longitudinal currents that charge the membrane are illustrated in Fig. 3.3B, for the part of the fiber over the cathode at $z = 2.5$ mm. On the proximal side, the longitudinal currents simply increase the transmembrane potential, as evidenced by the jump in transmembrane potential from 7.2 V at 4.5 μs to 21 V at 100 μs (Fig. 3.3A). Yet, on the distal side, the longitudinal currents initially discharged the membrane before beginning to charge it again, evidenced by the change in transmembrane potential from -5.6 V at 4.5 μs to 8.3 V at 100 μs.

The electroporating fiber exhibits qualitatively different behavior than the passive fiber, namely, the intracellular potential remains virtually the same between $t = 4.5$ μs and $t = 100$ μs in Fig. 3.2A. There is a small, but noticeable decrease in transmembrane potential near $\pm\pi/2$ (panel C), and a corresponding small increase in pore density (panel D), but the evolution is not nearly as dramatic as the passive fiber suggests. Indeed, there is only a 3.2% increase in total number of pores over the entire fiber from 4.5 to 100 μs, whereas the root-mean-square change in transmembrane potential of the passive fiber is 307% from 4.5 to 100 μs. Given that pore creation is very sensitive to transmembrane potential (Eq. 2.30), the passive fiber suggests a significantly greater increase in number of pores than 3.2%. However, in the electroporating fiber, no further charging of the membrane can occur, because current has essentially been shorted across the membrane due to large local pore density induced on the short time scale of transverse charging. Thus, electroporation on the fast time scale of transverse polarization drastically increases the conductance,

and the pores remain open with a time scale on the order of one second (Sec. 2.3.2). This lingering increase in conductance largely precludes any additional membrane charging and electroporation for the remainder of the 100 μs pulse. As a result, potential and current density distribution are virtually constant between 4.5 and 100 μs in Figs. 3.3A and 3.3B.

While electroporation on the time scale of membrane charging via transverse current dominates pore density for the region of fiber directly over the cathode, it is still unclear if it dominates for all longitudinal positions along the fiber. Fig. 3.4A shows the circumferential average pore density at time instants 4.5 and 100 μs as a function of longitudinal position. As with the pore density over the cathode in Fig. 3.2D, there is very little relative change in pore density from 4.5 to 100 μs for most of the fiber, thus, pore density for most of the fiber is dominated by the transverse current charging the membrane. However, near 0 mm and $\pm$6.5 mm, indicated by arrows in Fig. 3.4A, pore density increases several orders of magnitude from 4.5 and 100 μs. To determine if transverse or longitudinal behavior is responsible for these localized increases in pore density, derivatives with respect to z are artificially removed from Eq. 2.15 in the longitudinal problem (Sec. 2.1.3). The resulting system is the transverse problem (Sec. 2.1.2) and the longitudinal problem with only the mean membrane current $\overline{I_m}$ (longitudinal diffusion term and AF removed), i.e.,

$$C_m \frac{\partial f_m}{\partial t} = -\overline{I_m}. \tag{3.1}$$

In the full model, the mean membrane current $\overline{I_m}$ is a combination of the longitudinal and transverse effects, but in the absence of the longitudinal diffusion and AF terms, $\overline{I_m}$ is only affected by the mean component of the transverse currents, which is the case in Eq. 3.1. The pore density distribution, as a result of artificially removing longitudinal diffusion and AF, is shown in Fig. 3.4B. Here, the evolution of average

pore density is very similar in the range z=-6..6 mm, yet near ±6.5 mm at the ends of the fiber, the four order magnitude increase in pore density is not seen. Thus, this increase in pore density at the ends of the fiber is due to polarization of the membrane from longitudinal terms, but the increase at $z = 0$ mm is from only transverse effects. Given that molecular uptake is proportional to the circumferential mean of the pore density (Eq. 2.57 in Sec. 2.3.3), uptake in Fig. 3.4C exhibits the same qualitative behavior as pore density in Figs. 3.4A and 3.4B. The uptake at ±6.5 mm is larger in the full model (arrows), compared to the model that neglects longitudinal terms. Ultimately, the increase in uptake near ±6.5 mm due to longitudinal currents increases total uptake in the entire fiber by only 0.91%. However, it is these longitudinal currents that are neglected in previously published models, so further details of the mechanisms behind the enhancement in uptake from electroporation caused by longitudinal diffusion and AF terms are examined more closely in Sec. 3.2.

3.2 Importance of Longitudinal AF at Fiber and Tissue Levels

It is clear from Chapter 3.1 that relative to the passive fiber, the electroporating fiber is largely governed by the transverse currents, given that these currents charge the membrane on a fast time scale, electroporate a large region of membrane, which in turn discharges the membrane, suppressing further evolution of transmembrane potential magnitude and pore density. In these regions of membrane where there is large pore density, further electroporation cannot occur, given the pores stay open three orders of magnitude longer than membrane charging and discharging. However, near ±6.5 mm, the slower charging of the membrane by the divergence of longitudinal currents does bring about a small, but noticeable increase in pore density and molecular uptake, as shown in Fig. 3.4. While electroporation in a fiber subject to a uniform, mean-free field has previously been studied,[57,59] the mechanisms that arise from the divergence of longitudinal currents in a fiber subject to a nonuniform field

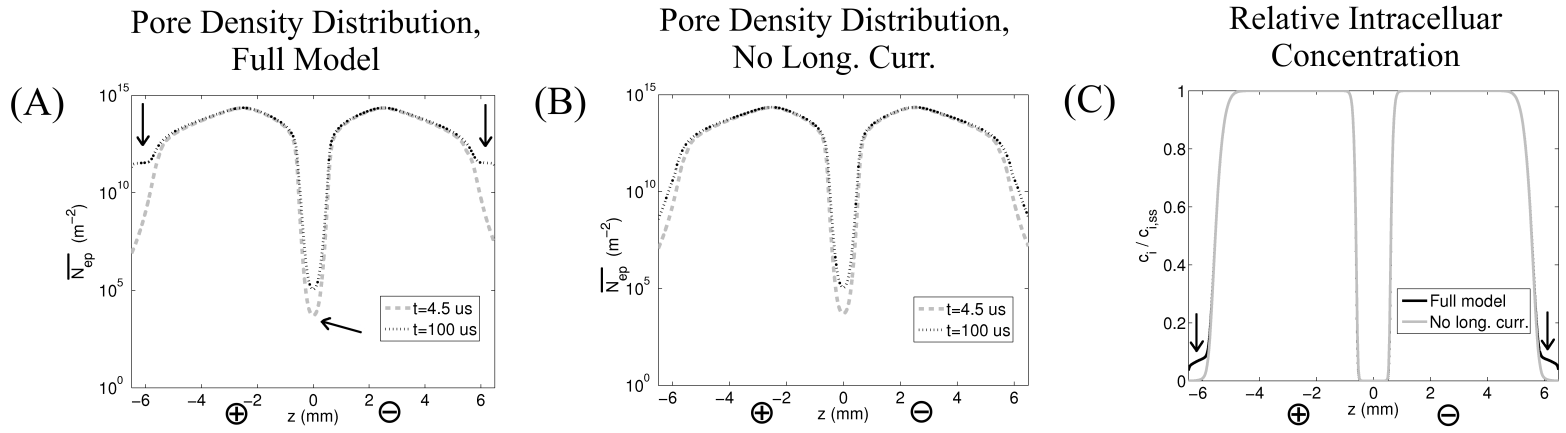

FIGURE 3.4: Longitudinal distribution of circumferential average pore density ($\overline{N_{ep}}$) and molecular uptake (c_i) along the entire length of the electroporating fiber close to electrodes. Positions of anode and cathode are marked with $\oplus$ and $\ominus$, respectively. Arrows indicate changes in pore density and uptake between 4.5 and 100 μs. (A) Longitudinal distribution of circumferential average pore density along fiber, at 4.5 and 100 μs, simulating the full model (full transverse and longitudinal problem). (B) Longitudinal distribution of circumferential average pore density along fiber, at 4.5 and 100 μs, removing longitudinal terms (full transverse problem, reducing longitudinal problem to Eq. 3.1). (C) Longitudinal distribution of intracellular molecular concentration, after all the pores have resealed. Concentration is reported relative to theoretical steady state intracellular concentration $c_{i,ss}$ in the two-compartment model (Eq. 2.58 in Sec. 2.3.3).

have not previously been investigated. In Secs. 3.2.1 and 3.2.2, focus is placed on the longitudinal currents, and in turn, their effect on the evolution of pore density and molecular uptake in an electroporating fiber. These mechanisms observed at the single fiber level dictate the tissue level observations presented in Sec. 3.2.3.

3.2.1 Electroporating Fiber Close to Electrodes

The divergence of the longitudinal currents are represented by two terms in the leading order equation for the longitudinal problem derived in Sec. 2.1.3: terms containing $\partial^2 \langle \Psi \rangle / \partial z^2$ and $\partial^2 f_m / \partial z^2$. The equation is repeated below for convenience,

$$\left(1 + \frac{1}{\gamma\mu}\right) C_m \frac{\partial f_m}{\partial t} = \frac{\sigma_i a}{2} \frac{\partial^2 f_m}{\partial z^2} + \left(1 + \frac{1}{\gamma}\right) \frac{\sigma_i a}{2} \frac{\partial^2 \langle \Psi \rangle}{\partial z^2} - \left(1 + \frac{1}{\gamma\mu}\right) \overline{I_m}. \qquad (3.2)$$

The first term on the right side of Eq. 3.2 is similar to a longitudinal diffusion term: the physical tendency to reduce the heterogeneous buildup of charge. The second term, containing the longitudinal AF $\partial^2 \langle \Psi \rangle / \partial z^2$, is the source term set up by the electrodes, which charges the membrane. The final term contains the mean membrane current $\overline{I_m}$, which evolves as the membrane is charged by currents.

The longitudinal diffusion term is only a secondary reaction to development of mean potential from primary sources, such as the activating function $\partial^2 \langle \Psi \rangle / \partial z^2$. Furthermore, excluding it from Eq. 3.2 yields only a 0.067% change in total uptake, compared to 0.91% when all longitudinal currents are excluded. Thus, the effect of the longitudinal diffusion term on total uptake is small enough that it is not taken into account in the following analysis. The longitudinal AF, the second term in the right side of Eq. 3.2, is the only longitudinal term remaining. Furthermore, it is the difference between the longitudinal AF and $\overline{I_m}$ that leads to evolution of mean transmembrane potential f_m, and consequently, evolution of pore density due to f_m. Thus, the longitudinal AF term $\left(1 + \frac{1}{\gamma}\right) \frac{\sigma_i a}{2} \frac{\partial^2 \langle \Psi \rangle}{\partial z^2}$ and the term $\left(1 + \frac{1}{\gamma\mu}\right) \overline{I_m}$ are shown for different versions of the model in Fig. 3.5.

Fig. 3.5A reveals the net difference between the longitudinal AF term and the mean membrane current $\overline{I_m}$ is significant at 4.5 and 100 μs for the passive fiber. Thus, at both time instants, the AF is charging the membrane and evolving the transmembrane potential, as was shown in Fig. 3.2B. The net difference in AF and $\overline{I_m}$ in the region of virtual electrodes (VEs) is much smaller than in the regions of fiber over the real electrodes (REs), so less membrane charging occurs and smaller transmembrane potential develops. This pattern is reversed in the electroporating fiber in panel B, where the net difference in current is smallest over the anode and cathode, but reaches larger magnitude outside of these regions. In the electroporating fiber, there are three categories of regions: the regions over the electrodes, the regions of $\overline{I_m}$ "spikes" shown by arrows at $t = 4.5$ μs, and the regions where $|z| > 6$ mm.

The first region, over the anode and cathode, the AF is nearly completely balanced by the mean membrane current $\overline{I_m}$. The physical mechanism was discussed in Sec. 3.1, still, further understanding can be gained from analyzing simplified versions of Eq. 3.2. Note that the following analysis is only for use in this following context, and is not meant to be a development in simplifying the model itself. Keeping this note in mind, neglecting the diffusion term and rewriting $\overline{I_m}$ in terms of mean-free and mean voltages, the equation for a passive fiber is obtained,

$$\left(1+\frac{1}{\gamma\mu}\right)C_m\frac{\partial f_m}{\partial t}=\left(1+\frac{1}{\gamma}\right)\frac{\sigma_i a}{2}\frac{\partial^2\langle\Psi\rangle}{\partial z^2}-\left(1+\frac{1}{\gamma\mu}\right)\frac{f_m-V_{rest}}{R_m}, \tag{3.3}$$

and the equation for an electroporating fiber is found,

$$\left(1+\frac{1}{\gamma\mu}\right)C_m\frac{\partial f_m}{\partial t}=\left(1+\frac{1}{\gamma}\right)\frac{\sigma_i a}{2}\frac{\partial^2\langle\Psi\rangle}{\partial z^2}-\left(1+\frac{1}{\gamma\mu}\right)\left\{\left(\frac{R_m+R_p}{R_mR_p}\right)f_m-\frac{V_{rest}}{R_m}\right\}, \tag{3.4}$$

where R_p is the membrane surface resistance due to electropores. R_p is obtained by dividing current density due to electroporation (Eq. 2.29) by Φ_m, and inverting the result, which converts the current density into surface conductance. As-

suming R_p is spatially and temporally invariant, time constants can be found from Eqs. 3.3 and 3.4,

$$\text{Passive: } R_m C_m = 10 \text{ ms} \quad \text{and Electroporating: } R_m R_p C_m/(R_m + R_p) = 1\ \mu\text{s}, \quad (3.5)$$

where $R_p = 100\ \mu\Omega\text{m}^2$ is representative of pore resistance in the region over the electrodes. Thus, membrane charging time is reduced by four orders of magnitude, illustrating the feasibility of Eq. 3.2 reaching steady state within 4.5 μs of turning on the pulse in the regions over the anode and cathode. Essentially, the time scale of membrane charging in the longitudinal problem is reduced to 1 μs, which is on the order of the time scale of membrane charging due to transverse currents: $aC_m/\sigma_i = 0.45\ \mu$s. This decrease in time scale is from transverse charging and electroporation of the membrane, and is introduced into the longitudinal problem via $\overline{I_m}$. Current in the region of the electrodes for the fiber that excludes longitudinal AF (Fig. 3.5C) behaves in the same manner, except mean membrane current $\overline{I_m}$ is zero because the longitudinal AF is excluded from this model.

The second region identified in Fig. 3.5B are the "spikes" in $\overline{I_m}$. Fig. 3.5C reveals that the four regions of fiber where there are "spikes" of mean membrane current $\overline{I_m}$ at 4.5 μs (shown by arrows), are largely a result of transverse currents charging and electroporating the membrane, as they appear in the version of the model excluding the longitudinal AF. These four regions show inward (negative) current flow, which is due to the negative bias of the resting potential leading to electroporation on the hyperpolarized side of the fiber first, as shown in Fig. 3.6A for $z = 5.5$ mm. The hyperpolarized side of the fiber electroporates on the order of 4.5 μs (Fig. 3.6A), introducing current flowing transversely across the fiber, as shown in Fig. 3.7A. The electroporating fiber exhibits large current density on the hyperpolarized side where there is high pore density, and a fraction of this current flows to the depolarized side of the fiber, where pore density is much smaller. The imbalance of resistive

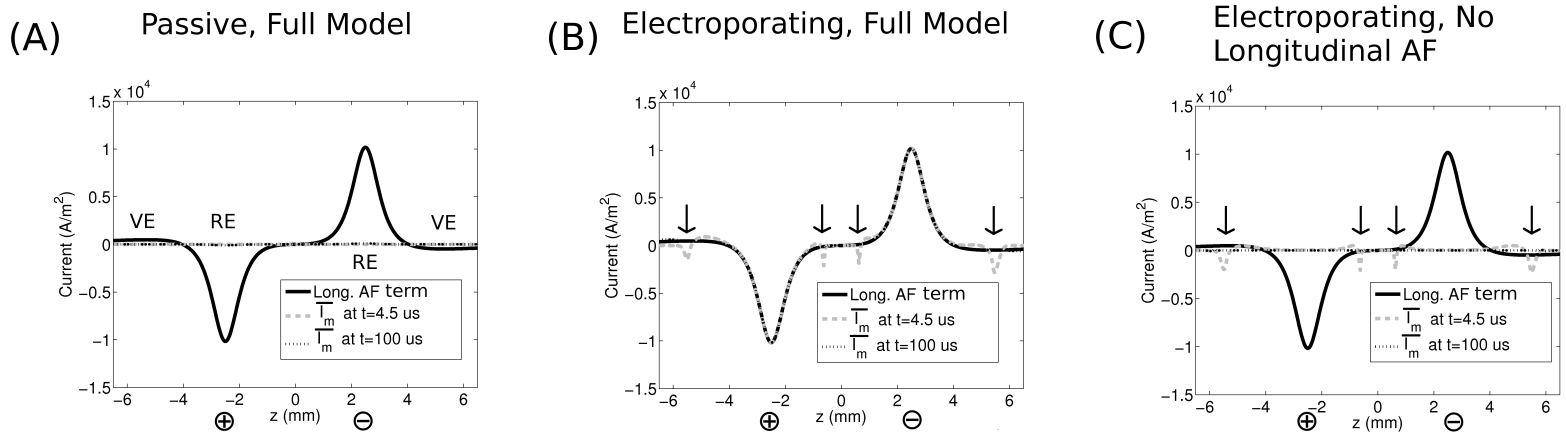

FIGURE 3.5: Longitudinal AF and mean membrane current $\overline{I_m}$ along entire length of fiber close to electrodes. Positions of anode and cathode are marked with $\oplus$ and $\ominus$, respectively. Arrows indicate regions of large $\overline{I_m}$. (A) Passive, full model simulating full asymptotic fiber model (full transverse and longitudinal problem). The letters "VE" mark the general positions of virtual electrodes, where net current flows opposite the direction under the real electrodes ("REs"), and thus, transmembrane potential is reversed. (B) Electroporating model, full asymptotic fiber model. (C) Electroporating model, removing longitudinal AF (full transverse problem, reducing longitudinal problem to Eq. 3.1). Longitudinal AF is still shown for reference, but not included in simulations.

membrane current between the hyperpolarized and depolarized side at 4.5 μs in Fig. 3.6B reveals there is capacitive charging of the membrane on the depolarized side, and that there is also current flow in the longitudinal direction (Fig. 3.7B).

The current that does flow across to the depolarized side charges the membrane there, as evidenced by the negative circumferential mean membrane current $\overline{I_m} = -2740$ A/m^2 at 4.5 μs in Fig. 3.6B. The charging of the membrane on the depolarized side of the fiber continues until transmembrane potential is large enough to elicit comparable pore density to the hyperpolarized side, as shown at 100 μs in Fig. 3.6A. The resulting increased conductance on the depolarized side reduces the magnitude of $\overline{I_m}$ by an order of magnitude (Fig. 3.6B) because now more current introduced on the hyperpolarized side is flowing across the membrane on the depolarized side through the increased conductance. Thus, the "spikes" in $\overline{I_m}$ in Fig. 3.5 disappear by 100 μs, and current from the longitudinal AF balances $\overline{I_m}$, indicating membrane charging and pore creation is at quasi-steady state. Therefore, as was the case for the region of fiber over the cathode, the transverse currents charge the membrane and increase the pore density, which precludes further charging and electroporation from the longitudinal currents.

Physically, most longitudinal current that enters a transverse slice of the fiber continues longitudinally, given pore density is relatively moderate, as shown in Fig. 3.3B. However, the small difference in longitudinal current between transverse slices is exactly balanced by mean current entering the fiber across the membrane, as shown by the asymmetry in current in Fig. 3.7A and negative value of $\overline{I_m}$ in fig. 3.6B. The passive fiber also exhibits nonzero $\overline{I_m}$ at 100 μs in Fig. 3.5A, but magnitude of current density is ten-fold smaller than in the electroporating fiber. In essence, electroporation ultimately increases the magnitude of $\overline{I_m}$ by increasing membrane conductance until $\overline{I_m}$ exactly balances the current from the longitudinal AF. However, the passive fiber must depend on membrane charging, increasing the magnitude of

transmembrane potential, until $\overline{I_m}$ balances the current from the longitudinal AF, which is a slow process that depends on longitudinal currents. The electroporating fiber temporally "skips ahead" to quasi-steady state when the currents are balanced in Eq. 3.2, as a consequence of the transverse currents charging and electroporating the membrane, which increase membrane conductance.

The third, and final region in Fig. 3.5B is where $|z| > 6$ mm. Comparing Figs. 3.5A and 3.5B reveals that the longitudinal current exhibits opposite sign from regions closer to the electrodes, indicating this region is where virtual electrodes (VEs) form. It is in this region where the profile of $\overline{I_m}$ is nearly identical to the passive, full model in panel A at 4.5 μs. Furthermore, current density in the passive and electroporating fiber are nearly identical in Fig. 3.8. There is virtually no trace of electroporation in this region at 4.5 μs, given that $\overline{I_m}$ is very close to zero in Fig. 3.5B, and pore density in Fig. 3.4A is orders of magnitude smaller than everywhere else along the fiber. The difference between current from the longitudinal AF and $\overline{I_m}$, and resulting membrane charging, electroporation, and molecular uptake between 4.5 and 100 μs (Figs. 3.4A and 3.4C), is entirely accounted for by the current that charges the membrane. As electroporation occurs due to charging of the membrane by these longitudinal currents, the magnitude of $\overline{I_m}$ approaches the magnitude of the longitudinal AF term, and at 100 μs, the two are equal (Fig. 3.5B). The mechanism by which this occurs is the same as for position $z = 5.5$ mm, except in this case it is the longitudinal AF that charges and electroporates the membrane, given that transverse currents are too weak to do so first. Increase in pore density primarily occurs on the hyperpolarized side of the fiber due to the negative bias of the resting potential (Fig. 3.8A), but the increase in pore density is still relatively small, as the longitudinal flow of current is barely disrupted in Fig. 3.8B.

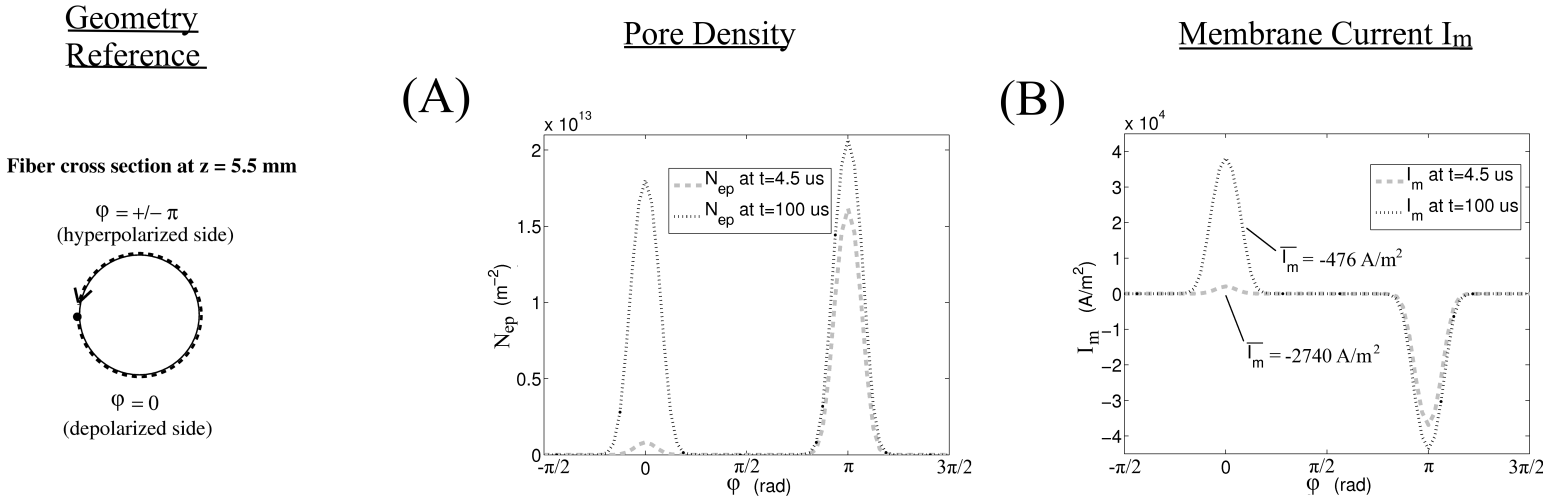

FIGURE 3.6: Circumferential pore density N_{ep} and membrane current I_m for cross-section of fiber at z=5.5 mm. This location highlights one of the "spikes" of $\overline{I_m}$ in Fig. 3.5 at 4.5 μs, and explains the existence of these spikes. (A) and (B) Circumferential pore density and membrane current for full electroporating fiber model, i.e., simulating full transverse and longitudinal problems.

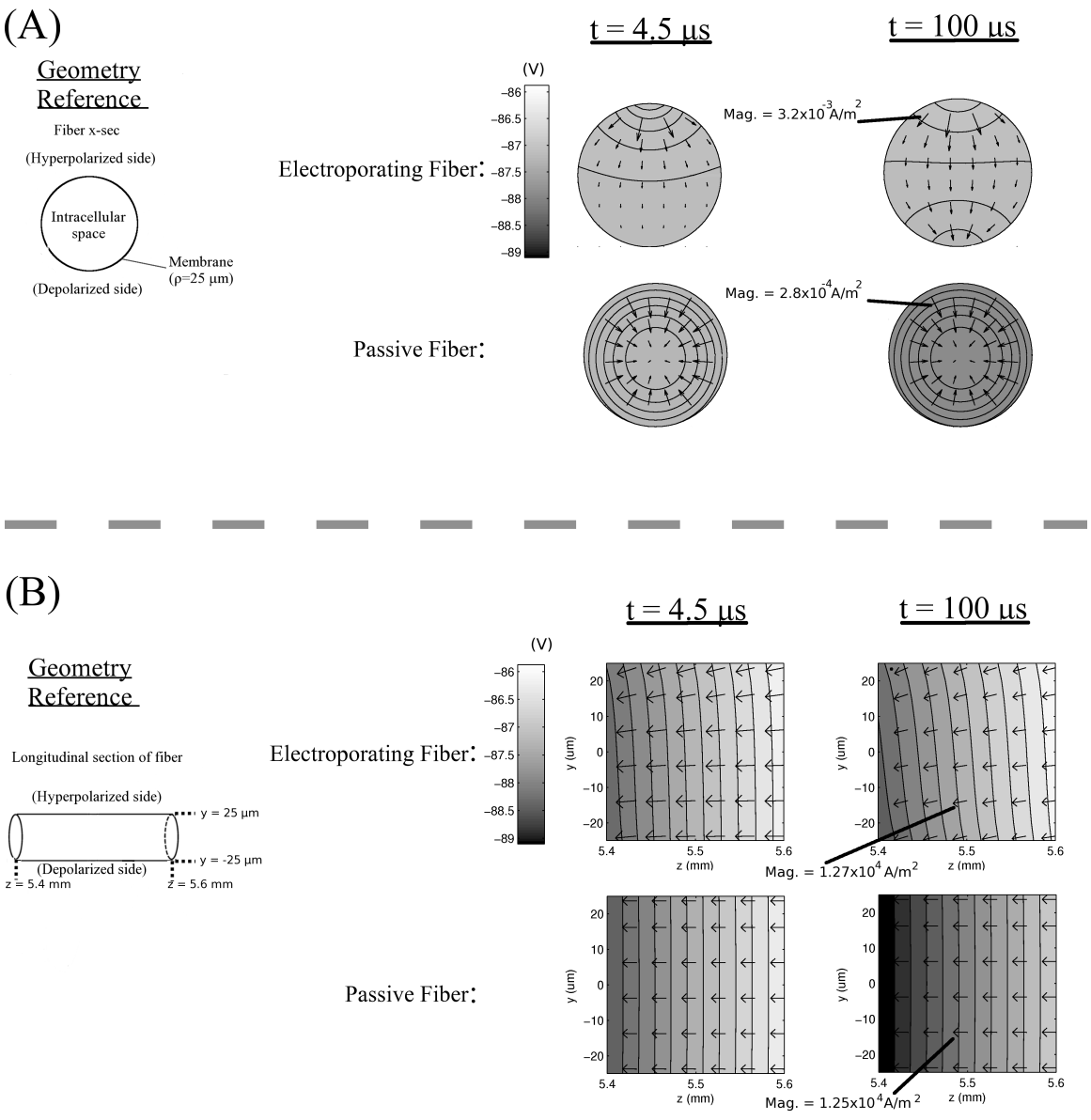

FIGURE 3.7: Current density and potential distribution in intracellular space in vicinity of $z = 5.5$ mm, i.e., in the vicinity of one of the "spikes" in $\overline{I_m}$ in Fig. 3.5B. Magnitude and direction of current density arrows is to scale within a single cross section, but is not comparable between different cross-sections. (A) Transverse cross-section at $z = 5.5$ mm for passive and electroporating fiber at two time instants. Magnitude of current density is displayed at one location in cross section. (B) Longitudinal cross-section in the vicinity of $z = 5.5$ mm for passive and electroporating fiber at two time instants. Magnitude of current density is displayed at one location in cross section.

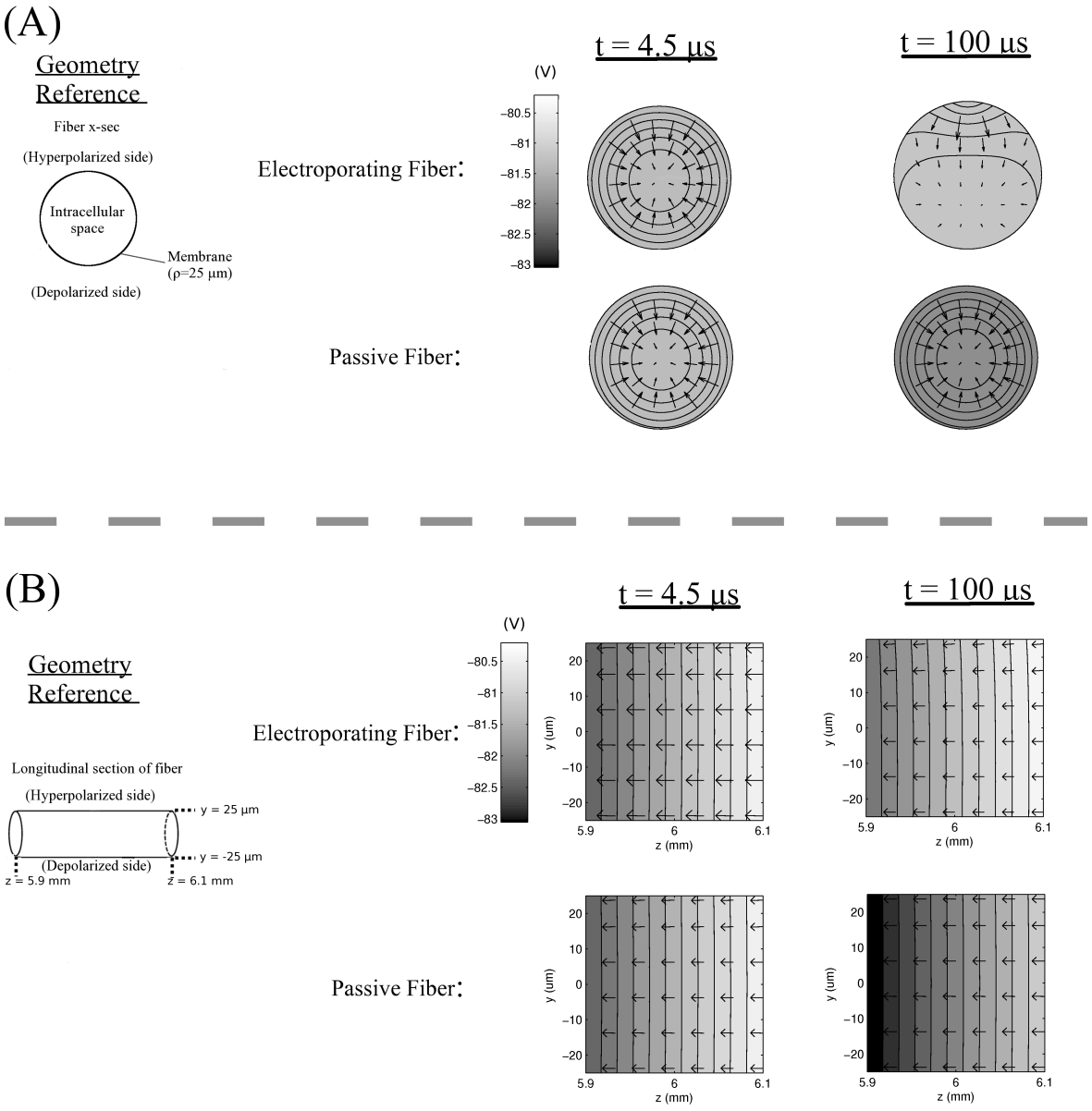

FIGURE 3.8: Current density and potential distribution in intracellular space in vicinity of $z = 6.0$ mm. Magnitude and direction of current density arrows is to scale within a single cross section, but is not comparable between different cross-sections. (A) Transverse cross-section at $z = 6.0$ mm for passive and electroporating fiber at two time instants. (B) Longitudinal cross-section in the vicinity of $z = 6.0$ mm for passive and electroporating fiber at two time instants.

3.2.2 Electroporating Fiber Far From Electrodes

Fig. 3.9 shows the same data as in Fig. 3.4 using same simulation parameters, except electrode-fiber distance is further: 1.44 mm instead of 0.48 mm. Comparing the two figures, the fiber further away shows smaller magnitude of pore density and uptake, as expected. Furthermore, unlike the close fiber, there is dramatic change in pore density between 4.5 and 100 μs at every position in z along the fiber. While there is some temporal evolution of pore density in the version of the model without longitudinal AF, it is not as pronounced as in the full model. Thus, the longitudinal AF contributes significantly to the formation of pores. In fact, maximum pore density in the full model is approximately ten-fold larger than the model without longitudinal AF. This difference in pore density results in maximum uptake of approximately ten-fold larger in the full model, and total uptake in entire fiber increases by nearly 2000% over the model without longitudinal AF. Clearly, the longitudinal AF has a significantly larger role in uptake for fibers that are further from the electrodes.

The temporal evolution of the circumferential average membrane current reflects the importance of including the longitudinal AF in simulation, as shown in Fig. 3.10. As expected, $\overline{I_m}$ in the electroporating fiber (panel B) is very similar to the passive fiber (panel A) at 4.5 μs, as the transverse component of the stimulus does not elicit significant creation of pores. However, between 4.5 and 100 μs, the pore density drastically increases over much of the fiber membrane (Fig. 3.9A), and $\overline{I_m}$ consequently increases over much of the fiber in Fig. 3.10B. Finally, $\overline{I_m}$ in the model without the longitudinal AF remains at small magnitude throughout the duration of the 100 μs pulse, with inward negative current developing due to the negative bias of the resting potential causing the hyperpolarized side of the fiber to electroporate first under the electrodes (Fig. 3.10C). For a fiber further from the electrodes, the longitudinal AF is clearly the primary influence on development of $\overline{I_m}$.

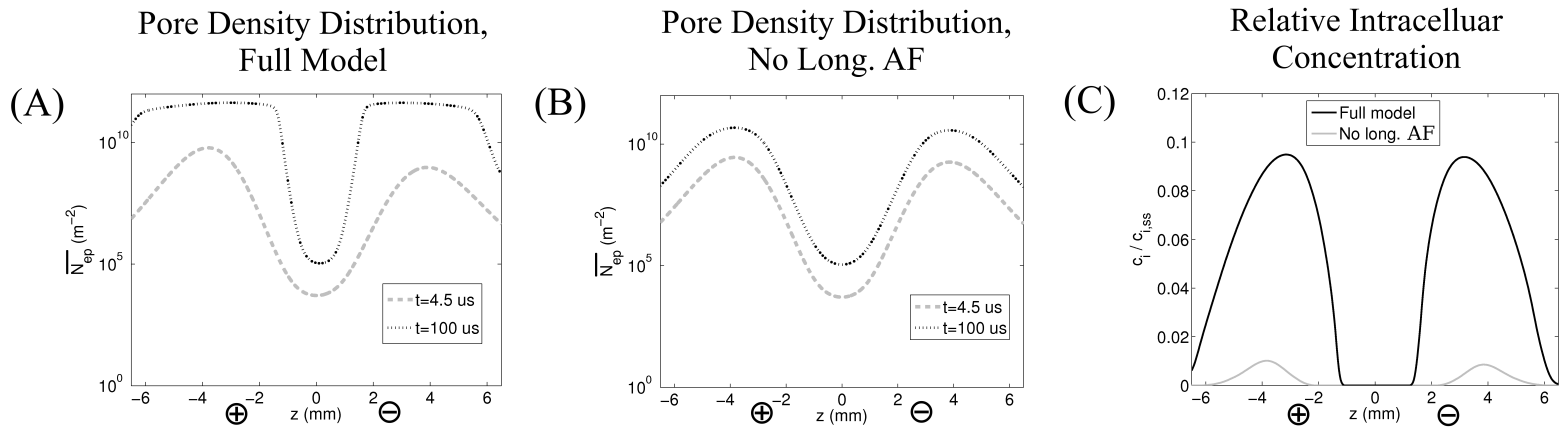

FIGURE 3.9: Longitudinal distribution of circumferential average pore density ($\overline{N_{ep}}$) and molecular uptake (c_i) along the entire length of the electroporating fiber far from electrodes. Positions of anode and cathode are marked with $\oplus$ and $\ominus$, respectively. (A) Longitudinal distribution of circumferential average pore density along fiber, at 4.5 and 100 μs, simulating the full model (full transverse and longitudinal problem). (B) Longitudinal distribution of circumferential average pore density along fiber, at 4.5 and 100 μs, removing longitudinal AF (full transverse problem, reducing longitudinal problem to Eq. 3.1). (C) Longitudinal distribution of intracellular molecular concentration, after all the pores have resealed. Concentration is reported relative to theoretical steady state intracellular concentration in the two-compartment model (Eq. 2.58 in Sec. 2.3.3).

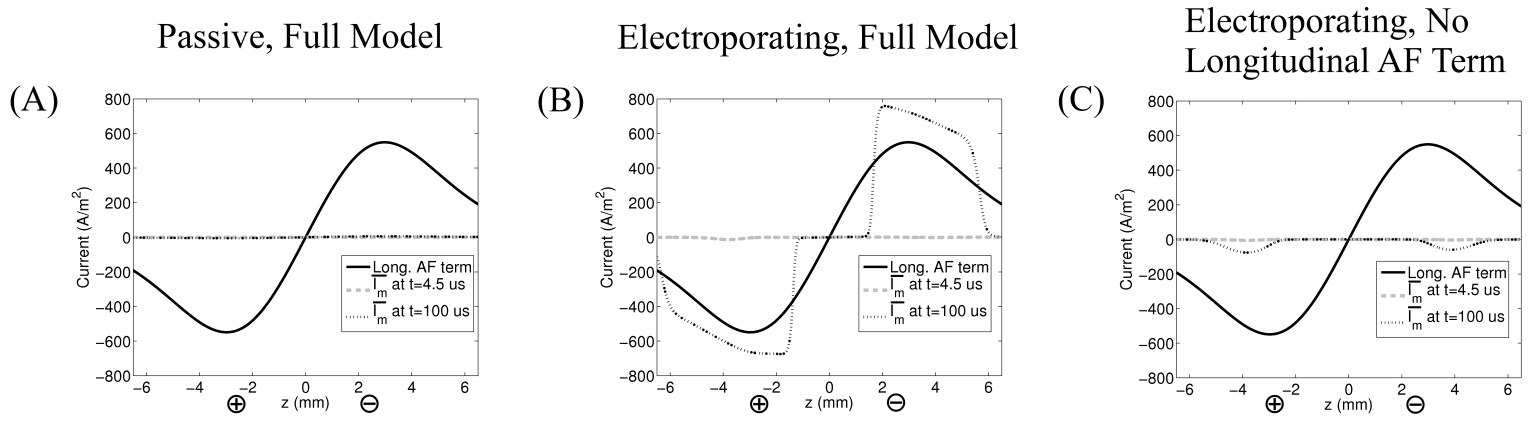

FIGURE 3.10: Longitudinal AF term and mean membrane current $\overline{I_m}$ along entire length of fiber far from electrodes. Positions of anode and cathode are marked with $\oplus$ and $\ominus$, respectively. (A) Passive, full model simulating both transverse and longitudinal problems (B) Electroporating, full model simulating both transverse and longitudinal problems. (C) Electroporating model, removing longitudinal AF (full transverse problem, reducing longitudinal problem to Eq. 3.1). Longitudinal AF is still shown for reference, but not included in simulations.

3.2.3 Entire Tissue

The increase in molecular uptake over the entire tissue is important to determine how the contribution of the longitudinal AF at the fiber level relates to the contribution of the longitudinal AF at the macroscopic tissue level. Fig. 3.11 shows contour plots of the molecular uptake over the entire tissue. Using a normal color gradient, there is no noticeable difference between molecular uptake from the full version of the model that includes the longitudinal AF (panel A), and the version that excludes it (panel B). This similarity between the two versions of the model is explained as follows. Uptake in a fiber close to the electrodes is enhanced 0.91% due to the longitudinal AF, while uptake in a fiber far from the electrodes is enhanced by 2000%. However, computing the total uptake over the entire fiber far from the electrodes (Fig. 3.9C) and over the entire fiber close to the electrodes (Fig. 3.4C), it is revealed that uptake in the far fiber is only 6.5% of the close fiber. Therefore, relative importance of the longitudinal AF on the tissue level cannot be judged on the single fiber level alone. While the longitudinal AF plays a major role at the individual fiber level far from the electrodes, in the context of the entire tissue, its effect on uptake remains relatively small. The transverse AF dominates for fibers closer to the electrodes, where a majority of the pores are created and where most of the molecular uptake occurs in the tissue. Over the entire tissue, the longitudinal AF increases uptake by 3.95%, which is much closer to the 0.91% increase in uptake for the close fiber than the 2000% increase in uptake for the far fiber.

Tissue molecular uptake viewed with an adjusted color gradient to view minute differences is shown in Figs. 3.11C and 3.11D. Here, it is apparent that for fibers close to the electrodes, the longitudinal AF enhances uptake near $z = \pm 6$ mm, and for fibers further from the electrodes it enhances uptake over a majority of the fiber, as observed in Secs. 3.2.1 and 3.2.2. In Fig. 3.11C, the increase in uptake from

longitudinal AF is a small "ring" of moderate uptake (grey color) on the periphery of the major uptake region (white region). However, the "ring" is broken in the region between the electrodes, where uptake is not affected by the longitudinal AF. It is also apparent that molecular uptake in the tissue exhibits nearly binary behavior. The uptake in the grey region on the periphery is small compared to uptake in the white region. Therefore, it is almost complete to classify uptake as either occurring and reaching steady state intracellular concentration, or occurring and leading to only small increases in intracellular concentration. However, it should be noted that even a small amount of uptake over a large are could result in significant contribution to total uptake in the tissue, which is examined more in Sec. 3.3.2

3.3 Model Variations: Effect on Uptake and Importance of Longitudinal AF

3.3.1 Orientation of Electrodes

Given the domination of the transverse AF in governing molecular uptake, it would be expected that orienting the electrodes transverse to the fibers yields larger uptake. This hypothesis is tested in Fig. 3.12. Here, the increase in tissue-wide uptake in changing from longitudinal orientation of electrodes to transverse orientation of needles is 75%. The qualitative difference between the distribution of the molecular uptake in Fig. 3.12A and Fig. 3.11A is that molecular uptake remains elevated for much of the space between electrodes. In fact, the 1 mm block of tissue between $y = -.5$ mm and $y = .5$ mm contains 20% of the uptake molecular uptake in the entire tissue. Furthermore there is a larger region of tissue where moderate amount of uptake occurs. The percentage of tissue where relative uptake is between 0.25 and 0.75 is 24% for transverse needles compared to 6.5% for longitudinal needles. This region of tissue contributes 28% to total uptake for transverse needles, compared to only 11% for longitudinal needles. The percentage of tissue where relative uptake

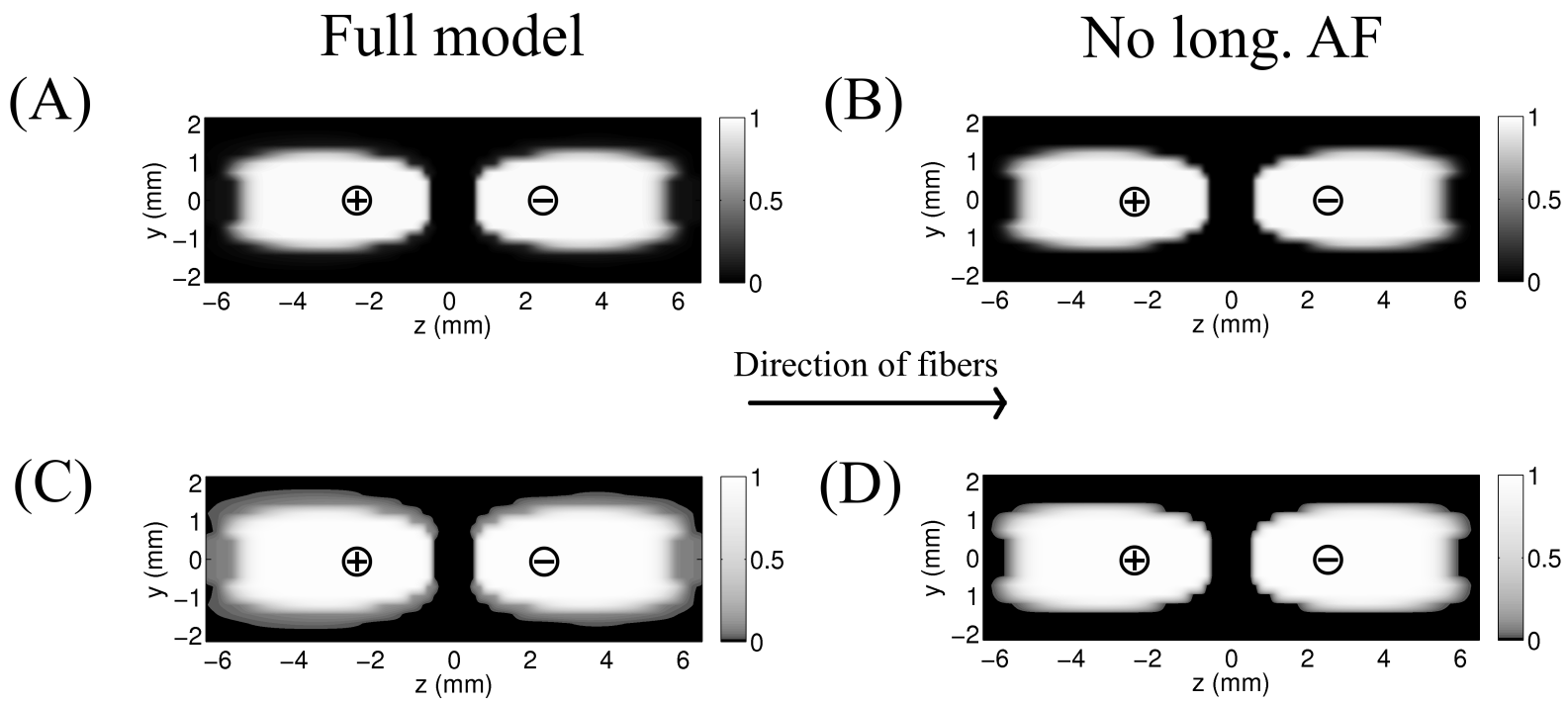

FIGURE 3.11: Molecular uptake in entire tissue for longitudinally oriented electrodes. Results are reported as intracellular concentration relative to steady state value of intracellular concentration, i.e., $c_i/c_{i,ss}$ (Eq. 2.58). Positions of anode and cathode are marked with $\oplus$ and $\ominus$, respectively. (A) Full model simulating both transverse and longitudinal problems. (B) Removing longitudinal AF (full transverse problem, reducing longitudinal problem to Eq. 3.1). (C) Same as panel A, except contour color gradient is altered to show minute changes in concentration. (D) Same as panel B, except contour color gradient is altered to show minute changes in concentration.

is greater than 0.75 is 35% for transverse needles compared to 28% for longitudinal needles. However, this region of tissue contributes only 68% to total uptake for transverse needles, compared to 84% for longitudinal needles. Therefore, the transverse needle orientation allows for significant increase in total uptake from more moderate amounts of uptake spread across a larger region of tissue.

Comparing Figs. 3.12A to 3.12B the uptake looks approximately the same regardless of whether or not the longitudinal AF is used, but comparing Figs. 3.12C to 3.12D, it is clear there is a small effect from including the longitudinal AF. The increase in uptake is in the region of tissue that is on the periphery of where the majority of uptake occurs, as was the case for longitudinally oriented electrodes. Integrating uptake over the entire tissue, the increase from including the longitudinal AF is 0.752%, compared to 3.95% for when the electrodes are positioned longitudinally to the fibers. Not only is the percent increase smaller in the case of transversely oriented electrodes, the actual value of the increase in uptake for transversely oriented needles is only 34% of that for longitudinally oriented needles. This overall smaller effect from the longitudinal AF for transversely oriented electrodes is expected, given that orienting the electrodes in this position amplifies the effects from the transverse AF.

3.3.2 Pulse Strength and Comparison to Other Models and Experiments

Fig. 3.13 shows contour plots of the intracellular concentration over the entire tissue for four pulse strengths typical in delivery of small molecules.[29,31] As observed for pulse strength of 800 V/cm in Sec. 3.2.3, for all pulse strengths molecular uptake exhibits a nearly binary behavior in the tissue space, where either uptake occurs and the steady state concentration is obtained, or there is only small increase in intracellular concentration. Due to this binary behavior, increasing the pulse strength enhances uptake by increasing region over which the steady state concentration is

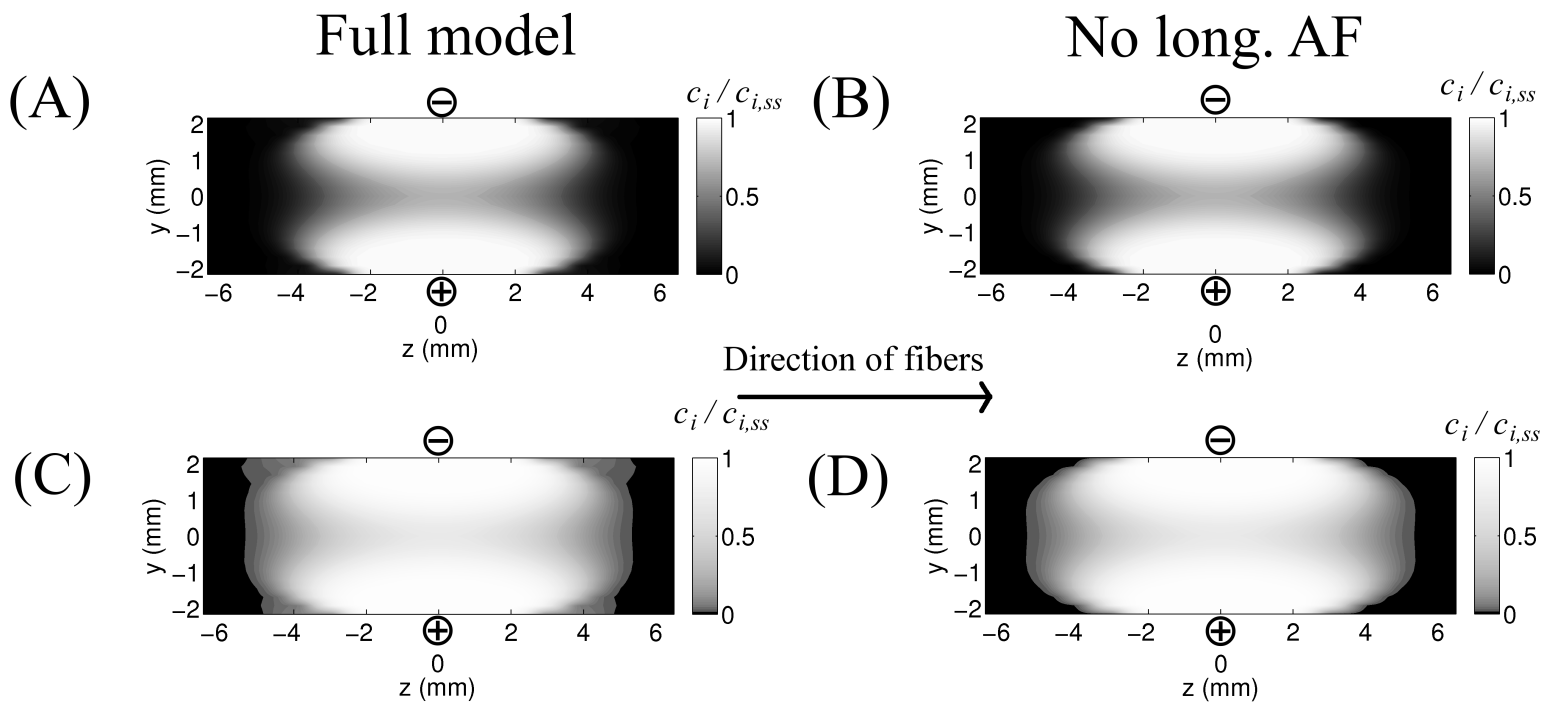

FIGURE 3.12: Molecular uptake in entire tissue for transversely oriented needles. Results are reported as intracellular concentration relative to steady state value of intracellular concentration, i.e., $c_i/c_{i,ss}$ (Eq. 2.58). Positions of anode and cathode are marked with $\oplus$ and $\ominus$, respectively. (A) Full model simulating both transverse and longitudinal problems. (B) Removing longitudinal AF (full transverse problem, reducing longitudinal problem to Eq. 3.1). (C) Same as panel A, except contour color gradient is altered to show minute changes in concentration. (D) Same as panel B, except contour color gradient is altered to show minute changes in concentration.

obtained, rather than slightly amplifying uptake where there already exists nonzero intracellular concentration.

Fig. 3.14A shows normalized total number of molecules as a function of pulse strength from the full version of the model and from the version excluding longitudinal AF. Total uptake versus field strength is linear (linear correlation coefficient is 0.9999 for both curves), and the increase in number of intracellular molecules from including the longitudinal AF is nearly independent of pulse strength (maximum difference between point-by-point difference between curves and mean difference between curves is only 1.6% of minimum uptake at pulse strength 400 V/cm). Therefore, the relative increase in uptake from including the longitudinal AF diminishes with increased pulse strength, simply because the magnitude of uptake increases (Fig. 3.14B). For small pulses, the relative increase in uptake from including the longitudinal AF reaches nearly 10%, and for 1000 V/cm the relative increase is reduced to 2.8%. The relative increase in uptake decreases at a slower rate as pulse strength is increased.

Other published models of uptake in muscle tissue do not simulate uptake, rather, the magnitude of the electric field $|E|$ is is compared to a threshold $|E|_{th}$ in determining electroporation and uptake.[29,30,103] Thus, for comparison to these experiments, four threshold values for intracellular concentration are chosen and reported relative to the steady state intracellular concentration $c_{i,ss}$: $0.1c_{i,ss}$, $0.117c_{i,ss}$, $0.13c_{i,ss}$, and $0.99c_{i,ss}$. Next, for each uptake threshold, regions of tissue that attain uptake threshold are mapped to the distribution of $|E|$. Looking at the "edges" of the region where uptake reaches threshold for all four pulse strengths, an average threshold value for field magnitude is found $|E|_{th}$. The region of tissue that attains $|E|_{th}$ is reported as a percentage of the size of the entire tissue in Fig. 3.15 for four different pulse strengths. Clearly, the ability of this threshold field method to reproduce uptake in the full model is dependent on choice of $|E|_{th}$, and it very nearly reproduces the

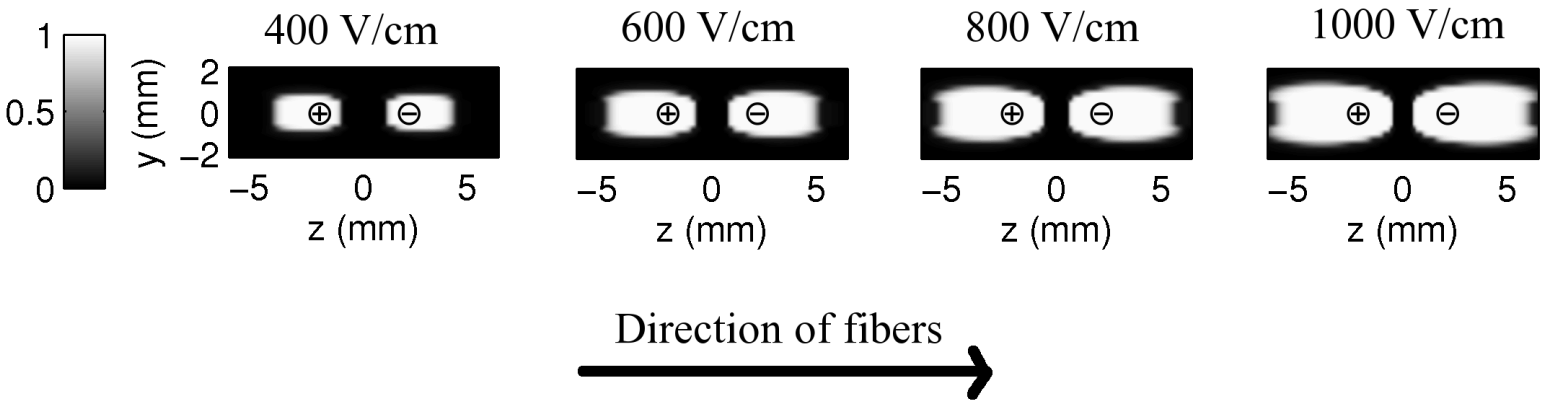

FIGURE 3.13: Molecular uptake in entire tissue versus pulse magnitude. Intracellular concentration of molecules is reported after all pores have resealed, and normalized to steady state value of intracellular concentration, i.e., $c_i/c_{i,ss}$ (Eq. 2.58). Positions of anode and cathode are marked with $\oplus$ and $\ominus$, respectively. Four different values of pulse strength are used, reported as the interelectrode voltage divided by the interelectrode distance: $2V_0/d$.

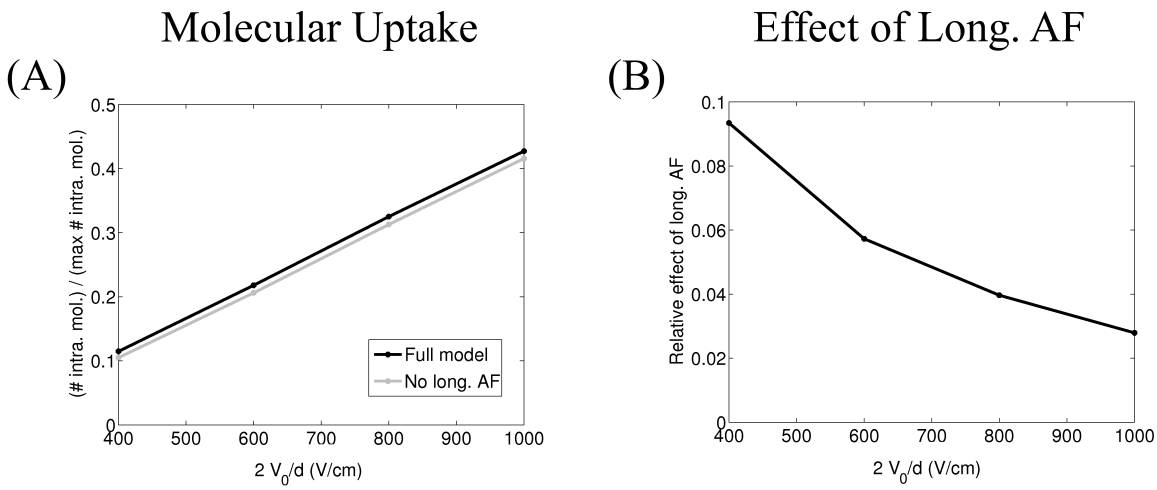

FIGURE 3.14: Effect of longitudinal AF on total tissue uptake for different pulse magnitudes. Uptake is reported after all pores have resealed. Four different values of pulse strength are used, reported as the interelectrode voltage divided by the interelectrode distance: $2V_0/d$. (A) Uptake both including and excluding the longitudinal AF is reported as the total number of molecules in the intracellular space normalized to maximum number of intracellular molecules if entire tissue reached steady state concentration. (B) Relative increase in tissue-wide uptake due to longitudinal AF for different pulse strengths.

full model when threshold is defined as 483 V/cm ($0.117c_{i,ss}$). Unlike uptake in the full model, predicted uptake from field threshold method is not linear, but the linear correlation coefficient for 483 V/cm case is 0.999. The average relative difference between the full model and the threshold field model over all pulse strengths is 3.31%, with maximum of 7.45% at pulse strength of 400 V/cm. If threshold is defined as when intracellular concentration is $0.1c_{i,ss}$ ($|E|_{th}$ = 298 V/cm) or $0.99c_{i,ss}$ ($|E|_{th}$ = 841 V/cm), then uptake is drastically overpredicted and underpredicted, respectively. The underprediction from using $0.99c_{i,ss}$ highlights that although spatial uptake regions in tissue behave in a binary fashion, the small amount of "background uptake" in the tissue does contribute to total uptake. Predicted uptake is also very sensitive to threshold choice. Increasing threshold 483 V/cm by 5.8% (511 V/cm) results in predicted uptake profile with larger linear correlation coefficient of 0.999996,

but increases average and maximum relative difference from the full uptake model to 10.2% and 14.8%, respectively.

While total uptake can be predicted well using the threshold field approach, the shape of the region of uptake in the tissue is less accurate. Using $|E|_{th} = 483$ V/cm threshold, the shape of the uptake area is closer to the full model for pulse strengths less than 800 V/cm, as shown in Fig. 3.16. The correlation coefficients for pulse strengths 400 and 600 V/cm are 0.969 and 0.956, respectively, while for 800 and 1000 V/cm they are 0.934 and 0.919. The relative root mean square differences for pulse strengths 400 to 1000 V/cm are 17.5%, 16.9%, 19.3%, and 20.9%. In general, the shape of uptake using the field threshold model is more narrow in the y-dimension than in the full model, but includes more uptake exactly midway between the electrodes. This pattern is especially pronounced for larger pulse strengths. Thus, the shape of uptake in the tissue is not predicted as well by the threshold field model, even though the predicted total uptake is relatively accurate.

Tissue-level uptake can be compared to actual uptake in experiments of small molecules performed by Grafstrom et al.,[31] given that electrode and tissue geometries, as well as pulsing protocols used in simulations are matched exactly to experiments. Experiments were carried out in rats, where radiolabelled DTPA is injected into the bloodstream and electric pulses are applied to the soleus muscle in one leg of the rat after accumulation of the molecule in the interstitial space.[31] The other leg of the rat is the control, and is not treated with electric pulses. Radioactivity in both muscles are measured 5-8 hours later, when 90% of the initially injected molecules have been excreted. Note that radioactivity can be related to number of radiolabelled DTPA molecules through the definition of the Becquerel, and number of molecules are related to concentration if a volume is given. Radioactivity measured in the treated muscle is a combination of molecules that entered the intracellular space ($K_{i,p}$) and 10% of the molecules that remained in the extracellular space after pore

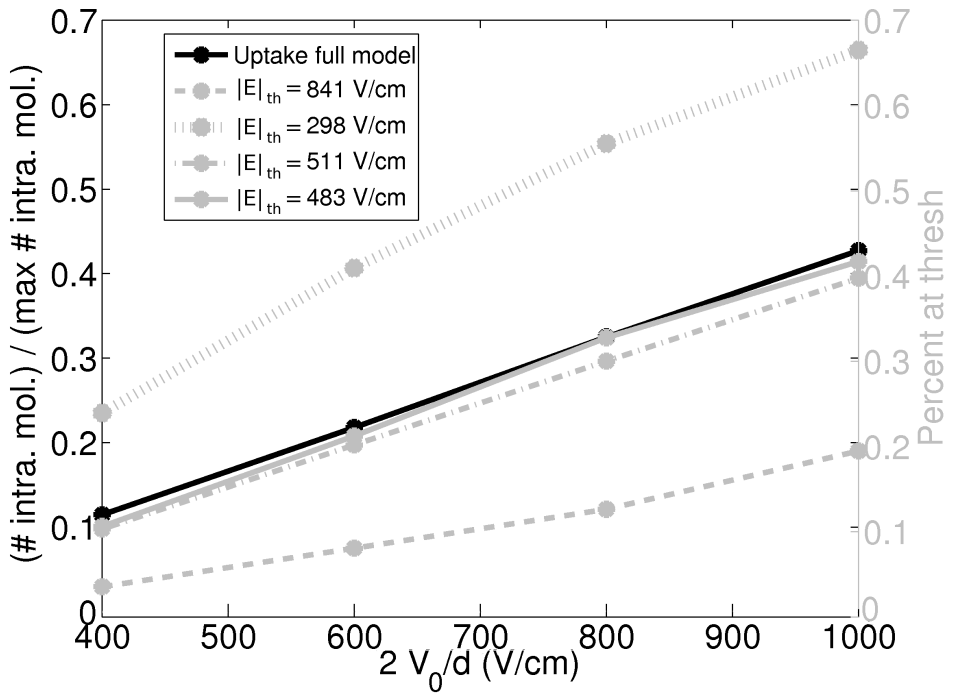

FIGURE 3.15: Total tissue uptake versus pulse strength predicted by threshold field model. Four different values of pulse strength are used, reported as the interelectrode voltage divided by the interelectrode distance: $2V_0/d$. Total uptake from the full model is calculated as total number of molecules in the intracellular space normalized to maximum number of intracellular molecules if entire tissue reached steady state concentration. Total uptake predicted by the threshold approach is calculated as the percent of tissue that achieves the threshold field strength. Three different field strength thresholds are used. For threshold $|E|_{th} = 483$ V/cm, the predicted uptake is very nearly equivalent to uptake predicted by full model, and lines nearly overlap.

resealed ($0.1K_{e,p}$). Radioactivity measured in the untreated muscle is simply 10% of the initial activity in the interstitial space ($0.1K_{e,c}$). Uptake ratio (UR) is measured and reported in experiments, and can be computed in the model,

$$\text{UR} = \frac{K_{i,p} + 0.1K_{e,p}}{0.1K_{e,c}}, \tag{3.6}$$

$K_{i,p}$ and $K_{e,p}$ are computed from integrating intracellular (c_i) and extracellular (c_e) concentrations over the intracellular and extracellular spaces, respectively, and $K_{e,c}$ is computed by integrating the constant initial extracellular concentration c_o over

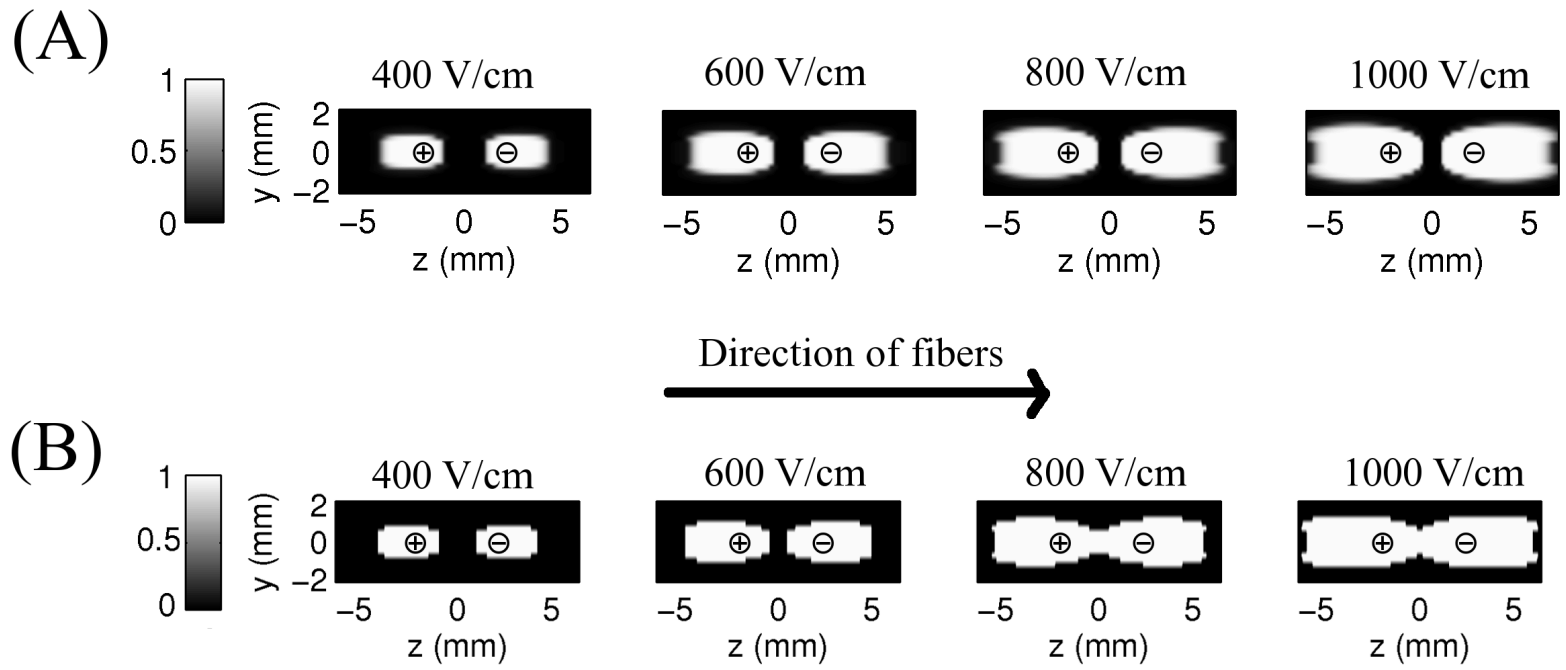

FIGURE 3.16: Simulated molecular uptake in entire tissue compared to predicted uptake using threshold field model. Positions of anode and cathode are marked with $\oplus$ and $\ominus$, respectively. Four different values of pulse strength are used, reported as the interelectrode voltage divided by the interelectrode distance: $2V_0/d$. (A) Intracellular concentration of molecule reported after all pores have resealed using the full model, and normalized to steady state value of intracellular concentration, i.e., $c_i/c_{i,ss}$ (Eq. 2.58). (B) Intracellular concentration of molecule predicted by threshold field method, reported as percent of tissue that achieves the threshold value of 483 V/cm.

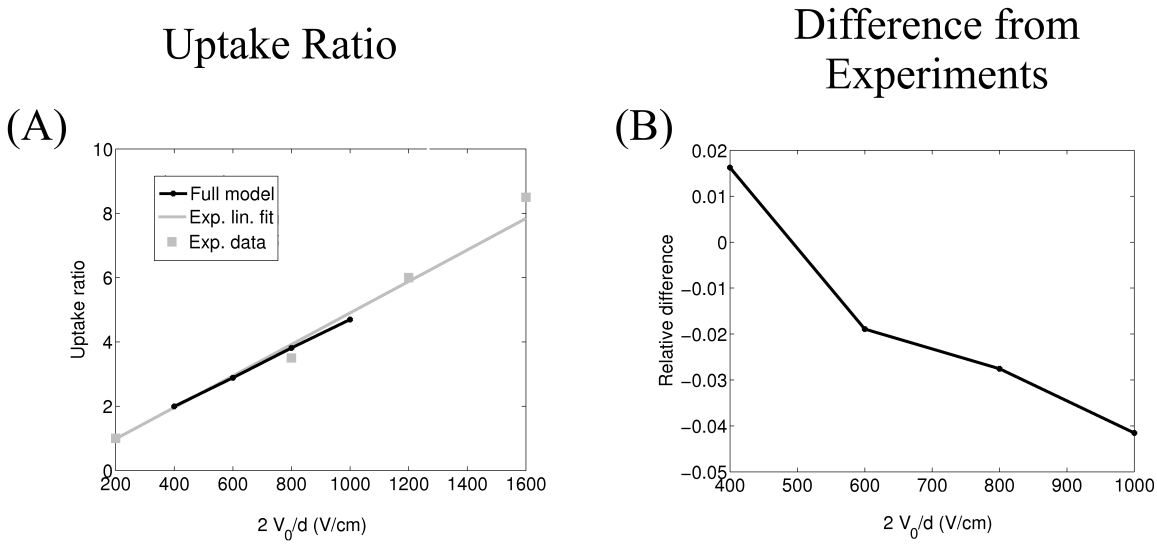

FIGURE 3.17: Tissue-wide UR: simulations versus experiments in literature. UR is reported after pores have resealed, and is relative to control muscle not treated by electric pulses, as explained in text. UR in experiments are reported using data from linear regression performed by the authors. Four different values of pulse strength are used, reported as the interelectrode voltage divided by the interelectrode distance: $2V_0/d$. (A) UR from simulations of the full asymptotic electroporating model compared to UR from experiments. Data shown for large range of pulse strengths in order to show experimental data that linear fit is based on. (B) Relative difference in UR between simulations and experiments.

the entire extracellular space (see Sec. 2.3.3 for introduction of c_o).

UR versus pulse strength is reported in Fig. 3.17A for both simulations of uptake from asymptotic electroporating fiber model and experiments performed by Grafstrom et al. In both model and experiments the UR is nearly a linear function of field strength. The linear correlation coefficients from fitting the curves in Fig. 3.17A to lines, for model and experiments, are 1 and 0.98 respectively. The slope of the model UR is 8% smaller than the slope of the experimental UR. For pulse strengths greater than 473 V/cm the model underpredicts UR observed in experiments, but the magnitude of the relative difference in UR is never greater than 5% between model and experiments.

3.3.3 Interfiber Distance

In all other simulations presented in this work, an interfiber distance of 1 μm was used, as specified in Table 2.3. While it is a property of muscle that fibers are closely packed, not all fibers in the tissue will have the same interfiber distance, contrary to the periodic fiber structure assumed in the simulations. Therefore, the effect of increasing the interfiber distance, and thus the boundary R_b around each fiber, is examined. Focus is placed on the effect changing interfiber distance has on the role of the longitudinal AF, and the mechanisms involved therein. Results are shown for a fiber close to the electrodes, 0.48 mm from the center of the needles, as in Chapters 3.1 and 3.2.1.

Fig. 3.18 compares the temporal evolution of circumferential average pore density ($\overline{N_{ep}}$) using three different values of interfiber distance. Fig. 3.18A reveals that increasing interfiber distance only slightly affects the circumferential average pore density for most of the fiber length. More specifically, the effect is smaller for $|z| < 6$ mm, or the region where the the transverse currents are the predominate source of membrane charging and electroporation. Fig. 3.18B offers a zoomed in view of $\overline{N_{ep}}$ near $z = 6$ mm. In this view, there are two observations of interest. First, for all z positions at t=4.5 μs, and for $|z| < 6$ mm at t=100 μs, the greater the interfiber distance the greater the pore density. The charging of the membrane via transverse currents is the responsible for this trend, given these currents dominate under these criteria.

The mechanism is best understood in a passive fiber, which isolates the membrane charging as interfiber distance is changed. Fig. 3.19A reveals that in a passive fiber on the time scale of transverse charging, the intracellular and extracellular fields are virtually zero due to the large resistance of the membrane, as expected. Increasing interfiber distance results in nearly no change in intracellular potential (between -

25 and 25 μm), yet results in larger deviation of the total extracellular potential from the primary potential (outside ± 25 μm), as shown in Fig. 3.19B. This larger extracellular deviation for larger interfiber distances is from the secondary potential having more space to develop. The further apart the fibers are, the further away that the current will start to bend in the angular direction φ around the fiber in response to the highly resistive membrane. It is this larger deflection in extracellular current that leads to larger deviations in secondary extracellular potential, resulting in larger magnitude of transmembrane potential shown in Fig. 3.20. Note that $|\Phi_m|$ is affected by interfiber distance on the proximal and distal sides of the fiber, but is not affected by interfiber distance where no charging occurs at $\pm\pi/2$. Ultimately, larger interfiber distance leads to larger magnitude of transmembrane potential from transverse charging, which leads to the greater pore density seen in Fig. 3.18 at 4.5 μs, and at 100 μs for $|z| < 6$ mm. Note that there is a limit to this generalization, where once fibers are far enough from each other, increasing the interfiber distance will not increase transmembrane potential from transverse charging.

The second observation in Fig. 3.18 is that, for $|z| > 6$ mm at t=100 μs, the greater the interfiber distance the smaller the pore density, which is exactly reversed from the aforementioned pattern observed for $|z| < 6$ mm at 100 μs, and for all z at 4.5 μs. Here, for $|z| > 6$ mm, charging via the longitudinal AF dominates creation of pores. Thus, to understand the relationship between interfiber distance and creation of pores in this region, the longitudinal problem is analyzed. Analysis begins with the homogenized equation in Appendix B for extracellular space: Eq. B.14. Eq. A.8 is substituted for circumferential average primary potential $\partial\overline{\Psi}/\partial\rho$, it is expressed in

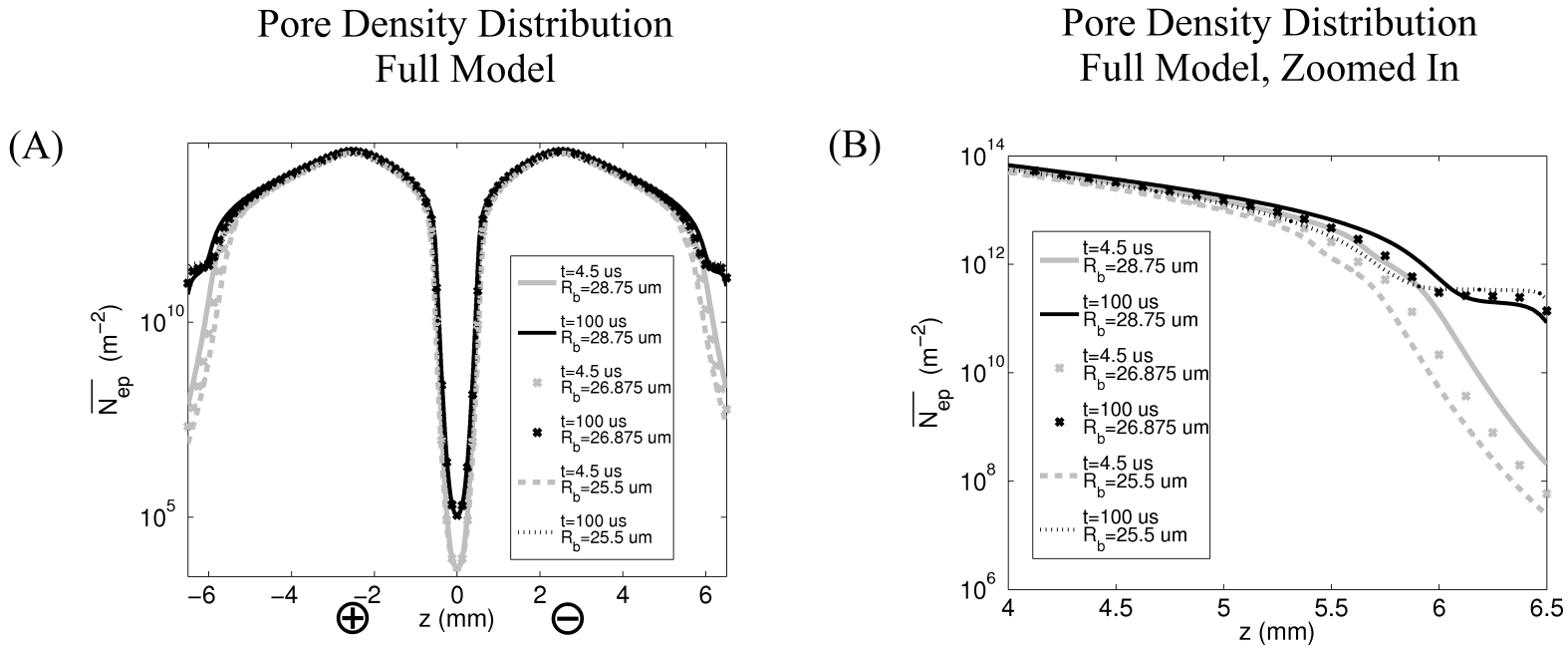

FIGURE 3.18: Longitudinal distribution of circumferential average pore density ($\overline{N_{ep}}$) along the entire length of the electroporating fiber: effect of interfiber distance. Results are from the full model (full transverse and longitudinal problem). Positions of anode and cathode are marked with $\oplus$ and $\ominus$, respectively. (A) Longitudinal distribution of circumferential average pore density along fiber, at 4.5 and 100 μs. Pore density distribution is shown for three different values of interfiber distance: 1 μm ($R_b = 25.5$ μm), 3.75 μm ($R_b = 26.875$ μm), and 7.5 um ($R_b = 28.75$ μm). (B) Same results as in panel A, but zoomed in near $z = 6$ mm, where the longitudinal AF has the largest effect on creation of pores between 4.5 and 100 us.

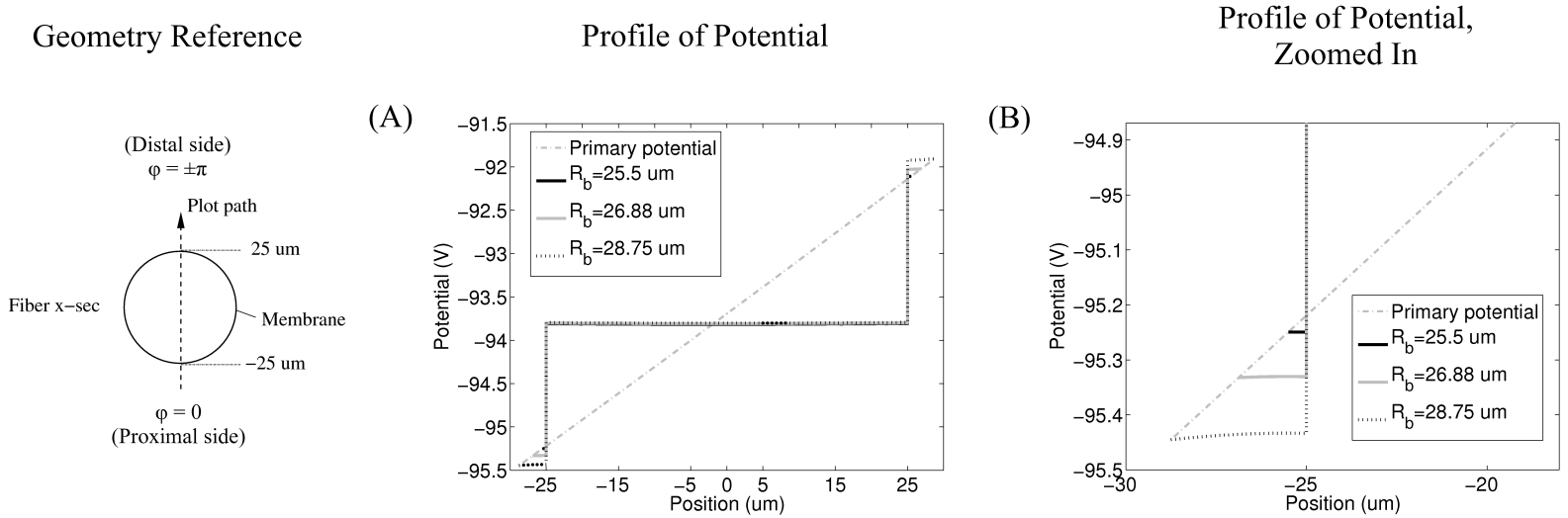

FIGURE 3.19: Total potential V_i and V_e profile on time scale of transverse membrane charging for passive fiber: effect of interfiber distance. Results are from the full model (full transverse and longitudinal problem). The primary potential Ψ is also shown. (A) Profiles are taken at $z = 5$ mm and at $t = 4.5$ μs for three different values of interfiber distance: 1 μm ($R_b = 25.5$ μm), 3.75 μm ($R_b = 26.875$ μm), and 7.5 um ($R_b = 28.75$ μm). (B) Same results as in panel A, but zoomed in on the intracellular and extracellular space near the membrane.

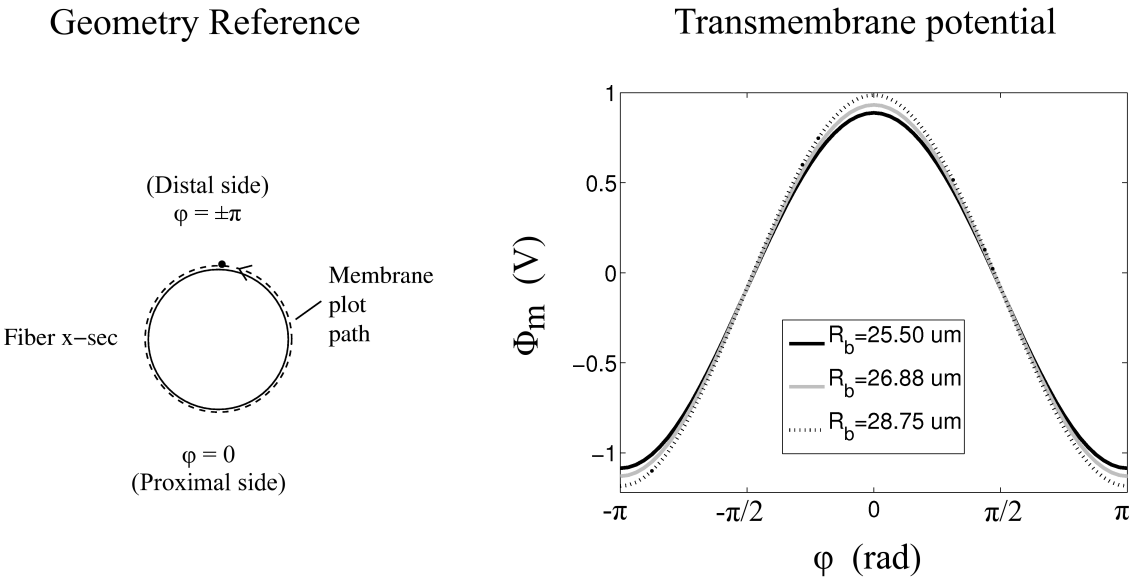

FIGURE 3.20: Transmembrane potential Φ_m on time scale of transverse membrane charging for passive fiber: effect of interfiber distance. Results are from the full model (full transverse and longitudinal problem), and are taken at $z = 5$ mm for three different values of interfiber distance: 1 μm ($R_b = 25.5$ μm), 3.75 μm ($R_b = 26.875$ μm), and 7.5 um ($R_b = 28.75$ μm). Profiles are shown at $t = 0.45$ μs rather than the typical 4.5 μs to ensure longitudinal charging has no effect on transmembrane potential, thus isolating the effects from transverse charging.

dimensional form, and both sides of the equation are multiplied by πa. The result is

$$\underbrace{2\pi a \Delta z C_m \frac{\partial f_m}{\partial t}}_{\text{I}} = -\underbrace{2\pi a \Delta z \overline{I_m}}_{\text{II}} + \underbrace{\sigma_e \pi a^2 \left(\left.\frac{\partial \langle \Psi \rangle}{\partial z}\right|_{z+\Delta z} - \left.\frac{\partial \langle \Psi \rangle}{\partial z}\right|_{z} \right)}_{\text{III}} - \underbrace{\sigma_e \pi (R_b^2 - a^2) \left(\left.\frac{\partial f_e}{\partial z}\right|_{z+\Delta z} - \left.\frac{\partial f_e}{\partial z}\right|_{z} \right)}_{\text{IV}}. \tag{3.7}$$

Each term in Eq. 3.7 is expressed as an average current density multiplied by the cross-sectional area normal to the flow of current, e.g., the average secondary longitudinal current multiplied by the transverse cross-sectional area of extracellular space: $(\sigma_e \partial f_e / \partial z|_z)$ * $\{\pi(R_b^2 - a^2)\}$. The resulting units of each term are amperes, so the charging of the membrane can now be understood intuitively. Reading terms

from left to right in Eq. 3.7, the capacitive current charging the membrane (group I) is reduced by the average current crossing the membrane (group II), increased by the difference in longitudinal current from primary potential (group III), and decreased by the difference in longitudinal extracellular current from secondary potential (group IV). Increasing interfiber distance, and thus R_b, increases the charge suppression effect from terms in group IV ($\partial^2 f_e/\partial z^2$ is same sign as $\partial^2 \langle \Psi \rangle / \partial z^2$).

Dividing both sides of Eq. 3.7 by $2\pi a \Delta z$ and letting $\Delta z \to 0$ more clearly shows the link to the longitudinal AF,

$$\underbrace{C_m \frac{\partial f_m}{\partial t}}_{\text{I}} = -\underbrace{\overline{I_m}}_{\text{II}} + \underbrace{\frac{\sigma_e a}{2} \frac{\partial^2 \langle \Psi \rangle}{\partial z^2}}_{\text{III}} - \underbrace{\frac{\sigma_e (R_b^2 - a^2)}{2a} \frac{\partial^2 f_e}{\partial z^2}}_{\text{IV}}. \tag{3.8}$$

Now, reading terms from left to right, the capacitive current density charging the membrane (term I) is reduced by the average current density across the membrane (term II), increased by the longitudinal AF (term III), and reduced by longitudinal extracellular diffusion from secondary potential (term IV). Increasing interfiber distance increases R_b, and thus, increases the suppression effect that the diffusion term (IV) has on the longitudinal AF term (III).

Finally, this effect observed in the extracellular space is also observed in the complete equation for the longitudinal problem. Dividing Eq. 2.15 by $(1 + 1/(\gamma\mu))$ and solving for the membrane charging term yields the cable equation,

$$C_m \frac{\partial f_m}{\partial t} = -\overline{I_m} + \underbrace{\frac{\sigma_e a(\gamma + 1)}{2(\gamma\mu + 1)}}_{\text{I}} \frac{\partial^2 \langle \Psi \rangle}{\partial z^2} + \underbrace{\frac{\sigma_i a \gamma \mu}{2(1 + \gamma\mu)}}_{\text{II}} \frac{\partial^2 f_m}{\partial z^2}, \tag{3.9}$$

where $\gamma = (R_b^2 - a^2)/a^2$ and $\mu = \sigma_e/\sigma_i$. Figure 3.21 illustrates the relationship between increasing R_b and the coefficients I and II in Eq. 3.9. Increasing interfiber distance, and consequently boundary radius R_b, decreases the coefficient of the longitudinal AF while increasing the coefficient of the diffusion term. Therefore,

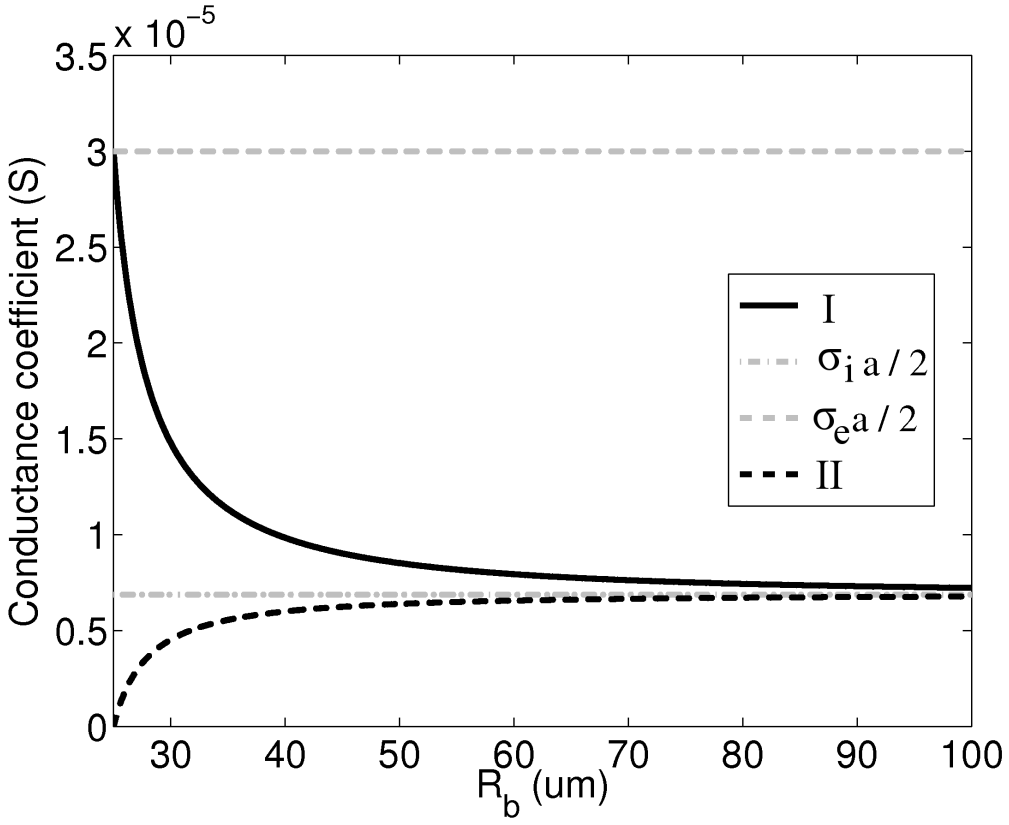

FIGURE 3.21: Conductance coefficient in longitudinal problem: effect of interfiber distance. The conductance coefficients I and II from Eq. 3.9 are shown as a function of the extracellular boundary radius R_b. $R_b = 25$ μm is equivalent to zero interfiber distance, and is increased to $R_b = 100$ μm, which is equivalent to 150 μm interfiber distance. Small and large extreme values of I and II are shown in the figure as $\sigma_i a/2$ and $\sigma_e a/2$, respectively.

increasing interfiber distance stifles charging of the membrane via the longitudinal AF, and amplifies the effect of diffusion term, which opposes any membrane charging from the AF ($\partial^2 f_m/\partial z^2$ is opposite sign of $\partial^2 \langle \Psi \rangle / \partial z^2$). Thus, the manner in which both terms I and II change with increasing R_b results in smaller pore density observed in Fig. 3.18 for $|z| > 6$ mm at $t = 100$ μs.

The relative effect of the longitudinal AF on molecular uptake, as interfiber distance is varied, is shown in Fig. 3.22. For $|z| < 6$ mm in all panels, where transverse currents dominate charging of the membrane, there is no difference in uptake from

including or excluding the longitudinal AF. This behavior is a result of the strong transverse currents that charge and electroporate the membrane much faster than longitudinal currents, altering $\overline{I_m}$ to counteract charging from terms I and II, as explained in Sec. 3.2. For $|z| > 6$ mm, charging via transverse current is not as strong, and $\overline{I_m}$ does not counteract charging from terms I and II (Sec. 3.2), and the longitudinal AF matters. Including the longitudinal AF has the largest effect for dense fibers in Fig. 3.22A, whereas it has the smallest effect for sparse fibers in Fig. 3.22C. In this region, charging of the membrane is dominated by the longitudinal AF, and given that pore density is suppressed as interfiber distance is increased, the relative contribution of the longitudinal AF to molecular uptake decreases as well. Furthermore, the steady state value of intracellular concentration ($c_{i,ss}$) increases with interfiber distance, as shown by Eq. 2.58, which further diminishes the additional uptake from including the longitudinal AF, relative to the uptake in the rest of the fiber. At the entire tissue level, relative increase in uptake due to the longitudinal AF ranges from 3.95% for the case of densely packed fibers ($R_b = 25.5$ μm), 0.823% for semi-dense packed fibers ($R_b = 26.88$ μm), and 0.267% for sparsely packed fibers ($R_b = 28.75$ μm).

A final observation in Fig. 3.22 is that for $|z| < 6$ mm, the length of fiber that reaches $c_{i,ss}$ decreases as interfiber distance is increased. This behavior is expected from reviewing Fig. 3.18 and the equations for molecular uptake (Eq. 2.57). Fig. 3.18 shows that for $|z| < 6$ mm, as interfiber distance is increased, there is only a small increase in pore density. This small increase is not enough to account for the increase in time scale of uptake as interfiber distance is increased. Given that molecules are conserved between intracellular and extracellular space (no-flux condition on boundary R_b), c_e can be expressed in terms of c_i,

$$c_e = \frac{c_o(R_b^2 - a^2) - c_i a^2}{(R_b^2 - a^2)}, \tag{3.10}$$

where c_o is the initial extracellular concentration of molecules. This relationship is used in Eq. 2.57a to find the time scale τ_{ss} for c_i to reach $c_{i,ss}$. The result shows that τ_{ss} depends on R_b,

$$\tau_{ss} \propto \left(1 - \frac{a^2}{R_b^2}\right). \tag{3.11}$$

Thus, as interfiber distance is increased, less of the fiber will reach steady state intracellular concentration due to the longer time scale of uptake.

3.3.4 Nonuniform Tissue Conductivities Due to Electroporation

A major assumption used in computing primary potential Ψ, and derivatives of Ψ for the activating functions used in the transverse and longitudinal problems (Secs. 2.1.2 and 2.1.3), is that the tissue conductivities do not change in response to electroporation. The validity of this assumption is tested by numerically solving for primary potential Ψ using two versions of a finite element model: one which has spatially uniform tissue conductivities in the tissue space, and another that has nonuniform tissue conductivities due to electroporation. Model and methods used in this analysis, and region of tissue with elevated conductivities (Fig. 2.17), are given in Sec 2.4. In analyzing the results, first, contour plots of primary potential Ψ are shown in Fig. 3.23 for the case of uniform and nonuniform tissue conductivities. Both models produce similar distributions of primary potential, except the drop in potential occurs over a larger distance moving radially out from the electrodes in the nonuniform conductivities case. This trend is especially noticeable in the z-dimension along the length of the fibers. This behavior is expected, given the increased conductivity around the electrodes moderates the magnitude of the field in the vicinity of the electrodes. This trend is also seen in the transverse AF $\partial\widetilde{\Psi}/\partial\rho$, which is based on the y-component of the electric field. Figs. 3.24A-3.24B show that in the vicinity of the cathode, the AF for nonuniform tissue conductivities is slightly smaller in magnitude

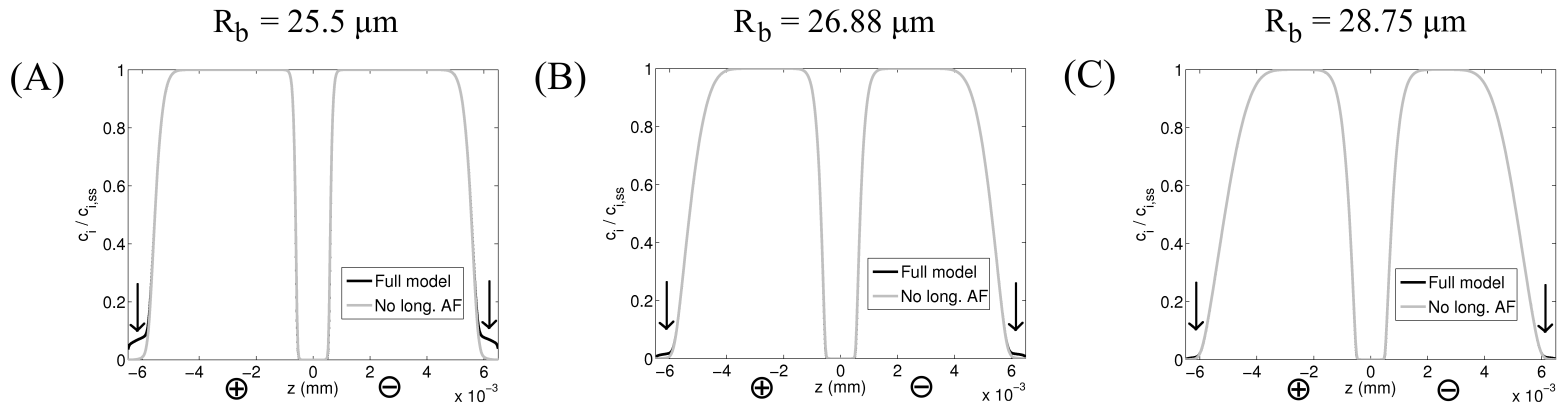

FIGURE 3.22: Role of longitudinal AF in molecular uptake: effect of interfiber distance. Concentration is reported relative to theoretical steady state intracellular concentration $c_{i,ss}$ in the two-compartment model (Eq. 2.58 in Sec. 2.3.3). Differences between including and excluding the longitudinal AF are shown with arrows, and positions of anode and cathode are marked with $\oplus$ and $\ominus$, respectively. For all panels, longitudinal distribution of intracellular molecular concentration $c_i/c_{i,ss}$ is shown, after all the pores have resealed, from including and excluding the longitudinal AF. Results are shown for three different values of extracellular boundary radius: (A) $R_b = 25.5$ μm, (B) $R_b = 26.88$ μm, and (C) $R_b = 28.75$ μm.

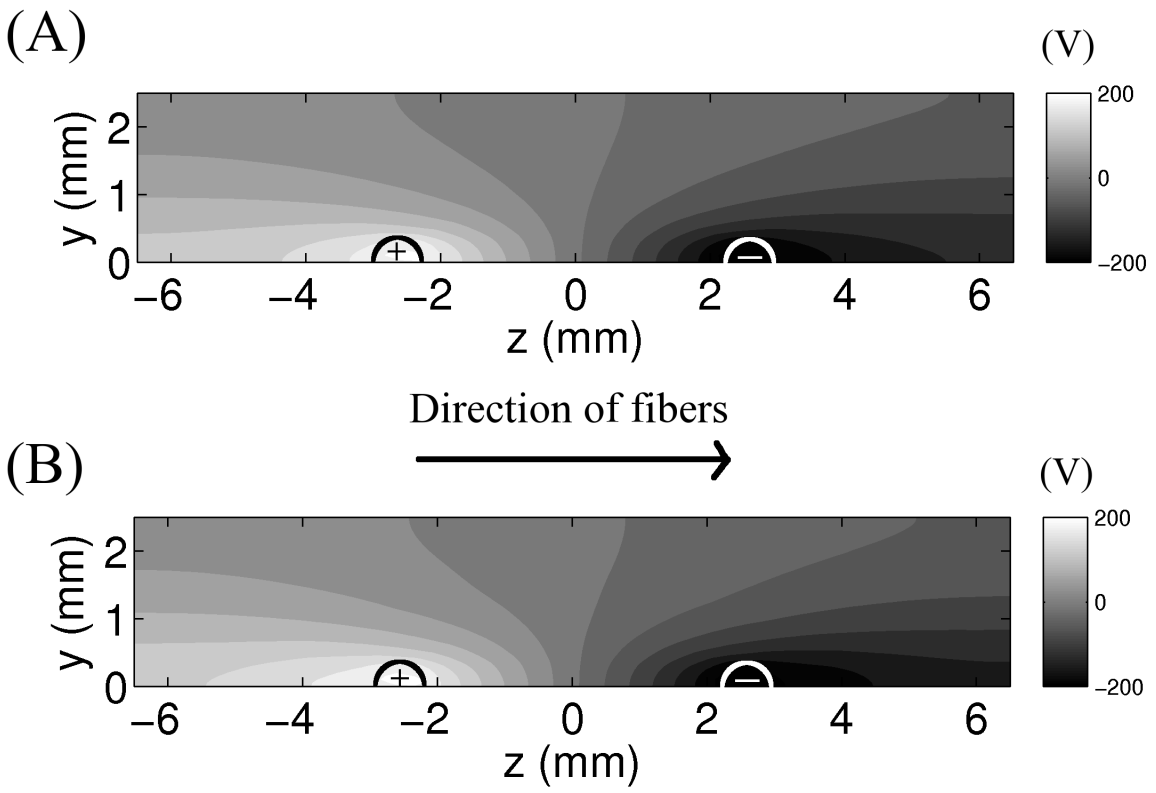

FIGURE 3.23: Contour plot of numerical primary potential Ψ, uniform versus nonuniform tissue conductivities. Only the top half of the tissue is shown, given symmetry about the line $y = 0$. Positions of anode and cathode are marked in the tissue space by plus and minus symbols enclosed by semicircles, respectively. Contour plots are shown for the uniform tissue conductivities model (A) and nonuniform tissue conductivities model (B).

than the uniform case. This observation is most pronounced for the fiber close to the electrodes, as there is virtually no difference between the AFs for a fiber far from the electrodes.

While the increased conductivity does decrease magnitude of field in the direct vicinity of the electrodes, it also keeps the field from decaying as much as in the uniform tissue conductivities case. Thus, the field retains a larger value further away from the electrodes where the tissue conductivity never changed. This effect is seen for the transverse AF $\partial\tilde{\Psi}/\partial\rho$ in Figs. 3.24A, 3.24C, and 3.24D, where the tissue with

nonuniform conductivities has larger magnitude of AF further from the electrodes near $z = \pm 6$ mm. This process results in smaller field magnitudes near the electrodes and larger field magnitudes further away.

Similar trends are seen in the longitudinal AF, $\partial^2 \langle \Psi \rangle / \partial z^2$, as shown in Fig. 3.25. In Fig. 3.25A, it is clear that the longitudinal AF computed using nonuniform tissue conductivities is smaller in the immediate vicinity of the electrodes at ± 2.5 mm, which was also observed in Fig. 3.24B for the transverse AF. Near the end of the fiber in Fig. 3.25B, the longitudinal AF is larger in magnitude for nonuniform tissue conductivities than uniform, which was also observed in Fig. 3.24C for the transverse AF. For a fiber far from the electrodes in Fig. 3.25C, the numerical error is nearly too great to determine qualitative trends. However, in general, the AF from the uniform tissue conductivities is smaller in magnitude than for the uniform case.

Figs. 3.24 and 3.25 reveal changes in the AFs from including or excluding changes in tissue conductivities due to electroporation, yet these AFs operate on different time scales in the actual asymptotic fiber model of electroporation. Thus, it is not immediately apparent how including or excluding changes in tissue conductivity affect molecular uptake in the model. To answer this question, the numerical transverse and longitudinal AFs are used in the asymptotic fiber model, and results of molecular uptake are shown in Fig. 3.26. Fig. 3.26A shows the effects of including versus excluding the longitudinal AF for tissue with uniform tissue conductivities. Similar to Figs. 3.4C and 3.9C that use the analytical AFs, including the longitudinal AF enhances uptake more for a fiber far from the electrodes compared to a fiber close to the electrodes. This same trend is seen in Fig. 3.26B using the AFs from tissue with nonuniform conductivities. Thus, in general, trends observed in molecular uptake using the analytical AFs (Figs. 3.4 and 3.9) are captured using the numerical AFs.

These molecular uptake results are understood in terms of the transverse and longitudinal AFs in Figs. 3.24 and 3.25. First, the fiber close to the electrodes is

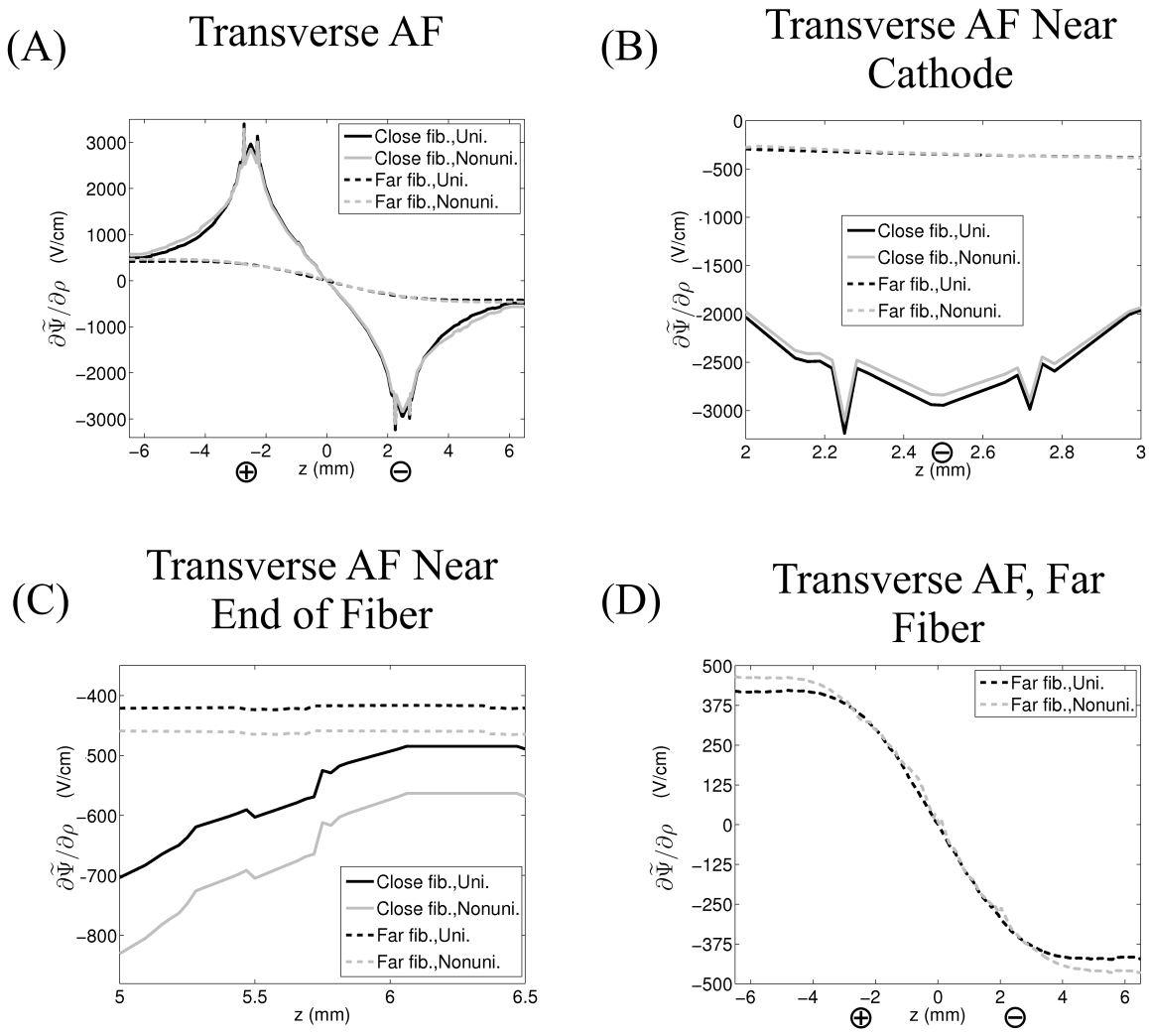

FIGURE 3.24: Numerical transverse AF, $\partial\widetilde{\Psi}/\partial\rho$, uniform versus nonuniform tissue conductivities. Positions of anode and cathode are marked with $\oplus$ and $\ominus$, respectively. Numerical error is seen in the data, especially in the vicinity of the electrodes at ± 2.5 mm. AFs for the non-electroporating (black line) and electroporating (light grey line) tissue are shown for the most proximal side of a fiber close (solid line, $b = 0.48$ mm) and far from the electrodes (dashed line, $b = 1.44$ mm). Transverse AF is shown for the entire fiber close and far from electrodes (A), in the vicinity of the cathode (B), near the end of the fiber (C), and for the far fiber only (D).

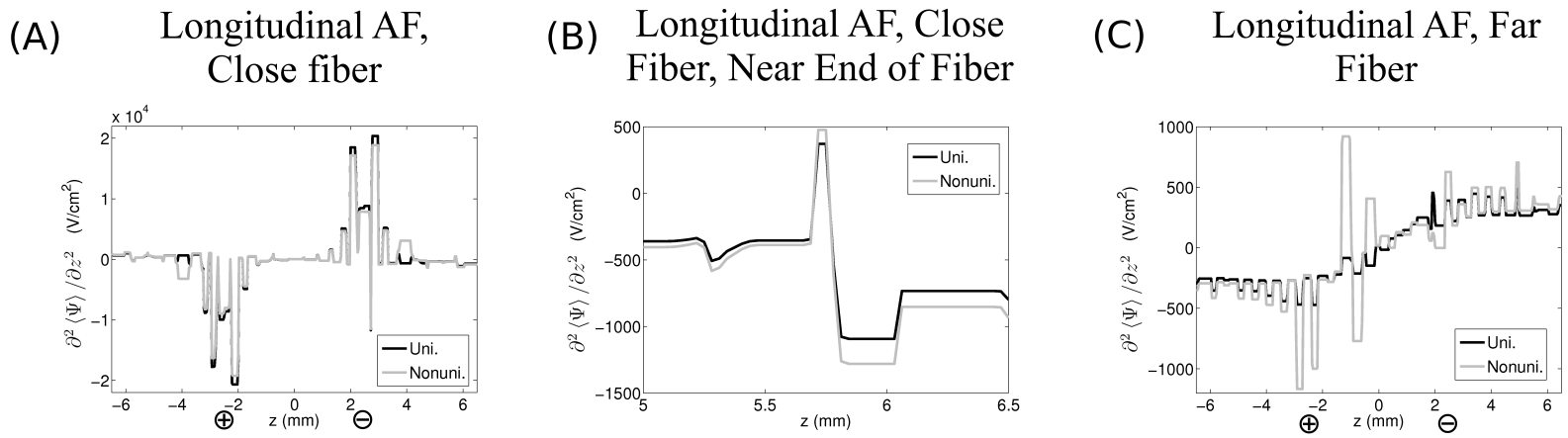

FIGURE 3.25: Numerical longitudinal AF, $\partial^2 \langle \Psi \rangle / \partial z^2$, uniform versus nonuniform tissue conductivities. Positions of anode and cathode are marked with $\oplus$ and $\ominus$, respectively. Numerical error is especially pronounced in the second derivative. AFs for non-electroporating (black line) and electroporating (light grey line) tissue are shown. AFs are shown for a fiber close ($b = 0.48$ mm) to the electrodes over the entire fiber (A) and near the end of the fiber (B). Finally, the AF is shown for a fiber far from the electrodes ($b = 1.44$ mm) over the entire fiber (C).

considered. As discussed in Secs. 3.1 and 3.2.1, molecular uptake reaches the steady state intracellular concentration for $|z| < 6$ mm regardless of whether of not the longitudinal AF is included. Thus, enhanced uptake from the longitudinal AF only occurs near the ends of the fiber for $|z| > 6$ mm. For $|z| > 6$ mm, the magnitude of the longitudinal AF is larger for tissue with nonuniform conductivities than for uniform tissue conductivities, as shown in Fig. 3.25B. Thus, it is expected that the longitudinal AF has a larger impact on molecular uptake in tissue with nonuniform conductivities. However, the exact opposite is observed, if the total uptake over the entire fiber is calculated from Fig. 3.26. For nonuniform tissue conductivities there is only 0.000119% change in total uptake by including the longitudinal AF, compared to 0.0230% for tissue with uniform conductivities. This apparent discrepancy is resolved by observing that the transverse AF also has a larger magnitude in the range $|z| > 6$ mm for nonuniform tissue conductivities in Fig. 3.24C. Thus, the larger transverse AF from nonuniform tissue conductivities operates on the short time scale of microseconds, charges the membrane, causes extensive electroporation, which suppresses charging of the membrane via the longitudinal AF. In other words, if small changes are made in both transverse and longitudinal AFs, the transverse AF prevails in terms of altering molecular uptake. The mechanism is manifested by larger uptake near $z = \pm 6$ mm in tissue with nonuniform conductivities (Fig. 3.26D), compared to tissue with uniform conductivities (Fig. 3.26C), and uptake in Fig. 3.26D is not affected by the longitudinal AF.

A very similar mechanism is observed for the fiber far from the electrodes, except that this mechanism operates over a majority of the fiber, not just for $|z| > 6$ mm. Fig. 3.24D shows that for a majority of the fiber length, the magnitude of transverse AF for nonuniform tissue conductivities is larger than the uniform case. Even though Fig. 3.25C reveals that the magnitude of the longitudinal AF for nonuniform tissue conductivities is larger than the uniform case, the effect is once again suppressed by

the larger transverse AF. Ultimately, including the longitudinal AF only enhances total uptake in the fiber by 21.5% for nonuniform tissue conductivities, compared to 93.2% for uniform tissue conductivities.

Now, the contribution of the longitudinal AF for uniform vs. nonuniform tissue conductivities is considered over the entire tissue. While the effect of the longitudinal AF on molecular uptake differs by two orders of magnitude between nonuniform and uniform tissue conductivities (0.000119% to 0.0230%) for a fiber close to the electrodes, in both cases the effect of the longitudinal AF is very small. For a fiber far from the electrodes, the contribution of the longitudinal AF differs by a factor of 4.3 between nonuniform and uniform tissue conductivities (21.5% to 93.2%), and the effect in both cases is substantial. However, the total uptake in the fiber far from electrodes compared to the close fiber is only 10.9% for uniform tissue conductivities, and 25.7% for nonuniform tissue conductivities. Thus, at the tissue-wide level, it is not expected that the effect of including the longitudinal AF on molecular uptake will be as large as these percentages, nor should there be as much difference between uniform and nonuniform tissue conductivities. Indeed, over the entire tissue, the enhancement in molecular uptake from including the longitudinal AF is only 3.77% for uniform tissue conductivities, and 3.51% for nonuniform tissue conductivities. Thus, in terms of measuring the effect of the longitudinal AF on molecular uptake, the difference between uniform and nonuniform tissue conductivities is only around 7%.

In terms of measuring total uptake in the entire tissue, results are qualitatively the same as those in Fig. 3.26, which show that uptake in the nonuniform tissue conductivities model is larger than the uniform model. Indeed, over the entire tissue, the nonuniform tissue conductivities model predicts 8.3% more molecular uptake than the uniform tissue conductivities model. This increase is expected, given that in the nonuniform tissue conductivities model both the transverse and longitudinal

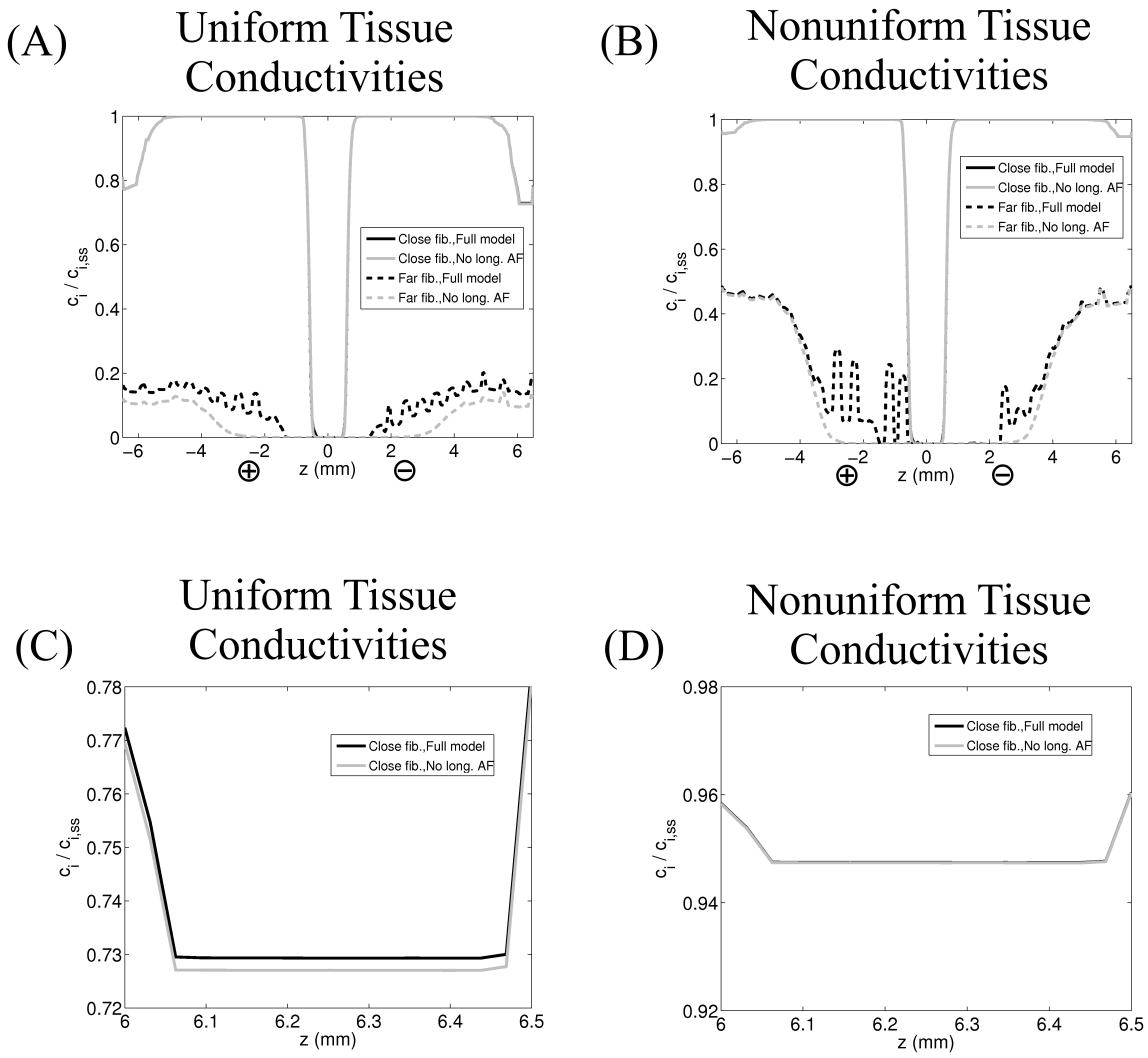

FIGURE 3.26: Longitudinal distribution of molecular uptake: uniform versus nonuniform tissue conductivities. Positions of anode and cathode are marked with $\oplus$ and $\ominus$, respectively. Uptake is reported after all the pores have resealed, and measured as intracellular concentration reported relative to theoretical steady state intracellular concentration in the two-compartment model (Eq. 2.58 in Sec. 2.3.3). (A) Longitudinal distribution of molecular uptake using numerical AFs that do not take into account changes in tissue conductivities due to electroporation. Uptake is shown for simulating the full model (full transverse and longitudinal problem) versus removing the longitudinal AF (full transverse problem, reducing longitudinal problem to Eq. 3.1) for fibers close and far from the electrodes. (B) Same data as panel A, except uptake is reported using numerical AFs that do take into account changes in tissue conductivity due to electroporation. (C) Same as panel A, but focused on the the end of the close fiber near $z = 6$ mm. (D) Same as panel A, but focused on the the end of the close fiber near $z = 6$ mm.

AFs have larger magnitudes in the regions of tissue where steady state intracellular concentration has not been reached (Figs. 3.24C, 3.25B, 3.26A, and 3.26B).

Finally, although the AFs from uniform and nonuniform tissue conductivities behave qualitatively as expected, where magnitude is smaller in the immediate vicinity of the electrodes and larger at more distal regions of tissue, it is worth comparing the analytical and numerical AFs to analyze the numerical error. Fig. 3.27 compares the analytical AFs derived from analytical solution of needles discussed in Sec. 2.2[75] to the numerical AFs calculated from the numerical solution from uniform tissue conductivities discussed in Sec. 2.4. The numerical transverse AF in Figs. 3.27A and 3.27B are fairly close approximations to the analytical AFs, yet there is some error. The correlation coefficient for both close and far fibers is 0.996, yet the relative root mean square error is 9.16% for the close fiber, and 17.7% for the far fiber. Error is especially pronounced in the longitudinal AF in Figs. 3.27C and 3.27D. For the close fiber, the correlation coefficient and relative root mean square error for the close fiber are 0.760 and 214%, and for the far fiber they are 0.947 and 45.2%. Large error near the ends of the fiber may be a result of computing potential in a finite size of tissue, whereas the analytical solution is computed for an infinitely large region of tissue. As the size of the tissue is increased, the numerical error near the ends does tend to decrease, yet error under the electrodes persists without much change (result not shown). In the case of the longitudinal AF, error under the electrodes increases with larger tissue size (result not shown).

The effect of numerical error on uptake is examined in Fig. 3.28. The correlation coefficient, relative root mean square error, and relative error in total uptake along the fiber close to the electrodes in panel A are 0.770, 32.3%, 15.5%. For the far fiber in panel B, these same metrics are 0.523, 115%, and 92.8%. The error in the AFs for the fiber close to electrodes is subdued in the uptake, because much of the error occurs under the electrodes where concentration reaches steady state in both models.

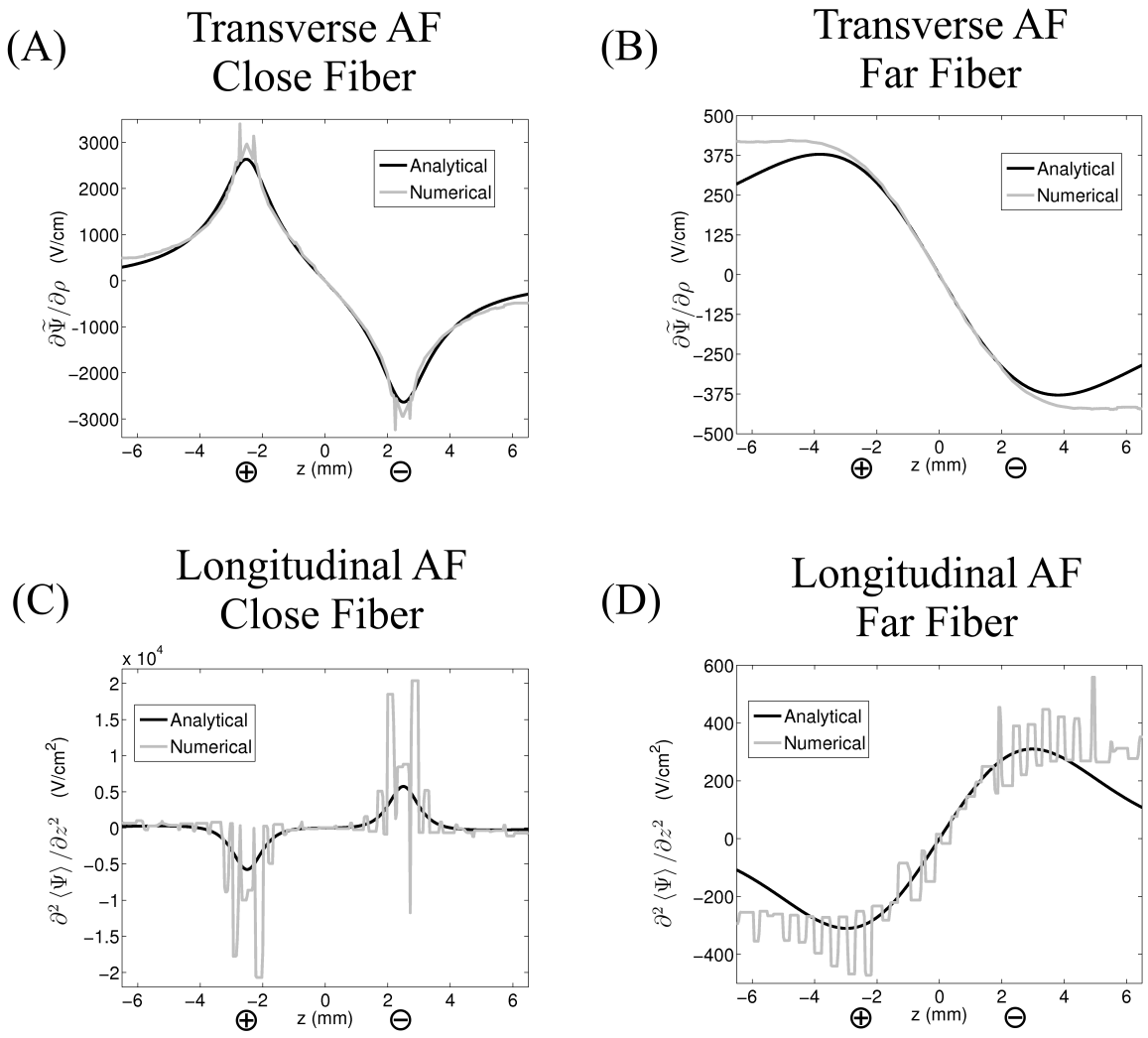

FIGURE 3.27: Transverse and longitudinal AFs, analytical versus numerical. Numerical AFs are calculated from assuming uniform tissue conductivities, i.e., non-electroporating tissue. Positions of anode and cathode are marked with $\oplus$ and $\ominus$, respectively. (A) Transverse AFs for the most proximal side of a fiber close to the electrodes ($b = 0.48$ mm). (B) Transverse AFs for the most proximal side of a fiber far from the electrodes ($b = 1.44$ mm). (C) Longitudinal AFs for a fiber close to the electrodes ($b = 0.48$ mm). (D) Longitudinal AFs for a fiber far from the electrodes ($b = 1.44$ mm).

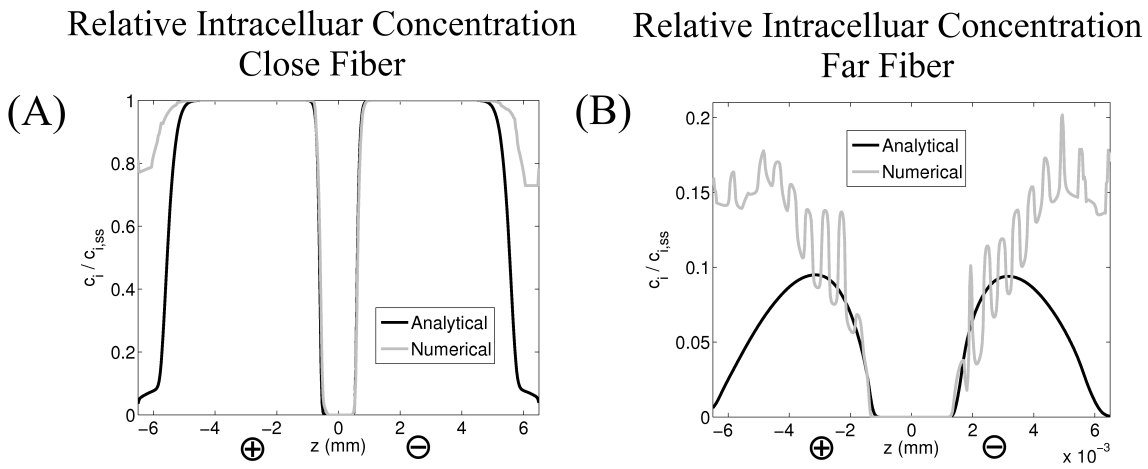

FIGURE 3.28: Longitudinal distribution of molecular uptake along electroporating fiber: analytical versus numerical AFs. Concentration is reported relative to theoretical steady state intracellular concentration $c_{i,ss}$ in the two-compartment model (Eq. 2.58 in Sec. 2.3.3). Positions of anode and cathode are marked with $\oplus$ and $\ominus$, respectively. Longitudinal distribution of intracellular molecular concentration, after all the pores have resealed, is shown for a close fiber ($b = 0.48$ mm) (A) and a far fiber ($b = 1.44$ mm) (B).

Furthermore, for the close fiber, given error is smaller for the transverse AF and that the transverse AF dominates uptake, the large error in longitudinal AF is not too important. In contrast, the fiber far from the electrodes does not reach steady state concentration anywhere along the fiber, and thus error in the AFs has a complete effect on error in uptake. Regardless, error in both close and far fibers is significant. Over the entire tissue, uptake using numerical AFs yields 1.3 times, or 30% more uptake than using analytical AFs.

4

Discussion

4.1 Accounting for Longitudinal and Transverse Effects in the Cable Equation

The connection between the longitudinal component of the electric field E_l generated from the electrodes, and the transmembrane potential of a muscle or nerve fiber, was made by McNeal[129] and Rattay.[60] These studies introduced into the classic cable equation the derivative of E_l, $-\partial E_l/\partial z$ as the forcing function, also known as the longitudinal AF. The longitudinal AF is traditionally expressed as the second derivative of the primary potential: $\partial^2\Psi/\partial z^2$. This dissertation work is in a unique position to assess the theoretical validity of this approach applied to an electroporating fiber, because we have rigorously derived our model from the 3D BVP. Equation 2.15, which governs the LO mean transmembrane potential, indeed has the form of a cable equation with the AF as proposed by McNeal and Rattay. Equation 2.15 uses as the AF the second derivative of the primary potential averaged over the fiber's cross-section, $\partial^2 \langle\Psi\rangle /\partial z^2$, rather than the primary potential evaluated on the fiber's axis, $\partial^2\Psi/\partial z^2$. However, in practice, this distinction is immaterial: the relative root-mean-square difference between these two AFs for a fiber 0.18 mm from the surface

of the electrodes (6/10 of the radius of needles) is about 0.5%, which results in only a 6.14x10^{-4}% difference in root-mean-square uptake in the entire fiber. Thus, this work validates the classical method of computing the fiber response to E_l by using the longitudinal AF in the cable equation.

Furthermore, this dissertation research introduces an additional term into the cable equation, $\overline{I_m}$, that accounts for the effect of the transverse component of the electric field E_t. The effect of E_t is accounted for in $\overline{I_m}$ indirectly. First, the effect of E_t on mean-free transmembrane potential ϕ_m in the transverse problem is seen in the transverse AF $\partial\widetilde{\Psi}/\partial\rho$ in Eqs. 2.13c and 2.13d. Second, $\overline{I_m}$ is computed in part from ϕ_m (Eqs. 2.17 and 2.28), as well as the pore density N_{ep} (Eq. 2.28), which is also computed in part from ϕ_m. Thus, there are two activating functions that are incorporated into cable equation of the longitudinal problem. The first is the traditional longitudinal AF, i.e., the term $\partial^2 \langle\Psi\rangle / \partial z^2$. The second is the transverse AF, i.e., $\partial\widetilde{\Psi}/\partial\rho$, which is accounted for by the presence of $\overline{I_m}$.

In the past, researchers have attempted to account for the effects of E_t by modifying the cable equation in various ways. Studies modeling passive fibers included a constant term, $-2aE_t$, in the right-hand side of the cable equation, where a is the fiber radius.[67,130] This term is compared to the term $\overline{I_m}$, and Figs. 3.5A and 3.10A confirms a nearly constant value for $\overline{I_m}$ in the case of the passive fiber. Undoubtedly, $|\overline{I_m}|$ would increase for pulses longer than 100 μs as the membrane charges and magnitude of transmembrane potential increases. However, a very different conclusion is drawn from analyzing the electroporating fiber. As show in Figs. 3.5B and 3.10B, $\overline{I_m}$ is a dynamic current that reaches magnitudes equal to or greater than the longitudinal AF term. Furthermore, this dynamic increase is different along the length of the fiber. For regions under the electrodes near $z = \pm 2.5$ mm, where electroporation drastically decreases the effective resistance of the membrane, $\overline{I_m}$ quickly reaches

magnitude on the order of longitudinal AF term. For regions of fiber further from the electrodes, where effective resistance of the membrane remains closer to passive value, $\overline{I_m}$ evolves in time more slowly. Thus, adding a time-independent term to the cable equation is not a suitable method of accounting for the effects from E_t in physiological processes like electroporation, where membrane conductance drastically increases.

Stimulation modeling studies by Wang et al. and Yu et al. have modified the cable equation by including the mean membrane current $\overline{I_m}$, which is the same modification in the cable equation of the asymptotic model.[68,131] The only discrepancy is how $\overline{I_m}$ is computed. In the asymptotic model, $\overline{I_m}$ is computed at all times by solving both the time-dependent transverse BVP and the cable equation. Yu et al. compute $\overline{I_m}$ from the steady-state solution of the transverse BVP, and subsequently, compute temporal changes in $\overline{I_m}$ from solving only the cable equation. Although the approach by Yu et al. is a simplification, results from simulating the asymptotic model indicate that it is a fairly well-suited simplification for an electroporating fiber. First, for a fiber close to the electrodes and longitudinal positions that have very large pore density, Fig. 3.5 indicates there is virtually no change in $\overline{I_m}$ between 4.5 and 100 μs. Thus, $\overline{I_m}$ does not need to be re-computed after the initial transverse polarization occurring within 4.5 μs. Second, for fibers close and far from the electrodes at longitudinal positions where pore density is smaller, Fig. 3.5 indicates there are temporal changes in $\overline{I_m}$ after 4.5 μs. However, for a fiber close to the electrodes, Figs. 3.7 and 3.8 reveals that at 4.5 μs, most of the current in the transverse direction is circumferential mean current, not mean-free. Thus, further charging and electroporating of the membrane after 4.5 μs is approximated well by only solving the 1D cable equation for changes in mean transmembrane potential. Indeed, for a fiber close to the electrodes at $b = 0.48$ mm with 800 V/cm pulse magnitude, there is only 1.89% difference in total uptake in the entire fiber by solving only the cable equation beyond 4.5 μs. For a fiber further

from the electrodes at $b = 1.14$ mm, solving for initial transverse polarization is not needed at all, given the effect of the longitudinal AF increases total fiber uptake by 2000% over transverse only model. Although the model proposed by Yu et al. is fairly well-suited for an electroporating fiber, it is absolutely critical to simulate the full transverse BVP before 4.5 μs for fibers close to the electrodes. Unlike nerve excitation, for fiber close to the electrodes, most of the nonlinear membrane dynamics of electroporation occur on the 4.5 μs time scale of transverse polarization.

4.2 Relative Importance of Longitudinal and Transverse AFs

The accuracy of using only the longitudinal AF has previously been investigated in modeling passive fibers, where the longitudinal AF has been shown to work well for larger electrode-fiber distances, but not for smaller distances.[67] In the latter case, effects of fiber polarization from E_t must also be considered. Simulations of an electroporating fiber confirm that the effects from longitudinal AF are more pronounced when the electrode-fiber distance is large. In Sec. 3.2.2 for pulse strength 800 V/cm and for a fiber far from electrodes at $b = 1.44$ mm, the total uptake within the entire fiber increases by nearly 2000% when the longitudinal AF is included. This drastic increase is significantly different to the 0.91% increase for a close fiber ($b = 0.48$) mm from the electrodes. However, relative importance of the longitudinal AF over the entire tissue cannot be judged on the single fiber level alone, given that uptake for a fiber far from the electrodes is very small compared to uptake for a fiber close to the electrodes. Ultimately, over the entire tissue, the longitudinal AF increases uptake by 3.95%. For electroporation, it is not enough to know the effect of the longitudinal AF at a single fiber; the amount of uptake that occurs in that fiber relative to fibers in the rest of the tissue also is a very important metric. This highlights the importance of simulating the entire tissue, which up until now has only been done with models of muscle tissue that do not include individual fiber geometry,[76,126] or

models that do include individual geometry but only for compact cells.[55,79]

Previous models have shown that a threshold value of the magnitude of electric field is an indicator of reversible electroporation, with decent comparison to experiments.[29,30] In Sec. 3.3.2 it was found that total tissue uptake could be predicted well using threshold field magnitude approach. However, the threshold field magnitude that provided the best fit to actual uptake simulations included not only the regions of tissue that attained steady state intracellular concentration, but also regions that attained at least 11.7% of the steady state intracellular concentration. Tissue uptake results in Fig. 3.11 show that the longitudinal AF is responsible for smaller uptake in part of the tissue. In fact, even though steady state intracellular concentration is not reached in these regions, excluding them results in total tissue uptake error of 3.95% for pulse strength of 800 V/cm, and at most 10% for pulse strength of 400 V/cm.

It is worth considering the practical significance of the longitudinal AF contributing at most 10% to molecular uptake in the entire tissue. Grafstrom et al. performed experiments on the gastrocnemius and soleus muscles of rats using very similar pulsing protocols as specified in the model in Table 2.3.[31] Among experiments on different rats, the relative standard deviation in molecular uptake ratio over the entire tissue was about 6%. Thus, in terms of reproducing experimental results, the maximum percent increase in uptake from including the longitudinal AF is on the same order as experimental variability, and by this measure is not very important to include in simulations of molecular uptake. However, it should also be noted that all other studies of electroporation-mediated uptake in muscle tissue do not take into account individual fiber geometry.[29,76] These studies base electroporation on field strength. From this perspective, it would be desirable to use the asymptotic electroporating fiber model, as it may more accurately measure the effect from the transverse component of the field, given that the transverse AF is actually calculated from 3D

cylindrical geometry. This topic is discussed in Sec. 4.3.2.

The ultimate practical comparison is to find the change in protein expression from delivering DNA by including or excluding the longitudinal AF. However, the results obtained in this work for delivery of a small molecule cannot be assumed to apply for large molecules such as DNA for many reasons, as discussed in Sec. 4.4.4. With that being made clear, it is worth noting that electrotransfer experiments in cell suspensions show that for every unit increase in μg / mL of DNA there is an amplified increase by as much as two-fold in expression, but the amplification factor may not be constant for all concentrations of DNA.[132,133] Even if uptake of DNA were added to the asymptotic electroporating fiber model, further research would need to be conducted to connect intracellular concentration of DNA to actual expression, which is the quantity measured in experiments and of the most importance in gene therapy.

Another practical consideration in evaluating the potential benefits of enhancing tissue-wide uptake from including the longitudinal AF is the spatial distribution of this enhancement in the tissue. For fibers close to the electrodes, the longitudinal AF enhances uptake only near the ends of the fibers, as shown in Fig. 3.11C. It is initially unclear if it is important to enhance uptake just near the ends of the fibers. Considering that on average there is a nucleus every 0.01 to 0.03 mm along the fiber, increasing the intracellular concentration over a length of fiber just 0.5 mm covers between 16 and 50 nuclei.[120] Once again, the results in this work cannot be linked directly to DNA uptake, but the positions of nuclei and how the spatial distribution of the increase in uptake due to longitudinal AF would be one of the practical considerations in modeling DNA uptake.

4.3 Model Variations: Effect on Uptake and Importance of Longitudinal AF

4.3.1 Orientation of Electrodes

It is clear that orienting the electrodes transverse to the direction of the fibers is more efficient than longitudinal orientation: doing so increases the uptake by 75%. A similar trend is found by Zupanic et al. in computer simulations of two electrodes in muscle tissue, where increase from orienting electrodes transversely results in a 20% increase in their objective function.[103] Their objective function took into account minimizing the volume of tissue that achieves irreversible electroporation, and maximizing the volume of tissue that achieves reversible electroporation, based on a field strength threshold approach. Reversible and irreversible electroporation field thresholds were determined from matching current calculated in model to current measured in experiments, similar to the procedure described in Sec. 2.4. While the asymptotic electroporating model does not account for irreversible electroporation, it does account for two key effects not taken into account by Zupanic et al.: simulation of individual fiber geometry and molecular uptake mechanisms. It may be that without modeling individual fiber geometry, the importance of electrode orientation is underpredicted.

Results from the asymptotic fiber model offer new mechanistic interpretations for why transversely oriented electrodes may provide more efficient uptake. First, the transverse AF is the primary influence on molecular uptake, given that it charges the membrane very fast, and effectively preempts charging of the membrane via the longitudinal AF. Orienting the electrodes in the transverse direction establishes a significant transverse AF for tissue between the electrodes, given that the electric field is generally more aligned with the direction normal to the membranes of the fibers. Second, uptake results show that the transverse orientation yields larger

region of tissue with moderate uptake, which contributes more significantly to total uptake than for the longitudinally oriented electrodes case. Effectively, the transverse orientation allows for a larger region of the tissue to have at least a small to moderate amount of uptake, offering more effective uptake compared to longitudinal electrodes. This observation may imply that electrodes should be positioned transverse to the fibers so that they span the entire thickness of the muscle tissue to be permeabilized, which corroborates other simulation studies where individual fiber geometry and membrane dynamics are neglected.[103] Finally, it is worth noting that in experiments, the effects of electrode orientation on molecular uptake is often not considered, and the findings of this study and Zupanic et al. provide motivation for future studies to include orientation as a parameter in studying and optimizing uptake in drug delivery.

4.3.2 Pulse Strength and Comparison to Other Models and Experiments

The fact that the increase in tissue-wide uptake from including the longitudinal AF is a constant value for all field strengths (Fig. 3.14) may point to a powerful generalization. It may be the case that only effects from the transverse AF need be simulated, and then simply a constant added to the uptake to account for the longitudinal AF. Certainly, for larger pulses where total uptake is very large, researchers would be justified in neglecting effects from the longitudinal AF altogether. Further studies would need to be performed in order to test if this constant increase in uptake is robust with respect to different pulsing protocols and tissues.

The linear increase in total uptake is closely tied to the nearly identical increase in percent of tissue that is exposed to a threshold value of electric field $|E|_{th}$, as shown in Fig. 3.15. Therefore, it appears that increasing the pulse strength exposes a larger region of tissue to at least $|E|_{th}$, the size of this region of tissue increases nearly linearly with pulse strength, which explains the linear relationship between

total uptake and pulse strength. Thus, previous models of electroporation-mediated uptake in muscle tissue that base uptake on $|E|_{th}$ appear to be appropriate for predicting total uptake in the tissue. However, it should be noted that predicted uptake is highly dependent upon choice of $|E|_{th}$. If the optimal value $|E|_{th} = 483$ V/cm used in Sec. 3.3.2 is increased by only 5.8%, then average relative difference between the full uptake model and the field threshold model increases from 3.31% to 10.2%. Furthermore, the field threshold model predicts a different shape for the region of uptake in the tissue, where more uptake is predicted exactly midway between the electrodes, compared to the full uptake model. Fig. 3.11 reveals that the lack of uptake midway between electrodes is a transverse phenomenon, and provides evidence that the transverse AF derived in Sec. 2.1.2 behaves differently than $|E|$ traditionally used in the literature.

The trends observed in simulations of total tissue uptake as a function of pulse strength agree with experiments on uptake of small molecules in soleus muscle of rat performed by Grafstrom et al. and Engstrom et al.[31,32] First, the uptake ratio measured in simulations and experiments are both nearly linear functions of field strength, and furthermore, these linear functions never differ by more than 5% over all pulse strengths (Fig. 3.17). Linear relationship between uptake and pulse strength has also been observed for other small molecules in muscle.[30] Furthermore, simulations show that increasing pulse strength results in a larger region of tissue over which uptake occurs, but not an increase in the intracellular concentration value in pre-existing regions of uptake at low pulse strengths (Fig. 3.13). This exact same mechanism was observed in experiments.[32] However, one discrepancy between the model and experiments is that the field threshold $|E|_{th} = 483$ V/cm found in Sec. 3.3.2 for electropermeabilization is six-fold larger than reported in experiments.[29] The discrepancy is likely due to using electroporation parameters based on artificial lipid bilayers, not muscle, as discussed in Sec. 4.4.1.

Understanding that increasing pulse strength increases uptake by exposing a larger region of tissue to steady state uptake provides a lesson for design of electrodes, where the geometry of the electrodes impacts the distribution of the field throughout the tissue. If the primary purpose of larger field strengths is to create a larger volume of tissue where pore density is great enough to allow intracellular concentration to reach steady state value, then perhaps smaller field strengths may be used by creatively designing electrodes to spread out electroporation over a larger region of tissue. Certainly, there is a core region of tissue where molecular uptake reaches steady state even at the lowest pulse strength of 400 V/cm (Fig. 3.13). Thus, energy is wasted in this region for all field strengths greater than 400 V/cm, because this region cannot attain greater uptake than it already has. In essence, it would appear better to spread out the effect of the electric pulse over tissue volume, decreasing electroporation near the electrodes and increasing it further from the electrodes, ultimately creating a more uniform field.

One solution may be electrode designs that have a larger surface area. However, if needle electrodes are used this increase in surface area must be balanced with increase pain and physical damages to muscle from inserting thicker needles into tissue. In the extreme, parallel plate electrodes may be better designs for increasing molecular uptake in electroporation-mediated molecular uptake. Other published studies have indicated that uptake may occur at lower pulse magnitudes when using electrodes with more surface area, such as plate and spatula electrodes.[30,134] However, plate electrodes must be applied across the skin, or the skin must be entirely removed, which poses practical barriers for use on humans. Nevertheless, the results here indicate that for a given pulse strength, creating a more uniform field throughout the tissue may extend the reach of membrane charging to areas of tissue where intracellular concentration has not yet reached steady state, while not compromising concentration reaching steady state in the vicinity of the electrodes.

Further qualitative comparisons of results in Chapter 3 can be made to experiments when considering the time scale of membrane charging and electroporation. First, charging of the muscle fiber membrane via transverse current leads to a drastic increase in membrane conductance on the order of microseconds for regions of membrane close to the electrodes (e.g., Fig. 3.3). In general, the time scale of the increase in membrane conductance due to creation of pores is dependent on pulse strength, and these dynamics have typically only been studied in compact cells. Taking this into account, it is worth noting that a drastic increase in membrane conductance within microseconds has also been observed experimentally in unfertilized sea urchin eggs in the presence of electric fields on the order of hundreds of V/cm.[135,136] Second, membrane charging beyond a few microseconds was observed in the asymptotic fiber model for regions of membrane not electroporated by transverse currents (e.g., Fig. 3.8), and this long time scale of charging has also been observed experimentally in the passive response measurements of muscle fibers.[137] Sec. 4.4.1 compares the theoretical time scale of the post-pulse decrease in membrane conductance to experimental results.

4.3.3 Interfiber Distance

Results in Sec. 3.3.3 indicate that interfiber distance has an impact on the enhancement in uptake from the longitudinal AF. Variations in interfiber distances does occur naturally in muscle tissue. It is estimated that the relative standard deviation in interfiber distance can be as high as 89%.[138] One source of variation may the distributed presence of blood vessels throughout the muscle tissue, as shown in Fig. 1.2C for the capillaries.[20,121] In a transverse cross section of tissue, it was found that there is at least one capillary per muscle fiber, and the position of the capillaries in the interstitial space will locally change the interfiber distance.[20,121] Where these capillaries are present, the interfiber distance is not solely controlled by the diam-

eter of erythrocytes, given that these cells can squeeze through capillaries. In fact, experiments show that although the diameter of erythrocytes may be as large 7 μm, most of the cells are able to pass through a channel only 2.9 μm in diameter.

Therefore, the range of interfiber distances in Sec. 3.3.3 include both extremes (1 and 7.5 μm), as well as a more moderate value of 3.75 μm. However, it would be misleading to use the moderate value of interfiber distance, given that capillaries do not line the entire circumference of the fibers, and therefore many angular positions around the fiber would have an interfiber distance close to 1 μm, as confirmed by images of muscle cross sections in Fig. 1.2.[106,121] Ultimately, the increase in tissue-wide uptake from the longitudinal AF may not be as much as 3.95% as observed when the interfiber distance is 1 μm, yet it is expected that it would not drop below 0.823% as seen with interfiber distance of 3.75 μm. Certainly, the absolute lowest bound would be 0.267% as seen for interfiber distance of 7.5 μm.

4.3.4 Nonuniform Tissue Conductivities Due to Electroporation

Results in Sec. 3.3.4 reveal a couple of important differences in molecular uptake from using nonuniform tissue conductivities compared to uniform conductivities. First, both at the fiber and tissue levels, the longitudinal AF has less effect on molecular uptake from using nonuniform tissue conductivities compared to uniform tissue conductivities. Effectively, in the nonuniform case, the magnitude of both the transverse and longitudinal AFs are increased in the region of fiber where the longitudinal AF has an effect on molecular uptake. For the fiber close to the electrodes this region is near the ends of the fiber (Figs. 3.24C and 3.25B), and for the fiber further away it is over an even greater length of the fiber (Figs. 3.24D and 3.25C). Given that the transverse AF charges the membrane orders of magnitude more rapidly than the longitudinal AF, and by doing so mitigates the effect from the longitudinal AF, it is the increased magnitude of the transverse AF that dominates over the increased

magnitude of longitudinal AF in terms of inducing uptake. Still, on the entire tissue level, the relative increase in uptake due to the longitudinal AF only differs by approximately 7% between uniform and nonuniform tissue conductivities models.

The second result from Sec. 3.3.4 is that the model using nonuniform tissue conductivities predicts 8.3% more uptake than the uniform conductivities model. Certainly, the direct practical significance of 8.3% is difficult to conclude, as discussed more generally at the end of Sec. 4.2. However, indirectly, the significance of this finding lies in the mechanism by which the nonuniform tissue conductivities model simulates more uptake. Relative to the uniform tissue conductivities model, the nonuniform conductivities model lowers the field and derivative of the field in the vicinity of the electrodes, while it increases it at more distal regions of the tissue. This process essentially creates more uniform membrane charging throughout the tissue, reducing charging for regions of tissue near the electrodes where steady state intracellular concentration has already been reached, and increasing charging for distal regions of tissue where steady state has not been reached. This mechanism may provide a clue for enhancing efficiency of molecular uptake. If the tissue conductivity can be increased locally around the electrodes before treatment with electric pulses, then molecular uptake over the entire tissue may be increased. For example, it may be interesting to evaluate the change in uptake from pretreating the region of tissue with concentrated salt solution where electrodes are to be inserted. However, it should also be noted that changing concentrations of ions has been shown to effect electroporation at the membrane level, so these changes would have to be taken into account too in evaluating pretreatment of tissue.[56]

The accuracy of the computed 7% difference in importance of the longitudinal AF between uniform and nonuniform models should be called into question, given it was found using numerical solutions of the AFs, which are prone to large numerical errors. First, individual fibers are considered. Using numerical AFs for uniform tissue

conductivities, the percent increase in uptake from the longitudinal AF for a fiber close to the electrodes is 0.0230%, compared to 0.91% using analytical AFs. The same values for a fiber far from the electrodes are 93.2% and 2000%. Thus, for both fibers close and far from the electrodes, the increase in uptake due to longitudinal AF can differ by a factor between twenty and forty from error in computing numerical AFs. However, for tissue-wide uptake using uniform tissue conductivities, the numerical AFs predict 3.51% increase in uptake due to longitudinal AF compared to 3.95% using analytical AFs, which only differ by a factor of a little more than one. Therefore, at the level of individual fibers, the computed relative importance of the longitudinal AF between using uniform and nonuniform tissue conductivities has very little accuracy. At the tissue level results are a little more trustworthy, but still riddled with error.

Comparing numerical to analytical AFs in Fig. 3.27 and resulting uptake in Fig. 3.28 reinforce the aforementioned observation that numerical error is debilitating at the individual fiber level. Furthermore, at the tissue level, total uptake differs by a factor of a little more than one, as was found when considering the effect of the longitudinal AF above. Thus, in terms of total tissue uptake, there is still significant error from numerical computation of AFs. The nature of electroporation does offer some evidence that numerical error may not be completely intractable as computational power continues to increase. While the longitudinal AF exhibits very large numerical error under the electrodes for a fiber close to the electrodes, the effect on uptake is mitigated due to the dominance of the transverse AF under the electrodes. The longitudinal AF exhibits less numerical error under the electrodes for a fiber far from the electrodes where it actually does play a larger role in uptake. Furthermore, the fact that over the entire tissue the first derivative in the transverse AF is the dominant mechanism governing uptake is encouraging, given there is less error compared to the second derivative in the longitudinal AF. Note that the original

definition of the AF by Rattay allows for analytical and numerical expression of the AF, so that derivatives from numerical solutions of primary potential are also valid AFs.[61]

4.4 Assumptions, Limitations, and Future Directions

Major assumptions used in the asymptotic electroporating fiber model that highlight important limitations in the model are discussed in this section. Based on these limitations, future directions for development of the model are also discussed. To enhance readability, the flow of subsections below start with assumptions made at the membrane level, and subsequently move to those made at the tissue level.

4.4.1 Electroporation Parameters and Dynamics

Parameters for electroporation in Eqs. 2.30-2.31 listed in Table 2.3 are based on experiments performed on uranyl modified black lipid membranes (BLMs) and unfertilized sea urchin eggs.[54,100] However, other studies base these parameters on experiments performed on skeletal muscle. Of particular importance are the rate of pore creation (α) and the characteristic voltage of electroporation (V_{ep}). Studies find that α may be between two-fold and two orders of magnitude larger than given in Table 2.3, and that V_{ep} may be one-half as large.[57,139] Furthermore, Stewart et al. increased the radius of the pores r_m from 0.8 nm to 20 nm to fit experimental membrane current curves for muscle membrane.[57]

These parameters were changed in Eqs. 2.30 and 2.31 to the most extreme values reported: where α was increased by two orders of magnitude, V_{ep} was reduced by half, and r_m was increased to 20 nm. The asymptotic electroporating fiber model was simulated using pulse strength $2|V_0|/d = 800$ V/cm (a typical pulse strength in experimental studies, and same strength used for results in Secs. 3.1 and 3.2), and the result is that the percent increase in tissue-wide uptake from including ver-

sus excluding the longitudinal AF approaches the order of machine error: $1x10^{-12}$%. This extremely small increase also holds for individual fibers close and far from the electrodes. Ultimately, the fast pore creation rate and small threshold for electroporation, coupled with much larger pores, means that the entire tissue reaches steady state intracellular concentration regardless of the inclusion of the longitudinal AF. This behavior is qualitatively different than the results in Chapter 3, where there still remained regions of tissue that did not reach steady state intracellular concentration, both from including or excluding the longitudinal AF.

While these results show that the relative contribution of the longitudinal AF is strongly dependent on choice of parameters in electroporation model, it cannot be determined if the muscle electroporation parameters found by Stewart et al. are entirely accurate. The parameters were found from a model of electroporation that assumes the pores to do not grow, and thus, the increase of pore radius from 0.8 to 20 nm does not coincide with theoretical considerations involved in derivation of the asymptotic equation for pore creation (Eq. 2.30).[48] Furthermore, setting radius of pores to a static 20 nm is not supported by other experiments, which indicate that electropores admit molecules with a hydrodynamic radius as large as 52 nm.[84] Furthermore, one study used rapid-freezing electron microscopy to visualize volcano-shaped pores as large as 120 nm in red blood cells after exposure to an electric field.[140]

It is likely that different optimal values for α and V_{ep} would be found from fitting muscle experiments to a model of electroporation that includes growing pores. Experiments on the semitendinosus muscle of a frog, as well as CHO cells and unfertilized sea urchin cells, indicate membrane conductance decreases with at least two different time scales after the pulse is turned off: milliseconds and seconds.[14,141,142] In consideration of theoretical studies, the millisecond time scale is hypothesized to be the fast decrease in the radii of electropores.[53] The slower time scale of seconds

is hypothesized to be from actual resealing of the pores into an intact membrane, and was found mathematically in Eq. 2.51.[53] Incorporating a growing pores version of the electroporation model in fitting parameters to muscle experiments may reveal that α is lower than predicted by Stewart et al.,[57] given that the decrease in membrane conductance on the order of milliseconds may be covered by shrinkage of pores rather than resealing of pores.

While optimization of parameters α and V_{ep} to muscle experiments has not been performed in a growing pores model of electroporation, results from electroporation models with growing pores that do not fit parameters to experiments provide some interesting insights. Filev et al. published a modeling study on spherical cells using the growing pores version of the asymptotic model of electroporation that reveal two interesting phenomena.[53] First, while large pores (23 to 419 nm radius) comprise only about 2% of pore population compared to the 98% for small pores ($\approx$ 1 nm radius), they contributed 66% to increased cell conductance from the electroporation process. Second, these large pores form on the border of the electroporated regions of the cell, not at the depolarized and hyperpolarized poles where small pores form.

These two findings have extremely interesting implications for molecular uptake in the muscle fiber. Given that large pores form on the border of electroporated regions of the cell, then these pores form not where the largest membrane charging occurs, but where a "moderate or small" amount of charging occurs. In the asymptotic electroporating fiber model, for a fiber close to the electrodes, these regions of moderate charging occur near the ends of the fiber, as shown by the two arrows on top in Fig. 3.4A. Furthermore, pore creation in these regions is dominated by the longitudinal AF. Given that Filev et al. found that large pores dominate the increase in conductance from electroporation in the spherical cell,[53] including growing pores in the muscle fiber model may increase the relative contribution of the longitudinal AF to molecular uptake. However, the impact may not be too large, given

that molecular uptake occurs via diffusion through pores during the seconds after the pulse is turned off, and Filev et al. found the large pores shrink to small pores within only 0.5 ms of the pulse being turned off. Including growing pores would also allow study of the spatial and temporal uptake of large molecules such as DNA. Current results suggest that uptake of these large molecules may occur later in the pulse near the ends of the fiber due to the long time scale of membrane charging via the longitudinal AF creating and growing pores near the ends of the fiber. Ultimately, electroporation with growing pores would add complex dynamics that may lead to unexpected results, and thus would be a logical next step in building upon the current version of the asymptotic electroporating fiber model.

4.4.2 Additional Membrane Dynamics

The only nonlinear membrane process included in the model is electroporation. In reality, the membrane of the muscle fiber is much more complex, including transverse tubules (T-tubules) that carry electrical currents inside the fiber, and ion pumps and channels involved in generating action potentials. Simulating these components of the membrane is outside the scope of the current work, yet their potential significance is briefly reviewed here. The T-tubule system has been shown to have a small effect on action potential duration in a cardiac fiber, which supports the possibility that they may have a small effect in an electroporating muscle fiber.[143] The level of detail in modeling electrical properties of muscle fibers needs to be increased in order to describe the electrical repercussions of these complex networks of tubules. Such complex models may become tractable as the computational power of workstations continues to increase.

Electrical properties of action potentials, on the other hand, are widely studied and relatively well-characterized. Still, modeling studies that combine electroporation and excitation are limited. One such study investigates the interplay between

electroporation and the action potential in the transmembrane potential (Φ_m) of a 1D cardiac fiber, using similar equations for electroporation current and creation of pores as Eqs. 2.29-2.31.[139] In these studies, membrane excitability was characterized by the Luo-Rudy dynamic model, and the effects from including or excluding electroporation current were investigated. It was found that without modeling electroporation, the relative root mean square error between simulations and experiments was 73.5%, but by including electroporation error was reduced to 4.27%. Without electroporation, the saturation of Φ_m observed in experiments could not be captured in the model. The ionic currents involved in excitation do effect the ability of the model to quantitatively predict Φ_m, however, if only the electroporation current is used the model exhibited very high qualitative agreement with experiments.

Another method of estimating the effects of including excitation currents in an electroporating muscle fiber is to consider the magnitude change in Φ_m and membrane conductivity due these currents. During an action potential Φ_m typically increases on the order of 100 mV. Given the exponential dependence of pore creation on Φ_m (Eq. 2.30), excitation current may have significant effects on the dynamics of electroporation. This effect may be especially pronounced if electroporation parameters are optimized for muscle, given that electroporation occurs faster and at smaller Φ_m in biological membranes compared to artificial lipid bilayers used in this work.[57,139] On the other hand, the membrane conductance increase during excitation is significantly smaller and for shorter duration than during electroporation: 1-2 orders of magnitude for a few milliseconds, compared to 3-4 orders of magnitude for as long as seconds during electroporation.[114,144,135] Ultimately, there is reason to believe that including excitation currents in the asymptotic fiber model may yield some quantitative change in electroporation and molecular uptake, but the qualitative trends are not expected to change drastically. Still, including excitation would be an interesting and relevant addition to the asymptotic fiber model.

4.4.3 Molecular Transport From Blood Vessels to Muscle Tissue

Reduction of the full conservation of mass equations to simpler two-compartment equations in Sec. 2.3.2 neglects transport from a third compartment: the capillaries and other blood vessels in skeletal muscle tissue. In electroporation-mediated delivery of small molecules in rat thigh muscle tissue performed by Grafstrom et al. and Engstrom et al.,[31,32] the molecules are injected into the bloodstream prior to electroporation, and thus the vessels in the muscle represent a third compartment for transport. Justification is given in Secs. 2.3.2 and 2.3.3, as well as Appendix E, for the initial conditions being that molecular concentration is uniform in the extracellular space. It is also assumed that the vessels act as an endless reservoir for the molecule, where the concentration is not depleted in the vessels as molecules move into the extracellular space of the muscle. In general this is not true, as shown by pharmacokinetic experiments and modeling of small molecules in a rat,[145] but over the 8.5 s time scale that pores are open and molecular transport occurs (Sec. 2.3.2), the molecular concentration of small molecules in the plasma of a rat is relatively constant.[145]

While the initial conditions of molecular concentration is addressed, the fact that blood vessels continue to supply molecules to the extracellular space as molecules move into the intracellular space has not been addressed. In short, the blood vessel "source" of molecules after time 0^+ is neglected from the molecular uptake model. One method to determine this source of molecules is to fit a triexponential function to diffusion of molecules in MRI studies.[146,147] In one particular study of the pharmacokinetics of methotrexate by Bishchoff et al.,[145] rat muscle transport is assumed to have three compartments: intracellular, extracellular, and tissue vasculature (e.g., capillaries).[115] By assuming no transport between extracellular and intracellular compartments, and that concentration is at steady state between capillary and ex-

tracellular compartments of muscle, they found an ODE for the exchange of molecules between the blood plasma in arteries and the extracellular space of muscle, with parameters fit to experiments.[115,145] This provides a source that may be added to the existing two-compartment model in Sec. 2.3.

To test the error from neglecting the source term of molecules from blood vessels, an extreme version of the asymptotic model of electroporation-mediated delivery was simulated, where extracellular concentration of molecule remains constant in time as uptake occurs. The extracellular concentration remains constant due to instantaneous refilling of molecules from vessels, and as previously stated the concentration in the vessels is assumed to be constant in time. Although this scenario is unrealistic, it provides an estimate of the maximum error from neglecting the source term from the blood vessels. Results show that for pulse strength $2V_0/d = 800$ V/cm, the enhancement in uptake from the longitudinal AF over the entire tissue is only 0.52%, compared to 3.95% when the source from the arteries is neglected (Sec. 3.2.3). Therefore, neglecting the source from the arteries may overestimate the effect of the longitudinal AF in tissue-wide uptake by as much as a factor of 8, and a similar overestimation factor is found for other pulse strengths between 400 and 1000 V/cm. The longitudinal AF plays a smaller role in uptake when a source of molecules is considered because the source increases the steady state intracellular concentration value and time needed to reach this steady state value (substitute $c_e = c_o$ for Eq. 3.10, and use in Eq. 2.57a). Thus, the much larger pore density created in the vicinity of the electrodes from the transverse AF has a direct effect on uptake, given that uptake does not level off at steady state concentration, as was the case in Fig. 3.4C. This amplifies the effect of transverse charging on uptake, and thus mitigates the effect from the longitudinal AF on uptake.

4.4.4 DNA Uptake

The most important molecule delivered to muscle fibers from a therapeutic perspective is DNA, and is thus a logical future alteration to the asymptotic fiber model. One of the most noticeable differences in modeling DNA is that the molecular weight can reach three to four orders of magnitude larger than the 400 Da molecule considered in this research, which has a couple of consequences in modeling. First, to model electropores large enough to admit DNA, the growing pores version of the asymptotic model of electroporation must be used instead of the non-growing pores version currently implemented (see Sec. 4.4.1).[49,51] Given that larger pores have been shown to form on the periphery of the electroporated regions in cells, the growing pores model with DNA may show that more uptake occurs in the periphery regions simply because this is the only region where pores are large enough to admit DNA.[53] For the muscle fiber, the peripheral regions are highly affected by the longitudinal AF, which may amplify the role of the longitudinal AF for DNA uptake.

The second consequence of modeling large DNA molecules is that transport via diffusion is very small compared to electrophoretic transport.[24,148,149] It would simply not be possible to remove the electrophoretic transport from either the transport in the volume spaces or the transport flux at the membrane (Secs. 2.3.2 and 2.3.3). This is exceptionally true given pulse protocols for DNA uptake are on the order of milliseconds instead of microseconds used for small molecules.[24,28,17] In electroporation-mediated experiments, the DNA is injected intramuscularly, and thus whole-body pharmacokinetic analysis is less important for delivery, and the primary focus is placed on transport in the interstitial space and across the membrane.[21,23,28,150,151] Since diffusion transport is so small, assuming uniform initial interstitial concentration of molecules before the pulse is turned on may no longer be justifiable, as argued in Sec. 2.3.3 for small molecules. Even with typical electrotransfer millisecond pulse

durations at a few hundred V/cm, DNA may only move a few micrometers, and thus may not justify assuming concentration is always uniform in the direction transverse to fibers.[148,152] If this is the case, removal of dependence of molecular concentration on φ and ρ would not be possible (the well-mixed condition in Sec. 2.3.2). It may still be possible to remove longitudinal transport in DNA uptake, given that DNA is not very mobile even during pulses.

Besides sheer size of DNA molecule, there are a number of other unique properties of DNA and electrotransfer that may need to be considered in modeling DNA uptake. First, it has been shown that there is a membrane adsorption phase in the internalization process of DNA, which may need to be considered.[88,89] This process may slow down transport, or provide a limiting step. Second, DNA is a polymer and behaves differently than a compact small molecule. For example, it has also been suggested by Henshaw et al. that DNA movement in interstitial space may have multiple phases, involving stretching in the presence of an electric field that decreases the effective radius of gyration, and relaxation between pulses that increases the effective radius of gyration.[153] This extra process in uptake may reduce the effective movement of DNA in the interstitium and across the membrane through pores. Interestingly, an endocytosis process has been suggested that occurs on a time scale several orders of magnitude longer than the time scale of the existence of pores large enough to admit DNA may play a role in uptake of DNA.[89,154] It is possible that modeling uptake only via electroporation captures only part of the process of DNA uptake.

4.4.5 Periodicity of Fibers

At the level of individual fibers in tissue, the assumption that that fibers are arranged in a periodic structure is an oversimplification of the fundamental geometry in biological tissue. As discussed in Sec. 4.3.3, the are large deviations in interfiber

distance in tissue. Furthermore, Fig. 1.2A reveals that the effective diameter of fibers varies from fiber to fiber, and that there are regions of connective tissue or large blood vessels between fascicles where interfascicle distance is much larger than interfiber distance. Still, the average interfiber distance is not expected to increase by too much given that the total area occupied by these regions is smaller than the area occupied by fibers within a fascicle, and the variation in interfiber distance to a maximum of 7.5 μm in Sec. 3.3.3 may be enough to cover the contribution of these larger interfiber distances.

Additionally, the aperiodic structure of muscle fibers is especially prominent in the vicinity of the electrodes, where the displacement of fibers from insertion of the needles is likely to push fibers together and decrease interfiber distance. In this case, from trends observed in Fig. 3.22, the increase in uptake from the longitudinal AF is expected to be amplified. Not only does the presence of the electrodes compact fibers, but the fibers also bend around the electrodes. Bending of the fibers is not unique to the site of needle insertion, as fibers also bend between the tendons they are attached to. Bending of the fiber may tend to decrease or increase the angle between the vector normal to the membrane and electric field vectors generated from electrodes. In the former case, the transverse AF magnitude would be larger, and in latter case it would be smaller. Bending may also affect the magnitude of the longitudinal AF. Finally, electrical pulses may cause muscle contraction, decreasing the interstitial space in certain regions of tissue, which would introduce a temporally-dependent aperiodic nature to the arrangement of fibers.[85]

Ultimately, to accurately model the effects of fiber bending, a numerical model would need to be developed with fiber geometries based on detailed geometries in muscle tissue. One of the primary barriers is the computational power needed to solve a full tissue model of multiple fibers in 3D. Aperiodic models of liver cells have been developed that simulate the dynamics of electroporation in 2D for a small

tissue space on the order of microns, but have yet to be extended to muscle fibers in 3D with tissue dimensions on the order of millimeters.[55,79] Intricate 3D geometries of tissue have also been simulated using finite element modeling, yet these models do not include individual cell geometry.[76,126] As computational power of personal workstations increase, full 3D spatiotemporal models of muscle tissue with aperiodic and complex individual fiber geometry may become more feasible.

4.4.6 Damage to Fibers

Damage to individual fibers has also been reported in other studies, but is not accounted for currently in the work presented here. Insertion of the needles during *in vivo* procedures can damage muscle around the needles. Damage can be reduced by making electrodes thinner, however, thinner electrodes concentrate the field more locally in tissue and can result in increased damage from the pulse.[85] Damage to the fibers closest to the electrodes has the greatest effect on tissue-wide uptake, given these are the fibers where the most uptake occurs. In general, the extent of damage to muscle once the pulse is turned on is dependent on electrode type, pulse magnitude, and pulse duration, with larger pulses and longer durations yielding the most damage.[23,30,150,155] In delivery of DNA, it has been shown that the presence of foreign DNA in the intracellular space and expression of this DNA plays a role in fiber damage, although the mechanism is not well understood.[150] Other explanations of muscle damage include Joule heating, irreversible electroporation in the membrane of the cell or constituent organelles, and conformation changes in ion channels.[7] While muscle damage may reduce optimal delivery of molecules, it is suggested that damage does not pose an insurmountable barrier. In one study it was shown that the damage to muscle fibers is only temporary, and two weeks after electropermeabilization that fibers appeared mostly normal.[23]

4.4.7 Effect of Electroporation on Tissue Conductivities

Sec. 3.3.4 of the Results presents an elementary analysis of the error from assuming tissue conductivities are uniform. Two major simplifications are made, yet these simplifications err on the side of overestimating the effect from changing tissue conductivities due to electroporation. First, the region of elevated tissue conductivities is assumed temporally static, whereas in experiments the region of elevated conductivities dynamically increases. The region is defined as the maximum region of tissue with elevated conductivities due to electroporation observed in previous experiments and modeling studies.[103,124,156] Smaller regions of increased conductivity during the process of electroporation would yield smaller perturbations in calculated AFs. Assuming a constant large region of elevated conductivities throughout entire simulations, as in this study, is expected to overestimate the effect from electroporation. A second assumption used is that there are only two possible values of tissue conductivities, whereas in experiments the tissue conductivities evolve through many different values. Assuming maximal change in conductivities in the asymptotic electroporating fiber model allows for the greatest perturbations in the AFs due to electroporation.[126]

One indication that these simplifications are not too extreme is found in observing the changes in the AFs between uniform and nonuniform tissue conductivities. As observed for transverse and longitudinal AFs in Figs. 3.24 and 3.25, including nonuniform tissue conductivities tends to decrease the magnitude of transverse and longitudinal AFs in the direct vicinity of the electrodes, while increasing them at more distal locations in the tissue. In essence, increasing the conductivities makes the electric field and the derivative of the field more uniform throughout the entire tissue. This same effect is also seen in other modeling studies on muscle and other tissues,.[125,29,103,55] Therefore, the qualitative trends in other studies are captured

even with the simplifications used in this study.

Nevertheless, a complete understanding of the qualitative and quantitative changes in molecular uptake and effects from the longitudinal AF would only come from major additions to the asymptotic electroporating fiber model. A revised algorithm is proposed, which builds on the numerical implementation of the model given in Sec. 2.1.4. Steps already given in Sec. 2.1.4 are summarized and condensed in order to highlight additions to the algorithm that account for dynamic tissue conductivities, given in italics below. Now that electroporation affects the tissue-wide conductivities and AFs, all fibers in the tissue must be solved simultaneously at each time step before proceeding to the next time step.

Outside time loop, *for all fibers in tissue*:

1. Set initial conditions at t=0:
   (a) Set all mean potentials to V_{rest}, all mean-free potentials to zero, and pore density in the membrane to zero
   (b) *Set transverse and longitudinal tissue conductivities (σ_t and σ_l) to their spatially uniform passive values, i.e., values assuming no electropores present*

At each time step within time loop:

1. *Compute membrane conductivity σ_m in z and φ for all fibers in tissue, by converting Eq. 2.28 to conductivity*
2. *Numerically solve for primary potential Ψ over entire tissue, taking into account local changes in membrane conductivity σ_m due to electroporation (see text below for more details)*
3. *Do for all fibers in tissue*

(a) *Compute source functions from derivatives of primary potential* Ψ

i. *At each position* z *along fiber, numerically compute AF* $\partial^2 \langle \Psi \rangle / \partial z^2$ *for use in longitudinal problem*

ii. *At each positions in* z *and* φ*, numerically compute AF* $\partial \widetilde{\Psi} / \partial \rho$ *for use in transverse problem*

(b) At each position in z along fiber:

i. Compute total transmembrane potential as the sum of the mean-free and mean transmembrane potentials: $\Phi_m = \phi_m + f_m$

ii. Compute transmembrane current $I_m(\Phi_m)$ at each angle φ on the membrane using Eq. 2.28

iii. Compute respective mean-free and mean transmembrane currents: $\widetilde{I_m}$ and $\overline{I_m}$

iv. At each φ along the membrane, solve Eq. 2.30 for pore density N_{ep} at $t + \Delta t$ using Φ_m and N_{ep} at current t

(c) At each position in z along fiber use $\widetilde{I_m}$ and AF $\partial \widetilde{\Psi} / \partial \rho$ to solve transverse problem (Eq. 2.13) for mean-free potentials at $t + \Delta t$

(d) Use $\overline{I_m}$ and $\partial^2 \langle \Psi \rangle / \partial z^2$ to solve longitudinal problem (Eq. 2.16) for mean potentials at $t + \Delta t$

A substantial amount of research and coding are needed in order to account for the changing tissue conductivities due to electroporation. One of the first details to notice is that using cylindrical geometry of individual fibers means that membrane conductivity σ_m in step 1 of the time loop depends on all three Cartesian coordinates x, y, and z at the tissue level (see Fig. 2.10). For a passive fiber the transverse conductivity in the x direction is equal to that in the y direction, however, this is no longer true after electroporation occurs. Thus, tissue conductivities must be

calculated in full 3D in step 2 of the time loop, not only in Cartesian coordinates z and y, as depicted in contour plots of the tissue space in Fig. 2.17. The three tissue conductivities would be $\sigma_x(x, y, z)$, $\sigma_y(x, y, z)$, and $\sigma_z(x, y, z)$.

Step 2 of the time loop used for solving primary potential Ψ based on local electroporation behavior is intentionally lacking detail, given the novel nature of doing this in muscle tissue with fiber geometry included. At first it may seem that a potential solution would be to solve a 3D version of the 2D elliptic equation for primary potential Ψ (Eq. 2.33), assuming a functional dependence of the conductivities tensor on changes in membrane conductivity σ_m. The parameters in the function could be fitted to experiments by comparing total current calculated over entire tissue in model to total current over entire tissue measured in experiments. This approach is similar to the work of Miklavcic's group discussed in Sec 2.4, except in this case the change in tissue conductivities would be triggered by the local value of membrane conductivity, not the local magnitude of the electric field (Eq. 2.59).[76,103,123,125] Furthermore, this approach is similar to the analysis used in Sec. 2.4, except that in this case the tissue conductivities would be allowed to change dynamically in space and time as electroporation at the membrane level occurs. However, measuring total tissue current is not very satisfactory given the novelty of the asymptotic model lies in the microscale fiber geometry and resulting electroporation dynamics. Furthermore, it is not immediately clear how to relate microscale $\sigma_m(\varphi, z)$ to tissue conductivities $\sigma_x(x, y, z)$, $\sigma_y(x, y, z)$, and $\sigma_z(x, y, z)$.

A more complete approach to solve primary potential Ψ in Step 2 of the time loop above may be to directly compute the tissue conductivities, and then use these tissue conductivities to solve a 3D version of the elliptic equation for primary potential (Eq. 2.33). First, focus is placed on the transverse tissue conductivities σ_x and σ_y. A potential approach is based on the theoretical work of Gielen et al.,[105] where a uniform field was considered in either the x or y-dimensions for an individual unit

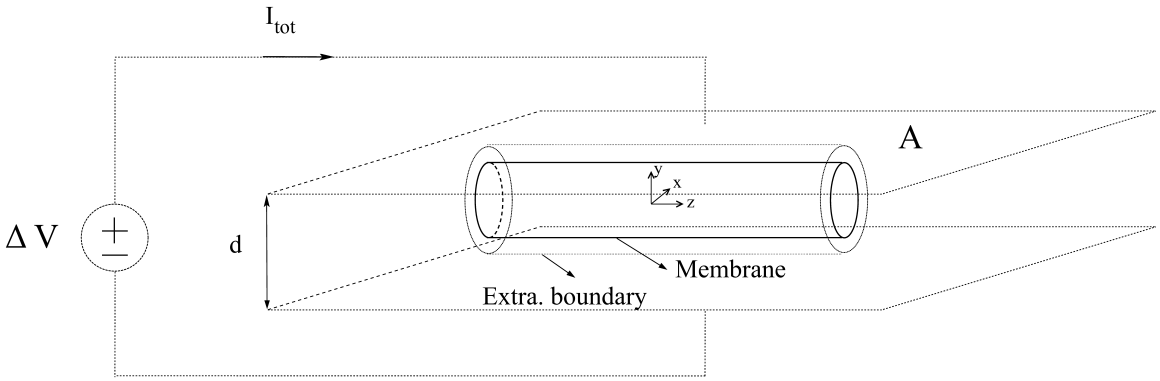

FIGURE 4.1: Setup for calculating transverse macroscopic tissue conductivities. Here, a unit fiber in the periodic lattice with extracellular boundary is shown in the presence of a uniform electric field generated by hypothetical plate electrodes of surface area A separated by distance d. The voltage drop across the unit is ΔV and total current delivered to the unit is I_{tot}. This setup is used to justify Eq. 4.1 for calculating macroscopic transverse tissue conductivities.

fiber or small collection of the periodic fibers, as illustrated for one fiber in the y-dimension case in Fig. 4.1. The definition of resistance is used to find the effective tissue conductivity,

$$\sigma_{x,y} = \frac{I_{tot} d}{\Delta V A}, \tag{4.1}$$

where I_{tot} is the total current delivered over surface area A across length d with change in voltage ΔV. The notation $\sigma_{x,y}$ is used to indicate this approach is applicable to orientations of the uniform field in both the x and y-dimensions (both transverse directions). In the asymptotic model I_{tot} may be calculated from the current density J by integrating J over surface area A, where J is calculated from microscopic conductivities, e.g., $J_y = -\sigma_i \partial V_i / \partial y$. J responds to changes in microscopic membrane conductivity σ_m, and in this way changes in σ_m due to electroporation could be incorporated into the macroscopic tissue conductivities. A similar approach was used by Weaver's group to calculate changes in the electrical properties of liver tissue during electroporation, but the system was converted into circuits and the program

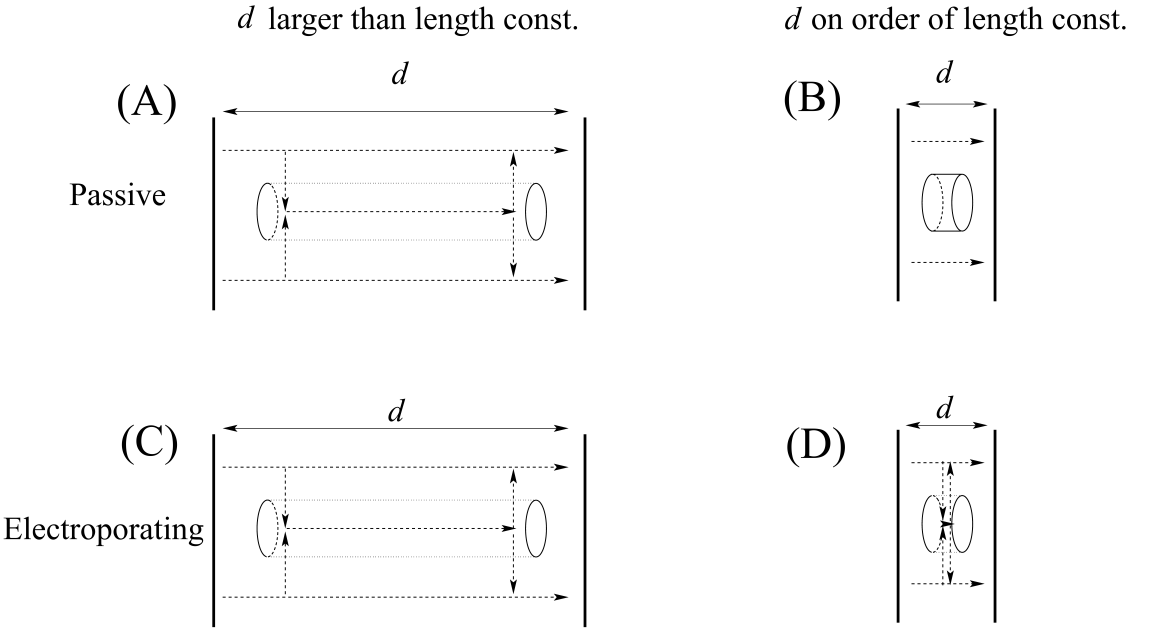

FIGURE 4.2: Dependence of longitudinal current flow on interelectrode distance. A section of fiber is shown in the presence of a longitudinal uniform electric field generated by hypothetical plate electrodes separated by distance d. Current lines are shown as dashed arrows, but are simplified in nature for illustration only. Illustration of current is shown for (A) non-electroporating fiber with large (A) and small (B) interelectrode distance compared to length constant, as well as electroporating fiber for large (C) and small (D) interelectrode distance compared to length constant.

SPICE was used to solve the circuits,.[55,79] Also, Weaver's group did not take into account directional dependence of electroporation and tissue conductivities, thus, their approach has never been applied to muscle tissue.

Gielen et al. applied longitudinal current to the extracellular space and found that longitudinal conductivity is a function of the distance between the electrodes.[105] This phenomenon is a consequence of current entering both extracellular and intracellular spaces for interelectrode distances much larger than the fiber length constant (Fig. 4.2A), but being confined to the extracellular space for interelectrode distances smaller or on the order of the length constant (Fig. 4.2B). Furthermore, if the longitudinal conductivity is measured using electrodes that are separated by a distance

that is many times larger than the length constant of the fiber, then longitudinal conductivity would not be expected to change much, if any, during electroporation, given that current already penetrates both the intracellular and extracellular spaces without electroporation (Figs. 4.2A and 4.2C). If electrodes are separated by a distance smaller or on the order of the length constant, then electroporation may make a difference in longitudinal conductivity, given that it will open up the intracellular pathway to current flow even over short lengths of fiber (Figs. 4.2B and 4.2D). This phenomenon may explain why Corovic et al. found a change in longitudinal conductivity of 2.5 with interelectrode distance of 5.2 mm, given that typical length constants of fibers are on the order of a millimeter.[126] The question becomes, over what length of fiber should one measure the effective longitudinal tissue conductivity? It appears that a more trustworthy or standardized method of calculating longitudinal tissue conductivity needs to be devised before the changes in conductivity due to electroporation can be implemented.

Another major challenge in implementing the algorithm above is that Ψ must be computed numerically instead of analytically, which can lead to large errors in computing the derivative transverse and longitudinal AFs: $\partial\widetilde{\Psi}/\partial\rho$ and $\partial^2\langle\Psi\rangle/\partial z^2$, respectively. This issue was discussed in Sec. 4.3.4, and our previous work shows that numerical error is not improved by using more sophisticated software packages.[75] Finally, in numerically computing Ψ at every time step increases the computational resources needed to solve the problem, in addition to the approximate 20 hours of computer runtime required to simulate the current version of the asymptotic electroporating fiber model out to 20 seconds, when all pores have resealed and uptake ends (x86-64, i7-2600 3.4 GHz Processor, 4 GB RAM, running MATLAB under Linux). The time required to solve the model may be reduced by using a more sophisticated discretization scheme requiring fewer nodes than the finite difference method, such as the boundary element method.[157]

5

Summary and Conclusions

Previous models of electroporation-mediated delivery in muscle tissue have neglected membrane charging due to the longitudinal AF, while studies of fiber stimulation dynamics have demonstrated the importance of the longitudinal AF.[29,62,63,64,65,66,76] One of the primary barriers to incorporating effects from the longitudinal AF in these previous models of electroporating muscle tissue is that the individual fiber geometry is not implemented. Rather, muscle geometry is only considered at the macroscale tissue geometry, and the tissue is considered to be anisotropic.[29,76] The research presented here derives an asymptotic fiber model that increases computational efficiency of modeling 3D, cylindrical fibers, and in doing so highlights the effects from the longitudinal AF and introduces a new AF: the transverse AF. To simulate electroporation, the asymptotic model of electroporation[48] is easily integrated into the asymptotic fiber model, and equations to model molecular uptake through these pores are derived from a conservation of mass equation that takes into account transport via diffusion and the electric field. In this manner, molecular uptake is simulated in a single, 3D cylindrical muscle fiber.

It is at the level of the individual fibers that the mechanisms behind charging

and electroporation of the membrane from transverse and longitudinal AFs are elucidated. In passive fibers close to the electrodes (0.18 mm from surface of needles), there is fast charging of the membrane due to polarization of the fiber from the transverse AF within the first few microseconds, and then slower charging due to longitudinal AF. However, there is virtually no flow of current across the membrane due to very large membrane resistance. On the other hand, for electroporating fibers close to the electrodes, the transverse AF charges the membrane within the first few microseconds, creating pores in the membrane, drastically increasing the local conductance of the membrane. This drastic increase in conductance effectively breaks down the membrane and discharges the membrane, exposing the intracellular space to the extracellular field, and precludes any further charging of the membrane from the slower acting longitudinal AF. For typical fiber geometry, electrode geometry, and pulsing protocols used in delivery of small molecules, this dominance of the transverse AF is observed for most of the length of a fiber close to the electrodes. However, for the 8% of fiber that is nearest the ends of the fiber, the transverse AF is too weak to yield electroporation, and electroporation primarily occurs on a longer time scale from charging via the longitudinal AF. Still, over the entire fiber close to the electrodes, the total uptake only increases by 0.91% from the longitudinal AF. In contrast, for more distal fibers four times the needle radius away from the surface of the needle (1.2 mm away from surface), the longitudinal AF dominates uptake and increases it by nearly 2000%. Due to this unique nature of electroporation, previous alterations to the cable equations to include dynamics effects of transverse charging in modeling stimulation are appropriate for modeling electroporation.[131] However, it is very important to fully simulate temporal dynamics of transverse charging during the first few microseconds, which means temporally static terms added to the cable equation are not appropriate.[67,130]

Based on periodicity and that fibers are independent of each other, multiple

fibers are simulated at different electrode-fiber distances to model tissue-wide uptake. Observing uptake on this scale reveals that the importance of including the longitudinal AF cannot be assessed at the single fiber level alone. While the longitudinal AF enhances uptake by 2000% for a fiber far from the electrodes, the total amount of uptake is very small in this fiber relative to the fiber close to the electrodes. Therefore, over the entire tissue, the enhancement in uptake from including the longitudinal AF is only 3.95% over the entire tissue for pulse strength of 800 V/cm, and reaches a maximum of 9.3% for 400 V/cm, the lowest pulse strength simulated. In practical terms, this error is on the order of the 6% experimental variability observed for molecular delivery to small animals,[31] and so neglecting the longitudinal AF is not expected to be very important in reproducing experiments. Therefore, the error from neglecting the longitudinal AF in previous theoretical studies is not expected to be very significant. However, it should also be noted that all other studies of electroporation-mediated uptake in muscle tissue do not take into account individual fiber geometry.[29,76] These studies base electroporation on field strength. From this perspective, it would be desirable to use the asymptotic electroporating fiber model, as it may more accurately measure the effect from the transverse component of the field, given that the transverse AF is derived from 3D cylindrical geometry.

The enhancement in uptake from the longitudinal AF depends on pulsing protocol and assumptions in the model. For a pulse strength of 1000 V/cm, the effect is 2.8%, while for 400 V/cm it is nearly 10%. By switching orientation of electrodes from longitudinal to transverse with respect to fibers for a pulse strength of 800 V/cm, the uptake enhancement from the longitudinal AF decreases from 3.95% to 0.752% because the transverse AF is amplified, which precludes charging from the longitudinal AF. Furthermore, the enhancement in uptake from the longitudinal AF decreases as the distance between fibers in tissue is increased. Finally, the model assumes the tissue conductivities are not affected by electroporation, which results in

an estimated error of only 7% in reporting the uptake enhancement from the longitudinal AF. However, numerically solving for the activating functions when accounting for changes in tissue conductivities from electroporation yields 30% estimated error in uptake. Thus, further investigation is needed to discern the error from assuming that tissue conductivities do not change from electroporation.

The asymptotic electroporating fiber model reproduces molecular uptake of small molecules in soleus muscle tissue of mice and rats quantitatively and qualitatively. Simulations and experiments both show that total tissue uptake is a linear function of field strength, and for field strengths between 400 and 1000 V/cm the percent difference between experiments and simulations is never more than 5%.[31] Furthermore, both models and experiments show that the increase in uptake from larger field strengths occurs because a larger region of tissue is being permeabilized, rather than enhancing uptake in regions already permeabilized.[31] In the model, this phenomenon is explained by local regions of tissue reaching steady state intracellular concentration of molecule, so that enhanced permeabilization will not enhance uptake. The total tissue uptake is predicted well by the assuming a threshold field magnitude $|E|_{th}$ for electroporation to occur, as often assumed in other models.[29,30] However, the spatial distribution of uptake throughout tissue predicted by the threshold field model is different than in the full uptake model, and the difference originates from the transverse AF. Finally, simulations show a 75% increase in uptake when orientation of electrodes are switched from longitudinal to transverse with respect to the muscle fibers, which is only qualitatively confirmed by other published theoretical model studies, where the increase is only 20%.[103] The model reveals that the mechanism behind this increase is the greater region of tissue that attains at least a moderate amount of uptake.

In general, the findings of this research suggest several considerations in optimizing molecular uptake in experiments on muscle tissue. First, results suggest design

of electrodes should focus on optimizing the volume of tissue permeabilized. This prescription is based on the fact that, for typical pulse magnitudes between 400 and 1000 V/cm, the limiting factor in terms of molecular delivery is not the intracellular concentration value in regions of tissue permeabilized, but rather, the actual volume of tissue that is permeabilized. Practically, this suggests design of needle electrodes that have multiple needles and/or large diameters, and that are spread out over the tissue, which is corroborated in other simulation studies.[103] These findings also corroborate studies using plate electrodes and novel spatula electrodes[30,134] to make the field more uniform throughout tissue. Second, given the overwhelming importance of the transverse AF in terms of controlling molecular uptake, electrode configurations should be designed to amplify the field transverse to the fibers, as well as extend the region over which this field remains sufficiently large. Finally, locally increasing the tissue conductivity around the electrodes may enhance total tissue uptake, given that this effectively increases the longitudinal and transverse AFs in regions of tissue far from the electrodes. This practically suggests a new direction in optimizing uptake that may involve increasing the tissue conductivity locally around the electrodes.

Future directions for improving upon the asymptotic electroporating fiber model are found in analyzing the limitations of the current version of the model. Membrane level electroporation parameters should be based on muscle experiments rather than artificial lipid bilayers, and the model of electroporation should allow for growing pores. Altering parameters may decrease the effect from the longitudinal AF, given that the membrane would be more prone to undergo electroporation on the time scale of charging via the transverse AF. On the other hand, allowing for growing pores may increase the contribution of the longitudinal AF to uptake, given that large pores may form in regions of tissue where the longitudinal AF dominates membrane charging. The effects of other membrane dynamics, such as action potentials, may play a minor role in electroporation, but are currently missing from the model. Also, the influx of

molecules into the interstitial space from surrounding capillaries is missing from the model, and it is shown that including this process may decrease the contribution of the longitudinal AF to molecular uptake.

DNA uptake is the most relevant application of molecular delivery in muscle, and many changes would need to be implemented, including removing assumptions that neglect the electrophoretic effect on transport and that enforce initial uniform molecular concentration in the interstitial space. DNA is a large polymer and exhibits many different transport properties from small molecules, and the entire model for molecular uptake would likely have to be completely rebuilt. Periodicity is assumed in the model, and accounting for the aperiodic nature of muscle fibers in tissue would require complex numerical models on computers that are powerful enough to simulate dynamics occurring at spatial and temporal scales that differ by several orders of magnitude. Finally, to accurately model the change in tissue conductivities due to electroporation, numerical simulations must be devised that relate changes in microscopic membrane conductivity to changes in macroscale tissue conductivities. Doing so would involve complex additions to the model that must especially focus on accurate representation of longitudinal tissue conductivity. These simulations must also find a way to overcome the numerical error associated with taking derivatives of potential to find transverse and longitudinal AFs.

Overall, the work presented here derives a novel, computationally efficient asymptotic fiber model that is useful in simulating membrane dynamics in 3D cylindrical fibers, including membrane charging from both longitudinal and transverse components of the pulse stimulus. This study introduces a novel transverse AF, in addition to the traditional longitudinal AF used in the cable equations. Due to the unique nature of electroporation, where membrane conductivity drastically increases on the time scale of membrane charging via the transverse AF, the longitudinal AF plays only a minor role in simulating molecular uptake. Therefore, this work supports the

use of traditional skeletal muscle electroporation models that neglect the longitudinal AF, yet, highlights the fact that these previous models do not include individual fiber geometry and may not properly account for charging of the membrane via transverse currents. Furthermore, the relative importance of the longitudinal AF is dependent on pulse parameters and assumptions made in the model. Thus, this work introduces the types of metrics to be considered in analysis, provides evidence that the longitudinal AF does play a small role in molecular uptake, and delivers a substantial core model on which to build more realistic models for electroporation-mediated molecular delivery. As models become more advanced, they will be able to enhance our understanding of the mechanisms involved in molecular delivery in skeletal muscle, and therefore provide guidance on optimizing delivery for potential therapeutic applications, such as gene therapy. Potential benefits to the clinical setting are far reaching, from DNA vaccines to treat cancer and HIV to increasing the mobility of those suffering from muscular dystrophy.[17]

Appendix A

Separation of I_m and $\partial\Psi/\partial\rho$ into the Mean-Free and Mean Components

[1]For any position φ, z along the fiber, the membrane current density is I_m,

$$I_m = \widetilde{I_m} + \overline{I_m}, \tag{A.1}$$

where the mean component $\overline{I_m}$ is the average of I_m over the fiber circumference and the mean-free component is $\widetilde{I_m} \equiv I_m - \overline{I_m}$.

The relative magnitudes of these components are now considered. In the scaling table (Table 2.1), the magnitude of I_m was assumed to be $\sigma_i V_c/a$; this approximates the maximum capacitive current that charges the membrane right after the stimulus is turned on. Once the membrane is charged, the current decreases, as it flows through the large membrane resistance R_m. Thus, a smaller unit is used, V_c/R_m, for

[1] Many of the ideas in this section are originally from our published article with Springer publishing (springerlink.com, DOI 10.1007/s11517-012-0870-3) in *Medical & Biological Engineering & Computing*: http://link.springer.com/article/10.1007%2Fs11517-012-0870-3.

the slower, mean component $\overline{I_m}$ of the current. Computing the ratio of magnitudes,

$$\frac{\overline{I_m}}{I_m} \sim \frac{V_c/R_m}{\sigma_i V_c/a} = \frac{a}{\sigma_i R_m} = \epsilon, \tag{A.2}$$

it is evident that the mean component $\overline{I_m}$ is $O(\epsilon)$. Consequently, the scaled version of formula (A.1) contains small parameter ϵ,

$$I_m = \widetilde{I_m} + \epsilon \overline{I}_m, \tag{A.3}$$

which is used as Eq. 2.11 in Sec. 2.1.1, and is used in Appendix B.

Similarly, the ρ-derivative of the primary potential can be written as

$$\frac{\partial \Psi}{\partial \rho} = \frac{\partial \widetilde{\Psi}}{\partial \rho} + \frac{\partial \overline{\Psi}}{\partial \rho} \tag{A.4}$$

where the mean component $\overline{\Psi}$ is the average of Ψ over the fiber circumference and the mean-free component is $\widetilde{\Psi} \equiv \Psi - \overline{\Psi}$. To show that $\partial\overline{\Psi}/\partial\rho$ is $O(\epsilon)$, a homogenization procedure is used similar to Appendix B.

The intracellular volume space v_i occupied by a Δz segment of a fiber is considered (Fig. A.1). Since electrodes are in the extracellular space, in intracellular volume space v_i the primary potential Ψ is governed by Laplace's equation. Using the divergence theorem, the integral of Laplace's equation over the intracellular volume v_i is converted into an integral of the primary potential gradient normal to the boundaries M, $E_{i,1}$, and $E_{i,2}$. The resulting equation in dimensionless variables is

$$\int_M \frac{\partial \Psi}{\partial \rho}\, ds + \epsilon \left(\int_{E_{i,2}} \frac{\partial \Psi}{\partial z}\, ds - \int_{E_{i,1}} \frac{\partial \Psi}{\partial z}\, ds \right) = 0. \tag{A.5}$$

Assuming that Ψ is constant over a Δz interval and using the definition of the mean component $\overline{\Psi}$, the first term in Eq. A.5 is evaluated as

$$\int_M \frac{\partial \Psi}{\partial \rho}\, ds = 2\pi \Delta z\, \frac{\partial \overline{\Psi}}{\partial \rho}. \tag{A.6}$$

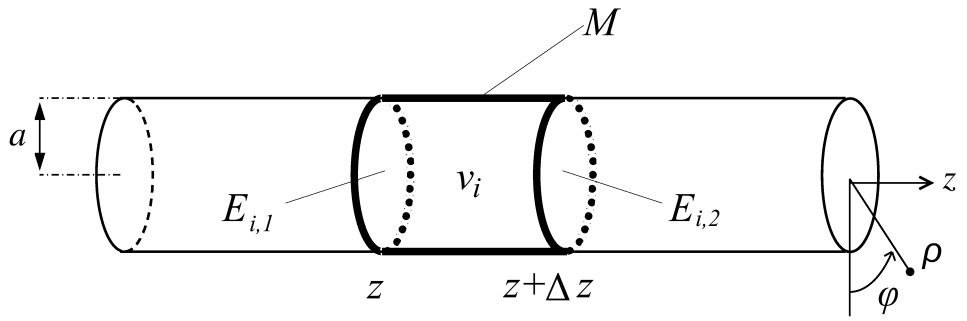

FIGURE A.1: Short length of fiber used in showing $\partial\overline{\Psi}/\partial\rho$ is $O(\epsilon)$. Short length of fiber is Δz long, that has intracellular volume v_i. The boundaries of the short length of fiber are membrane M, and end caps $E_{i,1}$ to $E_{i,2}$.

The second and third terms become

$$\epsilon\left(\int_{E_{i,2}}\frac{\partial\Psi}{\partial z}\,ds-\int_{E_{i,1}}\frac{\partial\Psi}{\partial z}\,ds\right)=\epsilon\pi\left(\left.\frac{\partial\langle\Psi\rangle}{\partial z}\right|_{z+\Delta z}-\left.\frac{\partial\langle\Psi\rangle}{\partial z}\right|_{z}\right),\tag{A.7}$$

where $\langle\Psi\rangle$ is the average of Ψ computed over the fiber cross-sectional area of the intracellular fiber space.

Substituting Eqs. A.6 and A.7 into Eq. A.5, and rearranging, yields

$$\frac{\partial\overline{\Psi}}{\partial\rho}=-\frac{\epsilon}{2}\,\frac{\left.\frac{\partial\langle\Psi\rangle}{\partial z}\right|_{z+\Delta z}-\left.\frac{\partial\langle\Psi\rangle}{\partial z}\right|_{z}}{\Delta z}\xrightarrow[\Delta z\to 0]{}-\frac{\epsilon}{2}\,\frac{\partial^2\langle\Psi\rangle}{\partial z^2},\tag{A.8}$$

which is used in Eq. 2.12 in Sec. 2.1.1 and in Appendix B.

Appendix B

Derivation of the Governing Equations for the Mean Potentials

[1]The governing equation for the LO mean potential in the longitudinal problem (Sec. 2.1.3) is derived using the homogenization process. The derivation begins with the scaled Laplace's equations in cylindrical coordinates (Eqs. 2.7a and 2.7b in Sec. 2.1.1), repeated here for convenience,

$$\frac{1}{\rho}\frac{\partial}{\partial\rho}\left(\rho\frac{\partial\Phi_i}{\partial\rho}\right)+\frac{1}{\rho^2}\frac{\partial^2\Phi_i}{\partial\varphi^2}+\epsilon\frac{\partial^2\Phi_i}{\partial z^2}=0 \qquad \text{in } \rho<a, \tag{B.1a}$$

$$\frac{1}{\rho}\frac{\partial}{\partial\rho}\left(\rho\frac{\partial\Phi_e}{\partial\rho}\right)+\frac{1}{\rho^2}\frac{\partial^2\Phi_e}{\partial\varphi^2}+\epsilon\frac{\partial^2\Phi_e}{\partial z^2}=0 \qquad \text{in } \rho>a. \tag{B.1b}$$

First, the intracellular potential Φ_i in the intracellular space is considered, in a small segment of fiber Δz long (Fig. B.1) Using the divergence theorem, the integral of Laplace's equation over the intracellular volume v_i is converted into an integral of the potential gradient normal to the boundaries M, $E_{i,1}$, and $E_{i,2}$. The resulting

[1] Many of the ideas in this section are originally from our published article with Springer publishing (springerlink.com, DOI 10.1007/s11517-012-0870-3) in *Medical & Biological Engineering & Computing*: http://link.springer.com/article/10.1007%2Fs11517-012-0870-3.

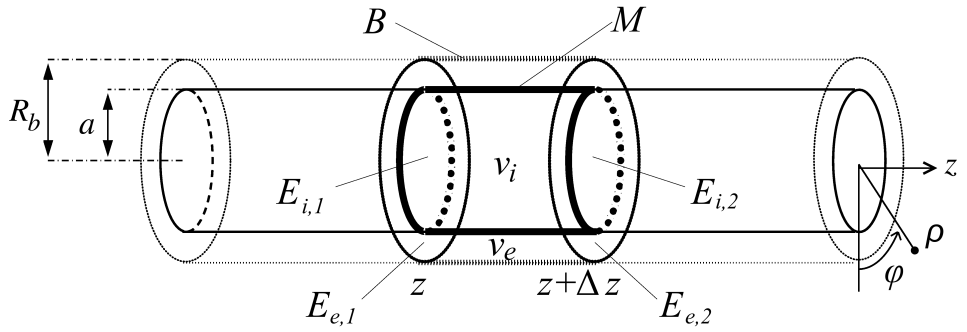

FIGURE B.1: Short length of fiber used to derive 1D equation for mean component of transmembrane potential in the longitudinal problem (Eq. 2.16). Short length of fiber is Δz long, that has intracellular and extracellular volumes v_i and v_e. The boundaries of the short length of fiber are membrane M, end caps $E_{i,1}$ to $E_{e,2}$, and extracellular boundary B. Boundary B is drawn with arbitrary radius R_b to allow for formulation of a general equation first, and then subsequently assuming the fiber is in an infinite extracellular medium to produce the specific equation.

equation is Eq. 2.14a in Sec. 2.1.3, repeated here,

$$\int_M \frac{\partial \Phi_i}{\partial \rho}\, ds + \epsilon \left(\int_{E_{i,2}} \frac{\partial \Phi_i}{\partial z}\, ds - \int_{E_{i,1}} \frac{\partial \Phi_i}{\partial z}\, ds \right) = 0. \tag{B.2}$$

Equation B.2 can be simplified as follows by considering each term in the equation in turn. For the first term, the continuity-of-current condition (Eq. 2.7c in Sec. 2.1.1) is substituted for the derivative in ρ,

$$\int_M \frac{\partial \Phi_i}{\partial \rho}\, ds = \int_z^{z+\Delta z} \int_0^{2\pi} \left(-\frac{\partial \Phi_m}{\partial \tau} - \epsilon \frac{\partial \Phi_m}{\partial T_s} - I_m - \frac{\partial \Psi}{\partial \rho} \right) d\varphi\, dz. \tag{B.3}$$

Potentials are replaced by their LO expansions that are separated into the mean-free and mean components (Eq. 2.10), and each term in Eq. B.3 is now considered in turn. First, it is recognized that $\partial \Phi_m^0 / \partial \tau \sim \partial \phi_m^0 / \partial \tau$ because f_m^0 is independent of τ. This term drops out because the integral of ϕ_m^0 over the fiber circumference is zero. Second, it is recognized that $\partial \Phi_m^0 / \partial T_s \sim \partial f_m^0 / \partial T_s$ because ϕ_m^0 is independent of T_s. Assuming that f_m^0 is constant over the Δz interval, the integral of f_m^0 over

M reduces to $2\pi\Delta z f_m^0$. The separation $I_m = \widetilde{I_m} + \epsilon\overline{I_m}$ (Eq. A.3 in Appendix A) is used to evaluate the double integral of I_m in Eq. B.3 as $2\pi\Delta z\epsilon\overline{I_m}$. Similarly, the separation of $\partial\Psi/\partial\rho$ given in Appendix A (Eq. A.4) is used to evaluate the double integral of the last term in Eq. B.3 as $2\pi\Delta z\partial\overline{\Psi}/\partial\rho$. Thus, Eq. B.3 is reduced to

$$\int_M \frac{\partial\Phi_i}{\partial\rho}\,ds = -2\pi\Delta z\left\{\epsilon\frac{\partial f_m^0}{\partial T} + \epsilon\overline{I_m} + \frac{\partial\overline{\Psi}}{\partial\rho}\right\}, \tag{B.4}$$

where a bar over a symbol denotes its average over the fiber circumference.

For the second term in Eq. B.2, the potentials are replaced by their LO expansions (Eq. 2.10). Since the mean intracellular potential f_i^0 is an average over the fiber cross-section, it is recognized that the surface integral of $\partial\Phi_i^0/\partial z$ can be substituted by $\partial f_i^0/\partial z$, which yields

$$\int_{E_{i,2}} \epsilon\frac{\partial\Phi_i^0}{\partial z}\,ds = \epsilon\pi\left.\frac{\partial f_i^0}{\partial z}\right|_{z+\Delta z}. \tag{B.5}$$

The third term in Eq. B.2 is reduced using a similar procedure, resulting in

$$\int_{E_{i,1}} \epsilon\frac{\partial\Phi_i^0}{\partial z}\,ds = \epsilon\pi\left.\frac{\partial f_i^0}{\partial z}\right|_{z}. \tag{B.6}$$

Substituting Eqs. B.4, B.5, and B.6 into Eq. B.2, and rearranging, yields

$$\frac{\left.\frac{\partial f_i^0}{\partial z}\right|_{z+\Delta z} - \left.\frac{\partial f_i^0}{\partial z}\right|_{z}}{\Delta z} = 2\left\{\frac{\partial f_m^0}{\partial T_s} + \overline{I_m}\right\} + \frac{2}{\epsilon}\frac{\partial\overline{\Psi}}{\partial\rho} \tag{B.7}$$

The last term in Eq. B.7 appears to be $O(1/\epsilon)$. However, it is in fact $O(1)$ because $\partial\overline{\Psi}/\partial\rho$ is $O(\epsilon)$ as shown by Eq. A.8 in Appendix A. Using Eq. A.8 and taking the limit $\Delta z \to 0$, the PDE governing the LO mean intracellular potential is obtained,

$$\frac{\partial^2 f_i^0}{\partial z^2} = 2\left\{\frac{\partial f_m^0}{\partial T_s} + \overline{I_m}\right\} - \frac{\partial^2\langle\Psi\rangle}{\partial z^2}. \tag{B.8}$$

A similar homogenization procedure is used for extracellular space, where the scaled Laplace's equation for extracellular potential Φ_e is integrated over a Δz segment of extracellular space surrounding the fiber (Fig. B.1). Using the divergence theorem, the integral of Laplace's equation over the extracellular volume v_e is converted into an integral of the potential gradient normal to the boundaries M, B, $E_{e,1}$, and $E_{e,2}$. The resulting equation is Eq. 2.14b in Sec. 2.1.3, repeated here,

$$-\int_M \frac{\partial \Phi_e}{\partial \rho} ds + \epsilon \left(\int_{E_{e,2}} \frac{\partial \Phi_e}{\partial z} ds - \int_{E_{e,1}} \frac{\partial \Phi_e}{\partial z} ds \right) + \int_B \frac{\partial \Phi_e}{\partial \rho} ds = 0. \tag{B.9}$$

Equation B.9 can be simplified as follows by considering each term in the equation in turn. For the first term, the continuity-of-current condition (Eq. 2.7d) is substituted for the derivative in ρ,

$$\int_M \frac{\partial \Phi_e}{\partial \rho}\, ds = \int_z^{z+\Delta z} \int_0^{2\pi} \left\{ \frac{1}{\mu} \left(-\frac{\partial \Phi_m}{\partial \tau} - \epsilon \frac{\partial \Phi_m}{\partial T_s} - I_m \right) - \frac{\partial \Psi}{\partial \rho} \right\} d\varphi\, dz, \tag{B.10}$$

where $\mu = \sigma_e/\sigma_i$ is the ratio of conductivities. Potentials are replaced by their LO expansions that are separated into the mean-free and mean components (Eq. 2.10), and each term in Eq. B.10 is now considered in turn. The same procedure and assumptions used for the intracellular space are enforced here, and Eq. B.10 is reduced to

$$\int_M \frac{\partial \Phi_e}{\partial \rho}\, ds = -2\pi \Delta z \left\{ \frac{1}{\mu} \left(\epsilon \frac{\partial f_m^0}{\partial T} + \epsilon \overline{I_m} \right) + \frac{\partial \overline{\Psi}}{\partial \rho} \right\}, \tag{B.11}$$

where a bar over a symbol denotes its average over the fiber circumference.

For the second term in Eq. B.9, the potentials are replaced by their LO expansions (Eq. 2.10). Since the mean extracellular potential f_e^0 is an average over the extracellular cross-section, it is recognized that the surface integral of $\partial \Phi_e^0/\partial z$ can be substituted by $\partial f_e^0/\partial z$, which yields

$$\int_{E_{e,2}} \epsilon \frac{\partial \Phi_e^0}{\partial z}\, ds = \gamma \epsilon \pi \left. \frac{\partial f_e^0}{\partial z} \right|_{z+\Delta z}, \tag{B.12}$$

where $\gamma = A_e/A_i$ is the ratio of cross-sectional areas of extracellular and intracellular space. The third term in Eq. B.9 is reduced using a similar procedure, resulting in

$$\int_{E_{e,1}} \epsilon \frac{\partial \Phi_e^0}{\partial z}\, ds = \gamma \epsilon \pi \left. \frac{\partial f_e^0}{\partial z} \right|_z . \tag{B.13}$$

The final term in Eq. B.9 drops out because $\Phi_e \to 0$ as $\rho \to \infty$. Alternatively, it is noted that $\partial \Phi_e^0/\partial \rho \sim \partial \phi_e^0/\partial \rho$ because f_e^0 is independent of ρ, and integrating $\partial \phi_e^0/\partial \rho$ over fiber circumference yields zero. Using this alternate logic shows that this final term drops out regardless of the size of the extracellular medium. Finally, a physical interpretation for neglecting this final term in Eq. B.9 is that fibers are very close, so that dynamics in one fiber are similar to those in the adjacent fiber, resulting in no flux at the boundary. This assumption is less accurate for fibers very close to the electrodes, where the electric field may change substantially even for a small change in distance from electrodes, which is a weakness of the current version of the model. Substituting Eqs. B.11, B.12, and B.13 into Eq. B.9 yields

$$\gamma\mu \frac{\left. \frac{\partial f_e^0}{\partial z} \right|_{z+\Delta z} - \left. \frac{\partial f_e^0}{\partial z} \right|_z}{\Delta z} = -2 \left\{ \frac{\partial f_m^0}{\partial T_s} + \overline{I_m} \right\} - \mu \frac{2}{\epsilon} \frac{\partial \overline{\Psi}}{\partial \rho} \tag{B.14}$$

The last term in (B.14) appears to be $O(1/\epsilon)$. However, it is in fact $O(1)$ because $\partial \overline{\Psi}/\partial \rho$ is $O(\epsilon)$ as shown by Eq. A.8 in Appendix A. Using Eq. A.8 and taking the limit $\Delta z \to 0$, the PDE governing the LO mean extracellular potential is obtained,

$$\gamma\mu \frac{\partial^2 f_e^0}{\partial z^2} = -2 \left\{ \frac{\partial f_m^0}{\partial T_s} + \overline{I_m} \right\} + \mu \frac{\partial^2 \langle \Psi \rangle}{\partial z^2}. \tag{B.15}$$

Subtracting Eq. B.15 from Eq. B.8 and approximating f_m^0 (average over the circumference) by $f_i^0 - f_e^0$ (the difference of area averages), the PDE for the LO mean transmembrane potential is obtained,

$$\frac{\partial^2 f_m^0}{\partial z^2} = 2 \left(1 + \frac{1}{\gamma\mu} \right) \left\{ \frac{\partial f_m^0}{\partial T_s} + \overline{I_m} \right\} - \left(1 + \frac{1}{\gamma} \right) \frac{\partial^2 \langle \Psi \rangle}{\partial z^2}. \tag{B.16}$$

Converting Eq. B.16 into original dimensional variables using the scaling table (Table 2.1) results in Eq. 2.15 in Sec. 2.1.3: the cable equation for a fiber in arbitrary size of extracellular space. For a fiber in an infinite extracellular space, $1/\gamma \to 0$, which implies $f_i^0 \to f_m^0$ and $f_e^0 \to 0$. In Eq. B.16, terms with $1/\gamma$ can be dropped, and expression in the original dimensional variables results in Eq. 2.16 in Sec 2.1.3: the cable equation for a fiber in infinite extracellular space.

Appendix C

Derivation of the Equation for Membrane Molecular Flux Through Electropores

The derivation begins with assuming that flux across the membrane is only significant in the transverse direction, given that the total surface area of the end caps of the fiber is three orders of magnitudes smaller than the rest of the membrane. Next, it is assumed that potentials and concentrations are 1D in the ξ-dimension across the membrane with thickness h, so that $\xi = 0$ is the intracellular side of the membrane interface and $\xi = h$ is the extracellular side of the membrane interface, as shown in Fig. C.1.[101,114] Membrane flux j_m is a modified Nernst-Planck equation that includes effects from the Born energy barrier arising from charged molecules traveling through electropores within the low permittivity space of the membrane,[100,101,102]

$$j_m = -D_m \left\{ \frac{\partial c_m}{\partial \xi} + \frac{c_m z_m e}{k_B T} \frac{\partial P_m}{\partial \xi} + \frac{c_m z_m e}{k_B T} \frac{\partial \mathbb{B}}{\partial \xi} \right\}, \tag{C.1}$$

where c_m is the concentration within the membrane, z_m is valence charge on molecule, T is temperature, P_m is the electric potential within the membrane, and $\mathbb{B}$ is the is the induced polarization charge on the membrane due to the Born energy barrier within

the membrane.[101] D_m is the diffusion coefficient of the molecules in the aqueous electropores, D_0, multiplied by the porosity of the membrane,[115]

$$D_m = D_0 \left(\pi r_m^2 N_{ep}\right) \tag{C.2}$$

where r_m is the radius of a pore and N_{ep} is the density of pores in the membrane (Sec. 2.2).

For convenience the definition $P_t(\xi) \equiv P_m(\xi) + \mathbb{B}(\xi)$ is used, and Eq. C.1 is rewritten as

$$j_m = -D_m \left\{ \frac{\partial c_m(\xi)}{\partial \xi} + \frac{c_m(\xi) z_m e}{k_B T} \frac{\partial P_t(\xi)}{\partial \xi} \right\}, \tag{C.3}$$

The steps and assumptions in the derivation are similar to those used by Barnett in deriving the 1D equation for conductance of a pore, taking into account the Born energy barrier.[101] First, equation C.3 is rewritten as

$$j_m = -D_m \exp\left[-\frac{z_m e}{k_B T} P_t(\xi)\right] \frac{\partial}{\partial \xi} \left\{ c_m(\xi) \exp\left[\frac{z_m e}{k_B T} P_t(\xi)\right] \right\}. \tag{C.4}$$

Both sides of Eq. C.4 are multiplied by $\exp\left[z_m e P_t(\xi)/(k_B T)\right]/D_m$, and the result is integrated along the length of the pore from $\xi = 0$ to $\xi = h$ (Fig. C.1). On the left side of the equation, recalling that j_m is independent of ξ if quasi-steady flow is assumed (Sec. 2.3.1), it is possible to take j_m outside of the integral. On the right side, the line integral of the derivative is equal to the change in value of the argument of the derivative. The result is

$$\frac{j_m}{D_m} \int_0^h \exp\left[\frac{z_m e}{k_B T} P_t(\xi)\right] \, d\xi = c_m(0) \exp\left[\frac{z_m e}{k_B T} P_t(0)\right] - c_m(h) \exp\left[\frac{z_m e}{k_B T} P_t(h)\right]. \tag{C.5}$$

It is assumed that the potential due to the Born energy barrier $\mathbb{B}(\xi)$ at $\xi = 0$ and $\xi = h$ can be redefined in terms of intracellular ($\mathbb{B}_i$) and extracellular ($\mathbb{B}_e$) potentials at the membrane interface: $\mathbb{B}(0) \equiv \mathbb{B}_i$ and $\mathbb{B}(h) \equiv \mathbb{B}_e$, respectively. Similarly,

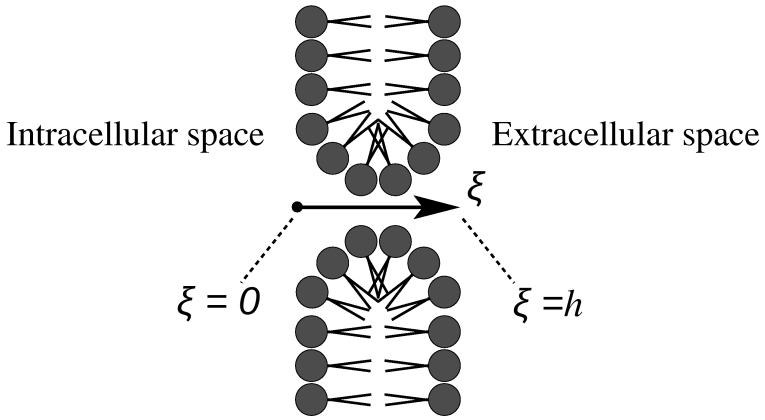

FIGURE C.1: Membrane geometry used to derive the equation for molecular membrane flux through pores (Eq. 2.46). An illustration of a zoomed in view of a single pore in the membrane is shown, along the with intracellular and extracellular side of the membrane. Derivation of membrane flux assumes 1D flow in the ξ-direction. In accordance with Barnett's work,[101] the membrane is assumed to have finite thickness h so that the Nernst-Planck equation can be integrated across the thickness of the membrane in the derivation.

it is assumed that concentration and potential at $\xi = 0$ and $\xi = h$ can be redefined in terms of the intramembrane concentration $c_m(\xi)$ and potential $P_t(\xi)$ at the intracellular and extracellular membrane interfaces (interface potential neglected): $c_m(0) = c_i$, $P_t(0) = V_i + \mathbb{B}_i$, $c_m(h) = c_e$, and $P_t(h) = V_e + \mathbb{B}_e$. In the previous equations, subscript i means intracellular and subscript e means extracellular. Using these specific values, Eq. C.5 is rewritten,

$$\frac{j_m}{D_m}\int_0^h \exp\left[\frac{z_m e}{k_B T}P_t(\xi)\right]\,d\xi = c_i \exp\left[\frac{z_m e}{k_B T}\left(V_i + \mathbb{B}_i\right)\right] - c_e \exp\left[\frac{z_m e}{k_B T}\left(V_e + \mathbb{B}_e\right)\right]. \tag{C.6}$$

Solving for j_m in Eq. C.6, and multiplying numerator and denominator of the right side of the resulting equation by $\exp\left[-z_m e(V_e + \mathbb{B}_e)/(k_B T)\right]$ yields

$$j_m = D_m \frac{c_i \exp\left[\dfrac{z_m e}{k_B T}\left(V_i - V_e + \mathbb{B}_i - \mathbb{B}_e\right)\right] - c_e}{\displaystyle\int_0^h \exp\left[\frac{z_m e}{k_B T}\left(P_t(\xi) - V_e - \mathbb{B}_e\right)\right]\,d\xi}. \tag{C.7}$$

It is assumed that the potential due to the Born energy barrier $\mathbb{B}(\xi)$ can be written in the form $\mathbb{B}(\xi) = z_m e \mathbb{F}(\xi)$, where $\mathbb{F}(\xi)$ has units J/C^2.[101] Function $\mathbb{F}(\xi)$ is assumed to be trapezoidal (Fig. C.2) and even symmetric with respect to membrane midplane, as proposed by Glaser et al.[100] As a result $\mathbb{F}(\xi) = \mathbb{F}(h - \xi)$, and $\mathbb{B}_i = \mathbb{B}_e$. Using these assumptions and the definition $P_t(\xi) \equiv P_m(\xi) + \mathbb{B}(\xi)$, Eq. C.7 becomes

$$j_m = D_m \frac{c_i \exp\left[\frac{z_m e}{k_B T}(V_i - V_e)\right] - c_e}{\int_0^h \exp\left[\frac{z_m e}{k_B T}(P_m(\xi) - V_e) + \frac{z_m^2 e^2}{k_B T}(\mathbb{F}(\xi) - \mathbb{F}_e)\right] d\xi}. \tag{C.8}$$

Eq. C.8 is rewritten in terms of nondimensional transmembrane potential $U = z_m e(V_i - V_e)/(k_B T)$ and nondimensional Born energy barrier $w(\xi) = z_m^2 e^2/(k_B T)(\mathbb{F}(\xi) - \mathbb{F}_e)$. Furthermore, the external field governing P_m across the thin membrane is assumed uniform[114,115] so that $P_m(\xi) - V_e = U(h - \xi)/h$, yielding

$$j_m = D_m \frac{c_i e^U - c_e}{\int_0^h \exp\left[U\frac{h - \xi}{h} + w(\xi)\right] d\xi}. \tag{C.9}$$

The integral in the denominator of Eq. C.9 is broken up into three integrals $\mathbb{I}_1$,$\mathbb{I}_2$, and $\mathbb{I}_3$ corresponding to the different regions of the trapezoidal energy barrier in Fig. C.2,

$$j_m = D_m \frac{c_i e^U - c_e}{\mathbb{I}_1 + \mathbb{I}_2 + \mathbb{I}_3}, \tag{C.10}$$

where $\mathbb{I}_1$ through $\mathbb{I}_3$ are integrals,

$$\mathbb{I}_1 = \int_0^l \exp\left[U\frac{h - \xi}{h} + \frac{w_o}{l}\xi\right] d\xi, \tag{C.11a}$$

$$\mathbb{I}_2 = \int_l^{h-l} \exp\left[U\frac{h - \xi}{h} + w_o\right] d\xi, \tag{C.11b}$$

$$\mathbb{I}_3 = \int_{h-l}^h \exp\left[U\frac{h - \xi}{h} - \frac{w_o}{l}(\xi - h)\right] d\xi. \tag{C.11c}$$

The term $w(\xi)$ from Eq. C.9 is expressed in Eq. C.11 in terms of the pore entrance length l, the nondimensional energy barrier $w_o = z_m^2 e^2/(k_B T)(\mathbb{F}_o - \mathbb{F}_e)$, and ξ (Fig. C.2). Evaluating the three definite integrals in Eq. C.11, and expressing the result in terms of the relative pore entrance length $n = l/h$ yields

$$\mathbb{I}_1 = \frac{nh}{w_o - Un}\left\{e^{w_o + U(1-n)} - e^U\right\}, \tag{C.12a}$$

$$\mathbb{I}_2 = -\frac{h}{U}\left\{e^{w_o + Un} - e^{w_o + U(1-n)}\right\}, \tag{C.12b}$$

$$\mathbb{I}_3 = -\frac{nh}{w_o + Un}\left\{1 - e^{w_o + Un}\right\}. \tag{C.12c}$$

Establishing two common denominators for the right side of Eqs. C.12a-C.12c, including the numerator from Eq. C.10, and algebraically simplifying yields Eq. 2.46 in Sec. 2.3.1,

$$j_m = \frac{D_m}{h}\frac{c_i e^U - c_e}{\dfrac{w_o e^{w_o - Un} - Un}{U\left(w_o - Un\right)}e^U - \dfrac{w_o e^{w_o + Un} + Un}{U\left(w_o + Un\right)}}. \tag{C.13}$$

Equation C.13 is not defined for $U = 0$, and an alternate equation must be derived. Setting $U = 0$ in Eqs. C.10 and C.11, yields

$$j_m = D_m \frac{c_i - c_e}{\displaystyle\int_0^l \exp\left[\frac{w_o}{l}\xi\right] d\xi + \int_l^{h-l} \exp\left[w_o\right] d\xi + \int_{h-l}^{h} \exp\left[-\frac{w_o}{l}\left(\xi - h\right)\right] d\xi}. \tag{C.14}$$

Evaluating the three definite integrals in the denominator of Eq. C.14, and expressing the result in terms of the relative pore entrance length $n = l/h$ yields Eq. 2.49 in Sec. 2.3.1,

$$j_m = \frac{D_m}{h}\frac{c_i - c_e}{\dfrac{2ne^{w_o}}{w_o} - \dfrac{2n}{w_o} + e^{w_o} - 2ne^{w_o}}. \tag{C.15}$$

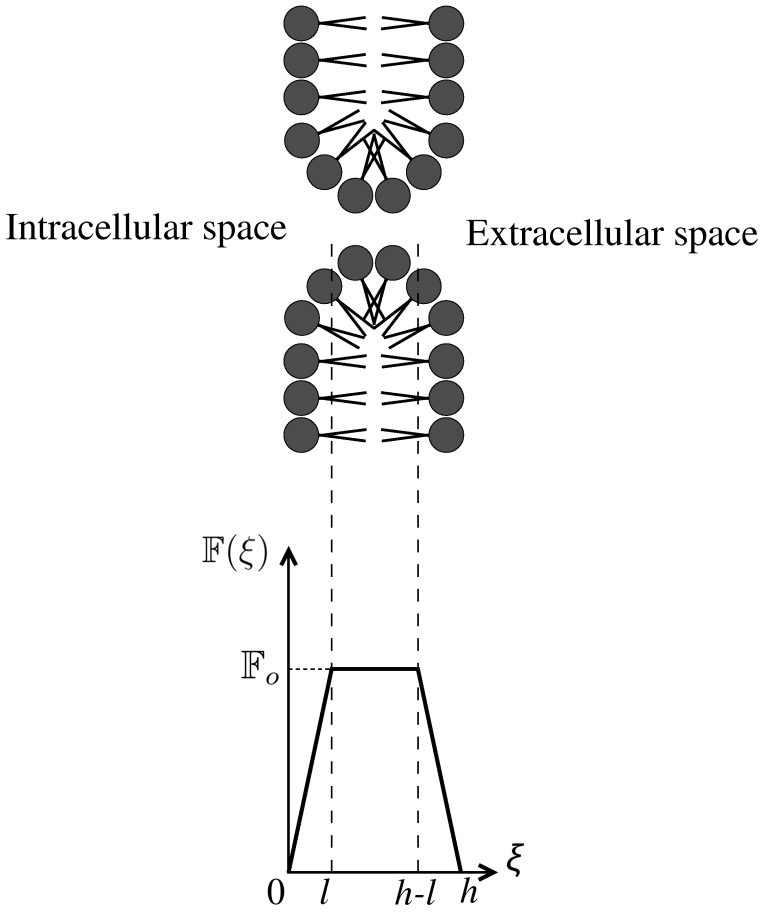

FIGURE C.2: Born energy profile shape used to derive the equation for molecular membrane flux through pores (Eq. 2.46). An illustration of a zoomed in view of a single pore in the membrane is shown, along the with intracellular and extracellular side of the membrane. The trapezoidal function $\mathbb{F}(\xi)$ used to determine the Born energy potential $\mathbb{B}(\xi)$ is shown below the membrane pore illustration. The function has a pore entrance length l, and a maximum value of $\mathbb{F}_o$ across the membrane thickness h.

Appendix D

Derivation of the Two-Compartment, 1D Longitudinal Molecular Diffusion Equations

The two-compartment, 1D longitudinal diffusion equations for molecular uptake (Sec. 2.3.2) are derived using the divergence theorem. The derivation begins with conservation of mass equations (Eqs. 2.43a and 2.43b in Sec. 2.3.1), repeated here for convenience,

$$\frac{\partial c_i}{\partial t} = \nabla \cdot \{D\nabla c_i - \mathbf{v_i} c_i\} \quad \text{in } \rho < a, \tag{D.1a}$$

$$\frac{\partial c_e}{\partial t} = \nabla \cdot \{D\nabla c_e - \mathbf{v_e} c_e\} \quad \text{in } a < \rho < R_b, \tag{D.1b}$$

First, Eq. D.1a governing the intracellular concentration c_i is considered. Using the divergence theorem, the integral of Eq. D.1a over the intracellular volume v_i is converted into an integral of the molecular flux normal to the boundaries M, $E_{i,1}$, and $E_{i,2}$ (Fig. D.1). Neglecting electric field transport (see Sec 2.3.2), the resulting equation is

$$\int_{v_i} \frac{\partial c_i}{\partial t} dv = D\left(\int_M \frac{\partial c_i}{\partial \rho} ds + \int_{E_{i,2}} \frac{\partial c_i}{\partial z} ds - \int_{E_{i,1}} \frac{\partial c_i}{\partial z} ds\right). \tag{D.2}$$

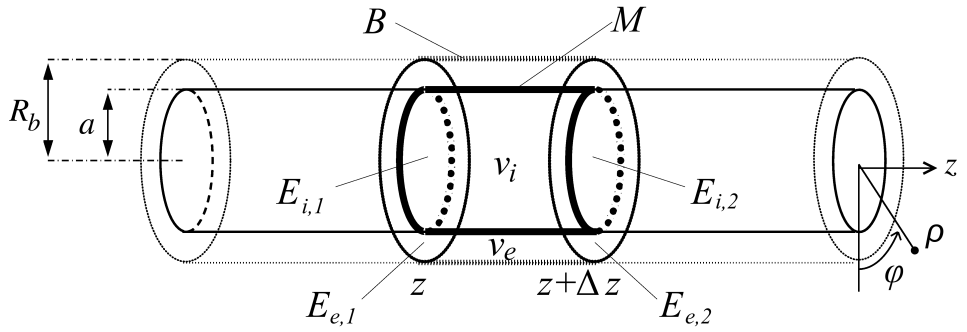

FIGURE D.1: Short length of fiber used to derive 1D molecular uptake equation (Eq. 2.54). Short length of fiber is Δz, that has intracellular and extracellular volumes v_i and v_e. The boundaries of the short length of fiber are membrane M, end caps $E_{i,1}$ to $E_{e,2}$, and extracellular boundary B. The quantity $R_b - a$ is one-half the distance between muscle fibers. No-flux boundary condition is applied on boundary B, and membrane flux j_m is applied on boundary M.

According to the continuity of flux condition (Eq. 2.45 in Sec. 2.3.1), $j_m = -D\partial c_i/\partial\rho$ if electric field transport is neglected, and Eq. D.2 becomes

$$\int_{v_i} \frac{\partial c_i}{\partial t} dv = -\int_M j_m ds + D\left(\int_{E_{i,2}} \frac{\partial c_i}{\partial z} ds - \int_{E_{i,1}} \frac{\partial c_i}{\partial z} ds\right), \tag{D.3}$$

which is Eq. 2.53a in Sec. 2.3.2.

Rewriting Eq. D.3 in terms of definite integrals results in

$$\begin{aligned}\int_z^{z+\Delta z}\int_0^{2\pi}\int_0^a \frac{\partial c_i}{\partial t}\rho\, d\rho\, d\varphi\, dz = &-a\int_z^{z+\Delta z}\int_0^{2\pi} j_m\, d\varphi\, dz \\ &+ D\int_0^{2\pi}\int_0^a \left(\left.\frac{\partial c_i}{\partial z}\right|_{z+\Delta z} - \left.\frac{\partial c_i}{\partial z}\right|_z\right)\rho\, d\rho\, d\varphi.\end{aligned} \tag{D.4}$$

Equation D.4 can be simplified by assuming c_i and membrane flux j_m are constant over the Δz interval, as well as assuming the "well-mixed" condition $c_i(\rho, \varphi, z) = c_i(z)$ (see Sec. 2.3.2). The result is

$$\pi a^2 \Delta z \frac{\partial c_i}{\partial t} = -a\Delta z \int_0^{2\pi} j_m\, d\varphi + D\pi a^2\left(\left.\frac{\partial c_i}{\partial z}\right|_{z+\Delta z} - \left.\frac{\partial c_i}{\partial z}\right|_z\right). \tag{D.5}$$

Expressing membrane flux in terms of the circumferential average $\overline{j_m}$, dividing by $\pi a^2 \Delta z$, and taking the limit $\Delta z \to 0$, Eq. D.5 is simplified to

$$\frac{\partial c_i}{\partial t} = D\frac{\partial^2 c_i}{\partial z^2} - \frac{2}{a}\overline{j_m}, \tag{D.6}$$

which is Eq. 2.54a in Sec. 2.3.2. Note the equation for circumferential average membrane flux,

$$\overline{j_m} = \frac{1}{2\pi}\int_0^{2\pi} j_m \, d\varphi. \tag{D.7}$$

A similar derivation is performed in the extracellular space, starting with the conservation of mass equation for extracellular concentration c_e (Eq. D.1b). Using the divergence theorem, the integral of Eq. D.1b over extracellular volume v_e (Fig. D.1) is converted into an integral of the molecular flux normal to the boundaries M, B, $E_{e,1}$, and $E_{e,2}$. Neglecting electric field transport (see Sec 2.3.2), the resulting equation is

$$\int_{v_e} \frac{\partial c_e}{\partial t} dv = D\left(-\int_M \frac{\partial c_e}{\partial \rho} ds + \int_{E_{e,2}} \frac{\partial c_e}{\partial z} ds - \int_{E_{e,1}} \frac{\partial c_e}{\partial z} ds + \int_B \frac{\partial c_e}{\partial \rho} ds\right). \tag{D.8}$$

According to the continuity of flux condition (Eq. 2.45 in Sec. 2.3.1), $j_m = -D\partial c_e/\partial \rho$ if electric field transport is neglected, and Eq. D.8 becomes

$$\int_{v_e} \frac{\partial c_e}{\partial t} dv = \int_M j_m ds + D\left(\int_{E_{e,2}} \frac{\partial c_e}{\partial z} ds - \int_{E_{e,1}} \frac{\partial c_e}{\partial z} ds + \int_B \frac{\partial c_e}{\partial \rho} ds\right), \tag{D.9}$$

which is Eq. 2.53b in Sec. 2.3.2.

An additional assumption is added that in the extracellular region the flux normal to the extracellular boundary B in Fig. D.1 is zero, i.e., the last term on the right side of Eq. D.9 is zero. This assumption is made with the knowledge that muscle fibers are packed tightly, so that the dynamics of electroporation and the resulting

uptake of molecules is very similar from one fiber to its adjacent neighbors in the tissue. If each fiber behaves similarly to its neighbors, then the no-flux boundary condition on boundary B is valid. Using the no-flux boundary condition on boundary B, and rewriting Eq. D.9 in terms of definite integrals results in

$$\begin{aligned}\int_z^{z+\Delta z}\int_0^{2\pi}\int_a^{R_b}\frac{\partial c_e}{\partial t}\rho\,d\rho\,d\varphi\,dz =& a\int_z^{z+\Delta z}\int_0^{2\pi} j_m\,d\varphi\,dz \\ &+ D\int_0^{2\pi}\int_a^{R_b}\left(\left.\frac{\partial c_e}{\partial z}\right|_{z+\Delta z} - \left.\frac{\partial c_e}{\partial z}\right|_z\right)\rho\,d\rho\,d\varphi.\end{aligned} \tag{D.10}$$

Equation D.10 can be simplified by assuming c_e and membrane flux j_m are constant over the Δz interval, as well as assuming the "well-mixed" condition $c_e(\rho,\varphi,z) = c_e(z)$ (see Sec. 2.3.2). The result is

$$\pi(R_b^2-a^2)\Delta z\frac{\partial c_e}{\partial t} = a\Delta z\int_0^{2\pi} j_m\,d\varphi + D\pi(R_b^2-a^2)\left(\left.\frac{\partial c_e}{\partial z}\right|_{z+\Delta z} - \left.\frac{\partial c_e}{\partial z}\right|_z\right). \tag{D.11}$$

Expressing membrane flux in terms of the circumferential average $\overline{j_m}$, dividing by $\pi(R_b^2-a^2)\Delta z$, and taking the limit $\Delta z\to 0$, Eq. D.11 is simplified to

$$\frac{\partial c_e}{\partial t} = D\frac{\partial^2 c_e}{\partial z^2} + \frac{2a}{R_b^2-a^2}\overline{j_m}, \tag{D.12}$$

which is Eq. 2.54b in Sec. 2.3.2. Taken together, Eqs. D.6 and D.12 describe the two-compartment, 1D longitudinal diffusion problem with flux on the membrane $\overline{j_m}$ connecting the intracellular and extracellular compartments.

Appendix E

Justification for Initial Uniform Interstitial Molecular Concentration

This simplification is justified by first making an estimate of the length scale of diffusion in a 2D cross section transverse to the muscle fibers before the electric pulse is turned on: $L_{d,0} = \sqrt{4Dt_{d,0}}$, where $t_{d,0}$ is the time the molecule has to diffuse in the interstitial space pre-pulse. Diffusion coefficient D is taken from Table 2.4. Time $t_{d,0}$ is estimated from experiments using the following logic. Most of the parameters involved in pulsing protocol and tissue geometries are based on small molecule uptake experiments by Grafstrom et al. and Engstrom et al.[31,32] In these experiments, a molecule with molecular weight 416 Da was introduced into the body of a rat via the femoral vein, and two minutes were allowed to pass before the electric pulse was applied to the soleus muscle. This is the time the molecule is allowed to reach the target muscle tissue, cross the blood vessel, and diffuse in the interstitial space. For small molecules with molecular weight of approximately 400 Da, the delivery is assumed limited by convection of the drug in blood vessels, and thus transport across the vessel wall is assumed nearly instantaneous.[115] Whole-body

pharmacokinetic models and experiments have shown that concentration of small molecules reach maximum in muscle within one to two minutes.[145] If it is assumed maximum concentration in muscle is achieved within one-and-a-half minutes, and that this time lapse accounts for circulation time only so there is no interstitial diffusion up until one-and-a-half minutes, then the molecules have thirty seconds to diffuse in the interstitial space before the pulse is turned on at the two-minute mark. Thus, the length scale of diffusion is $L_{d,0} = \sqrt{(4)(2.01\text{x}10^{-10})(30)} = 155$ μm.

The length scale of diffusion, $L_{d,0} = 155$ μm is compared to the maximum length scale associated with the interstitial space. Experiments have shown that in a transverse cross section of muscle tissue, there is at least one capillary per muscle fiber, as shown in Fig. 1.2C.[20,121] Assuming at least one capillary runs parallel to each fiber, only the 2D transverse cross section is of concern, and the maximum length scale of the interstitial space is the circumference around each fiber in the interstitial space. For the case of interfiber distance being 1 μm, the extracellular boundary radius is $R_b = 25.5$ μm, and the circumference is 160 μm. With a diffusion distance of 155 μm, and maximal interstitial length scale of 160 μm, assuming uniform interstitial concentration immediately before the pulse is turned on is expected to be fairly accurate. However, a global pharmacokinetic analysis of the molecule's transport in the entire body, as well as microscale models of mass transport across the blood vessels and within the interstitial space would need to be developed in order to fully justify this assumption.

Bibliography

1. C. Trollet, C. Bloquel, D. Scherman, and P. Bigey. Electrotransfer into skeletal muscle for protein expression. *Curr. Gene. Ther.*, 6(5):561–578, 2006.

2. J. Gehl. Electroporation: theory and methods, perspectives for drug delivery, gene therapy and research. *Acta Physiol. Scand.*, 177(4):437–447, 2003.

3. D. Luo and W. M. Saltzman. Synthetic DNA delivery systems. *Nat. Biotechnol.*, 18(1):33–37, 2000.

4. F. Andre and L. M. Mir. DNA electrotransfer: its principles and an updated review of its therapeutic applications. *Gene. Ther.*, 11:S33–S42, 2004.

5. K.B. Kaufmann, H. Buning, A. Galy, A. Schambach, and M. Grez. Gene therapy on the move. *EMBO Mol. Med.*, 5(11):1642–1661, 2013.

6. M. Cemazar, M. Golzio, G. Sersa, M. P. Rols, and J. Teissie. Electrically-assisted nucleic acids delivery to tissues *in vivo*: Where do we stand? *Curr. Pharm. Design.*, 12(29):3817–3825, 2006.

7. J. M. McMahon and D. J. Wells. Electroporation for gene transfer to skeletal muscles. *Biodrugs*, 18(3):155–165, 2004.

8. E. Marshall. Gene therapy death prompts review of adenovirus vector. *Science*, 286(5448):2244, 1999.

9. X-D. Wang, J-G. Tang, X-L. Xie, J-C. Yang, S. Li, J-G. Ji, and J. Gu. A comprehensive study of optimal conditions for naked plasmid DNA transfer into skeletal muscle by electroporation. *J. Gene. Med.*, 7(9):1235–1245, 2005.

10. D. Rabussay, N. B. Dev, J. Fewell, L. C. Smith, G. Widera, and L. Zhang. Enhancement of therapeutic drug and DNA delivery into cells by electroporation. *J. Phys. D. Appl. Phys.*, 36(4):348, 2003.

11. J. Gehl and L. M. Mir. Determination of optimal parameters for *in vivo* gene transfer by electroporation, using a rapid *in vivo* test for cell permeabilization. *Biochem. Bioph. Res. Co.*, 261(2):377–380, 1999.

12. U. Cegovnik and S. Novakovic. Setting optimal parameters for *in vitro* electrotransfection of B16F1, SA1, LPB, SCK, L929 and CHO cells using predefined exponentially decaying electric pulses. *Bioelectrochemistry*, 62(1):73–82, 2004.

13. D. Sel, A. M. Lebar, and D. Miklavcic. Feasibility of employing model-based optimization of pulse amplitude and electrode distance for effective tumor electropermeabilization. *IEEE T. Bio-Med. Eng.*, 54(5):773–781, 2007.

14. M-P. Rols and J. Teissie. Electropermeabilization of mammalian cells to macromolecules: Control by pulse duration. *Biophys. J.*, 75(3):1415–1423, 1998.

15. M-P. Rols, C. Delteil, M. Golzio, P. Dumond, S. Cros, and J. Teissie. *In vivo* electrically mediated protein and gene transfer in murine melanoma. *Nat. Biotechnol*, 16(2):168–171, 1998.

16. Q. L. Lu, G Bou-Gharios, and T. A. Partridge. Non-viral gene delivery in skeletal muscle: a protein factory. *Gene. Ther.*, 10(2):131–142, 2003.

17. P. Hojman. Basic principles and clinical advancements of muscle electrotransfer. *Curr. Gene Ther.*, 10(2):128–138, 2010.

18. L. Low, A. Mander, K. McCann, D. Dearnaley, T. Tjelle, I. Mathiesen, F. Stevenson, and Ottensmeier. C. H. DNA vaccination with electroporation induces increased antibody responses in patients with prostate cancer. *Hum. Gene. Ther.*, 20(11):1269–1278, 2009.

19. R-J. Hsu, K-M. Hsiao, M-J. Lin, C-Y. Li, L-C. Wang, L-K. Chen, and H. Pan. Long tract of untranslated CAG repeats is deleterious in transgenic mice. *Plos One*, 6(1):e16417, 2011.

20. G.M. Camerino, S. Pierno, A. Liantonio, M. D. Bellis, M. Cannone, V. Sblendorio, E. Conte, A. Mele, D. Tricarico, S. Tavella, A. Ruggiu, R. Cancedda, Y. Ohira, D. Danieli-Betto, S. Ciciliot, E. Germinario, D. Sandona, R. Betto, D. C. Camerino, and J-F. Desaphy. Effects of pleiotrophin overexpression on mouse skeletal muscles in normal loading and in actual and simulated microgravity. *Plos One*, 8(8):e72028, 2013.

21. H. Aihara and J. Miyazaki. Gene transfer into muscle by electroporation *in vivo*. *Nat. Biotechnol.*, 16(9):867–870, 1998.

22. G. Rizzuto, M. Cappelletti, C. Mennuni, M. Wiznerowicz, A. DeMartis, D. Maione, G. Ciliberto, N. A. Monica, and E. Fattori. Gene electrotransfer results in a high-level transduction of rat skeletal muscle and corrects anemia of renal failure. *Hum. Gene. Ther.*, 11(13):1891–1900, 2000.

23. I. Mathiesen. Electropermeabilization of skeletal muscle enhances gene transfer *in vivo*. *Gene. Ther.*, 6(4):508, 1999.

24. F. Andre and L. M. Mir. DNA electrotransfer: its principles and an updated review of its therapeutic applications. *Gene. Ther.*, 11(Suppl 1):S33–S42, 2004.

25. X-D. Wang, J-G. Tang, X-L. Xie, J-C. Yang, S. Li, J-G. Ji, and J. Gu. A comprehensive study of optimal conditions for naked plasmid DNA transfer into skeletal muscle by electroporation. *J. Gene. Med.*, 7(9):1235–1245, 2005.

26. I. Zampaglione, M. Arcuri, M. Cappelletti, G. Ciliberto, G. Perretta, A. Nicosia, N. L. Monica, and E. Fattori. *In vivo* DNA gene electro-transfer: a systematic analysis of different electrical parameters. *J. Gene Med.*, 7(11):1475–1481, 2005.

27. D. Yin and J-G. Tang. Gene therapy for streptozotocin-induced diabetic mice by electroporational transfer of naked human insulin precursor DNA into skeletal muscle *in vivo*. *FEBS Lett.*, 495(1-2):16–20, 2001.

28. L. M. Mir, M. F. Bureau, J. Gehl, R. Rangara, D. Rouy, J-M. Caillaud, P. Delaere, D. Branellec, B. Schwartz, and D. Scherman. High-efficiency gene transfer into skeletal muscle mediated by electric pulses. *Proc. Natl. Acad. Sci. USA*, 96(8):4262–4267, 1999.

29. S. Corovic, A. Zupanic, S. Kranjc, B. A. Sakere, A. Leroy-Willg, L. M. Mir, and D. Miklavcic. The influence of skeletal muscle anisotropy on electroporation: *in vivo* study and numerical modeling. *Med. Biol. Eng. Comput.*, 48(7):637–648, 2010.

30. J. Gehl, T. H. Sorensen, K. Nielsen, P. Raskmark, S. L. Nielsen, T. Skovsgaard, and L. M. Mir. *In vivo* electroporation of skeletal muscle: threshold, efficacy and relation to electric field distribution. *BBA-Gen. Subjects*, 1428(2-3):233–240, 1999.

31. G. Grafstrom, P. Engstrom, L. G. Salford, and B. R. R. Persson. 99mtc-dtpa uptake and electrical impedance measurements in verification of *in vivo* electropermeabilization efficiency in rat muscle. *Cancer Biother. Radio.*, 21(6):623–635, 2006.

32. P. E. Engstrom, B. R. Persson, and L. G. Salford. Studies of *in vivo* electropermeabilization by gamma camera measurements of (99m)Tc-DTPA. *Biochim. Biophys. Acta.*, 27(2-3):321–328, 1999.

33. C. Faurie, M. Golzio, P. Moller, J. Teissie, and M. P. Rols. Cell and animal imaging of electrically mediated gene transfer. *DNA Cell. Biol.*, 22(12):777–783, 2003.

34. S. Satkauskas, M. F. Bureau, M. Puc, A. Mahfoudi, D. Scherman, D. Miklavicic, and L. M. Mir. Mechanisms of *in vivo* DNA electrotransfer: respective contributions of cell electropermeabilization and DNA electrophoresis. *Mol. Ther.*, 5(2):133–140, 2002.

35. C. Chen, S. W. Smye, M. P. Robinson, and J. A. Evans. Membrane electroporation theories: a review. *Med. Biol. Eng. Comput.*, 44(1-2):5–14, 2006.

36. M. Tarek. Membrane electroporation: A molecular dynamics simulation. *Biophys. J.*, 88(6):4045–4053, 2005.

37. H. Leontiadou, A. E. Mark, and S. J. Marrink. Molecular dynamics simulations of hydrophilic pores in lipid bilayers. *Biophys. J.*, 86(4):2156–2164, 2004.

38. Q. Hu, S. Viswanadham, R. P. Joshi, K. H. Schoenbach, S. J. Beebe, and P. F. Blackmore. Simulations of transient membrane behavior in cells subjected to a high-intensity ultrashort electric pulse. *Phys. Rev. E*, 71(3):031914, 2005.

39. S. I. Sukharev, V. A. Klenchin, S. M. Serov, L. V. Chernomordik, and A. Chizmadzhev Yu. Electroporation and electrophoretic DNA transfer into cells. The effect of DNA interaction with electropores. *Biophys. J.*, 63(5):1320–1327, 1992.

40. B. J. Mossop, R. C. Barr, J. W. Henshaw, and F. Yuan. Electric fields around and within single cells during electroporation–A model study. *Ann. Biomed. Eng.*, 35(7):1264–1275, 2007.

41. A. Barnett and J. C. Weaver. Electroporation: A unified, quantitative theory of reversible electrical breakdown and mechanical rupture in artificial planar bilayer membranes. *Bioelectroch. Bioener.*, 25(2):163–182, 1991.

42. R. P. Joshi and K. H. Schoenbach. Electroporation dynamics in biological cells subjected to ultrafast electrical pulses: A numerical simulation study. *Phys. Rev. E*, 62(1):1025, 2000.

43. R. P. Joshi, Q. Hu, K. H. Schoenbach, and H. P. Hjalmarson. Improved energy model for membrane electroporation in biological cells subjected to electrical pulses. *Phys. Rev. E*, 65(4):041920, 2002.

44. S. A. Freeman, M. A. Wang, and J. C. Weaver. Theory of electroporation of planar bilayer membranes: Predictions of the aqueous area, change in capacitance, and pore-pore separation. *Biophys. J.*, 67(1):42–56, 1994.

45. R. P. Joshi, Q. Hu, K. H. Schoenbach, and H. P. Hjalmarson. Theoretical predictions of electromechanical deformation of cells subjected to high voltages for membrane electroporation. *Phys. Rev. E*, 65(2):021913, 2002.

46. R. P. Joshi, Hu Qin, and K. H. Schoenbach. Modeling studies of cell response to ultrashort, high-intensity electric fields-implications for intracellular manipulation. *IEEE T. Plasma Sci.*, 32(4):1677–1686, 2004.

47. R. P. Joshi, Q. Hu, K. H. Schoenbach, and S. J. Beebe. Energy-landscape-model analysis for irreversibility and its pulse-width dependence in cells subjected to a high-intensity ultrashort electric pulse. *Phys. Rev. E*, 69(5):051901, 2004.

48. J. C. Neu and W. Krassowska. Asymptotic model of electroporation. *Phys. Rev. E*, 59(3):3471, 1999.

49. J. C. Neu and W. Krassowska. Modeling postshock evolution of large electropores. *Phys. Rev. E*, 67(2):021915, 2003.

50. J. C. Neu, K. C. Smith, and W. Krassowska. Electrical energy required to form large conducting pores. *Bioelectrochemistry*, 60(1-2):107–114, 2003.

51. K. C. Smith, J. C. Neu, and W. Krassowska. Model of creation and evolution of stable electropores for DNA delivery. *Biophys. J.*, 86(5):2813–2826, 2004.

52. Y. Granot and B. Rubinsky. Mass transfer model for drug delivery in tissue cells with reversible electroporation. *Int. J. Heat. Mass. Transf.*, 51(23-24):5610–5616, 2008.

53. W. Krassowska and P. D. Filev. Modeling electroporation in a single cell. *Biophys. J.*, 92(2):404–417, 2007.

54. K. A. DeBruin and W. Krassowska. Modeling electroporation in a single cell: I. Effects of field strength and rest potential. *Biophys. J.*, 77(3):1213–1224, 1999.

55. A. Esser. Towards solid tumor treatment by irreversible electroporation: Intrinsic redistribution of fields and currents in tissue. *Technol. Cancer Res. T.*, 6(4):261–273, 2007.

56. K. A. DeBruin and W. Krassowska. Modeling electroporation in a single cell: II. Effects of ionic concentrations. *Biophys. J.*, 77(3):1225–1233, 1999.

57. D. A. Stewart, T. R. Gowrishankar, and J. C. Weaver. Transport lattice approach to describing cell electroporation: Use of a local asymptotic model. *IEEE T. Plasma. Sci.*, 32(4):1696–1708, 2004.

58. Q. Hu, S. Viswanadham, R. P. Joshi, K. H. Schoenbach, S. J. Beebe, and P. F. Blackmore. Simulations of transient membrane behavior in cells subjected to a high-intensity ultrashort electric pulse. *Phys. Rev. E.*, 71(3 Pt 1):031914–1 – 031914–9, 2005.

59. R. P. Joshi, A. S. Mishra, K. H. Schoenbach, and A. Pakhomov. Self-consistent analyses for potential conduction block in nerves by an ultra-short, high-intensity electric pulse. *Phys. Rev. E.*, 75(6 Pt 1):061906–1 – 061906–11, 2007.

60. F. Rattay. Analysis of models for external stimulation of axons. *IEEE T. Bio-Med. Eng.*, 33(10):974–977, 1986.

61. F. Rattay. Analysis of models for extracellular fiber stimulation. *IEEE T. Bio-med. Eng.*, 36(7):676–682, 1989.

62. B. J. Roth. Mechanisms for electrical-stimulation of excitable tissue. *Crit. Rev. Biomed. Eng.*, 22(3-4):253–305, 1994.

63. S. B. Knisley, B. C. Hill, and R. E. Ideker. Virtual electrode effects in myocardial fibers. *Biophys. J.*, 66(3):719–728, 1994.

64. E. A. Sobie, R. C. Susil, and L. Tung. A generalized activating function for predicting virtual electrodes in cardiac tissue. *Biophys. J.*, 73(3):1410–1423, 1997.

65. N. Trayanova, K. Skouibine, and P. Moore. Virtual electrode effects in defibrillation. *Prog. Biophys. Mol. Bio.*, 69(2-3):387–403, 1998.

66. P. J. Basser and B. J. Roth. New currents in electrical stimulation of excitable tissues. *Annu. Rev. Biomed. Eng.*, 2(1):377, 2000.

67. V. Schnabel and J. J. Struijk. Evaluation of the cable model for electrical stimulation of unmyelinated nerve fibers. *IEEE T. Bio-Med. Eng.*, 48(9):1027–1033, 2001.

68. H. Yu, C. Zheng, and Y. Wang. Improved cable function to represent the excitation of peripheral nerves. *First international conference on Neural Interface and control proceedings*, May 26-28(Wuhan, China):135–138, 2005.

69. W. Krassowska and J. C. Neu. Response of a single cell to an external electric field. *Biophys. J.*, 66(6):1768–1776, 1994.

70. K. Altman and R. Plonsey. Development of a model for point source electrical fibre bundle stimulation. *Med. Biol. Eng. Comput.*, 26(5):466–475, 1988.

71. R. P. Joshi and J. Song. Model analysis of electric fields induced by high-voltage pulsing in cylindrical nerves. *IEEE T. Plasma Sci.*, 38(10):2894–2900, 2010.

72. Y. Stickler, J. Martinek, and F. Rattay. Modeling needle stimulation of denervated muscle fibers: voltage-distance relations and fiber polarization effects. *IEEE T. Bio-med. Eng.*, 56(10):2396–2403, 2009.

73. S. Corovic, M. Pavlin, and D. Miklavcic. Analytical and numerical quantification and comparison of the local electric field in the tissue for different electrode configurations. *Biomed. Eng. Online*, 6, 2007.

74. S. B. Dev, D. Dhar, and W. Krassowska. Electric field of a six-needle array electrode used in drug and DNA delivery *in vivo*: Analytical versus numerical solution. *IEEE T. Bio-Med. Eng.*, 50(11):1296–1300, 2003.

75. L. Guo, J. P. Cranford, J. C. Neu, and W. K. Neu. Activating function of needle electrodes in anisotropic tissue. *Med. Biol. Eng. Comput.*, 47(9):1001–1010, 2009.

76. S. Corovic, L. M. Mir, and D. Miklavcic. *In vivo* muscle electroporation threshold determination: realistic numerical models and *in vivo* experiments. *J. Membr. Biol.*, 245(9):509–520, 2012.

77. E. Neumann, S. Kakorin, and K. Toensing. Fundamentals of electroporative delivery of drugs and genes. *Bioelectroch. Bioener.*, 48(1):3–16, 1999.

78. B. J. Roth. The electrical properties of tissues. In Joseph D. Bronzino, editor, *The Biomedical Engineering Handbook*, pages 126–138. CRC Press, Boca Raton, FL, 1995.

79. A. T. Esser, K. C. Smith, T. R. Gowrishankar, and J. C. Weaver. Towards solid tumor treatment by nanosecond pulsed electric fields. *Technol. Cancer. Res. Treat.*, 8(4):289–306, 2009.

80. T. R. Gowrishankar, K. C. Smith, and J. C. Weaver. Transport-based biophysical system models of cells for quantitatively describing responses to electric fields. *Proc. IEEE*, 101(2):505–517, 2012.

81. T. R. Gowrishankar and J. C. Weaver. An approach to electrical modeling of single and multiple cells. *P Natl. Acad. Sci. USA*, 100(6):3203–3208, 2003.

82. F. Aguel, K. A. Debruin, W. Krassowska, and N. A. Trayanova. Effects of electroporation on the transmembrane potential distribution in a two-dimensional bidomain model of cardiac tissue. *J. Cardiovasc. Electr.*, 10(5):701–714, 1999.

83. T. Ashihara and N. A. Trayanova. Cell and tissue responses to electric shocks. *Europace*, 7(s2):S155–165, 2005.

84. D. A. Zaharoff, J. W. Henshaw, B. Mossop, and F. Yuan. Mechanistic analysis of electroporation-induced cellular uptake of macromolecules. *Exp. Biol. Med.*, 233(1):94–105, 2008.

85. J. W. Henshaw and F. Yuan. Field distribution and DNA transport in solid tumors during electric field-mediated gene delivery. *J. Pharm. Sci.*, 97(2):69–711, 2008.

86. J. Li and H. Lin. Numerical simulation of molecular uptake via electroporation. *Bioelectrochemistry*, 82(1):10–21, 2011.

87. S. Movahed and D. Li. Electrokinetic transport through the nanopores in cell membrane during electroporation. *J. Colloid Interface Sci.*, 369(1):442–452, 2012.

88. E. Neumann, S. Kakorin, I. Tsoneva, B. Nikolova, and T. Tomov. Calcium-mediated DNA adsorption to yeast cells and kinetics of cell transformation by electroporation. *Biophys. J.*, 71(2):868–877, 1996.

89. M. Wu and F. Yuan. Membrane binding of plasmid DNA and endocytic pathways are involved in electrotransfection of mammalian cells. *Plos One*, 6(6):e20923, 2011.

90. M. Breton, L. Delemotte, A. Silve, L. M. Mir, and M. Tarek. Transport of sirna through lipid membranes driven by nanosecond electric pulses: An experimental and computational study. *J. Am. Chem. Soc.*, 134(34):13938–13941, 2012.

91. H. Leontiadou, A. Mark, and S. J. Marrink. Molecular dynamics simulations of hydrophilic pores in lipid bilayers. *Biophys. J.*, 86(4):2156–2164, 2004.

92. J. C. Neu and W. Krassowska. Homogenization of syncytial tissues. *Crit. Rev. Biomed. Eng.*, 21(2):137–199, 1993.

93. E. J. Hinch. *Perturbation methods*. Cambridge University Press, Cambridge, UK, 1991.

94. G. Dahlquist and A. Bjorck. *Numerical methods*. Prentice-Hall, Englewood Cliffs, NJ, 1974.

95. J. Crank and P. Nicolson. Practical method for numerical evaluation of solutions of partial differential equations of the heat conduction type. *Proc. Cambridge Phil. Soc.*, 43(1):50–67, 1947.

96. A. L. Hodgkin and W. A. H. Rushton. The electrical constants of a crustacean nerve fibre. *Proc. R. Soc. Lond. B3*, 133(873):444–479, 1946.

97. C. Dixon. *Applied Mathematics of Science and Engineering*. John Wiley & Sons, New York, NY, 1971.

98. J. P. Cranford, B. J. Kim, and W. K. Neu. Asymptotic model of electrical stimulation of nerve fibers. *Med. Biol. Eng. Comput.*, 50(3):243–251, 2012.

99. J.P. Wikswo Jr., S.F. Lin, and R. A. Abbas. Virtual electrodes in cardiac tissue: A common mechanism for anodal and cathodal stimulation. *Biophys. J.*, 69(6):2195–2210, 1995.

100. R. W. Glaser, S. L. Leikin, L. V. Chernormordik, V. F. Pastushenko, and A. L. Sokirko. Reversible electrical breakdown of lipid bilayers: formation and evolution of pores. *Biochim. Biophys. Acta.*, 940(2):275–287, 1988.

101. A. Barnett. The current-voltage relation of an aqueous pore in a lipid bilayer membrane. *Biochim. Biophys. Acta.*, 1025(1):10–14, 1990.

102. V. A. Parsegian. Ion-membrane interactions as structural forces. *Ann. NY. Acad. Sci.*, 264(1):161–174, 1975.

103. A. Zupanic, S. Corovic, D. Miklavcic, and M. Pavlin. Numerical optimization of gene electrotransfer into muscle tissue. *Biomed. Eng. Online*, 9(66):1–20, 2010.

104. K. R. Foster. Dielectric properties of tissues. In Joseph D. Bronzino, editor, *The Biomedical Engineering Handbook: Second Edition*. CRC Press, Boca Raton, FL, 1999.

105. F. L. H. Gielen, H. E. P. Cruts, B. A. Albers, K. L. Boon, and W. W-d. Jonge. Model of electrical conductivity of skeletal muscle based on tissue structure. *Med. Biol. Eng. Comput.*, 24(1):34–40, 1986.

106. R. S. Staron, W. J. Kraemer, R. S. Hikida, A. C. Fry, J. D. Murray, and G. E. Campos. Fiber type composition of four hindlimb muscles of adult fisher 344 rats. *Histochem. Cell. Biol.*, 111(2):117–123, 1999.

107. J. W. Heslinga and P. A. Huijing. Effects of growth on architecture and functional characteristics of adult rat gastrocnemius muscle. *J. Morphol.*, 206(1):119–132, 1990.

108. C. C. Peixinho, C. M. Resende, L. F. de Oliveira, and J. C. Machado. Ultrasound biomicroscopy for *in vivo* architectural characterization of gastrocnemius muscle from rats. *Conf. Proc. IEEE Eng. Med. Biol. Soc.*, 2010(1):4723–4726, 2010.

109. S. S. Segal, T. P. White, and J. A. Faulkner. Architecture, composition, and contractile properties of rat soleus muscle grafts. *Am. J. Physiol.*, 1986(3 Pt. 1):C474–C479, 1986.

110. S. V Gudjonsson. The body temperature in rats on normal and deficient diets. *J. Physiol.*, 74(1):73–80, 1932.

111. J. S. Schultz and W. Armstrong. Permeability of interstitial space of muscle (rat diaphragm) to solutes of different molecular weights. *J. Pharm. Sci.*, 67(5):696–700, 1978.

112. M. Arrio-Dupont, S. Cribier, G. Foucault, P. F. Devaux, and A. d'Albis. Diffusion of fluorescently labeled macromolecules in cultured muscle cells. *Biophys. J.*, 70(5):2327–2332, 1996.

113. A. S. Verkman. Solute and macromolecule diffusion in cellular aqueous compartments. *Trends Biochem. Sci.*, 27(1):27–33, 2002.

114. R. Plonsey and R. C. Barr. *Bioelectricity: A Quantitative Approach (2nd Edition)*. Kluwer Academic/Plenum Publishers, New York, NY, 2000.

115. G. A. Truskey, F. Yuan, and D. F. Katz. *Transport Phenomena in Biological Systems*. Pearson Prentice Hall, Upper Saddle River, NJ, 2004.

116. G. Pucihar, T. Kotnik, D. Miklavcic, and J. Teissie. Kinetics of transmembrane transport of small molecules into electropermeabilized cells. *Biophys. J.*, 95(6):2837–2848, 2008.

117. M. Puc, T. Kotnik, L. M. Mir, and Miklavcic D. Quantitative model of small molecules uptake after *in vitro* cell electropermeabilization. *Bioelectrochemistry*, 60(1-2):1–10, 2003.

118. M. Kanduser and Miklavcic D. Electroporation in biological cell and tissue: An overview. In E. Vorobiev and N. Lebovka, editors, *Electrotechnologies for Extraction from Food Plants and Biomaterials*. Springer Science+Business Media.

119. P. Nelson. *Biological Physics: Energy, Information, Life*. W.H. Freeman and Company, New York, NY, 2004.

120. J. C. Bruusgaard, K. Liestol, M. Ekmark, K. Kollstad, and K. Gundersen. Number and spatial distribution of nuclei in the muscle fibres of normal mice studied *in vivo*. *J. Physiol.*, 551(1):467–478, 2003.

121. A. B. Borisov, S-K. Huang, and B. M. Carlson. Remodeling of the vascular bed and progressive loss of capillaries in denervated muscle. *Anat. Rec.*, 258(3):292–304, 2000.

122. H. B. Lee and M. D. Blaufox. Blood volume in the rat. *J. Nucl. Med.*, 26(1):72–76, 1985.

123. M. Kranjc, F. Bajd, I. Sersa, E. J. Woo, and D. Miklavcic. *Ex vivo* and in silico feasibility study of monitoring electric field distribution in tissue during electroporation based treatments. *Plos One*, 7(9):e45737, 2012.

124. R. E. Neal, P. A. Garcia, J. L. Robertson, and R. V. Davalos. Experimental characterization of intrapulse tissue conductivity changes for electroporation. *Proceedings of the 33rd Annual IEE EMBS International Conference*, August 30 - September 3(Boston, Massachusetts, USA):5581–5584, 2011.

125. S. Davorka, D. Cukjati, T. S. Batiuskaite, L. M. Mir, and D. Miklavcic. Sequential finite element model of tissue electropermeabilization. *IEEE Bio-med. Eng.*, 52(5):816–827, 2005.

126. S. Corovic, I. Lackovic, P. Sustaric, T. Sustar, T. Rodic, and D. Miklavcic. Modeling of electric field distribution in tissues during electroporation. *Biomed. Eng. Online*, 12(16):10.1186/1475–925X–12–16, 2013.

127. K. W. Altman and R. Plonsey. Development of a model for point source electrical fibre bundle stimulation. *Med. Biol. Eng. Comput.*, 26(5):466–475, 1988.

128. W. Rall. Distributions of potential in cylindrical coordinates and time constants for a membrane cylinder. *Biophys. J.*, 9(12):1509–1541, 1988.

129. D. R. McNeal. Analysis of a model for excitation of myelinated nerve. *IEEE T Bio-Med Eng*, 23(4):329–337, 1976.

130. J. Ruohonen, P. Ravazzani, J. Nilsson, M. Panizza, F. Grandori, and G. Tognola. A volume-conduction analysis of magnetic stimulation of peripheral nerves. *IEEE T Bio-Med Eng*, 43(7):669–678, 1996.

131. Y. Wang, Q. Shen, and D. Jiang. A modified cable function for represent the excitation of peripheral nerves by transverse field induced by pulsed magnetic field. *Proceedings of the 23rd Annual EMBS International Conference*, October 25-28(Istanbul, Turkey):896–898, 2001.

132. V. A. Klenchin, S. I. Sukharev, S. M. Serov, L. V. Chernomordik, and Y. A. Chizmadzhev. Electrically induced DNA uptake by cells is a fast process involving DNA electrophoresis. *Biophys. J.*, 60(4):804–811, 1991.

133. H. Wolf, M. P. Rols, E. Boldt, e. Neumann, and J. Teissie. Control by pulse parameters of electric field-mediated gene transfer in mammalian cells. *Biophys. J.*, 66(2 Pt 1):524–531, 1994.

134. M. Dona, M. Sandri, K. Rossini, I. Dell'Aica, M. Podhorska-Okolow, and U. Carraro. Functional *in vivo* gene transfer into the myofibers of adult skeletal muscle. *Biochem. Bioph. Res. Co.*, 312(4):1132–1138, 2003.

135. M. Hibino, M. Shigemori, H. Itoh, K. Nagayama, and K. Jr. Kinosita. Membrane conductance of an electroporated cell analyzed by submicrosecond imaging of transmembrane potential. *Biophys. J.*, 59(1):209–220, 1991.

136. K. Kinosita Jr., I. Ashikawa, N. Saita, H. Yoshimura, H. Itoh, N. Nagayama, and A. Ikegami. Electroporation of cell membrane visualized under a pulsed-laser fluorescence microscope. *Biophys. J.*, 53(6):1015–1019, 1988.

137. B. Katz. The electrical properties of the muscle fibre membrane. *Proc. R. Soc. Lond. B*, 135(881):506–534, 1948.

138. R. L. Milton, R. T. Mathias, and R. S. Eisenberg. Electrical properties of the myotendon region of frog twitch muscle fibers measured in the frequency domain. *Biophys. J.*, 48(2):253–267, 1985.

139. K. DeBruin and W. Krassowska. Electroporation and shock-induced transmembrane potential in a cardiac fiber during defibrillation strength shocks. *Ann. Biomed. Eng.*, 26(4):584–596, 1988.

140. D. C. Chang and T. S. Reese. Changes in membrane structure induced by electroporation as revealed by rapid-freezing electron microscopy. *Biophys. J.*, 58(1):1–12, 1990.

141. T.R. Gowrishankar, U.W.E. Pliquett, and R.C. Lee. Dynamics of membrane sealing in transient electropermeabilization of skeletal muscle membranes. *Ann. N.Y. Acad. Sci.*, 888:195–210, 1999.

142. M. Hibino, H. Itoh, and K Kinosita Jr. Time courses of cell electroporation as revealed by submicrosecond imaging of transmembrane potential. *Biophys. J.*, 64(6):1789–1800, 1993.

143. M. Pasek, J. Simurda, G. Christe, and C. H. Orchard. Modeling the cardiac transverse-axial tubular system. *Prog. Biophys. Mol. Biol.*, 96(1-3):226–243, 2008.

144. F. Bezanilla, E. Rojas, and Taylor. R. E. Sodium and potassium conductance changes during a membrane action potential. *J. Physiol.*, 211(3):729–751, 1970.

145. D. B. Bischoff, R. L. Dedrick, D. S. Zaharko, and J. A. Longstreth. Methotrexate pharmacokinetics. *J. Pharm. Sci.*, 60(8):1128–1133, 1971.

146. T. Hayashi, T. Miyati, J. Takahashi, K. Fukuzawa, H. Sakai, M. Tano, and S. Saitoh. Diffusion analysis with triexponential function in liver cirrhosis. *J. Magn. Reson. Im.*, 38(1):148–153, 2013.

147. P.S. Collier. The possible range of values for apparent volume of distribution at steady-state when disposition may be characterized by a tri-exponential function. *Int. J. Pharm.*, 18(3):345–352, 1984.

148. J. W. Henshaw, D. A. Zaharoff, B. J. Mossop, and Yuan. F. Electric field-mediated transport of plasmid DNA in tumor interstitium *in vivo*. *Bioelectrochemistry*, 71(2):233–242, 2007.

149. Mir. L. M. Nucleic acids electrotransfer-based gene therapy (electrogenetherapy): past, current, and future. *Mol. Biotechnol.*, 43(2):167–176, 2009.

150. A. C. Durieux, Bonnefoy. R., T. Busso, and D. Freyssenet. *In vivo* gene electrotransfer into skeletal muscle: effects of plasmid DNA on the occurrence and extent of muscle damage. *J. Gene. Med.*, 6(7):809–816, 2004.

151. F. Liu and L. Huang. A syringe electrode device for simultaneous injection of DNA and electrotransfer. *Mol. Ther.*, 5(3):323–328, 2002.

152. D. A. Zaharoff and Yuan. F. Effects of pulse strength and pulse duration on *in vitro* DNA electromobility. *Bioelectrochemistry*, 62(1):37–45, 2004.

153. J. W. Henshaw, D. A. Zaharoff, B. J. Mossop, and F. Yuan. A single molecule detection method for understanding mechanisms of electric field-mediated interstitial transport of genes. *Bioelectrochemistry*, 69(2):248–253, 2006.

154. T. R. Gowrishankar, W. Chen, and R. C. Lee. Non-linear microscale alterations in membrane transport by electropermeabilization. *Ann. N.Y. Acad. Sci.*, 858(Sep 11):205–216, 1998.

155. J. M. McMahon, E. Signori, K. E. Wells, V. M. Fazio, and D. J. Well. Optimisation of electrotransfer of plasmid into skeletal muscle by pretreatment with hyaluronidase – increased expression with reduced muscle damage. *Gene. Ther.*, 8(16):1264–1270, 2001.

156. D. Miklavcic, D. Semrov, H. Mekid, and L. M. Mir. A validated model of *in vivo* electric field distribution in tissues for electrochemotherapy and for DNA electrotransfer for gene therapy. *Biochim. Biophys. Acta*, 1523(1):73–83, 2000.

157. L. J. Leon and F. A. Roberge. A new cable model formulation based on green's theorem. *Ann. Biomed. Eng.*, 18(1):1–17, 1990.

Biography

Jonathan Preston Cranford

Born: December 28, 1980 in Durham, North Carolina

Education

Ph.D.	Biomed. Eng. (BME)	May 2014	Duke University	Durham, NC
M.S.	BME	Sept. 2008	Duke University	Durham, NC
B.S.	BME	May 2004	NC State University	Raleigh, NC

Associations and Honors

ASME: American Society of Mechanical Engineers

BMES: Biomedical Engineering Society

NCAS: North Carolina Academy of Science

Sigma Xi: The Scientific Research Society

Reviewer for paper submitted to *IEEE 2011 American Control Conference*

Graduated NC State University Summa Cum Laude with ASABE and Progress Energy scholarships; member of Phi Kappa Phi, Tau Beta Pi, and NSCS

Publications and Presentations

J. P. Cranford, B. J. Kim, and W. K. Neu. Asymptotic model of electrical stimulation of nerve fibers. *Med. Biol. Eng. Comput.*, 50(3):243-251, 2012.

J. P. Cranford and W. Krassowska. Electroporation in a three-dimensional, time-dependent model of a skeletal muscle fiber. *Dynamics Days 30^{th} Annual International Conference on Nonlinear Dynamics*, Chapel Hill, NC, 2011.

L. Guo, J. P. Cranford, J. C. Neu, and W. K. Neu. Activating function of needle electrodes in anisotropic tissue. *Med. Biol. Eng. Comput.*, 47(9):1001-1010, 2009.

J. P. Cranford, X. Zhao, and W. Krassowska. Guidelines for controlling pore radii from nonlinear analysis of a two-dimensional model of electroporation *Proc. ASME IMECE 2007*, 2:307-308, 2008.

J. Cranford and W. Krassowska. Effects of ionic concentrations on density and size of pores created by electric pulses. *Proc. 2006 BMES Annual Fall Meeting*, Chicago, IL, 2006.